Effects of interfacial interactions on optical switching in magnetic heterostructures

Pierre Vallobra

THÈSE

Pour l'obtention du titre de :

Docteur de l'Université de Lorraine

Spécialité : Physique

Présentée par :

Pierre VALLOBRA

Effects of interfacial interactions on optical switching in magnetic heterostructures

Thèse soutenue publiquement le 5 février 2019 à Nancy devant le jury suivant :

Mme Alexandra MOUGIN	Directrice de recherche, LPS Orsay	Rapportrice
M. Vincent BALTZ	Chargé de recherche, Spintec	Rapporteur
M. Alexey KIMEL	Professeur, Radboud University	Examinateur
M. Jeffrey MCCORD	Professeur, Kiel University	Examinateur
M. Juan-Carlos ROJAS-SANCHEZ	Chargé de recherche, Université de Lorraine	Co-directeur de thèse
M. Stéphane MANGIN	Professeur, Université de Lorraine	Directeur de thèse

Institut Jean Lamour, UMRS CNRS 7168
Université de Lorraine – Pôle M4 : matière, matériaux, métallurgie, mécanique

Table of contents

Acknowledgements

This manuscript could not have been written without the help of many important people. I would like to thank them sincerely. I first want to thank all the member of my jury: Alexandra Mougin, Vincent Baltz, Jeffrey McCord and Alexey Kimel. I appreciated their careful reading of my manuscript and their scientifically relevant remarks on my work that gave me new perspectives. It has also been a pleasure to answer their question and to discuss with them.

I need to mention the people that turned my stay at San Diego into a wonderful time. Eric Fullerton made this possible by gathering all the conditions for me to be able to work on new and exciting physics. Marina Robenko and Iris Villanueva also helped me a lot with my administrative paperwork. Despite his thesis redaction, Robert Tolley was really available, patient and kind to help us to work. I also would like to thank Jefffey Brock for all the great time we had together doing the measurements and citing Top gun references. It is always a great pleasure to work with him. I also enjoyed the discussion I had with Majd Kuteifan, Rajasekhar Medapalli, Sheena Patel and Mohammed Salah El Hadri. In general, I met nice people in San Diego and they all contributed to create unforgivable memories.

This manuscript is the fruit of several collaborations. It has been a true pleasure to work with Jung-Wei Liao and to welcome him in Nancy. The queen's cakes he brought made our experiment time way sweeter. Working with Soong-Geun Je was also a great experience. I liked his professionalism and he has been able to transmit me his interest in great physics while performing his experiments.

Je remercie toutes les personnes à Vinci Technologies avec qui j'ai travaillé. Renaud Presberg m'a chaleureusement accueilli dans ces locaux. J'ai eu plaisir à travailler avec Jean-Philippe Fauvarque, Jean-Marc Vannieuwenhuyse et Nicolas Turpin.

Il est maintenant temps pour moi de remercier les gens à l'I.J.L. qui ont fait de ces 3 ans de thèse une période heureuse pour moi. Mes directeurs de thèse, Stéphane Mangin et Juan-Carlos Rojas-Sanchez ont toute ma gratitude. Stéphane a su, dès le début, m'intéresser au nano magnétisme et m'a permis de réaliser ma thèse dans les meilleures conditions possibles. C'est une personne qui tire les gens vers le haut, à travers la confiance qu'il leur accorde et les moyens qu'il met à leur disposition pour réaliser leurs idées d'expériences. Carlos est mû par la passion de la recherche. Cela a donc été extrêmement motivant pour moi de travailler avec quelqu'un d'aussi enthousiaste et gentil. J'ai aussi beaucoup travaillé et appris avec Michel Hehn. Tous ses conseils sur la P.V.D. et sur le magnétisme en général m'ont été précieux. Luc Moreau, Stéphane Suire et Sami Hage-Ali m'ont énormément aidé à installer la P.V.D. dans le nouveau bâtiment et à l'utiliser dans des conditions optimales. Grégory Malinowski a, quant à lui, rendu possibles mes expériences sur le laser. Je remercie aussi Gwladys Lengaigne et Laurent Badie pour m'avoir permis d'utiliser la salle blanche dans les meilleures conditions. Isabelle Fournelle et Aurore Calmels Emenot sont des personnes avec qui je n'ai pas directement travaillé mais dont le bureau est toujours un lieu chaleureux et agréable. J'ai apprécié travaillé avec Hélène Fischer, Philippe Lambert, Alexis Lartigue et Corentin Jannier.

Je me dois aussi de remercier les autres membres permanents de l'équipe 101 avec qui je n'ai pas travaillé mais qui contribuent à avoir une bonne ambiance de travail: Thomas Hauet, Jon Gorchon, Julius Hohlfeld, Karine Dumesnil, François Montaigne, Sébastien Petit Watelot, Christine Bellouard, Daniel Lacour et Stéphane Andrieu. L'agréable compagnie des doctorants et postdoctorants de l'équipe est aussi à souligner. Je remercie donc Gauthier, Kosseila, Kaushalya, Vincent, Maryam, Thai Ha, Anton, Filip, Elmer, Crosby, Ibrahim, Quentin, Jean-Lois et Charles. Je suis aussi le parcours de Yassine à New York. Je lui souhaite le meilleur pour la suite, même si je me fais très peu de soucis pour lui. Yong Xu et Boyu Zhang ont été pour moi de formidables partenaires de travail. Ils m'ont de plus énormément aidé pour le post-doc en Chine. Je suis content d'avoir pu mettre à profit les pauses café passées avec Romain et Mickael pour pouvoir utiliser leur logiciel APREX. Que ce soit durant mon stage ou durant ma thèse, j'ai toujours pu trouver une excuse pour aller dans le bureau de Sylvie Robert, où il fait bon discuter. Je remercie aussi Ludovic, Olivier, Guillaume, Arnaud, Marion, Sarah et Chris avec qui j'ai pu partager de bons moments passés autour d'un café, d'une thé, d'une bière ou d'une tondeuse. Je remercie aussi les membres actuels du crew interéquipe de doctorants, la dream team: Kathleen, Julien, Huyen et Aurelia. Chaque soirée jeu, pause-café ou gâteau de la semaine aura compté pour moi (sauf les moments où je perds, ça c'est pas cool). Je ne sais pas si je peux inclure Miguel dans ce groupe mais j'ai quand même envie de le citer, donc je le fais dans cette phrase. Je remercie aussi mes compagnons de pizza, Philou et Thibaud. Malgré leur betatitude, je les tolère. Je n'ai pas grand-chose à dire sur eux. Je me suis beaucoup ennuyé en leur compagnie car ce sont des gens sans grand intérêt. Je remercie aussi mon sempiternel colocataire, Alex, de m'avoir supporté tout ce temps. D'un colocataire de circonstance, il s'est transformé en un ami incontournable. Je dédie ce manuscrit ma famille, mes parents et mes frères.

General introduction

A material can have different properties if it is in 2D (one monolayer) or in 3D (a bulk material). In order to have material properties close to the 2D case, we grow them in thin films of typical thicknesses in the range of the nanometer. After more than 2000 years of use of bulk magnetic materials, we have thus seen in the twentieth century the emergence of thin films magnetic materials. By engineering thin films into heterostructures, i.e stacked thin layers; it is possible to observe a wide range of magnetic behaviors.

In 1988 Fert and Grunberg, simultaneously evidenced the giant magnetoresistance (GMR) phenomenon in such magnetic heterostructures [1] [2]. This has been the pioneer phenomenon establishing the field of spintronic that paved the way toward the commercialization of hard disks. In hard disks, the information is encoded in magnetic bits and their reading can be performed thanks to this giant magnetoresistance. A magnetic bit is composed of several magnetic uncoupled grains. In order to have reliable bits, they need to be stable, to be written and read fast enough. The writing process actually consists in the switching of the magnetization of the bit. The manipulation of the magnetization is thus a subject of primary importance fundamentally and practically. The most intuitive way to perform it is with an external field, but it is also possible to do it with other methods, as for instance with a spin current. In 1996 Beaurepaire *et al.* reported the first manipulation of the magnetization with a laser [3] on the picosecond timescale. This attracted great interest since it made the scientific community think that an ultrafast writing of the magnetic bits could be possible using light. This idea gave birth to the field of femtomagnetism, an area that is gathering always more attention. In 2007 Stanciu *et al.* demonstrated that it is possible to reverse deterministically the magnetization in a thin film of GdFeCo with the adapted helicity of the circularly-polarized light [4]. A right helicity results in an “up” state of the magnetization (or a bit of value 1) and a left helicity results in a “down” state of the magnetization (or a bit of value 0). This helicity-dependent reversal of the magnetization is called AO-HDS (all optical helicity dependent switching). AO-HDS has been shown to occur for a wide range of materials including ferrimagnets [5], synthetic ferrimagnets [6] or ferromagnets [7]. In this manuscript I will first present the effect of circularly polarized light on different material stackings: ferromagnetic/ antiferromagnetic interfaces and rare-earth free synthetic ferrimagnets.

The hard drive is not the only data storage technology that has been proposed for application. In 2008 Parkin *et al.* proposed the racetrack memory architecture [8]. This has been extensively studied as a promising alternative memory where magnetic domains are moved along a track. However in order for this type of memories to be functional there is the need to move magnetic domain walls at velocities above 100m/s [8]. However due to the pinning of domain walls at defects, the domain wall velocity could encounter a limit and this technology has not been finalized yet. In 2013 Fert proposed to keep the architecture of racetrack memories but to replace domains by magnetic quasiparticles, named skyrmions. Due to the Magnus force those skyrmions should avoid the defects when they propagate and should then not be subjected to the pinning that limited domain wall displacement. The Dzyaloshiinsky-Moriya interaction [9] [10] (DMI) can give rise to technologically relevant skyrmions [11]. The study of the DMI is then crucial to be able to tune skyrmions properties later. In this

manuscript I will present experiments concerning the displacement of DMI-stabilized structures (homochiral Néel domain walls) and the generation of skyrmions using femtosecond light pulses.

All the samples presented in this document have been fabricated using a PVD (physical vapor deposition), namely a magnetron sputtering system. The studied samples are thin films of heterostructures have thicknesses in the range of the nanometer. The limited thickness of the layer we grow is important because several magnetic properties arise from the interfaces between the layers. This is the case for the perpendicular magnetic anisotropy of all our samples. It stems from an enhancement of the orbital moment at the interface that is normally quenched in a bulk material for transition metals [12]. The DMI in thin films is also an interfacial phenomenon. I grew most of the samples in Nancy on the PVD8, a sputtering machine that I developed with Vinci Technologies during my thesis. Vinci Technologies is a company involved in different fields among which is the ultra-high vacuum technology. This company sponsored my thesis so I could install a new sputtering tool in the Institut Jean Lamour in Nancy. Using this highly technological tool I could grow different heterostructures of high quality. Some others samples were grown in Spintec (Grenoble), the Cavendish Laboratory (Cambridge) and the CMRR of UCSD (San Diego).

This manuscript is divided in four chapters. In the first chapter I introduce all the notions necessary to understand the physics involved and the relevance of my work, in particular the energetic terms involved and the magnetic configurations they can result in. Then I describe all the experimental setups and methods I used to grow samples, to magnetically characterize them and to study the effects of femto-second polarized light. In a third chapter I study the behavior of heterostructures exposed to a polarized light, in particular ferromagnetic/antiferromagnetic bilayer and rare-earth free synthetic ferrimagnets. Concerning the ferromagnetic/antiferromagnetic bilayer, I show that it is possible to reset the exchange bias field by exposing it to pulses of circularly polarized light. The sign of the rest exchange bias field depends on the helicity of the light. In the rare-earth free synthetic ferrimagnets I demonstrate that it is possible to control the AO-HDS behavior by tuning material parameters. In the last chapter I focus on the creation and manipulation of magnetic structures stabilized by DMI. In particular, I demonstrate the field-driven propagation of homochiral Néel domain walls and the laser-induced generation of skyrmionic bubbles. I show field-driven measurements of displacement of homochiral Néel domain walls that do not fit in the current theory of propagation in the creep regime. I also demonstrate for the first time the laser-induced generation of Néel skyrmionic bubbles.

Introduction générale

Un matériau peut avoir différentes propriétés, selon qu'il soit en 2D (une monocouche) ou en 3D (un matériau massif). Pour avoir un matériau aux propriétés proches du cas en 2D, on le fait croître en film mince d'épaisseur typique de l'ordre du nanomètre. Après plus de 2000 ans d'utilisation des matériaux magnétiques massifs, nous avons observé lors du vingtième siècle l'émergence des matériaux magnétiques en couche mince. En incluant ces films minces dans des hétérostructures, c'est-à-dire des empilements de couches minces ; il est possible d'observer un large panel de comportements magnétiques.

En 1988, Fert et Grunberg ont mis en évidence, dans de telles hétérostructures, la magnétorésistance géante (GMR) dans deux travaux séparés [1] [2]. Cette découverte a donné naissance au domaine de l'électronique de spin. Dans les disques durs actuels l'information est codée en bits magnétiques et leur lecture s'effectue grâce à cette magnétorésistance géante. Un bit magnétique est constitué de plusieurs grains de la taille du micromètre non couplés entre eux. Afin d'avoir des bits fiables ils doivent être stables, s'écrire et se lire facilement. Ecrire un bit magnétique revient à fait à renverser l'aimantation du bit. La manipulation de l'aimantation est donc un sujet important fondamentalement et expérimentalement. La manière la plus intuitive de manipulation d'aimantation est d'utiliser un champ magnétique extérieur mais il est aussi possible de le faire par d'autre biais tel par exemple des courants de spin. En 1996 Beaurepaire *et al.* ont pour la première fois montré qu'il était possible de manipuler l'aimantation d'un matériau ferromagnétique par un laser [3]. Cette exposure au laser provoque une désaimantation survenant à l'échelle de temps de la picoseconde. Ce fut une découverte majeure qui laissa penser qu'il serait possible dans le futur d'écrire des bits magnétiques avec de la lumière à des échelles de temps extrêmement courtes. Cela donna naissance au domaine du femtomagnétisme, un pan de la recherche en pleine expansion. En 2007, Stanciu *et al.* ont prouvé qu'il était possible de renverser de manière déterministe l'aimantation d'une couche mince de GdFeCo en adaptant l'hélicité de la lumière polarisée circulairement [4]. Les conventions sont qu'une hélicité droite résulte en un état d'aimantation positif (ou un bit de valeur 1) et une hélicité gauche résulte en un état d'aimantation négative (ou bit de valeur 0). Ce retournement de l'aimantation dépendant de l'hélicité peut être abrégé en RTO-DH (retournement tout-optique dépendent de l'hélicité). Différentes études ont été conduites pour montrer qu'il est possible d'obtenir du RTO-DH dans différents matériaux tels des matériaux ferrimagnétiques [5], ferrimagnétiques de synthèse [6] or ferromagnétiques [7]. Dans ce manuscrit je présente l'effet de la lumière polarisée circulairement sur différents empilements de matériaux : des bicouches ferromagnétique/antiferromagnétique et des ferrimagnétiques de synthèse ne comportant pas de terre-rare.

Le disque dur n'est pas la seule technologie de stockage de données à avoir été proposée à des fins industrielles. En 2008, Parkin *et al.* ont proposé l'architecture de la « mémoire rail ». Cette technologie étudiée en tant qu'alternative prometteuse implique de déplacer des domaines magnétiques le long d'un rail. Cependant il faut pouvoir déplacer les parois des domaines magnétiques à une vitesse dépassant les 100 m/s afin que ce type de mémoire soit fonctionnel. Du fait du piégeage des parois de domaines aux défauts, la vitesse des parois de domaines est limitée. Cette technologie n'a pour l'instant pas été finalisée. En 2013 Fert a proposé de garder cette architecture de mémoire rail mais

de remplacer les domaines par des quasi particules magnétiques, les skyrmions. Par effet Magnus ces skyrmions doivent théoriquement éviter les défauts quand ils se déplacent et ne devraient donc pas être sensible à ce piégeage qui entrave la propagation des parois de domaine. L'interaction Dzyaloshiinsky-Moriya interaction [9] [10] (IDM) peut permettre d'obtenir des skyrmions technologiquement viables [11]. L'étude de l'IDM est donc essentielle afin d'être capable d'ajuster convenablement les propriétés des skyrmions. Dans ce manuscrit je présente des expériences ayant trait au déplacement de structures magnétiques stabilisées par l'IDM (des parois de domaine de Néel homochirales) et à la création de skyrmions par impulsions laser.

Tous les échantillons présentés dans ce document ont fabriqués en utilisant de la pulvérisation cathodique magnétron. Les échantillons étudiés (ou couches minces) ont des épaisseurs de l'ordre du nanomètre. L'épaisseur limitée des couches que nous faisons croître est important car plusieurs propriétés magnétiques résultent des interfaces entre les couches. C'est le cas de l'anisotropie magnétique perpendiculaire de tous nos échantillons Elle a pour origine une augmentation du moment orbital à l'interface alors que ce moment est nul dans un matériau massif pour les métaux de transition. L'IDM dans les couches minces est aussi un phénomène d'interface. J'ai fait croître mes propres échantillons à Nancy sur la PVD8, un instrument de pulvérisation cathodique magnétron que j'ai développé avec Vinci Technologies durant ma thèse. Vinci Technologies est une entreprise impliquée dans différents domaines comportant entre autres la conception d'instruments liés à l'ultravide. Cette entreprise a sponsorisé ma thèse afin que je puisse au terme de cette dernière installer le nouvel instrument de pulvérisation cathodique magnétron dans les locaux de l'Institut Jean Lamour à Nancy. Grâce à cet outil technologiquement avancé j'ai pu faire croître différentes hétérostructures de grande qualité. Il me faut aussi mentionner que certains échantillons ont aussi été élaborés à Spintec (Grenoble), le laboratoire Cavendish (Cambridge) et le CMRR à UCSD (San Diego).

Ce manuscrit est divisé en quatre chapitres. Dans le premier chapitre j'introduis les notions nécessaires à la compréhension des phénomènes physiques discutés, en particuliers les termes d'énergies qui s'appliquent et les différentes configurations magnétiques qui peuvent en résulter. Ensuite je décris les dispositifs expérimentaux utilisés et les méthodes que j'ai utilisées pour fabriquer les échantillons, les caractériser magnétiquement et étudier les effets de la lumière femtoseconde polarisée circulairement. Dans un troisième chapitre j'étudie le comportement d'hétérostructures exposés à la lumière polarisée, en particulier des interfaces ferromagnétique/antiferromagnétique et des ferrimagnétiques de synthèse. Dans le dernier chapitre je me concentre sur la création et la manipulation de structures magnétiques stabilisées par l'IDM. En particulier je traite de la propagation de parois de domaine de Néel homochirales par champ magnétique et de la génération de bulles skyrmioniques par laser.

I) Theoretical background

The field of magnetism is a vast and complex subject of study and it would be impossible to cover all of its aspect in a thesis. In this part I present the basic principles ruling magnetic materials, especially thin films. I first describe the most important interactions and then present some particular magnetic configurations, for instance domain walls or skyrmions. I then present the exchange bias, a phenomenon that can occur when a ferromagnetic material is interfaced with an antiferromagnetic material. Finally I introduce ultrafast manipulation of the magnetization using ultrafast femtosecond laser pulses.

I.1) Basic notions of magnetism

In this part, I introduce the fundamental concepts of magnetism that are needed for a clearer comprehension of the manuscript, namely magnetic interactions and the resulting magnetic configurations.

I.1.1) Origin of magnetism

In general, an electron possesses two magnetic momenta; the orbital one $\overrightarrow{\mu_L}$ and the momentum of spin $\overrightarrow{\mu_S}$. Both are proportional to corresponding angular moments. They are expressed as follows:

$$\overrightarrow{\mu_L} = -\mu_B g_L \vec{L} \quad \text{and} \quad \overrightarrow{\mu_S} = -\mu_B g_S \vec{S} \tag{1.1}$$

Where $g_L = 1$ and $g_S = 2.0023$ are the Landé factors for the orbit (g_L) and the spin (g_S) respectively and $\mu_B = \frac{eh}{4\pi}$ is the Bohr magneton. The existence of an orbital angular momentum can be understood easily in a classical Bohr model of an electron orbiting around the nucleus. This momentum is just a kinetic moment of the rotation $\overrightarrow{L} = \vec{r} \times \vec{p}$. Even though it is tempting to understand the spin momentum with a classical picture of an electron spinning around itself this analogy is not rigourous. In 1922 Stern and Gerlach performed an experiment where they observed that the total magnetic magnetic moment of an isolated Ag atom with an external magnetic field takes discrete values. Since in Ag atoms the orbital moment is equal to zero, their net magnetic moments arise from the spin momentum. This is the first hint of the existence of the spin momentum and it at the same time demonstrated the limit of a classical model. For one atom we must consider all its electrons to obtain its net magnetization $\vec{M}$. Its expression is then in a solid:

$$\vec{M} = \frac{\sum_i \overrightarrow{\mu_i}}{V} \tag{1.2}$$

In this manuscript we will focus on the study of many atoms and then consider the magnetization of a wide volume. To have a standard notation we consider for the rest of the manuscript the quantity $\vec{M}$ as the total magnetization per unit of volume.

While most of the atoms are magnetic (the total magnetic moment is not equal to zero), a solid formed of magnetic materials is not necessarily magnetic if no external magnetic field is applied. The response

of a material to an external magnetic field is characterized by the magnetic susceptibility χ defined by $\vec{M}=\chi\vec{H}$, $\vec{H}$ being the applied field. For diamagnetic materials χ is a negative constant, for paramagnetic materials χ is a positive constant. For ferromagnetic materials χ is a matrix which values evolve with $\vec{H}$ and the magnetic history of the materials.

I.1.2) Magnetic interactions

Magnetic moments are subject to various interactions associated with different energy terms. The most important interaction terms are developed in this part. Those can be found in more details specific [13] [14].

I.1.2a) Zeeman interaction

A magnetic moment follows the external applied field $\overrightarrow{H_{ext}}$. This is called the Zeeman effect. The associated energy is expressed as:

$$E_{Zee} = -\mu_0 \, \vec{\mu}.\overrightarrow{H_{ext}} \tag{1.3}$$

This term tends to align a local magnetic moment $\vec{\mu}$ with an external field. The working principle of the magnetic compass relies on this interaction.

I.1.2b) Dipolar interaction

The dipolar field is the field created by a dipole of magnetic moment $\vec{\mu}$. If r is the distance of the magnetic moment $\vec{M}$ from the magnetic dipole the form of the dipolar field felt at this point of the space is:

$$\overrightarrow{H_{dip}} = \frac{1}{4\pi}\left[\frac{3(\vec{\mu}.\vec{r}).\vec{r}}{r^5} - \frac{\vec{\mu}}{r^3}\right] \tag{1.4}$$

The interaction between this field created by a dipole and the magnetic moment $\vec{M}$ is a Zeeman one and the resulting expression of the energy is:

$$E_{dip} = -\mu_0 \, \vec{\mu}.\overrightarrow{H_{dip}} \tag{1.5}$$

If we consider a bulk sample we have many dipoles that act at a long range so all the generated dipolar fields add to form a total field called the demagnetizing field $\overrightarrow{H_{dem}}$ that is opposite to the total magnetization if all the moments are parallel. This field depends on the shape on the sample for a uniform magnetization. Its general expression is:

$$\overrightarrow{H_{dem}} = -4\pi \, \overline{\overline{N_d}}.\overrightarrow{M_T} \tag{1.6}$$

$\overline{\overline{N_d}}$ is a demagnetization tensor that depends on the shape of the sample and $\overrightarrow{M_T}$ the total magnetic moment of the whole sample. If we consider a thin film elongated in the x and y direction we have N_{zz}=1 and the rest of the coefficients equal to 0. The resulting energy is:

$$E_{dem} = -\frac{1}{2}\mu_0 \overrightarrow{M_T}.\overrightarrow{H_{dem}} = 2\pi\mu_0 M_Z^2 = 2\pi\mu_0 M_S^2 cos^2\theta \quad (1.7)$$

θ is the angle between the magnetization and the demagnetizing field. We can notice that in this expression the demagnetizing field helps to put the magnetization in the plane of the sample.

I.1.2c) Magnetocristalline and effective anisotropy

In a bulk magnetic crystal there are some preferred directions of the total magnetization depending on the crystallographic structure. Those directions are called easy axis of magnetization (or just "easy axis" for convenience). For example in rare earth materials the crystal field sets the orbitals in preferred directions and has then an indirect effect on the spin through the spin-orbit coupling. In many cases and in the rest of this manuscript the anisotropy is considered uniaxial along the axis perpendicular to the plane of the sample and it gives the following expression:

$$E_K = -KVcos^2\theta \quad (1.8)$$

θ is the angle between the magnetization and the main magnetocristalline anisotropy axis. In practice the magnetic anisotropy depends on more phenomenon than just the bulk anisotropy. Thus we use an effective anisotropy term that includes the volume effects (K_V), the interfacial effects (K_S) and the demagnetizing field. Looking at the form of this anisotropy term in equation (1.8) one can observe that the demagnetization energy (1.7) can be written the same way. The expression of K_{eff} for a perpendicular easy axis of magnetization:

$$K_{eff} = K_V + \frac{K_S}{t} - 2\pi\mu_0 M_S^2 \quad (1.9)$$

The interfacial contribution of anisotropy (K_S) predicted by Néel [15] allows often in thin films to have a perpendicular magnetic anisotropy (PMA) axis. It is due to the hybridization at the interface between two materials. For instance this is the case in Co/Pt thin multilayers as we will discuss later. It is then of primary important to have thin layers of magnetic materials to increase the surface contribution of the anisotropy compared to the demagnetizing field and, to have a perpendicular anisotropy.

I.1.2d) Exchange interaction

Since electrons are fermions they are subject to the principle of exclusion of Pauli. This prohibits two electrons to be in the same exact state and forces the wavefunction of the electron to be antisymmetric. A consequence of this and the Coulomb interaction is the existence of an exchange interaction between two neighbor electrons having overlaps in their wavefunction. Its corresponding energy for two neighbors spins $\overrightarrow{S_1}$ and $\overrightarrow{S_2}$ is:

$$\varepsilon_{ex} = -2J_{12}\overrightarrow{S_1}.\overrightarrow{S_2} \quad (1.10)$$

J_{12} is called the exchange interaction constant (or integral).

There is also the analog of this formula for magnetic moments with A the exchange stiffness:

$$E_{ex} = -\mu_0 A_{ex}\overrightarrow{\mu_1}.\overrightarrow{\mu_2} \quad (1.11)$$

In practice we use an exchange stiffness between two neighbor atoms. Let us consider first the case of a material composed only of 1 chemical element (for instance Co). If A is positive, the magnetic moments of the Co atoms tend to align parallel and a net magnetic moment can arise. In this case the material is ferromagnetic. If A is negative, like in Mn, the magnetic moments on the atoms tend to set antiparallel with their neighbors and, there is no total magnetic moment. In this case the material is antiferromagnetic. The case of an alloy is a bit more complex. Let us consider the example of a CoTb alloy. In this material $A_{Co\text{-}Co}$ and $A_{Tb\text{-}Tb}$ are positive while $A_{Co\text{-}Tb}$ is negative and the magnetic moments of Co and Tb atoms are different. This results in two sublattices (one of Co and one of Tb) antiferromagnetically with each other. Depending on the relative concentration of Co and Tb the net magnetization can either be mainly along Tb moment or along Co moments. Such a material with sublattices of opposite directions of magnetization is ferrimagnetic. Any magnetic order set by the exchange interaction (ferromagnetic, ferromagnetic, and antiferromagnetic) is in competition with the thermal fluctuations. If the thermal energy is higher than the exchange energy the magnetic order is broken and the material is paramagnetic. The temperature of transition between a magnetically ordered state and a paramagnetic state is called the Curie temperature (T_C) for ferromagnetic and ferrimagnetic materials while it is called Néel temperature (T_N) for an antiferromagnetic material.

This exchange interaction exists between all the neighbor magnetic moments in a layer but also between two layers, for instance between a Co and an IrMn layer or a Co and a Ni layer as we will notice later in this manuscript.

I.1.2e) DMI interaction

The existence of a non-collinear interaction between neighbor spins has been discussed by Moriya in 1957 [9] from symmetry arguments in crystals. Its origin has been attributed to the spin orbit coupling in 1960 by Moriya [10] that found the following expression of the corresponding energy:

$$E_{DMI} = \overrightarrow{D_{12}}.(\overrightarrow{S_1} \times \overrightarrow{S_2}) \quad (1.12)$$

In this expression two spins are considered and $\overrightarrow{D_{12}}$ is oriented perpendicularly to the segment between the spins 1 and 2. This anisotropic exchange interaction is called the Dzyaloshinsky-Moriya interaction (DMI). This expression has been generalized by Fert and Levy in 1980 to spin glasses doped with heavy metal impurities [16]. The mechanism is not exactly the same since the DMI's previous expression came for the direct calculation of two interacting particles with a strong spin-orbit coupling (a 2 site interaction) while the 1980 one comes from the interaction of two spins through an metallic atom of high spin-orbit coupling (a 3 site interaction). In 1990 [17] Fert predicted that this 3 site interaction should also exist in thin films at the interface between a magnetic layer and a layer of a material with a high spin-orbit coupling (for instance Pt or Au) as shown on figure I.1. Two features are

mandatory for the existence of a net DMI: a high spin-orbit coupling and no central symmetry in a unit cell. In a central symmetry there is a punctual the DMI energy between two or three atoms but the total DMI energy in one unit cell is zero.

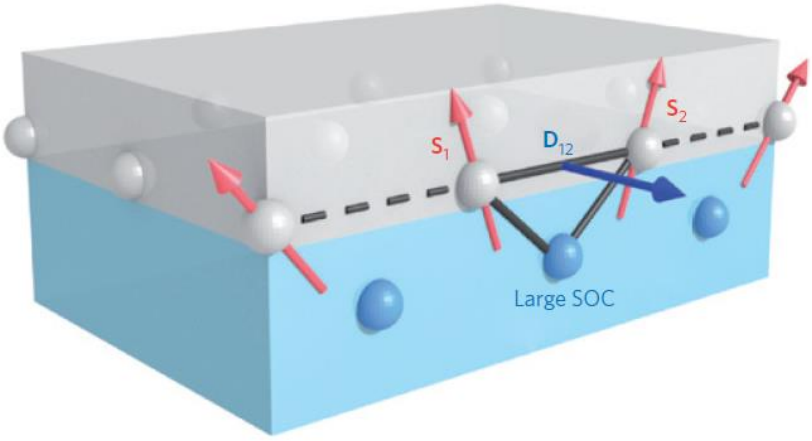

Figure I.1: Sketch of a DMI at the interface between a ferromagnetic metal (grey) and a metal with a strong SOC (blue). The DMI vector D_{12} related to the triangle composed of two magnetic sites and an atom with a large SOC is perpendicular to the plane of the triangle. Because a large SOC exists only in the bottom metal layer, this DMI is not compensated by a DMI coming from a symmetric triangle. Extracted from [18].

Let us focus on the 3 site DMI since it is the one present in our thin film heterostructures. For a better comprehension we consider the concrete example depicted in figure I.2.

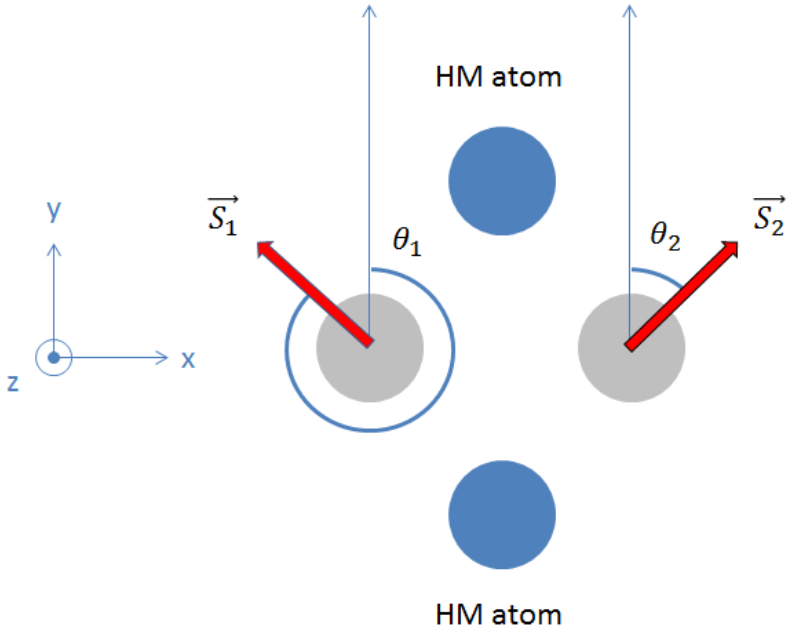

Figure I.2: Schematic of the angles involved in equation 1.13. of two heavy metal (HM) atoms interact with two spins, $\overrightarrow{S_1}$ and $\overrightarrow{S_2}$ respectively.

In this case, the two spins are coupled together through the top HM atom and through the bottom HM atom. The top and bottom HM atoms are in the example considered to be from the same chemical element (for instance Pt). If we consider the DMI from the bottom HM we obtain the following energy:

$$E_{DMI}^{bottom} = \overrightarrow{D_{12}^{bottom}} . (\overrightarrow{S_1} \times \overrightarrow{S_2}) \quad (1.13)$$

$$E_{DMI}^{bottom} = D\vec{z} . ([\|\overrightarrow{S_1}\|(\cos(\theta_1)\,\vec{y} + sin(\theta_1)\vec{x})] \times [\|\overrightarrow{S_2}\|(\cos(\theta_2)\,\vec{y} + sin(\theta_2)\vec{x})]) \quad (1.14)$$

$$E_{DMI}^{bottom} = \|\overrightarrow{S_1}\|\|\overrightarrow{S_2}\| D\vec{z}.[(sin(\theta_1)\cos(\theta_2) + sin(\theta_2)\cos(\theta_1)]\vec{z} \quad (1.15)$$

$$E_{DMI}^{bottom} = \|\overrightarrow{S_1}\|\|\overrightarrow{S_2}\|\, D\, \sin(\theta_1 - \theta_2) \quad (1.16)$$

To minimize the energy in expression 1.16, $\overrightarrow{S_1}$ and $\overrightarrow{S_2}$ must be perpendicular. The DMI gives then rise to whirling magnetic configurations as in figure I.1. If we now consider the total DMI energy for those two atoms, we obtain:

$$E_{DMI}^{total} = E_{DMI}^{bottom} + E_{DMI}^{top} \quad (1.17)$$

$$E_{DMI}^{total} = \overrightarrow{D_{12}^{bottom}} . (\overrightarrow{S_1} \times \overrightarrow{S_2}) + \overrightarrow{D_{12}^{top}} . (\overrightarrow{S_1} \times \overrightarrow{S_2}) \quad (1.18)$$

$$E_{DMI}^{total} = D\vec{z} . (\overrightarrow{S_1} \times \overrightarrow{S_2}) + D(-\vec{z}). (\overrightarrow{S_1} \times \overrightarrow{S_2}) = 0 \quad (1.19)$$

This result from equation 1.19 can be expanded to the case of a magnetic layer sandwiched between two layers composed of the same heavy metal, where there is thus there is no total DMI. If the two DMI constants for the top and the bottom interfaces are different there can then be a non-zero total DMI. For a given heavy metal/ferromagnetic (HM/FM) interface, even the sign of D depends on the materials involved. Indeed at a Pt/Co interface D is negative [19] while it is positive for a Pt/Ni interface [20].

In theory, if we have a stack HM_1/FM/HM_2 where HM_1= HM_2, the total DMI is equal to zero, however it is not always the case in practice. Theoretically, D at an interface depends only on the atoms at the interface, but in practice it varies according to different factors (roughness, intermixing …) that are still debated in the scientific community [20]. For instance in a Pt/Co/Pt layer there can be a non-zero total DMI because the roughness is different for the top and the bottom interfaces.

I.1.3) Magnetic configurations

The knowledge of the energetic contributions leads to the deduction of the main magnetic configurations they can create. The most stable magnetic configurations are obtained by minimizing the total energy given by the sum of the different contributions we have seen in section I.1.2.

I.1.3a) Magnetic domains

In 1907, Pierre Weiss postulated that in a magnetic material there can be domains of uniform magnetization that can be stable through a molecular field. It is known today that such domains exist to minimize the total energy. For instance if we consider in a simplistic model only the dipolar and the exchange energy we can justify the existence of such domains. While the exchange interaction tends to align neighbor magnetic moments, the dipolar one acts on a long range and tends to put moments antiparallel. Those domains of uniform magnetization are called Weiss domains. Examples of domain configurations are shown on figure I.3.

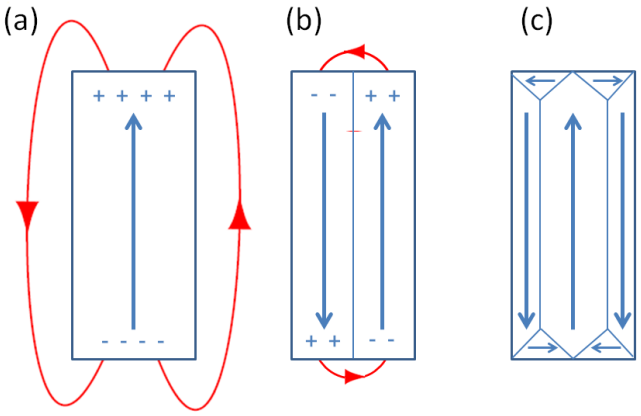

Figure I.3: Different magnetic domain configurations. The arrows represent magnetic moments and the (+) and (-) the local magnetic charges. (a) Single domain, (d) two domains and (c) complex multidomain state. Adapted from [21].

I.1.3b) Domain walls

Between two magnetic domains of opposite magnetization there exists a magnetization configuration called domain wall (DW). Domain walls are governed by the competition between exchange interaction and the effective anisotropy. Considering only those two energy terms we have the following expressions for the DW width (δ) and the DW density of energy per area (σ_0) respectively [14]:

$$\delta = \pi\sqrt{\frac{A}{K}} \tag{1.20}$$

$$\sigma_0 = 4\sqrt{AK} \tag{1.21}$$

There are several types of DWs but two of them are often encountered or used for modelling. The first one is the Bloch DW (shown in figure I.4.a)) where the rotation of the magnetization occurs in planes perpendicular to the normal vector of the domain wall. The other type is the Néel wall (shown in figure I.4.b)) where the magnetization rotates in the plane of the DW.

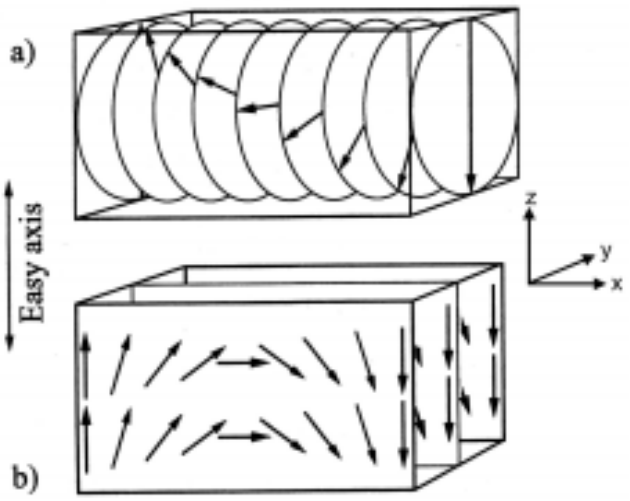

Figure I.4: Sketches of a (a) Bloch and (b) Néél domain wall configuration in sample exhibiting perpendicular magnetic anisotropy. Extracted from [22]

If the effective anisotropy axis lies in the plane of the sample then the domain walls have a Bloch type for a thickness above a critical thickness (this thickness depends on the material parameters) and a Néel type for below the critical thickness because of the dipolar field. For an effective anisotropy axis perpendicular to the plane of the film it is not that simple and the DW type depends on the DMI.
Without any DMI the films having a thickness above the critical one have Néel domain walls while the films with a thickness below the critical thickness should exhibit Bloch walls. In contrast, if the DMI is strong, Bloch walls are not favored anymore in thin films but monochiral Néel DWs are [23].
The two different chiralities of Néel DWs are shown on figure I.5 for a better illustration. The sign of the DMI determines which chirality is preferred in the film (clockwise or anti-clockwise). This can be seen from equation 1.16. Thus, the nature of the domain walls is a good indicator for the presence of a DMI and its sign. Along this line, SPLEEM observations of the DW in samples with different stacks were used to confirm the correlation between DMI and surface engineering in [Co/Ni] multilayers in contact either with Pt or Ir [24].

Figure I.5: Clockwise and anti-clockwise configurations for a Néel DW in a sample with an out of plane easy axis of magnetization. Each arrow represents a magnetic moment.

The switching of the total magnetization using an applied magnetic field occurs through two main processes: either a coherent rotation of the magnetization over the whole sample or a combination of nucleation and expansion of magnetic domains. The expansion of a domain occurs via propagation of

the domain wall separating adjacent domains. The propagation of DWs in magnetic films induced by an external out-of-plane magnetic field has been extensively studied. In an ideal magnetic system where no defects are present, the DW velocity depends first linearly on the applied field (steady motion) until it reaches a critical field called the Walker field (figure I.6.a)). Then the velocity of the DW decreases when increasing the applied field until it reaches back a linear regime (precessionnal motion). This decrease of the velocity with increasing H for $H \geq H_W$ is called the Walker breakdown and is linked to a wider precession of the magnetization of the domain wall in the plane of the sample.

A distinctly different behavior, as shown on figure I.6.a) is found when defects pinning the domain wall are present. For a low applied field H (or driving force f) the DW movement is in a creep regime [25]. In such a regime the pinning energy of the defects is too larger than the energy brought by an applied field and the slow movement of the DW relies on thermally activated jumps between the pinning sites. The expression of the velocity in the creep regime as a function of temperature and applied field is given by [26] :

$$v = v_0 \exp[-\left(\frac{T_{dep}}{T}\right)\left(\frac{H_{dep}}{H}\right)^{\frac{1}{4}}] \quad (1.22)$$

T_{dep} is defined as U_C/k_B with U_C being the height of the energy barrier at a pinning site. H_{dep} is the depinning field, the field needed to overcome the pinning energy barrier.

At higher fields the system is in a depinning regime where the pinning effect of defects is weak compared to the field. Finally the DWs reach a flow regime where there is no influence of the pinning points anymore and the velocity of the DWs evolves linearly as a function of the applied field. We can note that at high fields the propagation is both in the flow and precessionnal regimes.

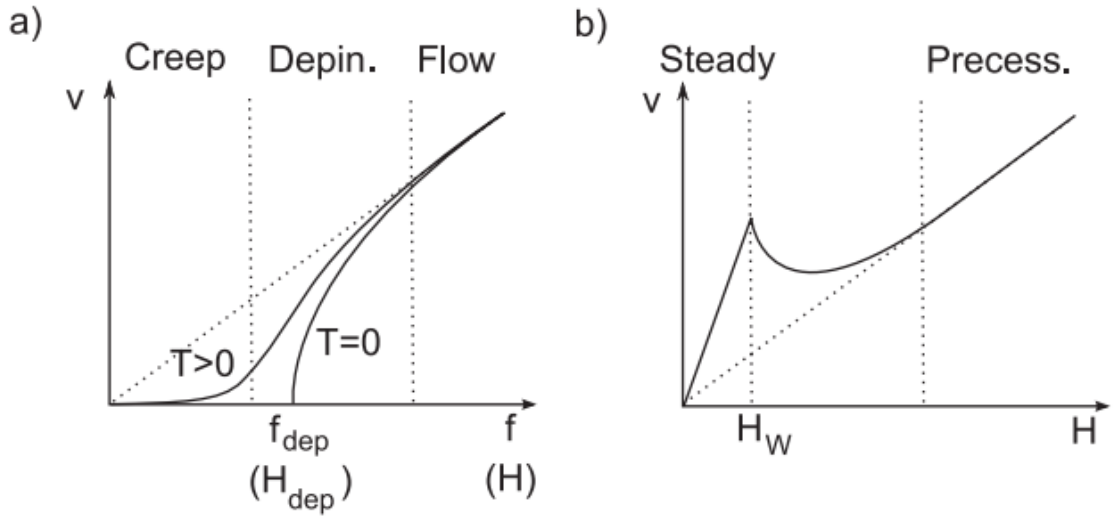

Figure I.6: (a) Theoretical variation of the velocity, *v*, of a 1D interface (domain wall) in a 2D weakly disordered medium submitted to a driving force, *f* (magnetic field, *H*), at zero and finite temperature, *T*. The creep, depinning, and flow regimes are labeled. (b) Regimes of domain-wall flow motion in an ideal ferromagnetic film without pinning. The steady and precessional linear flow regimes are separated by an intermediate regime which begins at the Walker field, H_W. Extracted from [27].

Measurements of DW velocities within the (x,y) plane of thin films with a perpendicular easy axis of magnetization can be used to measure DMI. We consider the simple case of a domain propagating along the x axis due to the magnetic field H_X. H_X is fixed and its sign depends on the propagation direction of the domains. Thus we can easily rewrite equation 1.22 as:

$$\mathrm{v} = \mathrm{v}_0 \exp\left[-\alpha(H_X) H_Z^{-\frac{1}{4}}\right] \tag{1.23}$$

α is a function of H_X with the expression :

$$\alpha(H_X) = \alpha(H_X = 0)\left[\frac{\sigma_{DW}(H_X)}{\sigma_{DW}(0)}\right]^{1/4} \tag{1.24}$$

$\sigma_{DW}(H_X)$ is the surface energy density of the domain wall. In our problem, it depends on several parameters including H_{DMI} the effective field associated with the DMI, σ_0 the energy density of a Bloch DW, δ the DW width, K_D the anisotropy energy, M_S the magnetization at saturation. By minimizing the surface energy density we can find its equilibrium expression as a function of these parameters :

- For $\frac{4K_D}{M_S\pi} > |H_X + H_{DMI}|$: $\sigma_{DW}(H_X) = \sigma_0 - \frac{\delta\pi^2 M_S^2}{8K_D}(H_X + H_{DMI})^2$
- For $\frac{4K_D}{M_S\pi} \leq |H_X + H_{DMI}|$: $\sigma_{DW}(H_X) = \sigma_0 + 2\delta K_D - \delta M_S\pi|H_X + H_{DMI}|$ (1.25)

In 2013 Je *et al.* generated round domains in a Ta(5nm)/ Pt(2.5nm)/Co(0.3nm)/Pt(1.5nm) sample with a perpendicular easy axis of magnetization grown by sputtering on a SiO_2 substrate. They generated round domains and applied an in plane field H_X of various strength. They then pulsed an out-

of-plane field H_Z =30 Oe. The image was taken with a magneto-optical Kerr effect microscope a single domain after each pulse and obtained the figure I.7.

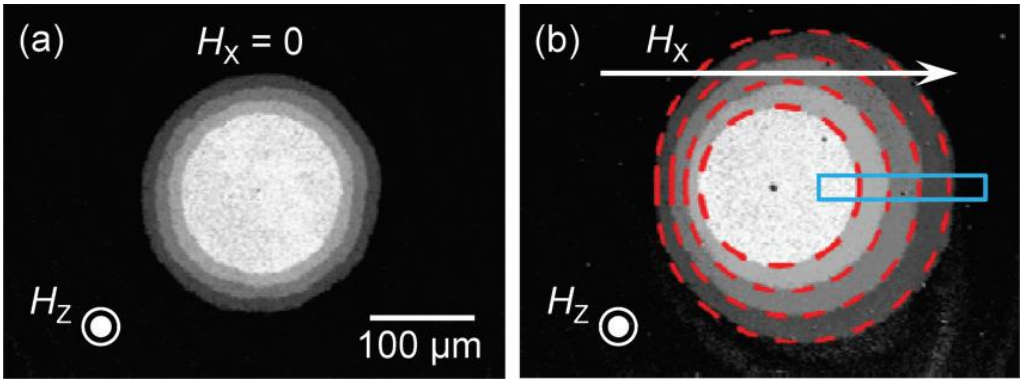

Figure I.7: Images of domain expansion by OOP field in a Pt/Co/Pt single layer for (a) H_X = 0 Oe and (b) H_X = 500 Oe. For each in plane field value the images are obtained by superposing the images taken each one after 4 consecutive pulses of out-of-plane field. Extracted from [28]

It is remarkable that for a zero in plane field the domain propagates in all directions while it propagates more in the direction of the field for H_X = 500 Oe. This result is in accordance with the present theory of DMI. For a zero H_X, the domain walls around the central domain have all the same chirality, the clockwise one and their energy is the same. Once a 500 Oe field is applied the symmetry is broken. For instance we compare the left and right DWs. For both sides the DMI term tends to make the chirality clockwise while the Zeeman term related to H_X tends to make the left domain chirality anticlockwise and the right domain chirality clockwise. The total energy is then lower for the right domain wall and its velocity higher than the left DW. This has also been deduced from the creep regime propagation law.

In this expression for a positive applied field H_X is positive on the right side of the domain and negative on the left side of the domain. When $H_X = -H_{DMI}$ the function v=f(H_X) has a local minimum so the value of H_{DMI} can be theoretically deduced from this graph. This method has then been extensively used to determine the strength of the DMI [29], [30], [31]. However this technique has been controversial. For instance Lavrijsen *et al.* claimed that the hypothesis of an effective field accounting for the DMI interaction is invalid and that a more precise expression of the DW energy is needed in some cases to obtain the DMI value [32]. Jué *et al* also claim that a dissipative term in the DMI expression should be taken into account to fit their data [33].

I.1.3c) Skyrmions

In 1962 Skyrme [34] predicted theoretically the existence of specific quasi-particles, skyrmions that in their magnetic form represent an intense subject of study. A skyrmion is a non-colinear texture that istheoretically topologically protected because it carries a topological charge. In the case of magnetic skyrmions this topological protection is in number S that measures the winding of a magnetic structure and its definition in the 2D limit is:

$$S = \frac{1}{4\pi} \int \vec{m}.(\partial_x \vec{m} \times \partial_y \vec{m}) dxdy \quad (1.26)$$

A skyrmion has a topological winding number being equal to ±1. A magnetic object cannot be transformed continuously into another magnetic object of a different topological number. For example a uniform magnetized domain has a topological number equal to zero so a skyrmion is theoretically topologically protected. In practice skyrmions have a protection that is associated with a finite energy barrier and they can be generated from ferromagnetic states by various ways, the most studied one is with current [35] [36] [37] [38] [30] [39].

The investigation of DMI in magnetic thin films was motivated by the search for those very promising for technological applications quasi particles. In thin films magnetic skyrmions are of two types: Bloch and Néel ones as seen on figure I.8. A Néel skyrmion is a round magnetic configuration where the magnetization rotates in its diameter in the radial direction like a Néel wall whereas in a Bloch skyrmion the magnetization rotation occurs in a plane perpendicular to the radial direction. Like domain walls, skyrmions in ultrathin films are Néel ones with a fixed chirality due to the DMI. From the technological point of view skyrmions in magnetic thin films could be integrated in racetrack memories [18]. The principle of a racetrack memory is a track with many magnetic domains, the magnetization of a domain corresponds to a bit and this domain is moved with a current to a field sensor in order to read the encoded information [8].
Because of the pinning of DW at structural defects that prevents currents to shift domains quickly enough to allow adequate data rates, racetrack memories are not today industrially implemented. However magnetic domains could be replaced by skyrmions in racetrack memories because magnetic skyrmions are subjects to the Magnus force that can allow them to avoid the structural defects.

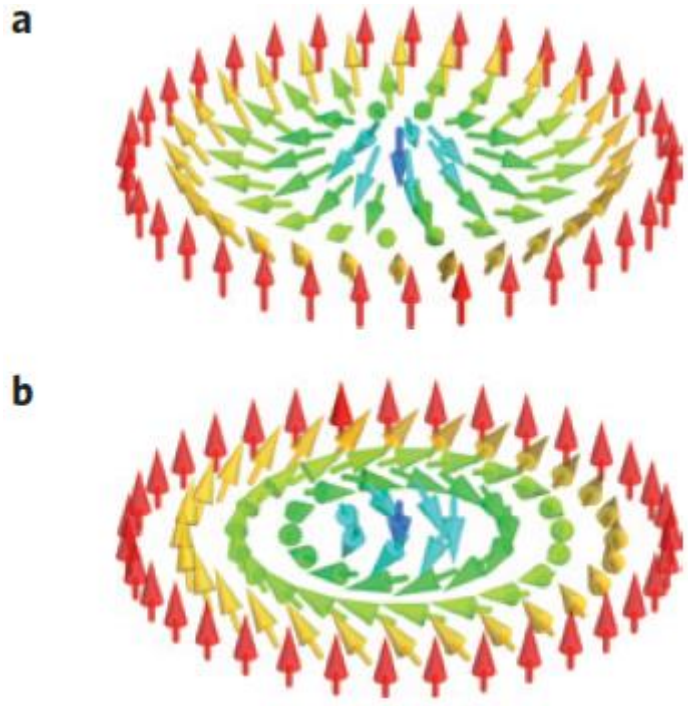

I.8: Sketches of a (a) Néél, and a (b) Bloch skyrmion in a sample exhibiting an out of plane easy axis of magnetization. Each arrow represents a magnetic moment. Extracted from [40]

Magnetic skyrmions were first exhibited in 2009 in bulk crystal [41] [42] [43]. Their formation in bulk crystals arises from the 2 site DMI interaction. In 2011 the first skyrmions in magnetic thin films were observed thanks to a 3 site DMI interaction [44] under room temperature in a Fe monolayer grown on top of an Ir(111) surface. Since 2015 many different engineered stacks have been exhibited to have skyrmions at room temperature, for instance Fe/Ni [45], $[Pt(4.5\ nm)/CoFeB(0.7\ nm)/MgO(1.4\ nm)]_{15}$ and $[Pt(3\ nm)/Co(0.9\ nm)/Ta(4\ nm)]_{15}$ [46], Pt/Co/MgO [47], Ir/Fe/Co/Pt [48] or Pt/Ni/Co/Ni/Au/Pt [30]. There are still challenges to be addressed to have skyrmions suitable for industrial purposes. They need to be small enough to have a high storage density (typically their radii must be under 10 nm), to be able to move quickly thanks to a low current density, to be easily generated, detected and deleted. All those aspects are well described in a 2017 review [49].

In this manuscript I will shed light on a specific way of generating skyrmions. The laser induced generation of skyrmions is the method we chose to study in this manuscript. It has not been extensively explored yet. In 2013 Finazzi *et al.* first generated skyrmions in a ferromagnetic alloy thanks to dipolar coupling using light but those were not homochiral [50]. In 2018, Berruto *et al.* have been able to generate skyrmions with light but in cryo-LTEM below room temperature [51].

In 2016 Jiang *et al.* were able to generate what they named skyrmion bubbles at room temperature with an electric current as seen on figure I.9. Those objects are round magnetic configurations with a radius in the order of the micrometer with a fully saturated core surrounded by a shell of homochiral Néel wall. Skyrmion bubbles share many features with skyrmions like a topological winding number being equal to ± 1 or the possibility to be moved by current.

The difference between skyrmions and bubbles is actually a subject of debate since there can be intermediate sizes between the skyrmion bubble and the skyrmion [52] [53] [54]. Skyrmion bubbles seem to be technologically irrelevant because of their large width but they are interesting subjects of study since they share many features with skyrmions. Observing a phenomenon on skyrmion bubbles can help to predict what can occur for skyrmions.

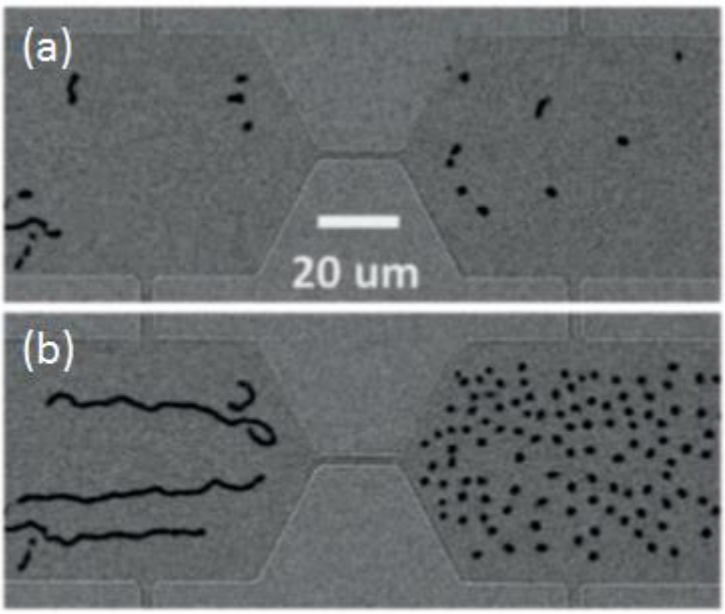

Figure I.9: Sparse irregular domain structures are observed at both sides of the device at a perpendicular magnetic field of B=0.5 Oe (b) Upon passing a current density of $j_e = 5 \times 10^5$ A/cm^2 through the device, the left side of the device develops predominantly elongated stripe domains, whereas the right side converts into dense skyrmion bubbles. Extracted from [55].

I.2) Exchange bias

I.2.1) Discovery of the phenomenon

Evidenced in 1956 by Meiklejohn and Bean [56], the exchange bias phenomenon has been then extensively studied in magnetic multilayers. Their pioneer experiment has been performed on a fine particle of cobalt. The external part of this particle was oxidized, resulting in a CoO shell and a ferromagnetic core of Co. Then a field sufficient enough to saturate the Co core was applied and the fine particle was cooled from 300K to 77K. At room temperature the CoO shell is paramagnetic and it is antiferromagnetic below 77K. A torque magnetometry measurement was performed and instead of a simple uniaxial anisotropy of the Co core they observed a unidirectional anisotropy. A shift of the hysteresis cycle of the Co particle was observed as seen on figure I.10. The sign of the shift in the hysteresis cycle depended on the sign of the applied field. At the time they already understood that this effect was due to the interface between the ferromagnetic Co and the antiferromagnetic CoO. What they called “exchange anisotropy” is today labeled as “exchange bias” since we have understood that it comes from the exchange interaction at the interface between the ferromagnetic and the antiferromagnetic materials.

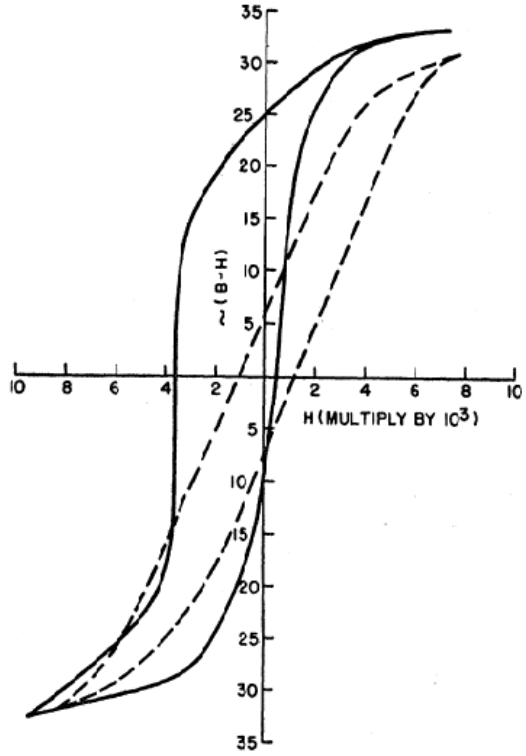

Figure I.10: Hysteresis loops of fine oxide-coated particles of cobalt taken at 77°K. The dashed lines show the hysteresis loop when the material is cooled in the absence of a magnetic field. The solid lines show the hysteresis loop when the material is cooled in a saturating magnetic field. Extracted from [56].

The very principle of the setting of the exchange bias can be easily understood using figure I.11. The sample temperature is set above the ordering temperature of the antiferromagnetic layer (AFM), T_N, so that the magnetic moments in the AFM are disordered. A magnetic field is then used to pin the FM layer magnetization in a given direction. The sample is then cooled below T_N. This procedure sets the exchange bias. The historical explanation used to describe this phenomenon is that during the cooling the exchange interaction between FM and AFM moments at the interface aligns AFM interfacial moments during their reorganizations with the FM interfacial moments.

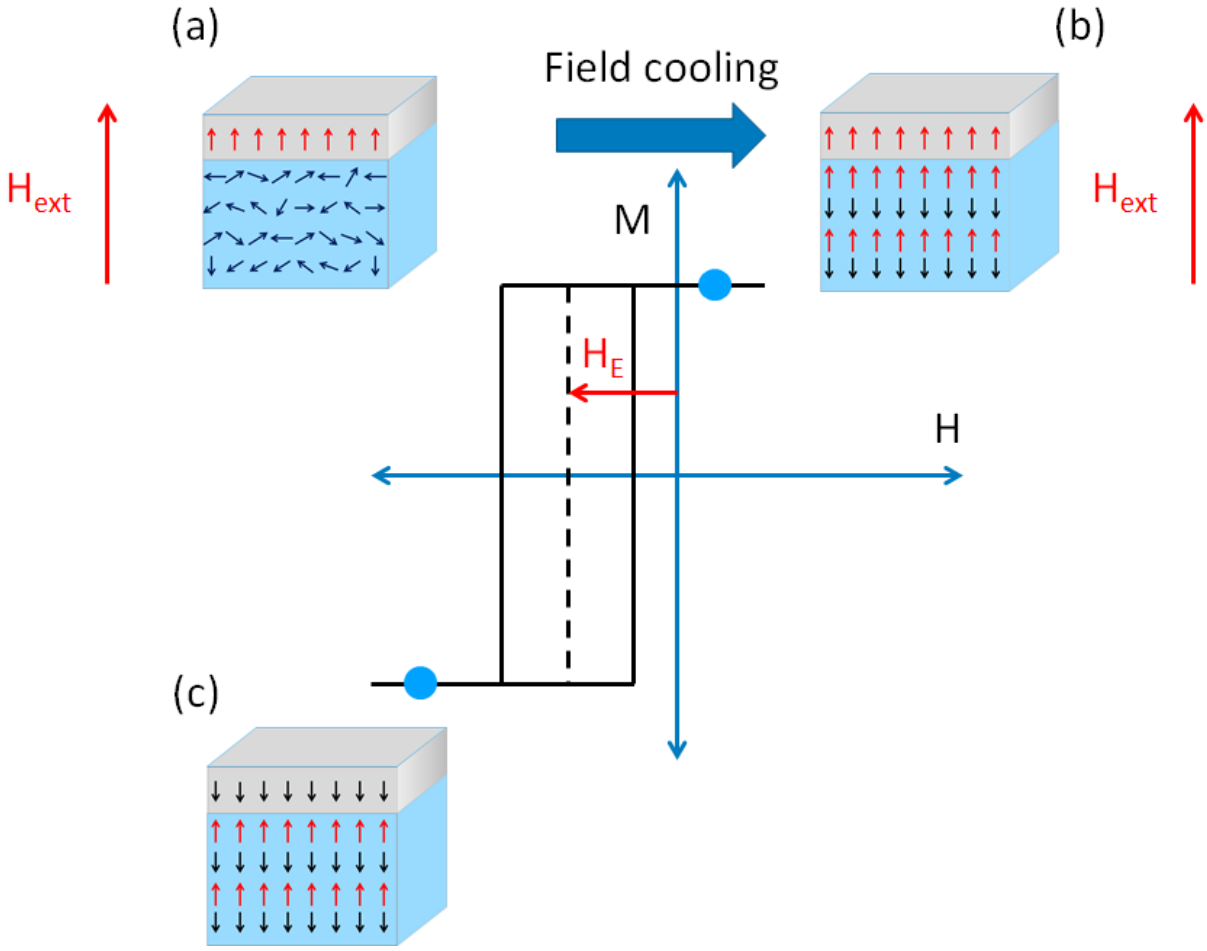

Figure I.11: Origin of the exchange bias. (a) The sample is first annealed at a temperature above the ordering temperature with an out-of-plane external field H_{ext} sufficient to saturate the FM layer then (b) it is cooled down to let the AFM configuration be reset. (c) Finally by applying a negative out-of-plane field the FM magnetic configuration remains while the AFM ordering remains unchanged. The field cooling results in an exchange bias field H_E opposite to the magnetization at the interface of the AFM.

In that case the energy per area unit of the magnetic system should be the following one:

$$E_S = -A\cos(\alpha-\beta) - K_{FM}t_{FM}\cos^2\alpha - K_{AFM}t_{AFM}\cos^2\beta - M_{FM}H_{ext}t_F\cos(\alpha-\theta_H) \qquad (1.27)$$

A is the exchange stiffness at the interface between the FM and the AFM. α (resp. β) is the angle between the line perpendicular to the plane of the sample and the moments of the FM (resp. the AFM). θ_H is the angle between the line perpendicular to the plane of the sample and H_{ext} , which is the external applied magnetic field. The thicknesses of the FM and the AFM layers are t_{FM} and t_{AFM} respectively. We consider that the anisotropy axis of the FM and the AFM are assumed to be perpendicular to the plane of the sample. K_{FM} and K_{AFM} are respectively the anisotropy constants of the FM and the AFM layers. For better comprehension purpose figure I.12 is a summary of the angles involved in equation 1.27.

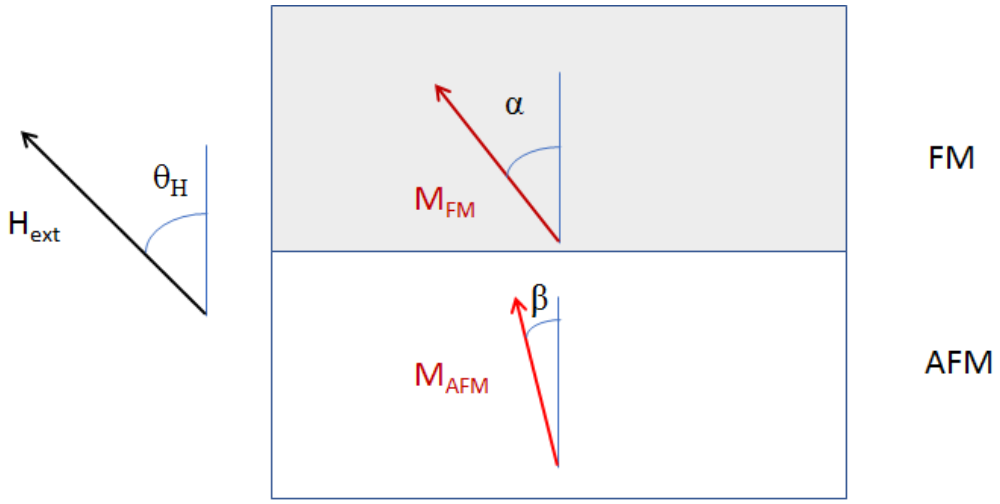

Figure I.12: Schematic of the angles involved in equation 1.27 resulting from a macrospin model. M_{AFM} represents the magnetization of one sublattice of the antiferromagnetic layer.

If we consider that the AFM moments are aligned with the anisotropy axis and that the applied field is along the anisotropy axis direction (θ_H =0) it gives us:

$$E_S = -A\cos(\alpha) - K_{FM}t_{FM}\cos^2\alpha - K_{AFM}t_{AFM} - M_{FM}H_{ext}t_{FM}\cos(\alpha) \quad (1.28)$$

The minimization of this energy in function of α gives us:

$$A\sin(\alpha) + 2K_{FM}t_{FM}\cos(\alpha)\sin(\alpha) + M_{FM}H_{ext}t_F\sin(\alpha) = 0 \quad (1.29)$$

There are three different possibilities:

$$\alpha = 0 \qquad \alpha = \pi \qquad \cos(\alpha) = -\frac{A+M_{FM}H_{ext}t_{FM}}{2K_{FM}t_{FM}} \quad (1.30)$$

A second derivation of the expression of the energy gives us the conditions of minimum [57]:

$$A\cos(\alpha) + 2K_{FM}t_{FM}[\cos^2(\alpha) - \sin^2(\alpha)] + M_{FM}H_{ext}t_{FM}\cos(\alpha) > 0 \quad (1.31)$$

α is minimum at 0 if $\frac{A}{t_{FM}} + M_{FM}H_{ext} + 2K_{FM} > 0$

α is minimum at π if $\frac{A}{t_{FM}} - M_{FM}H_{ext} - 2K_{FM} > 0$

The last possible minimum is not a stable state. This leads to the two values of coercive field:

$$H_C|_{\alpha=0} = -\frac{2K_{FM}t_{FM}+A}{M_{FM}t_{FM}} \quad and \quad H_C|_{\alpha=\pi} = \frac{2K_{FM}t_{FM}-A}{M_{FM}t_{FM}} \quad (1.32)$$

Calculating the EB field leads to the value:

$$H_{EB} = \frac{H_C|_{\alpha=0} - H_C|_{\alpha=\pi}}{2} = \frac{A}{M_{FM}t_{FM}} \quad (1.33)$$

The interfacial aspect of the exchange bias appears here with the thickness of the ferromagnet (t_{FM}) in the exchange field formula. The limit of this formula is that it is only theoretical because experimental values of the exchange field are at least two orders of magnitude higher than the theoretical value. This is due to two strong hypotheses made at the beginning, the monodomain state in the AFM and zero roughness at the interface of the FM and the AFM. Non-uniform magnetization configurations at the FM/AFM interface or domain walls in the AFM layer need to be considered.

I.2.2) Exchange bias models

On the first hand the difference between the experimental measurements of the exchange field and its theoretical value given by Meiklejohn and Bean, Mauri developed a more complex model where a domain wall can form in the depth of the AFM layer [58]. The formation of a domain wall in the AFM happens when the FM layer reverses, reducing the total energy of the system. This allows the reduction of the exchange field to obtain:

$$H_{EB} = \frac{2\sqrt{A_{AFM}K_{AFM}}}{M_{FM}t_{FM}} \tag{1.34}$$

On the other hand Malozemoff developed a model that takes in account the roughness at the interface between the FM and the AFM. Malozemoff published several papers [59], [60], [61] to describe the phenomenon happening due to this roughness. His model is called the “random field model”. Since then exchange bias has been a subject of intense research. Some well detailed reviews have been published on the subject [62] [63] [57] and cover the magnetic behaviors of many AFMs.

In Co interfaced with IrMn, the AFM we will focus on in this manuscript, exchange bias arises from uncoupled grains in the AFM, like in other AFM polycrystalline alloys (PtMn, NiMn or FeMn for instance) [64]. All grains are characterized by their anisotropy constant K, their volume V which follows a gaussian distribution as seen on figure I.13. In our polycrystalline AFM, the temperature that matters for the setting of the exchange bias is not exactly the Néel temperature but a temperature below it, the blocking temperature T_B. Each grain has its own blocking temperature. At T_B an AFM grain is not fully demagnetized but the energy barrier between the two stable antiferromagnetic configurations of the grain corresponds to the average thermal energy. The AFM grain configuration then can change between the stable configurations in the vicinity of the characteristic time given by the energy barrier. The blue grains in figure I.13 are the biggest ones and thus remain unswitched during a hysteresis loop (higher T_B) so they participate in the exchange field while the gray ones switch during the field sweeping because of their small volumes and participate in the coercive field (lower T_B). At the scale of one AFM grain there can be a high disorder and a high frustration due for instance to roughness and the AFM system can be considered as a spin glass. There are then two contributions in the exchange bias, a volume one for the low disorder grains and an interfacial one for the highly disorder spin glass regions between grains. Those two contributions can be distinguished by their evolutions with the AFM thickness and their temperature behaviors [65]. Indeed the grains are more thermally stable than the spin glass regions. As an effect, at 300K only the grains contribute to the exchange bias field.

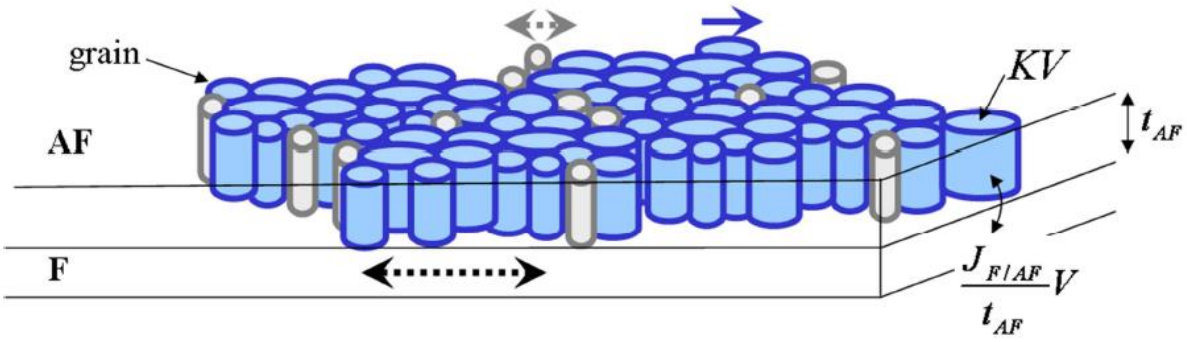

Figure I.13: Sketch of the FM/AFM bilayer at a finite temperature T_f. For comprehension purposes only the AFM grains are shown. The blue grains are the pinned one contributing to the exchange bias field at T_f due to their large volume. On the opposite at T_f the grey grains are unstable [66].

I.3) Ultrafast manipulation of magnetization using femtosecond polarized light

Manipulating the magnetization at a short timescale is a major challenge for both application and fundamental research. A possible way to perform it is with a femtosecond pulsed polarized light. This has been developed in the last twenty years since the pioneer work of Beaurepaire et al. [3] and is still an expanding topic of research. The ultrafast manipulation field now includes diverse phenomena, such as hot electron demagnetization [67] or single electrical pulse switching [68] . In the following part, we will focus on the exciting field of all optical switching (AOS) i.e. the possibility to switch the magnetization solely with light.

I.3.1) Experimental results

I.3.1a) Ultrafast demagnetization of Ni

In 1996 Beaurepaire *et al.* exposed a 22nm Ni layer to 60 fs laser pulses and measured the magnetization evolution as a function of time using a pump probe setup. The result is displayed on figure I.14. During the first picosecond the magnetization dramatically drop and recovers slowly for at least the following 15 ps. This is considered as the pioneer work in the field of ultrafast magnetization manipulation, named today femtomagnetism.

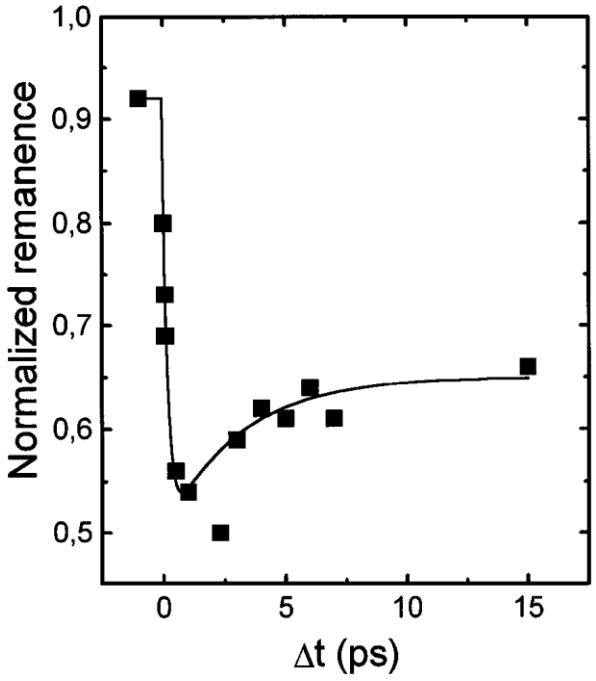

Figure I.14: Transient remanent longitudinal MOKE signal of a Ni(20 nm)/MgF_2(100 nm) film for 7 mJ/cm^2 pump fluence. The signal is normalized to the signal measured in the absence of pump beam. The line is a guide to the eye. [3]

To explain this striking result Beaurepaire invoked a phenomenological 3-temperature model, an expansion of the 2-temperature model. In this model 3 different baths, the electron, spin and lattice ones interact with each other through thermal exchange. The system of equations associated with this model is the following one:

$$\begin{cases} C_e(T_e)\frac{dT_e}{dt} = -G_{el}(T_e - T_l) - G_{es}(T_e - T_s) + P(t) \\ C_s(T_s)\frac{dT_s}{dt} = -G_{es}(T_s - T_e) - G_{sl}(T_s - T_l) \\ C_l(T_l)\frac{dT_l}{dt} = -G_{el}(T_l - T_e) - G_{sl}(T_l - T_s) \end{cases} \quad (1.35)$$

Here e, s and l stand for electron, spin and lattice respectively. C_i represents the specific heat of the i bath, T_i its temperature and G_{ij} the interaction constant between the I and j baths. The simulated evolution of the 3 baths is displayed on figure I.15.b). During the first picosecond, the electron system absorbs light (represented by P(t)) and increases its temperature. Then the electrons exchange heat with the spin system, which leads to their demagnetization. The electrons also exchange heat with the lattice but at a slower rate so the spin temperature has time to increase during 2 picoseconds, before the spin-lattice interaction slowly leads to a remagnetization.

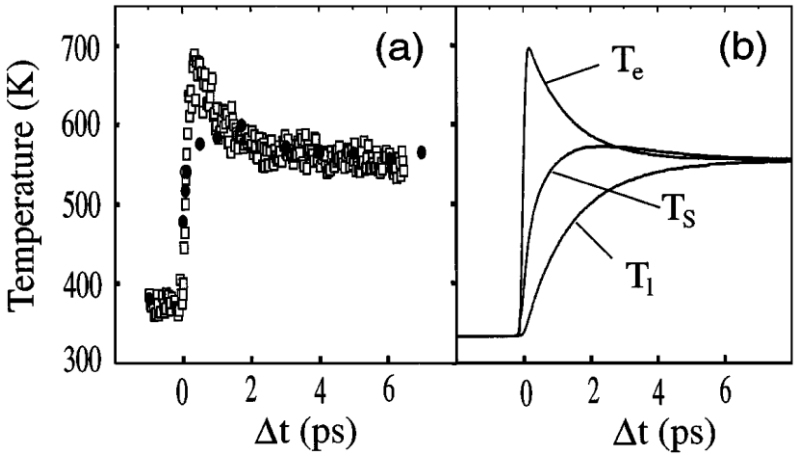

Figure I.15: (a) Experimental spin (T_s) and electron (T_e) temperatures estimated as explained in the text. (b) Calculated spin (T_s), electron (T_e), and lattice (T_l) temperatures from Eqs. (1.35). Extracted from [3].

I.3.1b) All optical helicity independent switching

In 2007 Stanciu *et al.* demonstrated that it is even possible to switch the local magnetization using only femtosecond polarized light. This is called all optical switching (AOS). There are two types of AOS processes, all optical helicity-dependent switching (AO-HDS) and all optical helicity-independent switching (AO-HIS). In this part we focus on AO-HIS. This phenomenon was first exhibited in 2011 [69] by Radu *et al* in a $Gd_{25}Fe_{65.6}Co_{9.4}$ of 30nm exhibiting strong PMA. Using each time one single pulse of linearly polarized light they have been able to reverse the total magnetization from one saturated state to the other. Using X-ray magnetic circular dichroism they probed the magnetization evolution of the two sublatices of Gd and Fe to reveal a switching time under 6 ps as seen on figure I.16.

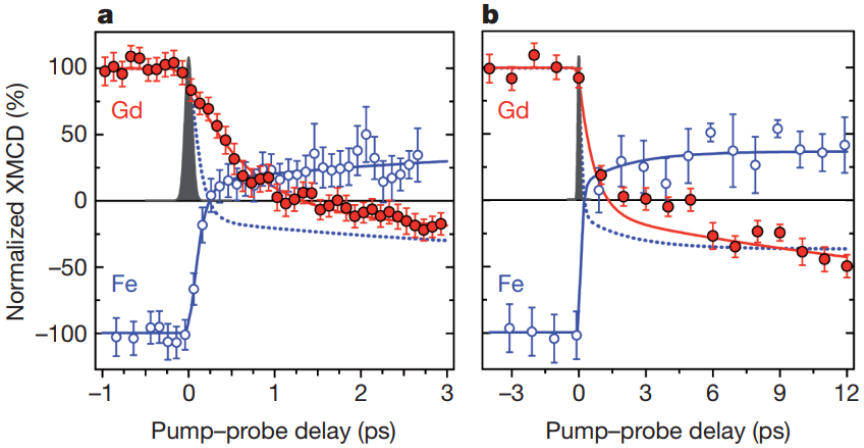

Figure I.16: Element-resolved dynamics of the Fe and Gd magnetic moments measured by time-resolved XMCD with femtosecond time-resolution. (a) Transient dynamics of the Fe (open circles) and Gd (filled circles) magnetic moments measured within the first 3 ps. (b) As (a) but on a 12 ps timescale. Error bars of the experimental data represent the statistical standard error. The measurements were performed at a sample temperature of 83K for an incident laser fluence of 4.4 mJ/cm^2. Experimental time resolution of 100 fs is depicted by the solid gaussian profile. Extracted from [69].

This ultrafast switching is attributed to different demagnetizing times of the two sublattices, respectively 100 ± 25 fs and 430 ± 100 fs for Fe and Gd. Since Fe demagnetizes faster than Gd, there is a ferromagnetic-like state. The reason behind such a state is still being investigated but it has not yet reached a scientific consensus. For instance it has been shown that a transient ferromagnetic-like state also exists in a FeTb alloy but it does not lead to a switching of the net magnetization [70]. In 2012 Ostler *et al.* have been able to demonstrate the repeatability of the AO-HIS measurements by taking a MOKE image after each laser pulse. For few years, GdFeCo alloys were the only materials where AO-HIS was reported, until recently when Lalieu *et al.* showed that this process can occur also in Co/Gd bilayers [71].

I.3.1c) All optical helicity dependent switching

In 2007, Stanciu *et al.* have been able to perform for the first time AO-HDS [4]. First, they have been able to image the magnetic domains in a 20 nm thick $Gd_{22}Fe_{74.6}Co_{3.4}$ using a Faraday microscope as seen on figure I.17.a). The black domains are magnetized along $-\vec{z}$ while the white domains are magnetized along $+\vec{z}$. Switching with the σ^+ (resp. σ^-) helicity, they have been able to set the magnetization along $+\vec{z}$ (resp. $-\vec{z}$). This helicity dependent switching of the magnetization was called all optical helicity dependent switching (AO-HDS). Sweeping with a linearly polarized light, they obtained a mix of both types of domains.

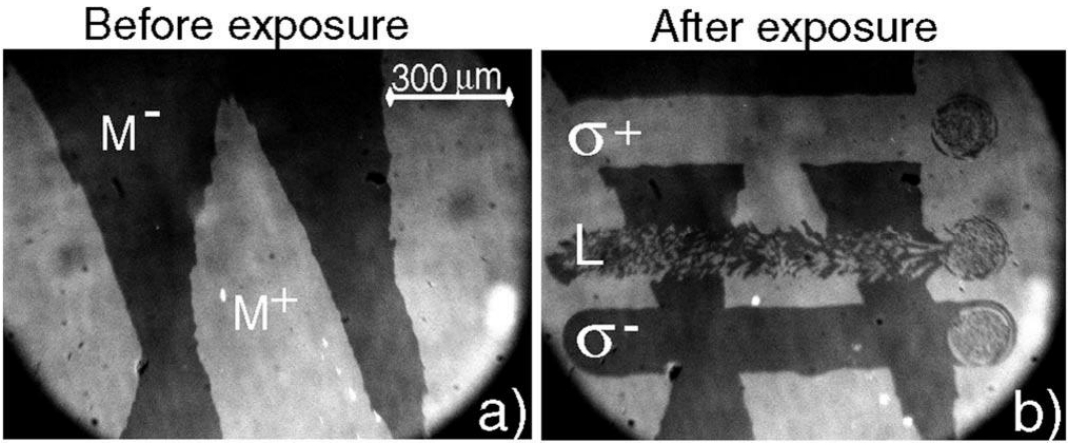

Figure I.17: Faraday image of a 20 nm thick $Gd_{22}Fe_{74}.6Co_{3.4}$ with dark contrast standing for positive magnetization and clear contrast for negative magnetization. (a) Image of the initial multidomain state. (b) Image obtain after sweeping of left, right and linear polarized light with a speed around 30 µm/s and a fluence of 11.4 mJ/cm^2 . Extracted from [4].

The width at half maximum of each pulse in this experiment is of 40 femtosecond while the repetition rate is 1 kHz. The time between two pulses seems then long enough compared to the length of the pulse to make legitimately the hypothesis that sweeping of the laser occurs by small discrete steps of laser pulses where the magnetic system has time to reach an equilibrium between two pulses. The study of a fixed laser beam can then be relevant to understand how the sweeping switching occurs. They decided to perform this fixed beam experiment and to send pulses with left, right and linear polarization of the light. The resulting images are shown on figure I.18.

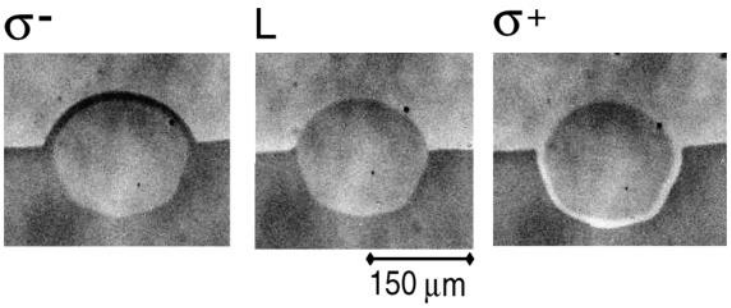

Figure I.18 : Images of the laser spot focused onto a domain wall during the 1 kHz pulsed laser excitation with linear (L), right-(σ-), and left-handed (σ+) circular polarization. The images were obtained for a pulse fluence of about 11.4 mJ/cm^2. In all three cases the central region of the optically excited area is demagnetized (gray color) due to extensive heating. Extracted from [4]

From those images, two areas can be distinguished: a demagnetized area in the center and a switching ring on the edge of the spot. The central area is demagnetized because the laser fluence here is high enough to increase the temperature above T_C, so that when the system cools down, it breaks into small domains. The switching ring is characteristic from the polarization of the light. For instance it sets opposite directions of magnetization for left and right polarizations while it does not exist for the linear one. Then by sweeping the laser on the sample one leaves a track of the switching ring that depends on the helicity.

After the discovery of all optical switching in GdFeCo alloys, helicity dependent all optical switching has been demonstrated to occur in rare-earth/transition metal ferrimagnetic materials [5] [72] [6] [73] such as CoTb, DyCo or HoFeCo. Those studies where initially motivated by the fact that such two different sublattices could also exhibit a single pulse switching due to different demagnetizing times but it turned out that it is a helicity dependent mechanism. At the time, the idea of an antiferromagnetic coupling needed to achieve the switching was widespread so Mangin *et al.* also grew multilayers alternating rare-earth and transition metal multilayers antiferromagnetically coupled between each other (for instance $[Tb/Co]_N$ or $[Ho/Co]_N$) and demonstrated that AO-HDS can occur in it [6]. Following the same intuition the same authors decided to design rare-earth free synthetic ferrimagnet. They thus demonstrated AO-HDS in a Ta(4 nm)/Pd(3 nm)/[Co(1 nm)/Ir/Co(0.4 nm)/Ni(0.6 nm)/Pt(0.3 nm)/Co(0.4 nm)/Ir]$_5$/Pd(3 nm). To the knowledge of the author, no other report of AO-HDS in a RE-free synthetic ferrimagnet has been made yet.

In 2014, Lambert *et al.* demonstrated for the first time AO-HDS on ferromagnetic materials [7], namely $[Co/Pt]_N$ and $[Co/Ni]_N$ multilayers. This shows there is no need of antiferromagnetically coupled magnetic moments to obtain AO-HDS. Their study has been mainly focused on Co/Pt multilayers. They evidenced that AO-HDS can be obtained for numbers of repeat below 4, indicating that the dipolar field is the discriminating factor. This has been confirmed later by the argument that the size of the magnetic domains must be larger than the size of the spot [74]. Lambert *et al.* also did the sweeping experiment on a $[Co(0.4nm)/Pt(0.7nm)]_3$ sample exhibiting AO-HDS but applied a small static out-of-plane field as seen on figure I.19. The aim of this experiment is to understand if the helicity of the light can act as an effective field. For instance sweeping the laser with a σ^+ helicity and -7 Oe has almost the same effect than a linear polarization. It is then tempting to say that the σ^- in this case creates an

effective out-of-plane field of 7 Oe even if it is an oversimplification of the problem. The authors also demonstrated the possibility to perform AO-HDS in FePt granular media. This has been seen as a breakthrough since this material was at this time used in the commercialized hard disks.

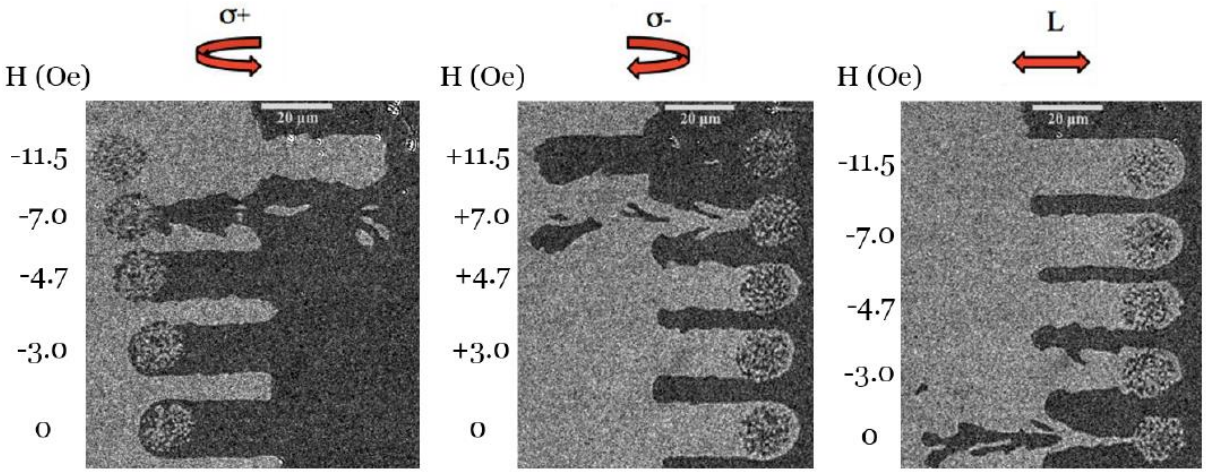

Figure I.19: Magnetic response of a [Co(0.4 nm)/Pt(0.7nm)]$_3$ multilayer to the combined effect of optical excitation and an external magnetic field starting with two domains and a domain well in the middle of each image. The magnitude of the magnetic field is shown to the left of each line scan and the average laser power was 523 nW. Extracted from [7].

The AO-HDS in $[Co/Pt]_N$ multilayers has then been investigated later using Hall cross measurements [21]. The power of the laser has been adjusted to obtain in the center of the spot a demagnetized area and a switching ring on the edge. In the experiment, the switching ring is at the center of the Hall cross as seen on figure I.20. The AO-HDS behavior has been probed by measurement of the Hall voltage and the result is seen on figure I.21. The helicity dependent switching actually occurs in two steps. When exposed to the laser, the magnetization goes to zero with many pulses then the sample remagnetizes depending on the helicity. Interestingly the authors have observed the same two steps process for the AO-HDS of a CoTb alloy. This 2 step process has been experimentally confirmed by Medapalli *et al.* [75]. They also have been able to isolate the DW propagation step of the process with laser fluence below the switching threshold and concluded that this regime could only be driven by a heat gradient because the DW motion should last longer than the time of the pulse application. A more detailed study of this DW propagation regime was then achieved by the same groups [76].

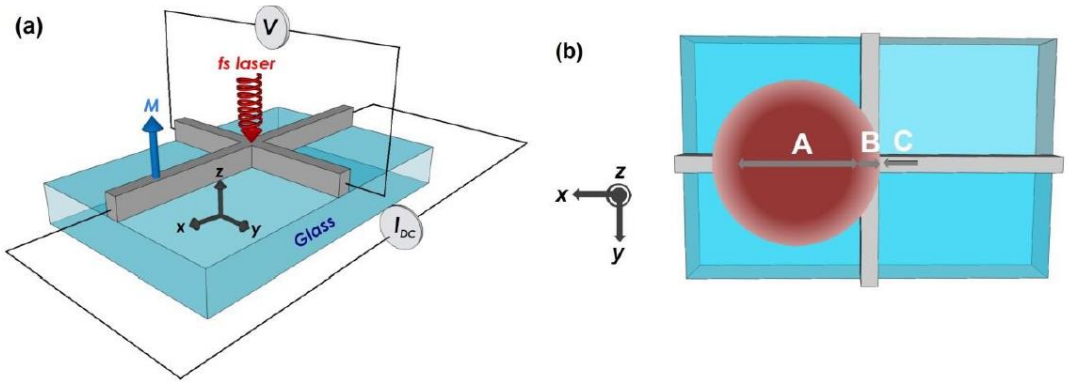

Figure I.20: (a) Schematic of the studied 5 µm-wide Hall crosses with perpendicular magnetization (z axis); a DC current is injected along the x direction while the anomalous Hall voltage V_{Hall} is measured along the y direction with a time resolution of 1 µs. The 60 µm FWHM fs laser beam is illuminated perpendicular to the film plane on the x axis at a fixed position about 40 µm from the center of the Hall cross. (b) Schematic representation of the different areas of the fs laser beam: "A" where multiple magnetic domains are obtained, "B" where AOS is obtained and "C" where no change of magnetization is induced. Extracted from [77].

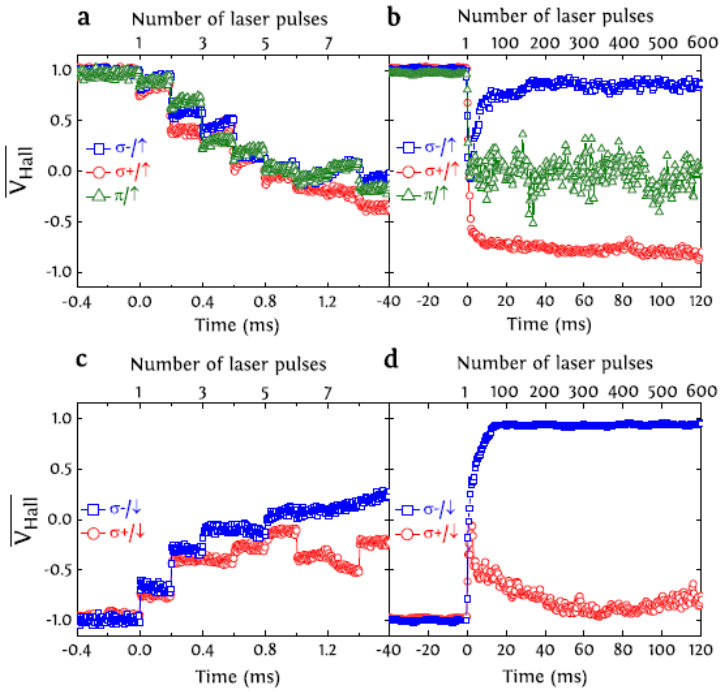

Figure I.21: Multiple pulse helicity-dependent switching of Pt/Co/Pt Hall crosses. (a) and (b) Time evolution of the anomalous Hall voltage of a 5 µm wide Pt(4.5)/Co(0.6)/Pt(4.5) Hall cross initially saturated "up", under the action of a 35-fs laser beam with a 5 kHz repetition rate and a fluence of 10 mJ/cm2. The helicity-dependent switching of the studied Hall cross is governed by a two-step process at two different timescales: a)helicity-independent demagnetization within the first 1ms. b) helicity-dependent reversal measured on a 120 ms timescale. (c) and (d), the same behavior is measured as (a) and (b) with initial saturation. Extracted from [78].

I.3.2) Theoretical framework

I.3.2a) 3 temperature model

Several attempts have been made to describe theoretically the observed ultrafast switching behaviors. The oldest one is the 3 temperature model since it lasts from the first paper including an experiment of ultrafast demagnetization. However it does not directly provide the evolution of the magnetization only by itself. The standard equation of motion of the magnetization is the Landau-Lifschitz-Gilbert equation (LLG) [79] [80]and it can be written as:

$$\frac{\partial \vec{M}}{\partial t} = -\gamma \mu_0 \vec{M} \times \vec{H}_{eff} + \frac{\alpha}{|\vec{M}|} \vec{M} \times \frac{\partial \vec{M}}{\partial t} \tag{1.36}$$

μ_0 is the vacuum permeability, γ the gyromagnetic ratio and α the Gilbert damping. $\vec{H}_{eff}$ is the sum of the external field and all the other effective fields accounting for the various interactions (DMI, Heisenberg exchange, dipolar,…). The equation without the damping term is called the LL equation and describes the precession of the magnetization around the effective field. The damping term effect is to reduce the amplitude of the precession over time until the magnetic moment is aligned with the effective field. The LLG equation is efficient to describe magnetization dynamics but it does not take into account the temperature, so it cannot describe thermally driven ultrafast dynamics. Brown made an attempt to include the role of the temperature in the LLG equation by adding effective field accounting for thermal fluctuations [81], which amplitude is of the following form:

$$H_{therm,i} = \delta_i(t) \sqrt{\frac{2\alpha k_B T}{\gamma_0 M_S V}} \tag{1.37}$$

V is the volume of the magnetic layer, i refers to the 3 dimensions of space. $\delta_i(t)$ is a random Gaussian function of value fulfilling the criteria $\langle \delta_i(t) \rangle = 0$ and $\langle {\delta_i}^2(t) \rangle = 0$. However it does not apply for temperatures close to T_C. Indeed when the system temperature gets closer to this temperature the longitudinal component of the magnetization tends to zero and this cannot be taken into account only by adding a conservative term in the LLG equation. This limitation led to the setting of another temperature dependent equation of magnetization dynamics, the Landau-Lifschitz-Bloch (LLB) equation.

The LLB equation comes from the combination of the temperature independent LLG equation and the high temperature Bloch equation [82]. Its expression is the following one:

$$\frac{\partial \vec{m}}{\partial t} = \gamma \left(-\vec{m} \times \vec{H}_{eff} + \frac{\alpha_{||}}{m^2} (\vec{m}.\vec{H}_{eff}) \vec{m} - \frac{\alpha_{\perp}}{m^2} \vec{m} \times \vec{m} \times \vec{H}_{eff} \right) \tag{1.38}$$

Here $\vec{m} = \frac{1}{M_S} \vec{M}$. $\vec{H}_{eff}$ is the effective field that includes also the thermal Brownian field. $\alpha_{||}$ and $\alpha_{\perp}$ are respectively the longitudinal and transverse damping parameters. Their evolutions as a function of the temperature under T_C are :

$$\alpha_{||} = \alpha \frac{2T}{3T_C} \tag{1.39}$$

$$\alpha_{\perp} = \alpha(1 - \frac{T}{T_C}) \quad (1.40)$$

One can observe that the reduction of magnetization at temperatures close to T_C in the LLB equation is due to the longitudinal damping parameter. Coupling the LLB to a 3 (respectively 2) temperature model is a way to study the magnetization dynamics by first calculating the temperatures of the spins (respectively the electrons) and injecting it into the LLB equation. This has been used to model the ultrafast demagnetization behavior observed experimentally [83]. However this process is unable to describe a helicity dependent all optical switching behavior. Indeed there is a need for a term breaking the symmetry between the spin populations to be able to observe a switching. Furthermore this term must depend on the helicity of the light. Two types of symmetry breaking effects can be considered, the thermal and the athermal ones.

I.3.2b) Inverse Faraday Effect

The interaction between light and magnetism can manifest in several ways. When a light is transmitted through a magnetic material, a rotation of its polarization occurs. This is known as the Faraday effect. The reciprocal effect exists, known as the inverse Faraday effect (IFE). Due to the IFE a circularly polarized light going through a magnetic material could induce a magnetic moment. This effect has been first observed in a non-absorbing material [84] [85] [86]. The IFE is often described by effective field acting on the local magnetic moments and its phenomenological expression is the following one:

$$\vec{H}_{IFE}(t,r) = \chi\epsilon_0[\vec{E}(t,r) \times \vec{E}^*(t,r)] \quad (1.41)$$

ϵ_0 is the vacuum permittivity and χ the optical susceptibility and $\vec{E}(t,r)$ is the electric field associated with the light. It can be deduced from this expression that the sign of this field is opposite for opposite helicities of the light. Kimel *et al.* demonstrated in 2005 for the first time that it was possible to manipulate, non-thermally, at a femtosecond timescale, the magnetization depending on the helicity of the light in a $DyFeO_3$ [87]. This can be seen on figure I.21. One major interest of this method is that no cooling time is necessary. They demonstrated that a 200 fs laser pulse of a fluence of 500 mJ/cm^2 has an equivalent effect in the material as an external applied field of 3000 Oe.
In 2014 Battiato *et al.* calculated theoretically the corrections on the density matrix from second order perturbation that led to the induced IFE magnetic moment [88]. On the simulation aspect, there has been an attempt to combine the 3 temperature model with the LLB equation and take this IFE field as a symmetry breaking element to explain helicity dependent switching in rare earth/ transition metal alloys [89]. With the discovery of AO-HDS in ferromagnets, there was a need to adjust the phenomenological calculations to the experimental results. Cornelissen *et al.* have been able to reproduce by simulations the results obtained in ferromagnetic materials ($[Co/Pt]_N$ multilayers) using the IFE as a symmetry breaking factor and a derivative of the 3 temperature model taking into account the conservation of the total angular momentum, the microscopic 3 temperature model. Interestingly their results are valid for an IFE field lasting in the order of 0.1 ps because of the spin orbit coupling. This is an intriguing result since it implies that the IFE field lasts longer than the length of the pulse. Furthermore, there is a need for experimental investigation of the IFE in metals.

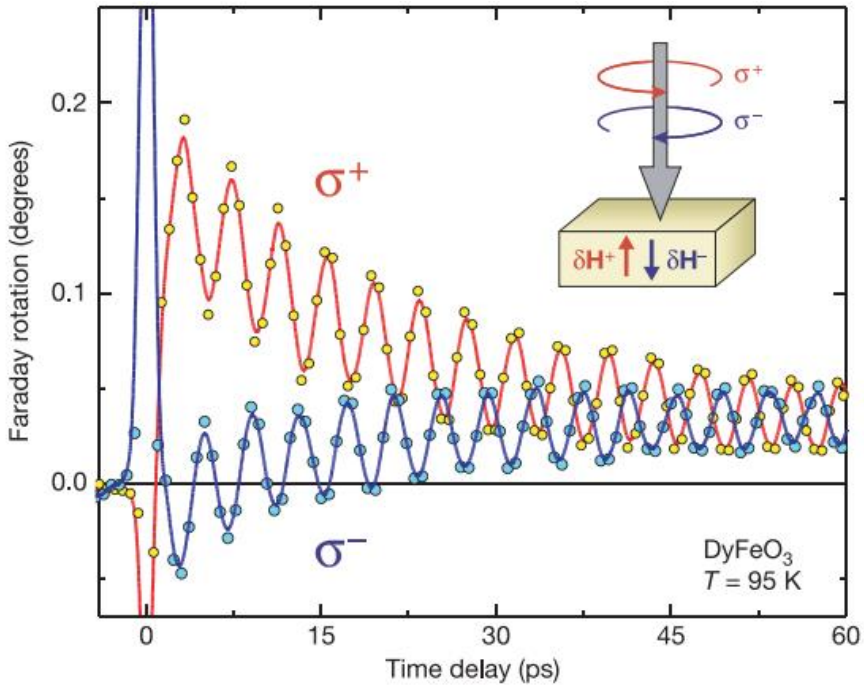

Figure I.22: Magnetic excitations in DyFeO3 probed by the magneto-optical Faraday effect. Two processes can be distinguished: (1) instantaneous changes of the Faraday effect due to the photoexcitation of Fe ions and relaxation back to the high spin ground state S = 5/2; (2) oscillations of the Fe spins around their equilibrium direction with an approximately 5 ps period. The circularly polarized pumps of opposite helicities excite oscillations of opposite phase. Inset shows the geometry of the experiment. Vectors δH^+ and δH^- represent the effective magnetic fields induced by right-handed σ+ and left-handed σ- circularly polarized pumps, respectively. Extracted from [87].

I.3.2c) Magnetic circular dichroism

Another symmetry breaking factor that has been invoked to explain AO-HDS is the magnetic circular dichroism (MCD). The MCD is a difference of absorption between left and right circularly polarized light depending on the magnetic orientation of the material. In 2012 Khorsand *et al.* exhibited the role of the MCD in the switching process of a GdFeCo layer [90]. They looked into the range of fluences at which the switching can occur that they called Δ. They compared the spectral dependence of Δ, the IFE field and the MCD as seen on figure I.22. It appears that Δ and the MCD both have a weak spectral dependence while the IFE field (and also the Faraday rotation) has a strong spectral dependence. This leads to the MCD as being a promising factor for the optical switching of GdFeCo layers compared to the IFE field.

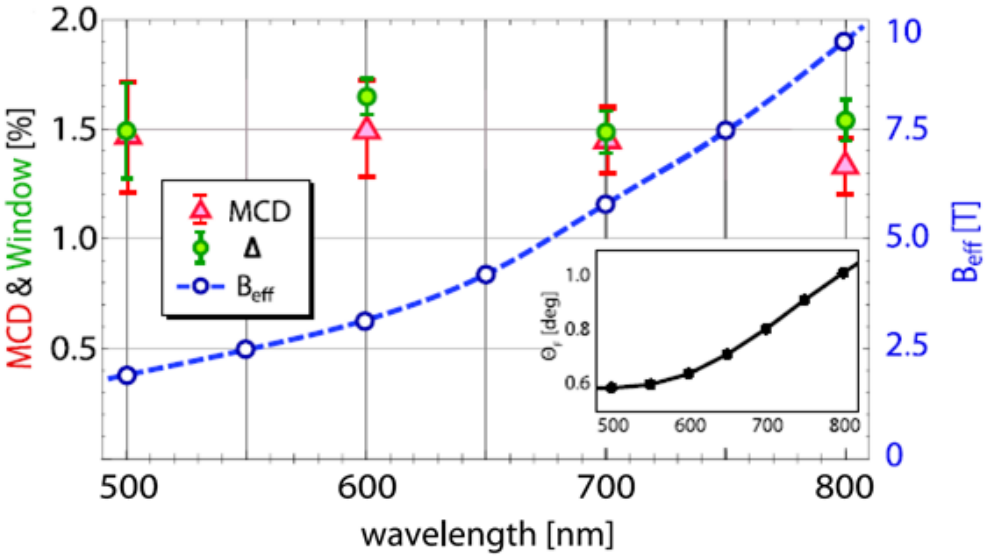

Figure I.22: The spectral dependence of the window Δ, IFE field Beff , and MCD in GdFeCo. In the inset the spectral dependence of the Faraday rotation θ_F is shown. Extracted from [90].

MCD has also been exhibited as the determining factor for AO-HDS in a granular medium in 2016 by Gorchon *et al.* [91]. This material is composed of uncoupled grains. Each grain has a temperature dependent attempt time τ_{ab}between two states "a" and "b" at a time given by the Néel-Brown formula [92]:

$$\tau_{ab} = \tau_0 \exp\left(\frac{K(T)V}{k_B T}\right) \tag{1.42}$$

The term $\frac{K(T)}{T}$ in the exponential is decreasing with the temperature, so the attempt time in hotter grains is smaller. For instance if the MCD is such that grains in the state "a" are more absorbent the grains in the state "b" their temperature will be higher after a pulse so their attempt time will be smaller, leading to a higher probability of change of state in a given time. The less absorbent state is in this model favored by the MCD. As a result they demonstrated that they were able to reproduce by simulation the AO-HDS behavior in FePt granular media with a low MCD of 0.5%. The specificity of their model is that it is applied in a system with no dipolar nor exchange couplings. The authors claimed that this switching process could also occur in a full film. Yet no simulation demonstrating a switching via MCD in a Co/Pt multilayer has been reported to our knowledge.

I.4) Conclusion

In this part, I have introduced some basic notions necessary to understand my thesis work on the interaction of light with magnetic thin films heterostructure. It started with some fundamental concepts to understand magnetic configurations in magnetic thin film. Then I described some more specific aspects such as skyrmions, DMI-induced phenomena and exchange bias effect. I then summarized some of the results obtained recently on light induced magnetization manipulation using femtosecond laser pulses. Ultra-fast demagnetization and all optical switching are presented.

The possible mechanism explaining all optical helicity dependent switching such as inverse Faraday effect and magnetic circular dichroism are discussed.

II) Experimental Setup

From the elaboration of the first sample to the publication of the obtained results many instruments are necessary. The aim of this part is to describe the instruments I used during my thesis and the physical principles involved. First, we will focus on the techniques involved to obtain the samples. Then we will take a bit of time to describe the pieces of equipment involved in the magnetic characterization of the samples. Finally, we will direct our attention on the laser system present at the IJL in Nancy.

II.1) Heterostructure elaboration

II.1.1) Magnetron sputtering deposition system

II.1.1.a) Presentation of the system developed with Vinci Technologies

In order to obtain magnetic thin films, several techniques are available, as for instance molecular beam epitaxy (MBE) or pulsed laser deposition (PLD). In this manuscript, all the samples have been elaborated in a magnetron sputtering tool. A magnetron sputtering tool is an enhanced type of sputtering tool. The principle of sputtering can be understood with figure II.1.

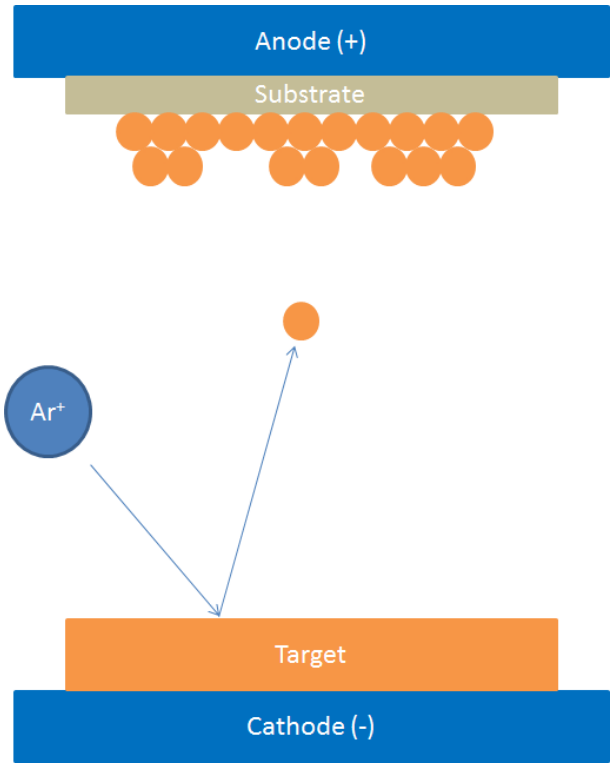

Figure II.1: Schematic of a sputtering system

In an ultra-high vacuum chamber (at a pressure around 5. 10^{-8} Torr), argons atoms are injected. Then, a high voltage (of the order of hundreds of volts) is applied between the cathode (-) and the anode (+). As an effect, Ar atoms are ionized into Ar^+. Ar^+ ions are then electrically attracted by the cathode and hit the target because it is placed above the cathode. The target is composed of pure elements that we want to have in our final sample, for instance Cu. Then, due to the collision between Ar^+ ions and the (Cu) target, (Cu) atoms are ejected from the target. Their trajectory is, in our case, mostly ballistic given that they have no specific electric charge. Since target atoms are ejected in every direction in the chamber, only a small part of the atoms reaches the substrate placed on top of the chamber. Those atoms together form the deposited layer. One parameter that is critical to achieve sputtering is the number of Ar^+ ions. The number of Ar atoms initially present is not a limiting factor because Ar atoms are constantly injected into the chamber, but their ionization is not granted. The main mechanism of ionization of Ar atoms is through collision with electrons. An electron colliding with an Ar atom can eject another electron from the Ar atom (ionization of the Ar atom) and at its turn, the newly ejected electron can collide with another Ar atom. The initial ionization of Ar atoms can then create a cascade phenomenon and, if the ionization rate is high enough, the Ar^+ plasma can be self-sustainable. In order to keep this ionization rate stable over time, a magnetron magnetic field is present at the surface of the target. Its role is to confine electrons, both from the Ar^+ plasma and the target, due to the Lorentz force in the vicinity of the target. Magnetron sputtering can be used to grow layers composed of a single element or can be used to form alloys. There are two possibilities in that case: either the sputtered target is already an alloy (this is the case for IrMn), or the different species come from different targets (as it is the case for CoTb or GdFeCo). For the deposition of conducting materials, we apply mainly a DC current to the considered target. For the deposition of insulating materials, we use

a RF current to prevent the accumulation of charges on the surface of the target. One can note that it is possible to use a pulsed DC current to sputter insulating targets but we did not use it.

The magnetron sputtering system we use in IJL has been developed by Vinci Technologies and is named PVD8. The development and installation of this system was a goal of my CIFRE thesis supported by Vinci Technologies. This system has been first built in Nanterre, in the building of Vinci Technologies. I went several times to Nanterre to make sure that it was suitable to grow good quality thin films needed for research projects. I also made sure that the system was optimized concerning for instance the mechanical properties of the substrate holder or the use of the power sources. When I was in Nancy, I also characterized the lateral homogeneity of the thickness of the deposited films under several conditions. We made sure that the spatial heterogeneity was less than 5% on the full substrate holder. Once we verified that the system had fulfilled all those criteria, we moved it to Nancy. When we installed it in Nancy, we had to take into account the gas injections, the flow of water and even the electricity supply. Now the system works well and like other users I grow different samples with it. The conception and installation of the PVD8 was beneficial for both the IJL and Vinci Technologies. On one hand, the spintronic team in IJL has now in Nancy a tool perfectly adapted to our needs to grow thin films of high quality, and on the other hand, Vinci Technologies has developed a new and competitive product, the PVD8, which they will be able to sell to new customers worldwide.

Founded in 1968, Vinci Technologies had developed over the decades a broad activity on geophysics and oil. In 2008, MECA 2000, a French company, leader of the ultra-high vacuum technology, ran out of business. Vinci Technologies then absorbed its knowledge and, thanks to its infrastructures, became a leader in the ultra-high vacuum field, first in France and later worldwide. They were also involved in ambitious projects that shed light on their innovation skills. For instance they built the longest ultra-high vacuum tube of the world. Thanks to its length of 70 meters, this tube can be connected to plenty of under vacuum instruments. It enables the user to move samples on different pieces of equipment under vacuum without having to expose it to a higher pressure and a higher risk of contamination. Vinci Technologies developed also several instruments such as a PLD or the PVD8.

The PVD8 is composed of two chambers. The first one is the deposition chamber where we grow the samples and it is the chamber under the highest vacuum. We open this chamber only when we want to change a target or do maintenance operations. There are 8 slots for targets in order to be able to do co-sputtering and also grow multilayers. We typically use a power of 100W for the targets. The second chamber is the introduction chamber. We introduce the substrates inside this chamber at atmospheric pressure then let it pump until the pressure is about 10^{-7} Torr. The pressure in this chamber can go from atmospheric pressure to 10^{-7} Torr in 15 minutes. After that, we open the gate between the two chambers to transfer the substrates in the deposition chamber and begin the deposition process.

Figure II.2: Picture of the Vinci system used for deposition in IJL

II.1.1.b) Key parameters

A magnetron sputtered grown layer can be characterized by different parameters, for instance its thickness, its roughness or its purity. The purity of the layer depends on the base pressure inside the sputtering chamber. The roughness of a layer and, more generally, its structure depends mainly on different parameters. For instance, in 1977, Thornton [93] exhibited the role of the Ar pressure and the substrate temperature on the structure of thick (25µm) metallic films. We grew mainly layers of the order of the nanometer but many of the same concepts developed by Thornton can still be applied to our samples. For instance, the lower the energy of the sputtered atom, the rougher the layer. This is due to a higher surface mobility of energetic adatoms (atoms on the surface of the substrate). There are mainly two ways to increase this energy. The first one is to increase the electric power developed between the anode and the cathode. It increases the Ar ions velocity and gives them a higher kinetic energy that will be transferred to the sputtered atoms of the target. Another way to increase the energy of the adatoms is to decrease the argon pressure; decreasing the Ar pressure enhances the mean free path of atoms ejected from the target because they experience fewer collisions with the Ar atoms. With each collision the atoms from the target transfer their kinetic energy to the Ar atoms. Thus, their final energy once they are on the surface of the substrate is higher if they experience fewer collisions. In the case of a heavy metal target, it can be useful to increase the pressure of Ar to reduce the kinetic energy of sputtered atoms from the target because too energetic atoms can damage the surface previously grown. This has been for instance used to prevent Ir atoms to damage a previously grown Co surface [20].

A key parameter to know is the deposition rate of a target. It can be expressed in nm/s. The use of a piezoelectric quartz crystal in the deposition chamber gives a rough idea of that rate's value.

This crystal dilates when a current is applied through it. The resonance frequency actually depends on the weight of the crystal. By depositing a material on this crystal, its weight changes and so does its resonance frequency. Thus, it is possible to access the deposition rate. For calibration purposes, we use mostly profilometry and X-ray reflectivity (XRR). For profilometry, we deposit typically 30nm of the target that we want to calibrate on a Si substrate with lines of resin. After lift-off we measure the height of the remaining lines and average it for a better precision. For XRR measurements, we grow first a 50 nm thick layer on top of a Si substrate. We then do a $\theta/2\theta$ measurement at low angles and, by fitting the peaks, it is possible to access the deposited thickness [94]. Once we have calibrated the deposition speed for a target for a set of conditions (flow of argon, pressure…), we consider that it does not change over time. We then use this deposition rate to know the time we need in order to obtain a certain thickness of the material. We have to do new calibrations if we change a target or if the target has been used for a long time. Indeed it becomes eroded with use, which leads to an alteration of the magnetic field at its surface. This applied in particular to a magnetic target. A typical DC deposition rate in our magnetron sputtering tool is between 0.02 nm/s and 0.07 nm/s.

II.2) Characterization of magnetic properties

To understand the magnetic behavior of a sample, several techniques exist, that probe either the local or the global magnetic configuration. During my thesis, I used several of them. Each of them has its own advantages and drawbacks but by combining them, it is possible to carry out a complete study.

II.2.1) Magnetometry measurements: MOKE

II.2.1.a) Principle of Kerr and Faraday effects

Magneto optics (MO) effects are the results between the interplay of light and magnetism. The first evidenced MO effect was the Faraday effect, discovered in 1845 [95]. The second one, the Kerr effect, was demonstrated in 1876 [96] , based on the same physics. Since then, various MO effects have been revealed as the Voigt, Zeeman or Cotton-Moutton effects. Let us consider the electric field associated with the light propagation in the +z direction of a Cartesian coordinate system. The general expression of the complex electric field is [97]:

$$\vec{E} = E_0(\vec{x} + e^{i\delta}\vec{y})e^{i(\omega t - kz)} \quad (2.1)$$

where $e^{i\delta}$ corresponds to the phase between x and y components of the field and E_0 is its magnitude. If $e^{i\delta}$=i, the light is right circularly polarized. If $e^{i\delta}$= -i, the light is left circularly polarized. A linearly polarized light along the axis $\vec{x}$ is then an equal sum of the two helicities. For any value of δ that is not a multiple of $\pi/2$, the polarization is only elliptic. In our example, we consider a linearly polarized light, thus we need to study the change that occurs on both of its components, the left and right helicities. The description of the propagation of an electric field in a uniform media is dictated by the k constant or the refractive index n. Both quantities are linked in the simplest case by the dispersion relation:

$$k = \frac{n\omega}{c} \tag{2.2}$$

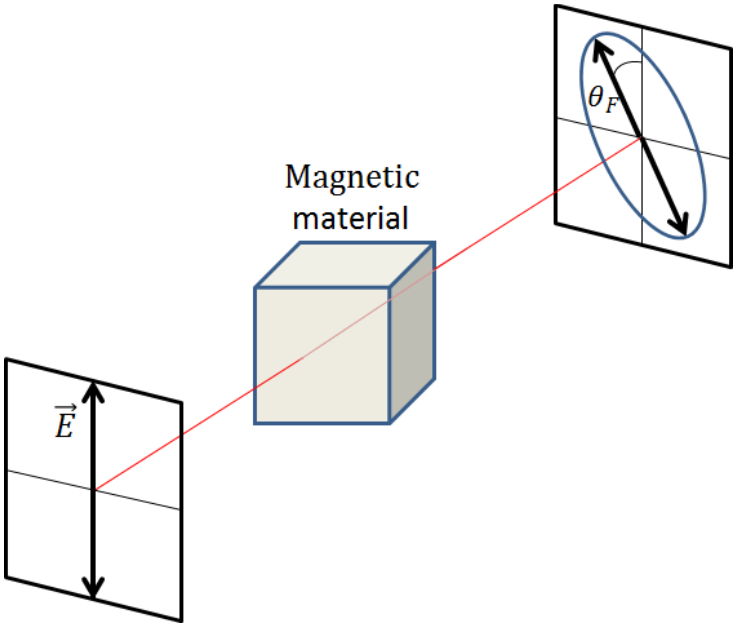

Figure II.3: Illustration of the Faraday effect when a linearly polarized light passes through a magnetic material. The outcoming light is elliptically polarized with a big axis rotated of θ_F to the initial axis of polarization of the light.

While the refractive index is equal to 1 in vacuum, it is not the case in every medium. Indeed "n" is a complex number that depends on several parameters as for instance the nature of the medium or wavelength of the light. Under a given set of conditions, two distinct refractive indexes can apply to the left and right helicities. n_+ (respectively n_-) is the refractive index that is applied to the right (respectively to the left) helicity. We can decompose n_+ and n_- in real and imaginary parts:

$$\begin{cases} n_+ = N_+ + i\kappa_+ \\ n_- = N_- + i\kappa_- \end{cases} \tag{2.3}$$

The resulting electric fields for right and left polarized light of the same amplitude are:

$$\begin{cases} \text{RCP:} \quad \vec{E}_{RCP} = E_0(\vec{x} + i\vec{y})e^{i(\omega t - (N_+ + i\kappa_+)\frac{z\omega}{c})} \\ \text{LCP}: \quad \vec{E}_{LCP} = E_0(\vec{x} - i\vec{y})e^{i(\omega t - (N_- + i\kappa_-)\frac{z\omega}{c})} \end{cases} \tag{2.4}$$

$$\begin{cases} \vec{E}_{RCP} = e^{-\frac{z\omega}{c}\kappa_+} \; E_0(\vec{x} + i\vec{y})e^{i(\omega t - N_+\frac{z\omega}{c})} \\ \vec{E}_{LCP} = e^{-\frac{z\omega}{c}\kappa_-} \; E_0(\vec{x} - i\vec{y})e^{i(\omega t - N_-\frac{z\omega}{c})} \end{cases} \tag{2.5}$$

If we consider d as the distance of propagation of the light through the material and $\Phi_F = \frac{\omega d}{2c}(n_+ - n_-)$ we obtain in the end an expression of the total electric field $\vec{E}_{tot}$ by adding the two contributions of the right and left circular polarizations:

$$\vec{E}_{tot} = E_0 e^{i(\omega t - (n_+ + n_-)\frac{d\omega}{2c})}(cos(\Phi_F)\,\vec{x} + sin(\Phi_F)\,\vec{y}) \tag{2.6}$$

Φ_F is a complex quantity called the complex Faraday angle that can be written as :

$$\Phi_F = \theta_F + i\varepsilon_F \tag{2.7}$$

ε_F is called the Faraday ellipticity and is not null if $\kappa_+ \neq \kappa_-$. For instance, if we have $N_+ = N_-$ and $\kappa_+ \neq \kappa_-$, one helicty is more absorbed than the other, then the two circular polarizations do not have the same amplitude anymore and the total polarization becomes elliptical with the same major axis of polarization. When κ_+ and κ_- also depend on the magnetic field inside the material, we have magnetic circular dichroism (MCD).

θ_F is called the real Faraday angle and is defined by the expression (2.7). It accounts for a phase delay between the left and right polarizations of the light originating from the real parts of the refractive indexes (N_+ and N_-) that keep both amplitudes constant. If we have $N_+ \neq N_-$ and $\kappa_+ = \kappa_-$, then the polarization is still linear but with an axis of polarization rotated from θ_F. When N_+ and N_- also depend on the magnetic field inside the material, we have magnetic circular birefringence (MCB). For instance in the first experiment of Faraday where the light propagated through a glass, there was no absorption, so Faraday observed only a rotation of the polarization axis due to the MCB. The magnetic materials we use in the laboratories are often absorbing (for instance Co, Fe or Ni) and then subject to both MCD and MCB. Both contributions are then summarized in the complex Faraday angle Φ_F.

This rotation of the polarization also occurs due to magnetic circular birefringence (MCB) in any material where there is a magnetic field. For instance the local magnetization in ferromagnetic can also yield a Faraday rotation. This is the phenomenon used to probe the magnetization of a ferromagnetic material. The relation between the field B inside the material and the rotation angle is:

$$\theta_F = B d\, \nu \tag{2.8}$$

ν is an intrinsic parameter called the Verdet constant. The Kerr effect lies on the same principle of rotation of the polarization but it revolves around the reflected light while the Faraday effect involves the transmitted light. It is also a technique used to know the magnetic state of a sample. When occurring in magnetic materials, the Kerr effect is called MOKE (magneto-optical Kerr effect). As seen in figure II.4, there are different configurations for a MOKE microscope. The choice of the configuration depends on the component of the magnetization that the user wants to probe. For a longitudinal configuration, we probe the component of the magnetic moment in the same direction as the propagation of the light (a). In the transversal mode, we probe the component of the magnetic moment in the plane of the sample and perpendicular to the direction of propagation of the light. For both configurations, we need to have a non-zero incidence angle with the surface of the film (c). For a polar configuration we send the light perpendicular to the surface of the film to probe the out-of-plane component of the magnetic moment (b). During my thesis, I used only the polar MOKE configuration since I was interested in samples exhibiting a large PMA.

During my thesis, I also used Kerr microscopy to be able to image the magnetic configuration and to perform locally hysteresis loops. I performed out-of-plane hysteresis loops using Kerr both in San Diego and in Nancy on the same model of instrument, an Evico MOKE microscope. It has a spatial resolution of 1.2 μm. It is possible to apply an out-of-plane magnetic field with a maximum amplitude of 8000 Oe. Using a different coil geometry in San Diego, it was also possible to apply a field of maximum 3200 Oe in the plane of the sample and to pulse an out-of-plane field of 100 Oe. The length of the field pulse can be tuned from 0.1 ms to 1 s.

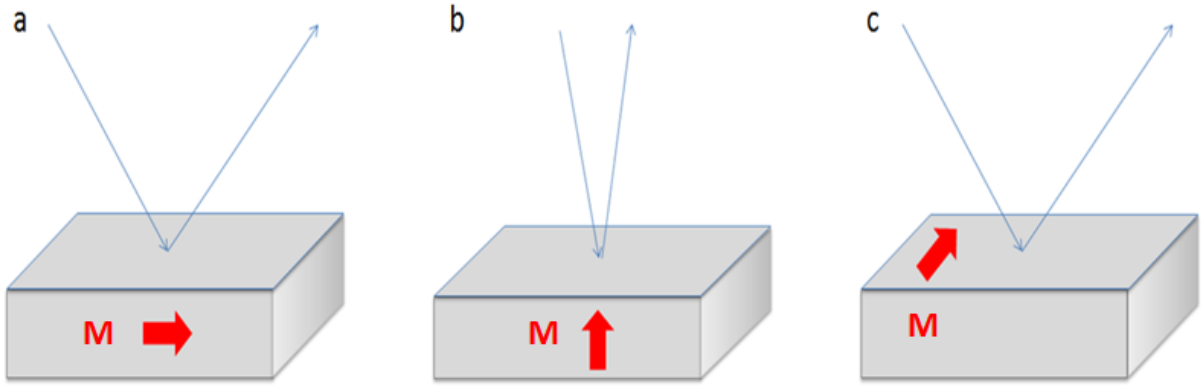

Figure II.4: Illustration of the MOKE microscope in the (a) longitudinal, (b) polar and (c) transversal configurations.

II.2.2) Characterization of magnetic properties: VSM

In order to extract magnetic parameters as the effective anisotropy, the magnetization at saturation or the coercive field, the most widespread technique is the VSM (vibrating sample magnetometer) [98]. The principle of the measurement is to make the sample oscillate close to a coil. The coil feels an oscillating magnetic field associated to the local magnetic moment of the sample measured. This oscillating field induces a current in the coil that is proportional to the flux in the loop of current. By measuring the resulting voltage in the coil it is then possible to obtain the flux and consequently the magnetic moment of the sample. We can thus obtain in-plane or out-of-plan hysteresis loops by applying external fields to the sample. Different models of VSM exist, depending on the detection threshold wanted. The more precise one is a SQUID VSM, with an empirical detection limit in the range of 10^{-8} emu suitable for instance for measurements of ferrimagnetic samples. We measured hysteresis loops for ferromagnetic samples and using PPMS (property measurement system) VSM that has a detection threshold in the range of 10^{-6} emu. This PPMS VSM works also in a range of temperature from 1.9K to 400K and it can be used to performed M(T) measurements from which we can extract the Curie temperature of a sample. Hysteresis loops have been performed in San Diego and Nancy using respectively a 3T Versalab and a 7T Magnetic Properties Measurement System (shown in figure II.5).

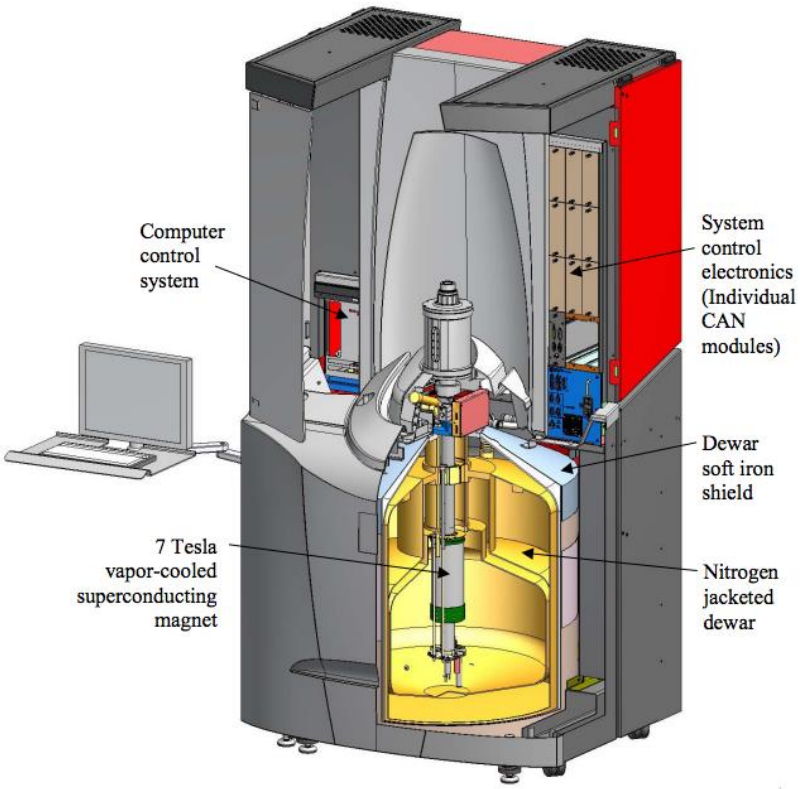

Figure II.5: Schematic of the 7T Magnetic Properties Measurement System SQUID VSM I used in Nancy to perform hysteresis loops. Extracted from [99]

II.3) Laser setup

Since the pioneer work of Beaurepaire *et al.* [3], the interplay between light and magnetism has been a vast topic for researchers. Generating compressed light with a high fluence is not a goal easy to achieve. The aim of this part is to explain some basics principles linked with the laser setup at the IJL.

II.3.1) Principle

II.3.1.a) Generation of laser

First built in 1986 by Moulton [100], Ti: sapphire laser is the most common type of ultrafast laser because of its tunable wavelength from 680 nm to 1130 nm. Its pulse length can go down to 5 fs. As seen on figure II.6, its maximum of emission is around 790 nm. Because its maximum of absorption is close to 490 nm, it can be typically pumped with a Nd:YAG laser. The model of Ti: sapphire laser we use in Nancy is a Vitara, commercialized by Coherent Inc. With a Kerr-lens modelocking (KLM), it is possible to obtain durations of the pulses lower than 20 fs, a repetition rate of 5 kHz and a spectral selection centered at 800 nm with a bandwidth of 50 nm. KLM is based on the fact that the material

crossed by the laser, a nonlinear optical medium, has a refractive index which increases with the laser fluence. The special evolution of the refractive index then follows the Gaussian spatial distribution of fluence of the beam. This results in the creation of short and monochromatic pulses from continuous waves of polychromatic light. In the end, an aperture selects shortest and more intense pulses.

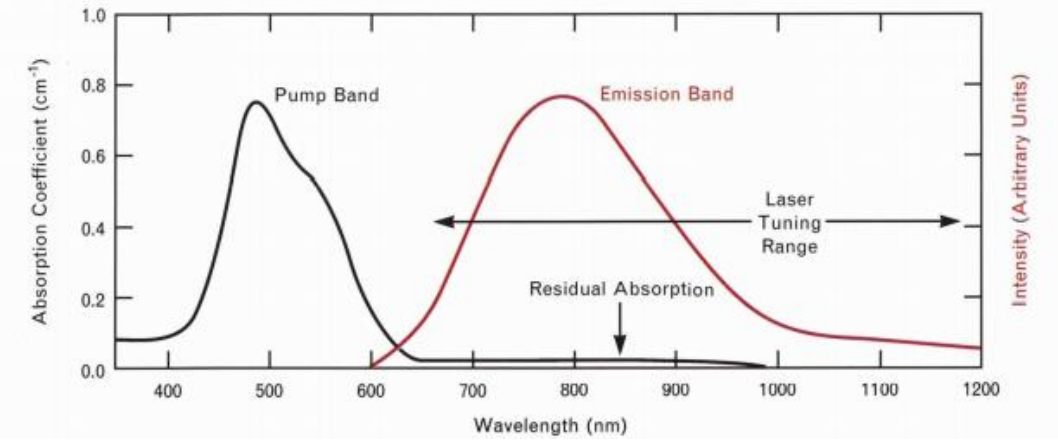

Figure II.6: The emission and absorption bands of Ti:AI20 3. The absorption band, which peaks near 490 nm, occurs in the blue-green region of the spectrum and allows Ti:$AI_2 0_3$ to be pumped by argon-ion lasers, frequency-doubled Nd:YAG lasers, copper-vapor lasers, or flashlamps. The emission band peaks near 790 nm. A weak absorption band that overlaps the emission band is known as the residual absorption. Extracted from [101]

II.3.1.b) Amplification

Once the laser pulses are created, they need to be amplified to be useful. Present in our system as in most of the femtosecond lasers, the chirped pulse amplification (CPA) has been introduced by Strickland *et al.* [102]. A scheme of the CPA principle is shown on figure II.7. The pulse is first temporally stretched by a grating pair. The low-frequency components of the light have a shorter path in each grating than its high-frequency components so the beginning of the resulting pulse is composed of low-frequency light and the end is composed of a high-frequency light. The duration of the stretched pulse is typically between 10^3 and 10^5 times longer. Once the pulse stretching achieved, the laser pulse can be amplified by a factor of 10^6 because it will not damage the amplifier optics now. The amplification steps itself is called the regenerative amplification and it occurs in a cavity where the laser passes around 10 times through sapphire crystal that stores the energy. When the laser pulse energy is high enough it is then released from the cavity. Once the pulse has been safely amplified, it is recompressed to its original duration by another grating pair.

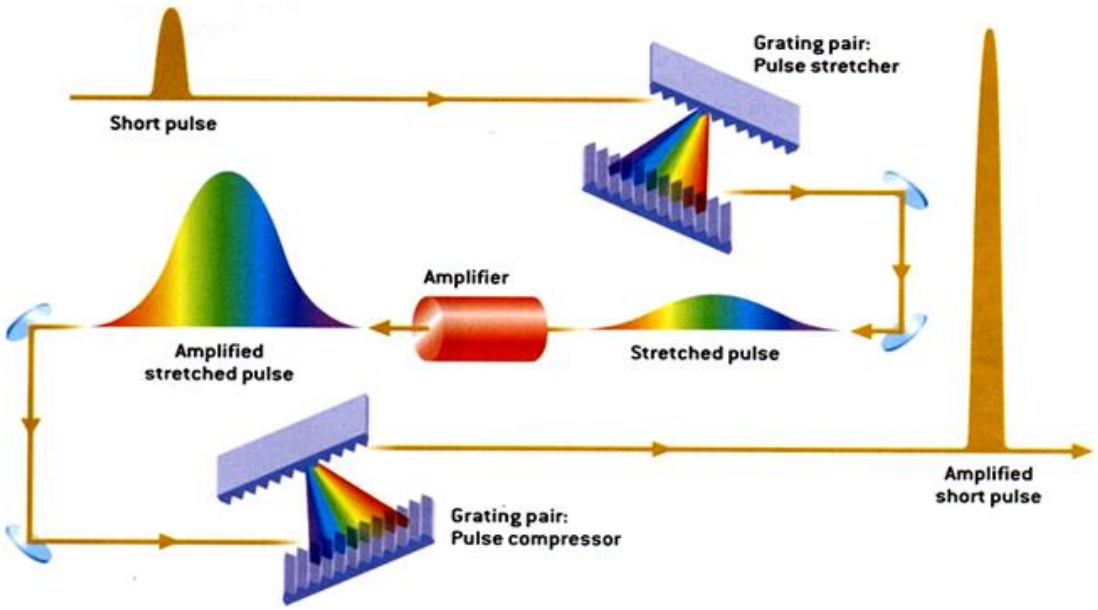

Figure II.7: Principle of chirped pulse amplification. The laser is first temporally stretched by passing through grating pair, then amplified and finally recompressed to obtain an amplified pulse of the same length as the initial pulse. Extracted from [103].

II.3.2) Laser setup

All the experimental results involving a femtosecond light presented in this manuscript have been performed on the femtosecond laser setup present at the IJL. Once the laser has been generated and amplified, it goes through a pulse picker to tune the repetition rate or even select single pulses. The light is then linearly polarized by passing through the first Glen-Taylor polarizer of the optic line. It crosses then a half-wave ($\lambda/2$) and a quarter-wave ($\lambda/4$) plates that respectively induce a phase delay of π and $\pi/2$ between the components of the light propagating along the fast and the slow optical axes of the wave plate. The half wave plate role is to tune the laser fluence needed for the experiment. The role of the quarter wave plate is to polarize circularly (either left or right) the previously linearly polarized light. Then the lens focuses the beam on the sample such that the beam diameter is 50µm on the sample. After reaching the sample, the laser still needs to be blocked at some point, either for the safety of the user, or to protect the camera (this is the role of the filter that only let the light from the LED pass).

The LED sends the probe light that will be used to image the magnetic configuration of the sample. It emits a linearly polarized light at 680 nm. The first polarizer on this optical line works in pair with the analyzer (which is actually another polarizer but is named this way from his role in the setup). To obtain a high Kerr contrast both polarizer must have their axis almost perpendicular. The CCD cameral role enables us to image the magnetic contrast. It provides images of 2448 x 2048 pixels with a pixel size of 0.13 µm. The imaged area is then bigger than the size of the laser spot on the sample and is possible to place the spot on the center of the image. On top of this well-established setup, it is possible to add other instruments as small coils to provide an out-of-plane magnetic field or a multimeter as the one used by El Hadri in 2016 [78].

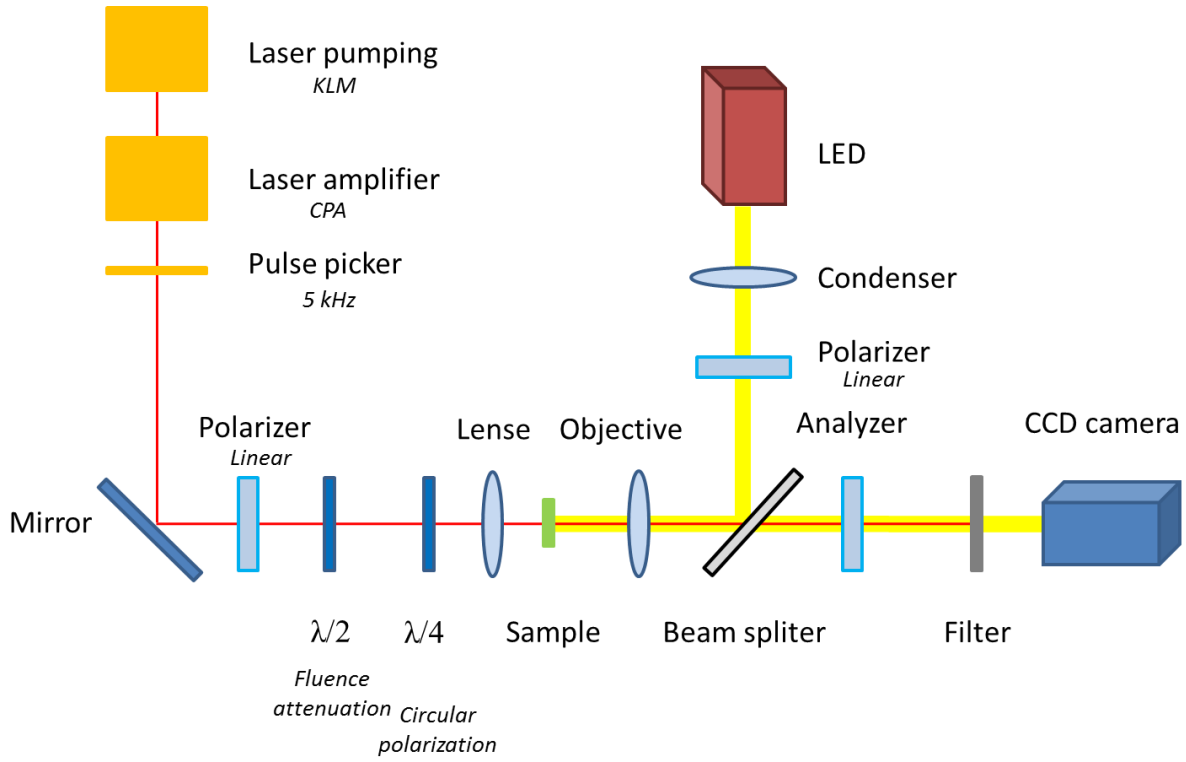

Figure II.8: Experimental setup for laser dedicated to the exposure of the sample to femtosecond light and its static MOKE imaging.

II.4) Conclusion

We have introduced in this part most of the instruments I used during my PhD thesis. Those involve thin film growth, magnetic characterizations or short pulses of circularly polarized light. I performed those measurements both at IJL in Nancy and at CMRR in San Diego. As we will see in the experimental parts, some films have been grown in Spintec (Grenoble) and in Cavendish Laboratory (Cambridge). The magnetic characterizations of the samples discussed in part III.2) have also been carried out in Cambridge.

III) Effect of the femtosecond light on exchange related phenomenon

III.1) Effect of the femtosecond light on a ferromagnet/ antiferromagnet interface

Résumé en français: Dans cette partie nous nous intéressons à l'influence de la lumière polarisée sur une bicouche antiferromagnetique/ferromagnetique. En particulier nous allons étudier l'interface IrMn/[Co/Pt]xN. L'effet de la lumière polarisée sur des couches ferromagnétiques et ferrimagnétiques ayant été étudié, il semble naturel d'étudier à son tour l'effet de la lumière sur une couche antiferromagnétique. Cependant ce n'est pas une chose aisée compte tenu de la faible réponse des couches antiferromagnétiques à un champ magnétique externe et la difficulté de sonder les configurations magnétiques de l'IrMn par MOKE. Nous avons donc choisi d'étudier le changement de configuration à l'interface de l'IrMn à travers son effet sur le [Co/Pt]xN, à savoir l'existence d'un décalage d'échange dans le cycle d'hysteresis de la couche ferromagnétique. Nous verrons dans un premier temps comment évolue ce décalage d'échange en fonction des paramètres des matériaux (épaisseurs de Co, Pt, IrMn, ordre de croissance des couches et nombre de répétition des couches de [Co/Pt]). Tous ces paramètres ont une influence sur le décalage d'échange. Dans un second temps nous ferons varier les paramètres du laser (fluence, nombre d'impulsions laser, hélicité de la lumière, ou application simultanée d'un faible champ magnétiques). Notre but est de comprendre le rôle de l'hélicité de la lumière sur l'interface FM/AFM. Dans un troisième temps nous nous pencherons sur les conséquences pratiques que peuvent avoir nos résultats sur la création de zones de nucléation et de direction de propagation de paroi privilégiés. Une partie des résultats obtenus dans cette partie ont déjà été publiés [104].

English summary: In this part we are interested in the effects of the exposure of an AFM/FM bilayer to a polarized light. In particular we study the IrMn/[Co/Pt]xN interface. The effects of the polarized light has already been studied on ferromagnetic and ferrimagnetic layers, it seems natural to study the effect of the light on an antiferromagnetic layer. However this is not an easy task given the really small effects of an applied magnetic field on the antiferromagnetic layers and the difficulty to probe the magnetic configuration of the IrMn with a MOKE microscope. We then chose to study the change of the interfacial configuration of the IrMn by its effect on the $[Co/Pt]_N$, i.e the existence of an exchange bias field in the hysteresis cycle of the FM layer. First we will look at the evolution of the exchange bias as a function of materials parameters (thicknesses of Co,Pt, IrMn, order of growth of the layers and number of repeats of the $[Co/Pt]_N$ multilayer. All the parameters have a strong influence

on the exchange bias. Secondly we will change the laser parameters (fluence, number of light pulses, helicity of the light or simultaneous application of a small out-of-plane magnetic field). Our goal is to understand the role of the helicity of the light on the AFM/FM interface. Finally we will take a look at the practical consequences of our results on the creation of areas of nucleation and preferential directions of propagation. Some of the experimental results described in this part have been already published [104].

III.1.1) [Pt/Co]/IrMn multilayers

III.1.1.a) Properties of Co/Pt multilayers

The ferromagnetic material we use in this part is a [Pt/Co] multilayer exhibiting a strong perpendicular magnetic anisotropy. The perpendicular magnetic anisotropy in [111] textured Pt/Co multilayers has been evidenced for the first time in 1988 [2]. It has been first attributed to the formation of a CoPt alloy at the interface between Co and Pt. Actually the interfacial anisotropy and subsequently the PMA in these films is mainly due to the hybridization of the 5d shells of the Pt and the 3d of the Co at the Co/Pt interface. In this hybridization the strong spin orbit coupling of the Pt plays an important role. In 1994 Weller *et al.* [105] measured an enhancement of 0.15μ_B per Co atom of the orbital magnetic moment of the hybridized Co atoms in Pt/Co multilayers. Interestingly the magnetic moment of the Pt at the interface also increases to 0.6μ_B (with an orbital contribution of 0.03 μ_B) per Pt atom for the first Pt layer and decreases exponentially [106]. The lattice mismatch also plays a role in the increase of the interfacial anisotropy via the strain at the Co/Pt interface as investigated in 1996 by Kyuno *et al.* [107]

III.1.1.b) Properties of IrMn antiferromagnetic layer

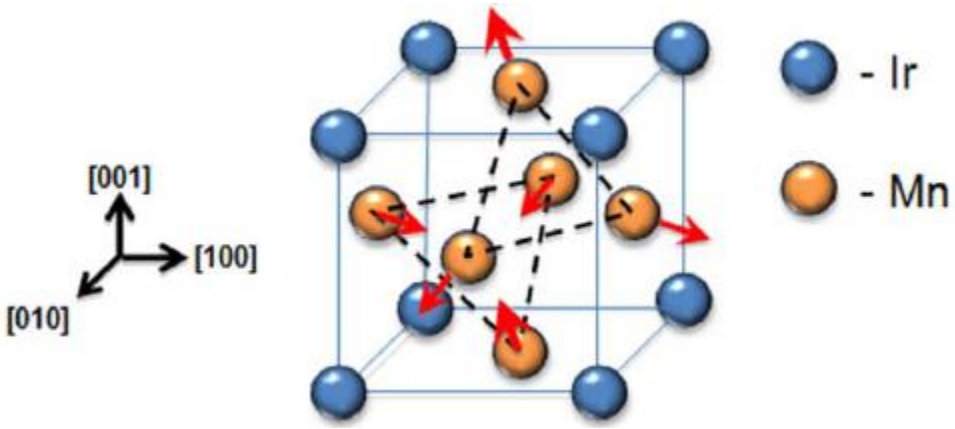

Figure III.1: Crystallographic structure of the $L1_2$-IrMn3 phase. The red arrows account for the local magnetization of the Mn atoms. Extracted from [108].

The antiferromagnetic material we use in this study is $IrMn_3$. There are two phases of IrMn used for applications, the $L1_2$ and the chemically disordered γ. In the Ll_1-$IrMn_3$ the magnetic moments are carried by the Mn atoms as on figure III.1. The resulting magnetic moment of one unit cell is the sum of all the moments of Mn atoms and is zero. In the disordered γ phase, the phase obtained from magnetron sputtering, Mn atoms do not have any preferential site and also yield in a null magnetic moment. The blocking temperature of the IrMn is close to 250°C [109] and depends on the thickness of IrMn layer [110].

III.1.2) Optimization of the stack

III.1.2.a) Influence of the IrMn thickness on the exchange bias

Using DC magnetron sputtering with a base pressure of 4.10^{-8} Torr we grew Ta(3nm)/Pt(5nm)/[Pt(2nm)/Co(0.6nm)]$_2$/IrMn(t_{IrMn})/Pt(3nm) samples on both Si and glass substrates (with t_{IrMn} =5, 6, 7, 8, 9 and 10nm). In order to set the exchange bias field, we annealed the sample at 270°C during 1 hour with a positive out-of-plane field of 25 kOe. To control the properties of our films we performed hysteresis loops using the SQUID VSM in the out-of-plane geometry. All the samples exhibited an out-of-plane easy axis of magnetization and exchange bias. The resulting values of the exchange field are shown on figure III.2.

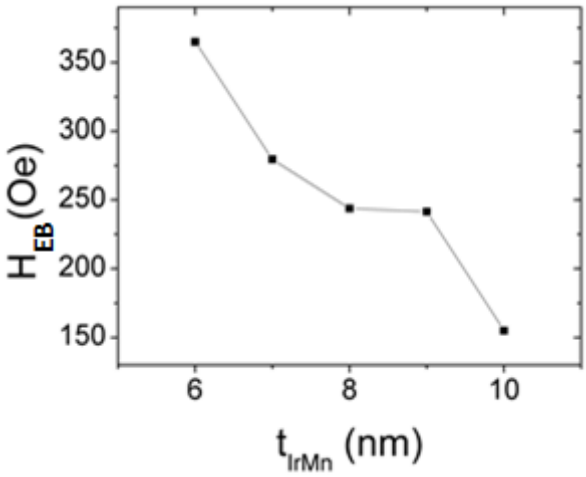

Figure III.2: Evolution of the exchange field (He) as a function of the thickness of IrMn (t_{IrMn}) obtained from perpendicular hysteresis cycles performed in a SQUID VSM.

As observed in figure III.2 the exchange bias field decreases when we increase the IrMn thickness, which is consistent with other studies [111] [112]. It is due to the fact that grains with the highest volumes are not pinned during the annealing process since their anisotropy energy scales with their volume and thus they do not contribute to the exchange bias field in average since they stay randomly pinned. By increasing the IrMn thickness, we increase the average volume of the grains and the number of grains with a volume high enough to stay pinned during the annealing process.

III.1.2.b) Influence of the insertion of a Pt interlayer

To tune the exchange bias field it is possible to add a thin Pt interlayer between the Co and the IrMn layers. This interlayer has two opposite effects: it increases the PMA of the Pt/Co because of the hybridization at the supplementary interface with the Co but it also tends to decrease the exchange coupling between Co and IrMn [113]. It has also been shown that the Pt interlayer acts as a barrier for the diffusion of Mn and Ir atoms in the Co layer [114]. As mentioned in this paper and also observed on figure III.3, the insertion of interlayer of Pt leads to a decrease of the exchange bias field. They observe the enhancement of the exchange bias field only for a thickness of Co lower than 0.4 nm and not at 0.6nm. This is explained by the diffusion of the IrMn layer inside the Co layer. We finally decided not to use a Pt interlayer for our next stacks to have a higher exchange bias field.

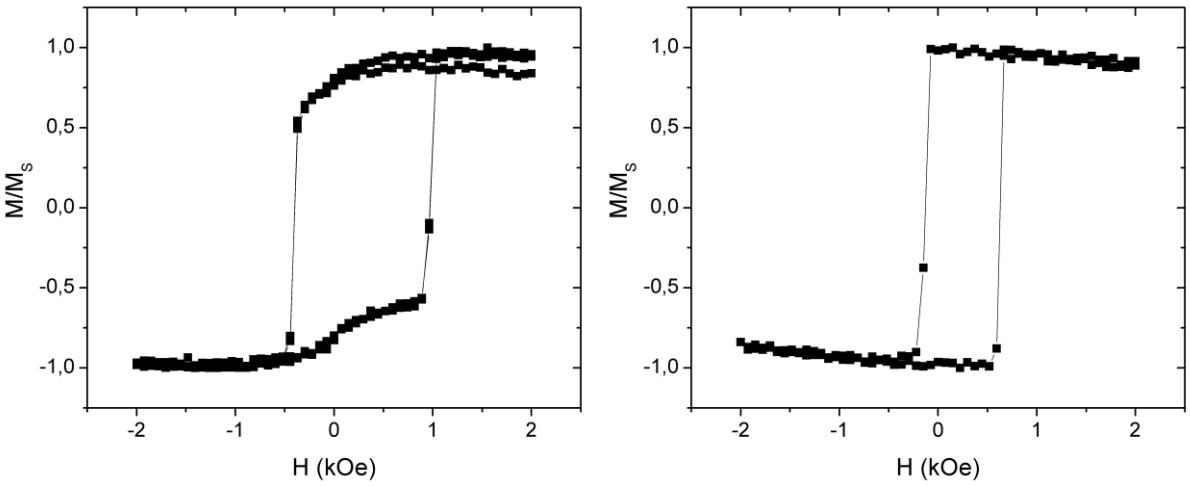

Figure III.3 : Hysteresis cycle of annealed a) [Co(0.6nm)/[Pt(2nm)]2/IrMn(7nm) and b) [Pt(2nm)/Co(0.6nm)]2/Pt(3A)/IrMn (7nm) obtained on SQUID VSM in the out-of-plane geometry.

III.1.2.c) Inversion of Co/Pt and IrMn

In this part, we take a look at the difference between a $[Pt(2nm)/Co(0.6nm)]_2$/IrMn (7nm) and a IrMn (7nm) /$[Co(0.6nm)/ Pt(2nm)]_2$ sample. An interesting point is the fact for both samples without any annealing the sample with IrMn exhibits EB. This has already been observed in the literature [115]. As it can be noticed in figure III.4, the exchange bias field is stronger for a top IrMn layer. It is consistent with the literature and explained by the fact that the Co layer grows in a magnetic saturated state so if we grow the IrMn layer after the interfacial exchange sets the exchange bias naturally. In agreement with the literature, again, the exchange bias field is this time stronger for a bottom IrMn than for a top one in our experiment.

Sample	Before annealing		After annealing	
	H_{EB} (Oe)	H_C (Oe)	H_{EB} (Oe)	H_C (Oe)
IrMn(7nm)/[Co(0.6nm)/Pt(2nm)]$_2$/Pt(3nm)	125	375	400	500
[Pt(2nm)/Co(0.6nm)]$_2$/IrMn(7nm)/Pt(3nm)	260	360	290	700

Figure III.4: Exchange bias and coercive fields of [Pt(2nm)/Co(0.6nm)]2/IrMn (7nm) and IrMn (7nm) /[Co(0.6nm)/ Pt(2nm)]2 samples before and after annealing.

The aim of this part is to choose a FM/ AFM bilayer made of a $[Co/Pt]_N$ multilayer (FM) and an IrMn layer (AFM) to be able to perform laser experiment on it and may be observe a change on the exchange bias field provoked by the laser exposure. We will mainly focus our study on bottom IrMn samples because of their stronger exchange bias field after annealing. Indeed a higher exchange bias field is more suitable for quantitative comparison of the EB fields obtained from different experiments involving the laser. However for non-quantitative studies as the one just explained next we will also use a top IrMn samples to show that the stacking between $[Co/Pt]_N$ and IrMn does not play a role.

III.1.3) AO-HDS in IrMn/[Co/Pt] xN multilayers

III.1.3.a) AOS of the exchange-biased ferromagnetic layer

In 2014, Lambert *et al.* [7] demonstrated AO-HDS on a Co/Pt multilayer. Our first goal here is to verify if AO-HDS still occurs for a biased $[Co/Pt]_N$ multilayer. We exposed the samples Glass/Ta(3nm)/Pt(5nm)/[Pt(2nm)/Co(0.6nm)]$_2$/IrMn(t_{IrMn})/Pt(3nm) of the section III.1.2.c) to the femtosecond laser described on the setup chapter (section II.3.2) through the Pt(3nm) capping layer. We swept the laser on the samples at a speed of 5µm/s with three different polarizations of the laser (σ+, L and σ-). The result of such a sweeping for t_{IrMn} = 8nm is shown on figure III.5. We conducted the experiment on samples with various IrMn thicknesses, because the IrMn thickness has a strong influence on the contrast of the images obtained with the Faraday microscope. Indeed we have been able to observe the AO-HDS of the FM layer for thicknesses of IrMn of 6, 7 and 8 nm as seen on figure III.5 but for thicknesses higher than 8 nm we have no information on effect of the light on the ferromagnetic layer.

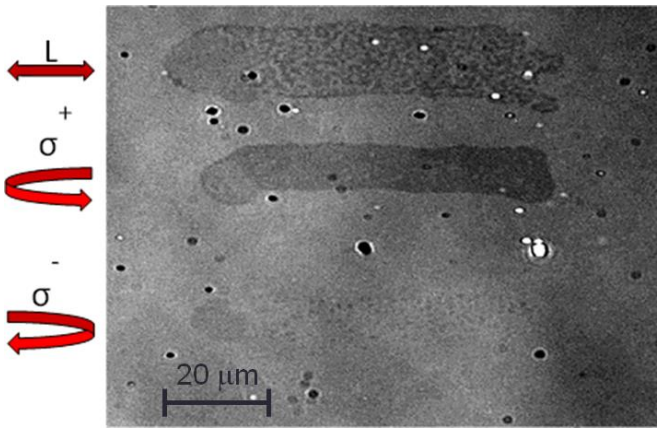

Figure III.5: Faraday imaging after the sweeping of a right-circularly (σ^-), a linear L and a left-circularly (σ^+) polarized laser beam over the Glass/Ta(3nm)/Pt(5nm)/$[Pt(2nm)/Co(0.6nm)]_2$ /IrMn(8nm)/Pt(3nm) sample at a sweeping speed of 5µm/s. For all exposures to the laser the fluence was 8.9 mJ/cm^2. The magnetization of the sample has been saturated in the –z direction before the sweeping of the laser.

It is already remarkable that the Co/Pt switching can be observed even when the ferromagnetic layer is coupled to an antiferromagnetic layer.

III.1.4) Effects on the exchange bias

III.1.4.a) Effects of the AOS of the ferromagnetic layer for N=2 on EB

In this part we study the evolution of the EB field after the laser exposure process on a Glass/Ta(3nm)/Pt(5nm)/IrMn(7nm)/$[Pt(2nm)/Co(0.6nm)]_2$/Pt(3nm) sample. The Faraday image of the samples (figure III.6) indicates a typical AO-HDS process. We decided to directly perform the laser sweeping experiment, without previous annealing, in order to prevent any degradation of interfaces during the annealing process. As seen on figure III.7.a), the Glass/Ta(3nm)/Pt(5nm)/IrMn(7nm)/[Co(0.6nm)/Pt(2nm)]x2/Pt(5nm) sample already showed an exchange bias on the as-grown sample. The hysteresis loops reported in fig. III.7b-d) were measured on areas where the laser beam was swept with σ^-, L and σ^+ polarizations, respectively. This shows without any ambiguity that σ^+ polarized light induces a negative exchange bias field whereas σ^- polarized light induces a positive exchange bias field. After sweeping the laser, the bias direction, the final state of the $[Co/Pt]_N$ magnetization and the interfacial IrMn moments are thus aligned, independently of the initial bias direction. The process is reversible and the sign of the exchange bias for the same area of the sample can be reversed with subsequent sweeping of the beam with opposite helicity.

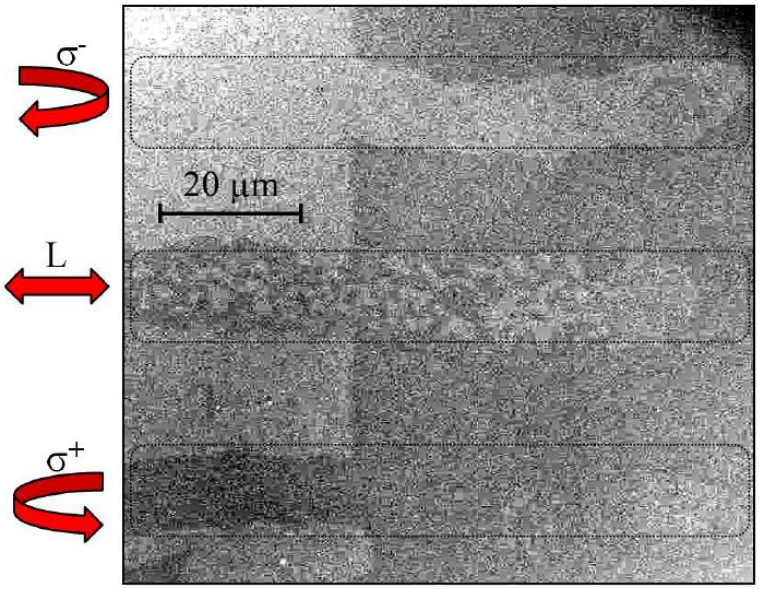

Figure III.6: Faraday imaging after that, a right-circularly (σ^-), a linear L and a left-circularly (σ^+) polarized laser beam have been swept over the Glass/Ta(3nm)/Pt(5nm)/IrMn(7nm)/[Co(0.6nm)/Pt(2nm)]$_2$/Pt(5nm) sample at a sweeping speed of 5µm/s. For all exposure to the laser the fluence was 8.9 mJ/cm^2. The magnetization of the sample was saturated in the –z direction before the sweeping of the laser.

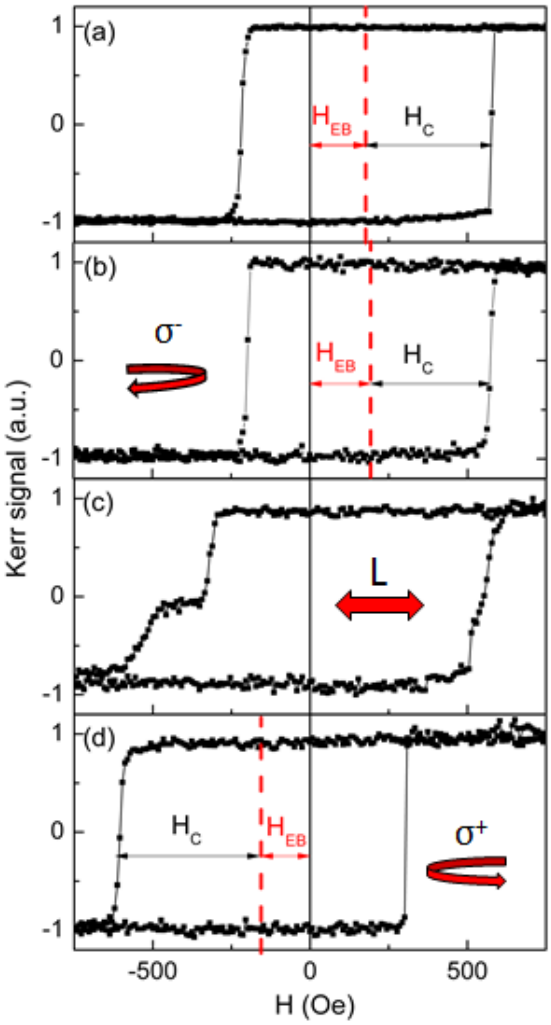

Figure III.7: Results obtained on an exchange biased sample Glass/Ta(3nm)/Pt(5nm)/IrMn(7nm)/$[Co(0.6nm)/Pt(2nm)]_1$/Pt(5nm) a) Faraday imaging after that, a right-circularly (σ^-), a linear L and a left-circularly (σ^+) polarised laser beam were swept over the sample at a sweeping speed of approximately 10 µm/s. Kerr signal Hysteresis loop obtained on a) a non-exposed sample area (as grown sample) b) on an area where a right-circularly polarised, (σ^-) laser beam was swept, c) area where a linearly polarised (L) laser beam was swept d) area where a left-circularly polarised, (σ^+) laser beam was swept. For all exposures to the laser, the fluence was 8.9 mJ/cm^2.

III.1.4.b) Effects of the AOS of the ferromagnetic layer for N=1 on EB

We performed the same experiment with a Glass/Ta(3nm)/Pt(5nm)/[Pt(2nm)/Co(0.6nm)] /IrMn(7nm)/Pt(3nm) that is also as-grown (it has not been annealed). The resulting MOKE image and hysteresis loops are shown on figure III.8. We also obtained a switching pattern on the MOKE image III.8.a. The results are similar to the case were N=2, except for one point, the linear helicity. For two repeats of Co/Pt, the linearly polarized light creates up and down domains and the resulting hysteresis cycle is composed of two different branches as in Malinowski *et al.* [116]. For one repeat of Pt/Co the

sweeping drags in this experiment a domain of negative magnetization and the resulting Kerr loop is shifted to the positive, just like the σ- does. This is different from the sweeping experiment with N=2. At this point we can submit the hypothesis that the linear helicity has a different effect on EB field after laser sweeping because it has a different effect on the $[Co/Pt]_N$ magnetization. The underlying question is which one influences the other. Actually, domain wall dragging by linear polarization has already been observed in $[Co/Pt]_N$ samples of 1 repeat [78] and it was not due to the influence of an AFM layer. We attribute the origin of the phenomenon to be the same in our sample as in the literature. This leads to the conclusion that the reset of the EB is in our samples a consequence of the Co/Pt final orientation after laser exposure and not the opposite.

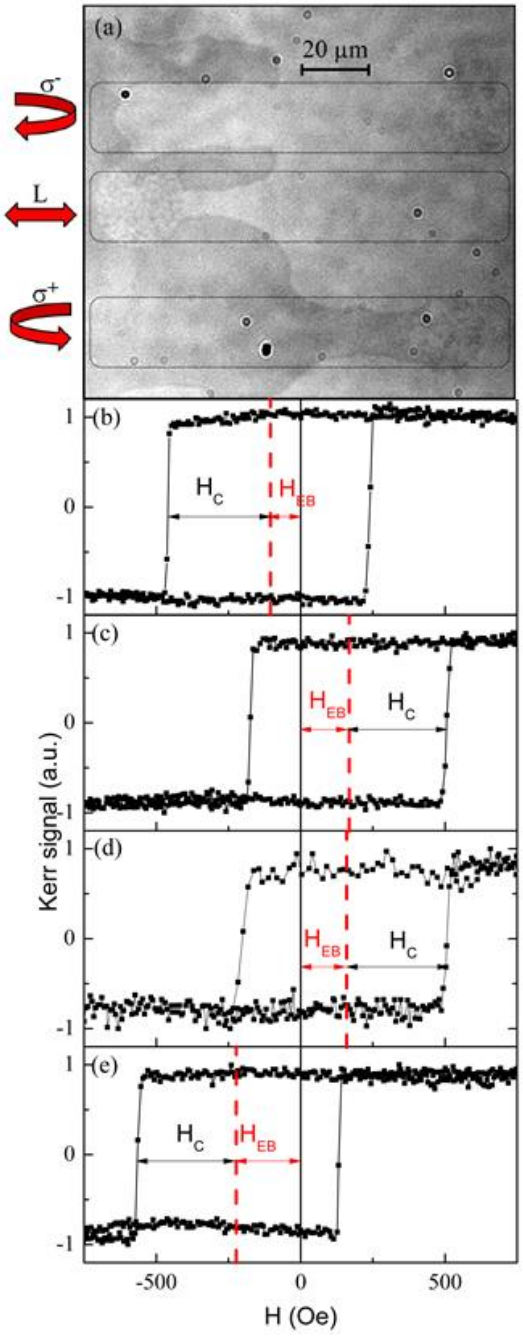

Figure III.8): Results obtained on an exchange biased sample Glass/Ta(3nm)/Pt(5nm)/IrMn(7nm)/[Co(0.6nm)/Pt(2nm)]/Pt(5nm). Kerr signal hysteresis loop obtained on a) a non-exposed sample area (as grown sample) b) on an area where a right-circularly polarised, (σ^-) laser beam was swept, c) area where a linearly polarised (L) laser beam was swept d) area where a left-circularly polarised, (σ^+) laser beam was swept. For all exposures to the laser the fluence was 8.9 $\mathrm{mJ/cm^2}$.

III.1.4.c) Effects of the application of a small out-of-plane magnetic field on EB

To confirm the role of the orientation of the FM layer we studied the combined effects of the laser and an applied magnetic field on the N=1 film. Figure III.9 compares the effect of sweeping a circularly polarised laser beam (fig III.9.a)) with sweeping a linearly polarised laser beam while applying a magnetic field sufficiently large to saturate the magnetization of the sample exposed to the light (fig III.9.b)), on the local hysteresis loop. This demonstrates that the effect of σ^+ (resp. σ^-) polarization on the exchange bias field and coercive field is similar to the effect of a linear polarization and a positive (H↑, 3 Oe) (resp. negative (H↓, -3 Oe)) applied magnetic fields.

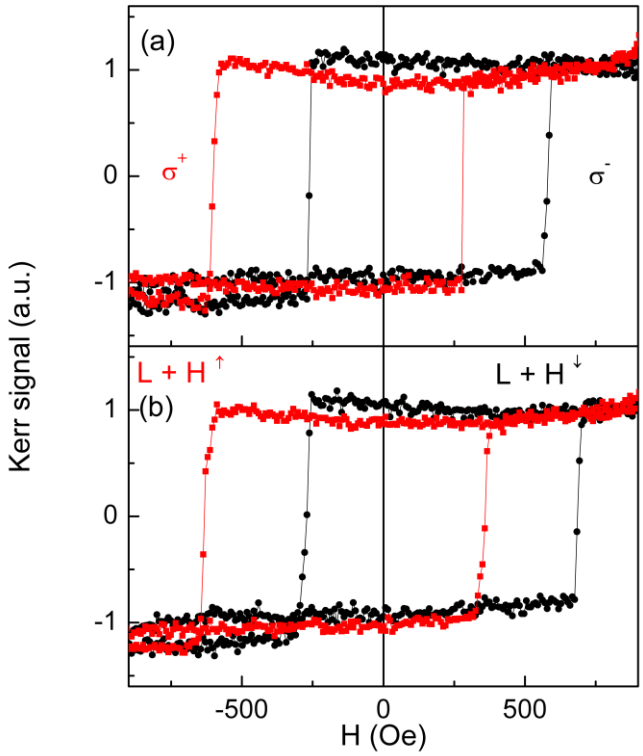

Figure III.9: Hysteresis loop of Glass/Ta(3nm)/Pt(5nm)/IrMn(7nm)/[Co(0.6nm)/Pt(2nm)]$_1$/Pt(5nm.) Comparison between a) the effect of a right-circularly (σ^-), or a left-circularly (σ^+) polarised laser beam with b) the combined effects of a linearly polarised light and an applied magnetic field, up or down. The fluence of the laser was 8.9 mJ/cm^2.

Lambert *et al.* [7] demonstrated that applying a σ^+ (resp. σ^-) or applying a linearly polarized light simultaneously to positive field (resp. negative) sets the FM layer magnetization in the same direction. Figure III.9 shows furthermore that applying an σ^+ (resp. σ^-) and applying a linearly polarized light simultaneously to positive field (resp. negative) also sets the EB field in the same direction. Once again the sign of the EB is opposite to the final direction of the magnetization of the Co/Pt.

III.1.4.d) Effects on exchange bias of a laser fluence under the switching threshold

At this point, the explanation that the evolution of the EB field after sweeping is a consequence of the final orientation of the FM seems robust. However it cannot be easily differentiated from a direct role of the helicity of the light on the AFM itself. We conducted another experiment to make the difference between both theories clearer. We conducted the following experiment: the magnetization of the FM layer was initially set either positive or negative by an applied magnetic field and then the laser was swept with reduced laser fluence, just under the fluence threshold of the $[Co/Pt]_N$ switching (5.7 mJ/cm^2). As shown in Fig. III.10 the resulting exchange bias depends only on the orientation of the $[Co/Pt]_N$ magnetization before the light is applied. Our interpretation is the following. The effect of the light on the AFM in this experiment is only to bring heat. The laser heats the grains of the AFM responsible for the EB. Those grains become unpinned because their temperature is above their blocking temperature. When laser exposure is over, the AFM grains cool down. During the cooling of the AFM, the magnetic configurations of the AFM grains at the FM/AFM interface align with FM magnetization due to the exchange coupling.

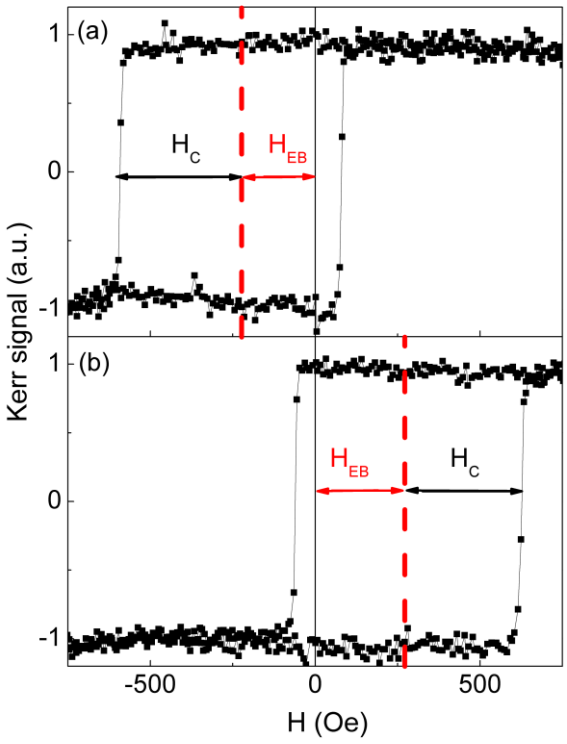

Figure III.10: Hysteresis loop of Glass/Ta(3nm)/Pt(5nm)/IrMn(7nm)/$[Co(0.6nm)/Pt(2nm)]_1$/Pt(5nm) obtained in an area where a linearly polarized laser with a fluence just under the switching threshold (5.7 mJ/cm^2) has been swept as the FM magnetization is previously saturated a) down and b) up.

We can note that the resulting exchange bias field is almost equal to the coercive field.

III.1.4.e) Variation of the number of light pulses

We performed static beam experiments with a fluence above the switching threshold (8.9 mJ/cm^2) on the same sample. The initial magnetization was saturated along the $+e_Z$ vector and the helicity used was σ^-. We sent then different numbers of light pulses (1, 20 and 50 000 light pulses) on different virgin areas of the sample. In practice we begin to send 1 laser pulse on a virgin area of the sample, then move the sample laterally to 150 μm and we send 20 pulses on this new region, we move laterally to 150 μm again and send 50 000 laser pulses on a third virgin region of the sample.

For each exposed region we observed a disk on MOKE microscope and local hysteresis loops were measured at different positions going from the centre of the disk to outside of it (figure III.11). Since the laser intensity is Gaussian and its centre corresponds to the one of the disk, studying the evolution of the exchange bias and coercive field as a function of the distance from the laser beam centre gives us information on their laser fluence dependence. The exchange bias and coercive field have been extracted from the local hysteresis loops and their evolution as a distance r from the centre of the disk is displayed on figure III.12.

Examining figure III.12 we can observe two different evolutions of the exchange bias field: its evolution as a function of the number of pulses and its spatial evolution at a certain distance r from the centre of the beam. It appears clearly that the exchange bias field is higher for a higher number of pulses. The switching of the Co/Pt layer is a pulse cumulative process as described by El Hadri *et al.* [78]. Since the FM magnetization gets closer to its down state when the number of pulses is increased, the exchange bias field value is higher. This is consistent with our hypothesis that the exchange bias field is set by the FM magnetization when we light pulses are sent. The analysis of the spatial evolution of the exchange bias field is a bit more complex. According to Lambert *et al.* [7] when we expose a $[Co/Pt]_N$ multilayer to a circularly polarized light, 3 distinct remarkable areas emerge: the centre of the beam where the sample is demagnetized, an area with a ring shape, where the switching of the $[Co/Pt]_N$ occurs, called the switching rim and the outside of this rim where no change in the Co/Pt magnetization is observed. Interestingly we can also divide the spatial profile of the exchange bias field observed in figure III.12 into three different parts. In the centre of the beam, the exchange bias field is close to zero, at R_C the exchange bias field is maximum and for $r>R_C$ the exchange bias field is equal to the one in the rest of the sample. The spatial profile of the exchange bias field and the spatial profile of the FM magnetization then superpose well and we observe one striking result: the exchange bias field variations follow the ones of the FM magnetization as if the FM magnetization sets up the exchange bias field. Figure III.13 is a schematic of the magnetic configuration in the bilayer after the 50 000 laser pulses sent on the sample.

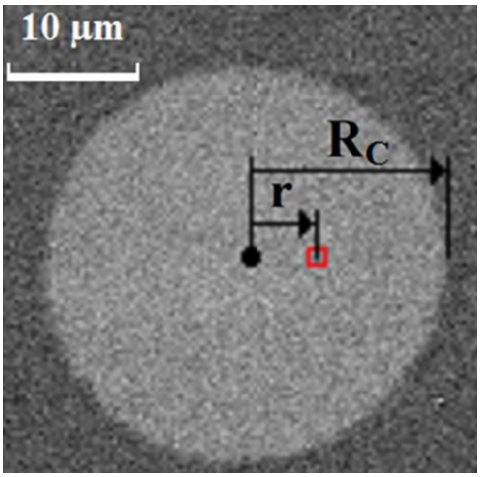

Figure III.11: MOKE microscope image of the sample after a single laser pulse. The red square at a distance r from the centre indicates where the hysteresis loop is performed. The fluence of the laser was 8.9 mJ/cm^2.

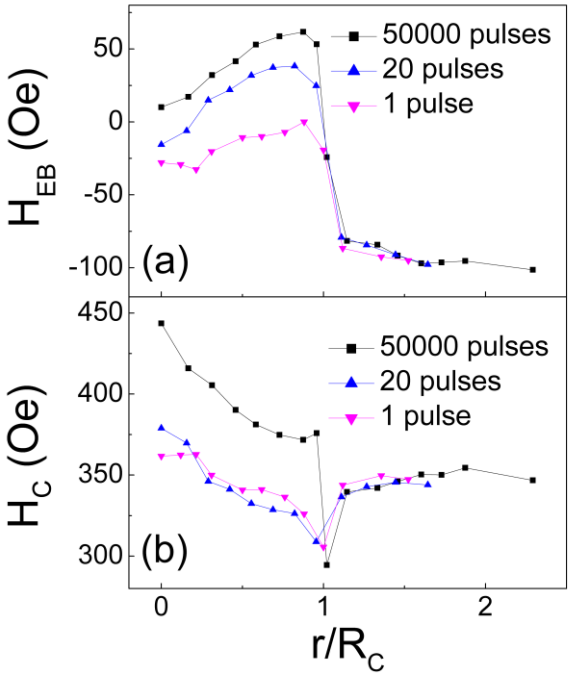

Figure III.12: Results obtained on Glass/Ta(3nm)/Pt(5nm)/IrMn(7nm)/[Co(0.6nm)/Pt(2nm)]$_1$/Pt(5nm).(a) Exchange bias field (H_{EB}) and (b) coercive field (H_C) as a function of the position (r) from the centre of a laser spot after a single pulse (full triangles pointing up), 20 pulses (full triangles pointing down) and after 50 000 pulses (full squares). The fluence of the laser used is 8.9 mJ/cm^2.

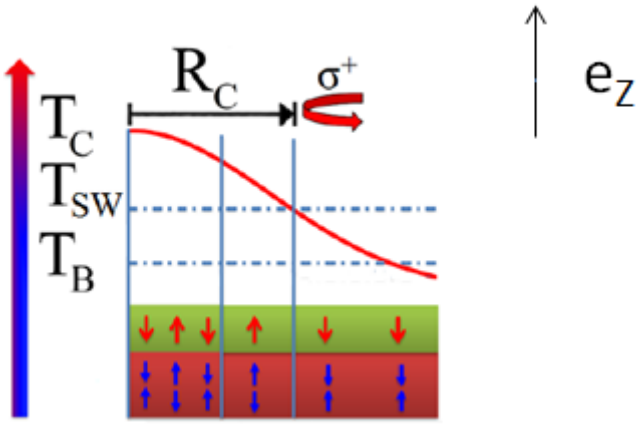

Figure III.13: Sketch of the laser intensity profile and the corresponding magnetic configuration. Above T_C both FM and AFM interfacial moments form randomly oriented domains. Between T_C and T_{SW} both the FM and interfacial AFM moments are pinned along the e_Z vector. Between T_{SW} and T_B FM and interfacial AFM moments are pinned along the - e_Z vector.

III.1.4.f) Discussion on the mechanism

In this part, we detail the mechanism that we believe to be responsible for our results. The key factor is the temperature. For the thicknesses of Co and Pt we used, the Curie temperature (T_C) of the Co/Pt multilayer is in the literature higher than 640 K [117]. The switching temperature (T_{SW}), defined as the temperature where the laser induces a switching of the magnetization in the FM layer, has been shown to be slightly smaller than T_C [5]. For this thickness, the blocking temperature (T_B), the temperature that one needs to reach to obtain a zero exchange bias whatever the orientation of the AFM grains was before, is equal to 420K [65].

To illustrate our understanding of the sweeping measurement with a fluence above the switching threshold, we consider the example of figure III.14. This case can be explained more easily than other cases. Initially the FM magnetization is saturated along –z and the EB is positive as sketched on figure III.14. We sweep the laser to the right with a σ^- helicity. In region (A) neither the AFM or the FM orientations are affected since their temperature is below T_B. This corresponds to the case $r>R_C$ in figure III.11. In region (B), the temperature is included between T_B and T_{SW}. In this region, the AFM grains get unpinned while the FM layer keeps its magnetic orientation. In region (C) both the FM and the AFM are unpinned since the laser fluence brings both temperatures above T_{SW}. From region (D) to (E), the AFM cools down through T_B with a FM magnetized along +z. The exchange at the interface between the AFM and the FM reorients the AFM interfacial grains responsible for the EB and consequently the EB field reverses. The effect of the light on the reset of the EB is not an intrinsic effect of the light on the AFM but depends on the FM orientation.

Introduced in 1996 [3], the three temperature model is used to describe the interactions between three different reservoirs, electrons (T_E), spins (T_S) and the lattice (T_L). If we compare the estimated evolutions of those temperatures after laser pulses from references [118] and [119] with the blocking temperature we observe that only spins and electrons can reach this temperature in the IrMn layer. Consequently, the exchange bias field can be totally reset thanks to the sudden increase of

the electron and spin temperatures few picoseconds after the laser exposure. At first sight, this seems to be incoherent with the model of thermally activated AFM grains that is used in the regular field cooling process to set the EB field [120]. However the ultrafast response of an FM/AFM bilayer to optical excitation has already been studied in NiFe/NiO [121] and [122] and a quenching of the EB was demonstrated to occur while the spin and electron temperatures overcome T_B while the lattice temperature is under T_B. The reset of the EB occurs, in those cases, at the timescale of the spin-lattice relaxation time (150 ps for the first reference and 215 ps for the second one). The reset of the EB in our sample must then also occur during this spin-lattice relaxation time after the laser exposure. We can also note that a partial EB field reset by laser exposure has already been observed in a Ni/FeF_2 bilayer [123] with no mention to the relevant temperature to describe this physical phenomenon.

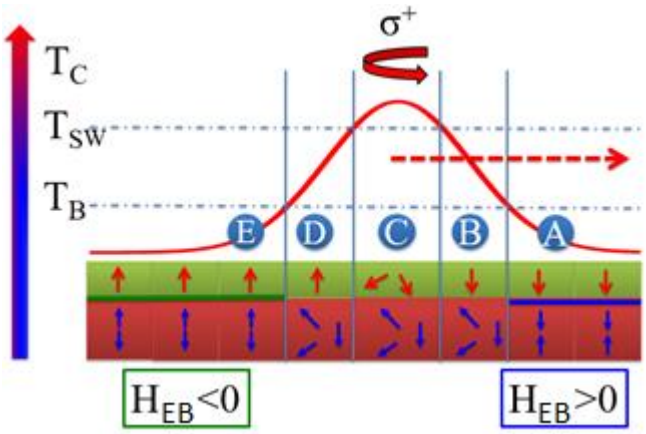

Figure III.14: Sketch of the effect of a sweeping beam on the AFM/FM magnetic configuration in A) the laser power is too low to influence either the AFM and FM magnetic configuration. Initially, the FM magnetisation is pointing down and the exchange bias is positive. For B) the power is large enough to demagnetize the AFM C) the left-circularly polarisation (σ^+) and the laser fluence allows the FM switching from down to up while the temperature is above the AFM blocking temperature. D) The AFM layer is cooled down through its blocking temperature with a FM layer magnetization pointing up which leads to a negative exchange bias.

III.1.4.g) Looking for an intrinsic effect of light on the antiferromagnetic layer

After these experiments, we wanted to conduct a more systematic and quantitative study. For this, we conducted several sweeping experiments on the IrMn/[Co/Pt] sample. First we used a fluence just below the switching threshold (5.7 mJ/cm^2). We changed different parameters to evaluate their respective role. Those parameters are: the sign of the saturation field applied to set the initial FM magnetization before the sweeping, the sign of the small field applied during the sweeping of the laser (either 3 Oe, -3 Oe or no magnetic field) and the helicity used (here σ^+ and σ^-). After the sweeping of the laser we measured the exchange bias field in the centre of the track left by the sweeping of the

laser. It is important to note that for each experimental condition, the laser was swept on a virgin region, a region where we never swept the laser before. The results of these experiments are summarized in the figure III.15.

The first remark that can be made on this figure is that the sign of the exchange bias field is determined only by the initial state of the magnetization in the Co/Pt. Indeed, the exchange bias field obtained is positive for a negative saturation field, and negative for a positive saturation field. The field applied during the experiment seems to have quite no effect on the final state. It is still consistent with the fact that the Co/Pt layer is not altered during the sweeping whatever the applied field and the helicity are.

Saturation field	Applied field during sweeping (Oe)	Helicity	H_{EB} centre (Oe)
-	0	σ+	124
-	+3	σ+	266
-	-3	σ+	184
-	0	σ-	162
-	+3	σ-	173
-	-3	σ-	168
+	0	σ-	-235
+	+3	σ-	-229
+	-3	σ-	-256
+	0	σ+	-221
+	+3	σ+	-241
+	-3	σ+	-246

Figure III.15: Results obtained on Glass/Ta(3nm)/Pt(5nm)/IrMn(7nm)/[Co(0,6nm)/Pt(2nm)]x1/Pt(5nm). Summary of the sweeping measurements obtained below the switching threshold of ferromagnetic layer, at 5.7mJ/cm^2.

We conducted the same set of experiments than in figure III.15 but with a fluence of the laser above the switching threshold of the Co/Pt. The results are shown on figure III.16. The data analysis is in that case more complicated because of the possible reorientation of the Co/Pt. However we find some results already exhibited sooner in this manuscript. Indeed if there is no applied field, a σ^+ helicity results in a positive EB field and a σ^- helicity results in a negative EB field. We observe that when we

add a positive (respectively negative) field to a σ^+ helicity (respectively σ^- helicity) the resulting EB field is also positive (respectively negative). This is consistent with the fact that the signs of the helicity and the magnetic field pin the Co/Pt magnetization in the same orientation in this case. In the case where the helicity of the light and the sign of the applied field tends to set the orientation of the Co/Pt multilayer magnetization in opposite orientations we always observe that the sign of the EB field is determined by the sign of the applied field. This indicates that 3 Oe is enough in our case to overcome the helicity of the light and pin the FM magnetization.

For some cases the resulting EB field has strong spatial variations in the direction perpendicular to the sweeping direction. This is directly linked to the Gaussian distribution of fluence of the laser. We measure in those cases the EB field at the edge of the beam too to characterize this. For instance for the case of an initial negative saturation, no field applied during the sweeping and a σ+ helicity (the second line on figure III.16 the EB field measured in the centre is negative while the resulting EB field at the edge is positive. Our interpretation is that in the center of the beam the final state of the FM layer results to the helicity of the light since the laser fluence here is above the switching threshold of the FM while at the edge the helicity of the light has no effect on the FM orientation due to the lower fluence so the final EB field results only from the initial FM state.

Saturation field	Applied field during sweeping (Oe)	Helicity	H_{EB} centre (Oe)	H_{EB} edge (Oe)
-	0	σ+	-213	185
-	+3	σ+	-201	193
-	-3	σ+	204	
-	0	σ-	66	
-	+3	σ-	-140	204
-	-3	σ-	204	
+	0	σ-	225	-212
+	+3	σ-	-214	
+	-3	σ-	199	-184
+	0	σ+	-246	
+	+3	σ+	-255	
+	-3	σ+	71	-227

Figure III.16: Results obtained on Glass/Ta(3nm)/Pt(5nm)/IrMn(7nm)/[Co(0.6nm)/Pt(2nm)]x1/Pt(5nm). Summary of the sweeping measurements obtained above the switching threshold of ferromagnetic layer, 8.9 $\mathrm{mJ/cm^2}$.

III.1.5) Patterning areas of nucleation

III.1.5.a) Addressing the shape of the areas of nucleation

In all the previous experiments, the exchange bias field has been controlled in specific areas where the laser has been shined. In this part, we show that it is possible to control domain nucleation and propagation by modifying the exchange bias field in certain areas.

For this we grew a sample of Ta(3nm)/Pt(5nm)/IrMn(7nm)/[Co(0.6nm)/Pt(2nm)]$_2$/Pt(3nm) using DC magnetron sputtering. Its hysteresis cycle as-grown is shown on figure III.17. The sample has an as-grown negative exchange bias field.

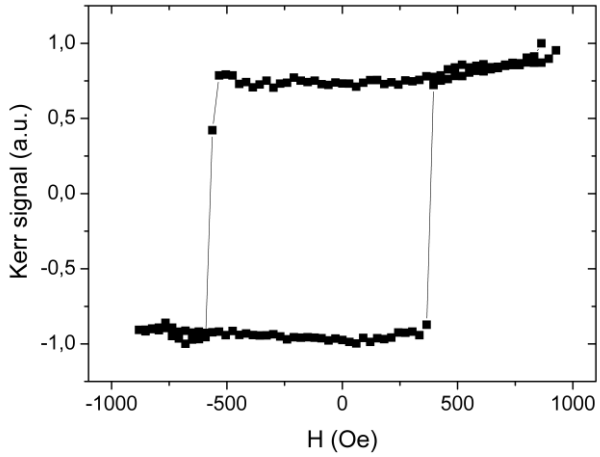

Figure III.17: Hysteresis loop of a Glass/Ta(3nm)/Pt(5nm)/IrMn(7nm)/[Co(0.6nm)/Pt(2nm)]$_2$/Pt(3nm) sample obtained with a MOKE in the out-of-plane geometry.

Before any exposure to the laser, we saturated the sample with an out-of-plane positive magnetic field. We then swept the laser on the sample with a linear helicity and a fluence of 4.6 mJ/cm^2, which was below the fluence necessary to reverse the magnetic state of the Co/Pt. We then imaged the sample on the area previously exposed to the laser with a MOKE setup under some specific conditions. We saturated the sample with a negative field and imaged the domains by increasing the field little by little from -1000 Oe to the saturation field. This can be seen on figure III.18.

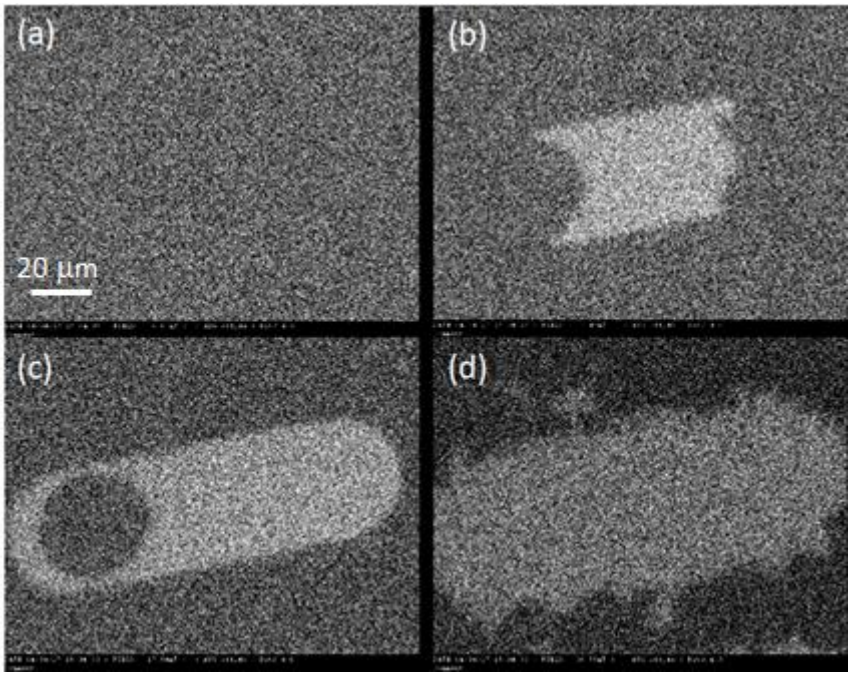

Figure III.18: MOKE images of the sample. The sample has been first exposed to the laser, then moved to the MOKE setup and exposed to a strong negative field (-1000 Oe) and the field has been increased little by little to observe the pattern of the magnetic domains at a) 60.8 Oe, b)74.5 Oe, c)175.4 Oe and 365.5 Oe.

On the image III.18.a), the applied magnetic field is 60.8 Oe and the sample is still fully saturated down. On the image III.18.b), the magnetic field is 74.5 Oe and we can see that a domain begins to nucleate in the region where we have swept the laser. This is due to the fact that, where the laser was swept, the hysteresis cycle of our sample is more shifted toward the negative field. By increasing the field value from 74.5 Oe (b) to 175.4 Oe (c), we achieve the nucleation of the whole region previously exposed to the laser. At a larger field (365.5 Oe) the nucleated domain propagates to the rest of the sample since we reached the propagation field of the region unaltered by the laser.

On figure III.18 we saturated the sample with a negative magnetic field and increased the field little by little. On figure III.19 we imaged the same place on the sample but we saturated the sample with a positive field and decreased the field little by little.

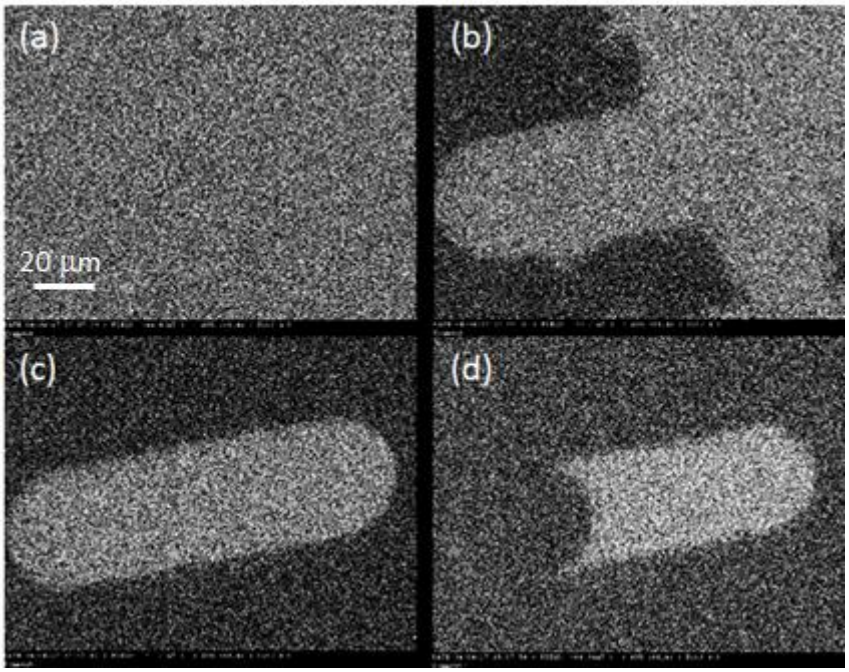

Figure III.19: MOKE images of the sample. The sample has been first exposed to the laser, then moved to the MOKE setup and exposed to a strong positive field (1kOe) and the field has been decreased little by little to observe the pattern of the magnetic domains at a) -444 Oe, b)-502.3 Oe, c)-532.8 Oe and -649.4 Oe

On image III.19.a) the magnetic field is -444 Oe and the sample is still saturated up. On image III.19b), at -502.3 Oe, down domains have formed on the sample (the dark ones) but the area where the sample was swept remains unaffected (still up domain). On figure c), at -532.8 Oe, the entire sample is saturated down, except on the track left by the laser. On figure III.19d), at -649.4 Oe the up-domain on the track of the laser begins to shrink and will after disappear when the entire sample is saturated down. Figures III.18 and III.19 show that the track of the laser is the first nucleation place, when we apply a positive magnetic out-of-plane field after having saturated with a negative field. When we first saturate the sample with a positive field and apply a negative field, it is the last propagation place when we sweep from positive to negative values of the out-of-plane applied magnetic field.

This experiment shows that it is possible to create domain wall nucleation locations using the femtosecond polarized light. We decided to change locally the EB value using laser fluence below the switching threshold of the FM layer because the track made by the laser is more homogeneous. In the case of a power above the switching threshold, the track left by the sweeping of the laser is more complex. The track is composed of an inner part influenced by a higher laser fluence (above switching threshold) and an outer part which is influenced by a lower laser fluence (below the switching threshold).

We also swept the laser on the sample, making different patterns using a laser fluence below the switching threshold of the $[Pt/Co]_2$. The initial saturation of the magnetization of the sample before the laser is swept is negative. After the laser sweeping, we observed on MOKE microscope how magnetization reverses. The areas where the magnetization reverses first are the areas exposed to the laser. They are shown on figure III.20.

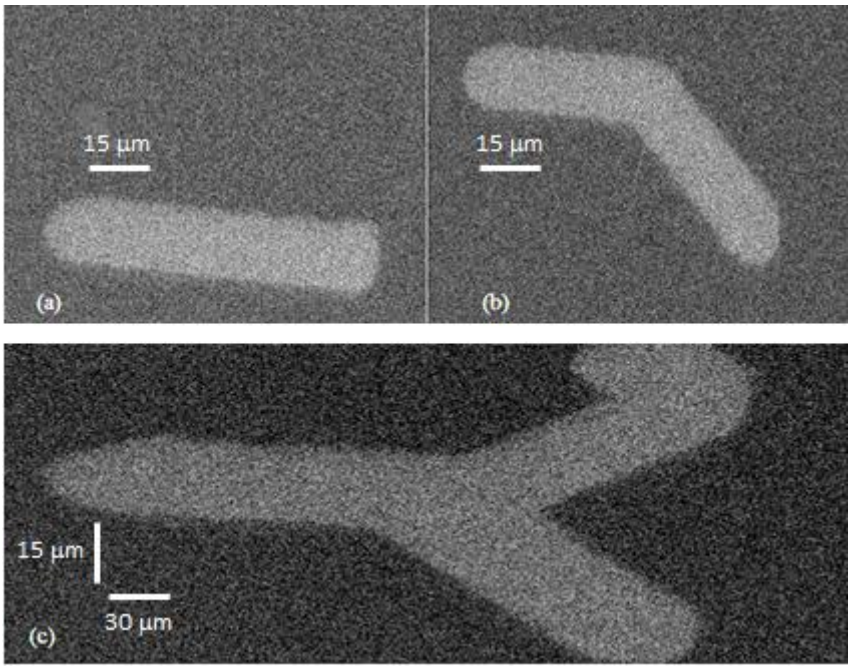

Figure III.20: MOKE images of the sample exposed to laser under the laser switching laser threshold of the Co/Pt bilayer.

Figures III.20.a) and III.20.b) show that it is possible to draw different patterns by sweeping the laser in different directions. For the figure III.20.c) the pattern has been made in two steps. The first step consists in sweeping the laser from the left to the right corner on the top. For the second time, we swept from the left to the right corner at the bottom. With this sweeping process the laser is swept twice on some regions and once on other regions. However, this does not seem to affect the nucleation pattern. All those MOKE images taken tends to show that it is possible to design with the laser any preferential nucleation shape, even by sweeping the laser several times on the same place.

III.1.5.b) Addressing the direction of propagation

The next step in the manipulation of magnetic domain after the creation of areas of nucleation is the control of the direction of propagation of the domain walls. For this, we saturated the FM layer in the negative direction thanks to an external static field and followed the procedure described in figure III.21.

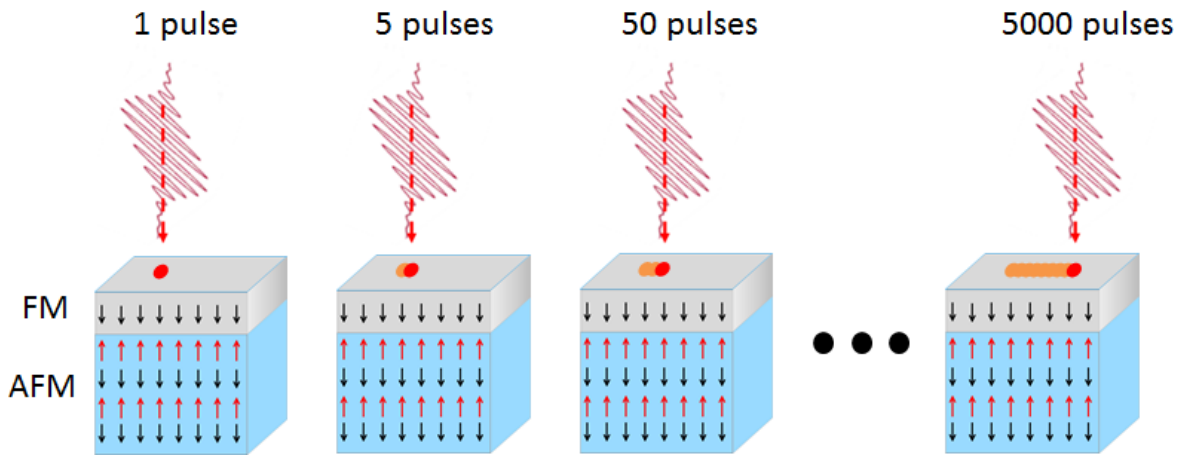

Figure III.21: Schematic of the procedure followed to design a nucleation area with a preferential direction of propagation of the domain wall. Starting from a negatively saturated ferromagnetic layer, a single laser pulse is sent on a virgin area on the sample. Then the sample is moved laterally of 20 µm to then send 5 laser pulses, move the laser laterally of 20µm to send 50 pulses. This operation of lateral displacement of the sample and exposure to laser pulses has been repeated for 50, 100, 200, 500, 1000, 2000 and finally 5000 pulses. The laser fluence is 9.6 mJ/cm^2. Its polarization is σ^-.

The procedure consists in sending a light pulse, moving the sample laterally, sending 5 light pulses and moving the sample laterally, sending 50 light pulses and moving laterally and so on until 5000 pulses. Because the lateral displacement of the sample (20 µm) is smaller than the radii of the laser spot (25 µm) a part of the area that has been exposed to the first laser pulse has also been exposed to the following 5 pulses as seen on figure III.21. At the end of the procedure, the resulting area exposed to the laser has a shape similar to a line. The point of this procedure lies in the fact that the EB field increases with the number of pulses as seen on figure III.12, so there must be an EB field spatial gradient along the line from the area exposed to the first laser pulse to the area exposed to the last 5000 pulses. Using MOKE microscope, we then imaged the region exposed to the laser as seen on figure III.22.

On the MOKE setup, we first saturated negatively the sample and increased the value of the field from the negative to the positive to nucleate domains of positive magnetization as seen on figure III.22.a) taken at 406.8 Oe (the darker domains are up domains and the whiter domains are up domains). On figure III.22.b), at a 492.6 Oe, we observe that domains of negative magnetization have reversed around the area previously exposed to the laser but not inside it. On figure c) at 566 Oe we observe that the domain of positive magnetization has propagated from the right of this area to almost its center. On figure d) and e) the domain has even more propagated toward the left because of the increase of the field to 577.8 Oe and then to 600.1 Oe. The propagation of the domain of positive magnetization on the left side of the area is finally completed on figure f) at 611.5 Oe. This demonstrates that we can create an area where we dictate the direction of domain walls through an EB field spatial gradient.

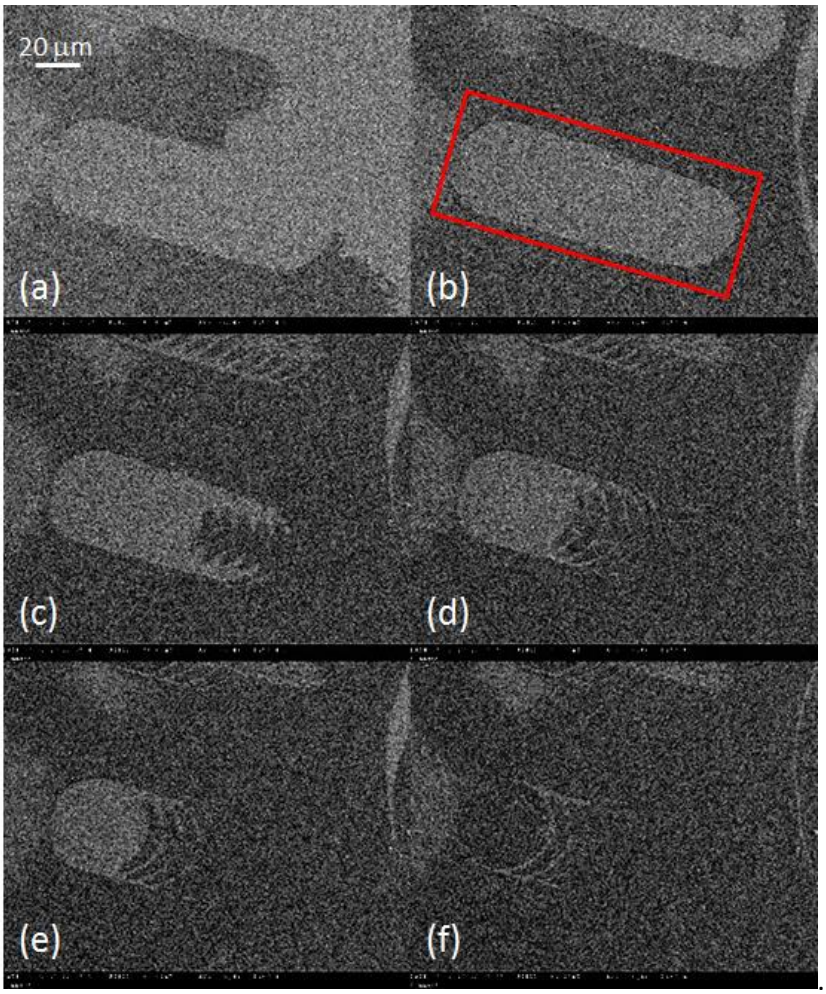

Figure III.22: MOKE images. For all images the sample has been saturated down and the magnetic field has been increased to record successively the images a) at 406.8 Oe, b) at 492.6 Oe, c) at 566 Oe, d) at 577.8 Oe, e) at 600.1 Oe and f) at 611.5 Oe. The area inside the red rectangle in image b) is the area exposed to the laser during the procedure described in figure III.21.

III.1.6) Conclusion and perspectives

In this section we have studied the effect of polarized femto-second light pulse on ferromagnetic/ antiferromagnetic (FM/AFM) heterostructures showing exchange bias effect. Choosing the appropriate $[Pt/Co]_N$/IrMn samples we have demonstrated that it is possible to control the exchange bias field using circularly polarized light laser pulses . We attribute this phenomenon to an increase of the electronic temperature in the IrMn layer coupled to a pinning of the Pt/Co layer. The key parameters seem to be the ordering temperature of the two materials, namely the blocking temperature (T_B) and the Curie temperature (T_C). In our case T_B is lower than T_C. The laser allows the FM layer to impact the AFM magnetic configuration at the interface when the bilayer is cooled. We verified our hypothesis by changing the fluence of the laser, applying simultaneous out-of-plane fields or by changing the number of pulses. We have then exhibited that this local reversal of the

exchange bias field can be used to create areas of preferential nucleation and even decide the way domain walls propagate inside these areas.

III.2) Effect of the femtosecond light on a synthetic ferrimagnet

Résumé en français: Le renversement tout optique de matériaux ferrimagnétiques de synthèse a été montrée en 2014 [6] mais n'a pas depuis été étudié en profondeur. C'est ce qui a motivé l'étude présentée dans cette partie. Pour élaborer de tels matériaux, nous nous sommes en premier lieu intéressés à des couches minces ferromagnétiques à anisotropie magnétique perpendiculaire dont l'aimantation peut être renversée par la lumière polarisée. Notre choix s'est porté sur le Co et le CoFeB. Nous avons fait croitre des monocouches de ces matériaux par pulvérisation cathodique magnétron et avons vérifié leurs propriétés magnétiques et leur réponse à une excitation par la lumière polarisée. Nous avons ensuite fait croître des bicouches couplées antiferomagnétiquement à partir de ces monocouches afin de pouvoir en trouver certaines dont l'aimantation se renverse optiquement. Ces bicouches sont soit constituées de deux couches de Co deux couches de CoFeB ou d'une couche de chaque. Après avoir fait varier différents paramètres nous sommes venus à la conclusion que le paramètre déterminant pour le retournement tout optique est la différence des températures de Curie de chaque monocouche. Les résultats sont reproduits par des simulations qui prennent comme hypothèse centrale l'existence d'un champ de Faraday inverse. Le travail montré dans ce chapitre est le fruit d'une collaboration entre plusieurs laboratoires. Les échantillons ont été élaborés au laboratoire Cavendish de l'université de Cambridge et les cycles d'hystérésis ont été mesurés au même endroit. Les mesures nécessitant un laser femtoseconde ont été effectuées à l'institut Jean Lamour. Les simulations ont été effectuées conjointement aux départements de physique des universités de Berlin et de Salamanque.

English summary: All optical switching in ferrimagnets has been first demonstrated in 2014 [6]. Further studies on this topic are presented in this chapter. To produce such materials we first focused on ferromagnetic materials exhibiting PMA and having a magnetization reversible through exposure to polarized light. We chose Co and CoFeB layers. Using DC sputtering we grew monolayers of those materials, and then we verified their magnetic properties and their response to the polarized light. Secondly, we grew synthetic ferrimagnetic bilayers from the previous monolayers in order to exhibit some subject to HD-AOS. Those bilayers are either made of two Co layers or two CoFeB layers or one layer of each. Looking at the different parameters we varied, we concluded that the key parameters for our study are the two Curie temperatures of the monolayers. Simulations reproducing the experimental results have been performed with the major hypothesis of the existence of an inverse Faraday Effect field. The work shown in this chapter results from a collaboration between different laboratories. The samples' growth and the hysteresis loops have been performed at the Cavendish lab or the Cambridge University. Laser measurements have been performed at the institute Jean Lamour. The simulations have been conducted both in the physics departments of the Universities of Berlin and Salamanca.

III.2.1) Femtosecond light on isolated Co/Pt layers

III.2.1.a) Hysteresis loops

Using DC sputtering with a base pressure under 5.5 x 10^{-8} Torr we grew Glass/ Ta (3 nm)/Pt (4 nm)/Co (t_{Co})/Pt (4 nm) samples with t_{Co}= 0.49, 0.6, 0.73, 0.8, 0.9 and 1 nm. We first made sure those sample exhibited an out-of-plane easy axis of magnetization. This has been done by performing hysteresis loops using MOKE in Cambridge. A typical magnetic hysteresis loop of the sample for t_{Co} = 0.6nm is shown on figure III.23. This clearly demonstrates an out-of-plane easy axis of magnetization of this sample.

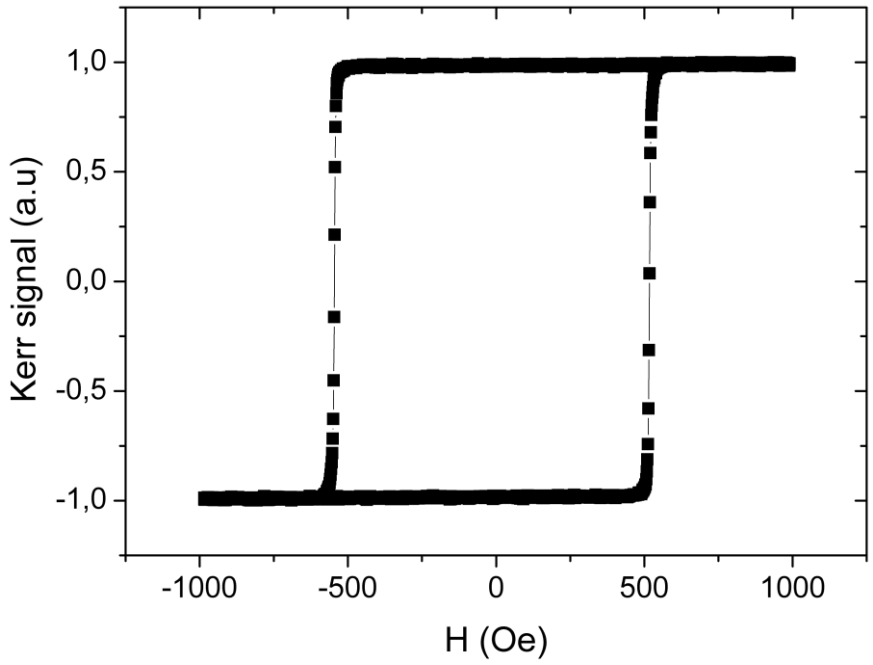

Figure III.23: Perpendicular MOKE hysteresis loop of a Ta (3 nm)/Pt (4 nm)/Co (0.6 nm)/Pt (4 nm) sample.

We obtain similar hysteresis loops for the other Co monolayers indicating their out-of-plane easy axis of magnetization.

III.2.1.b) MOKE HD-AOS on Co/Pt layers

We then looked at their exposure to the femtosecond light. We swept the laser on the samples at a speed of 1.4 µm/s with left handed and right handed light helicity after having saturated along –z. The laser fluence was 2.12 mJ/cm^{2}. A typical HD-AOS pattern obtained for the sample with 0.6 nm of Co is shown on figure III.24. Similar images were obtained for the other thicknesses of Co indicating also their HD-AOS behavior. This has already been observed in this material [7] and is thus not surprising.

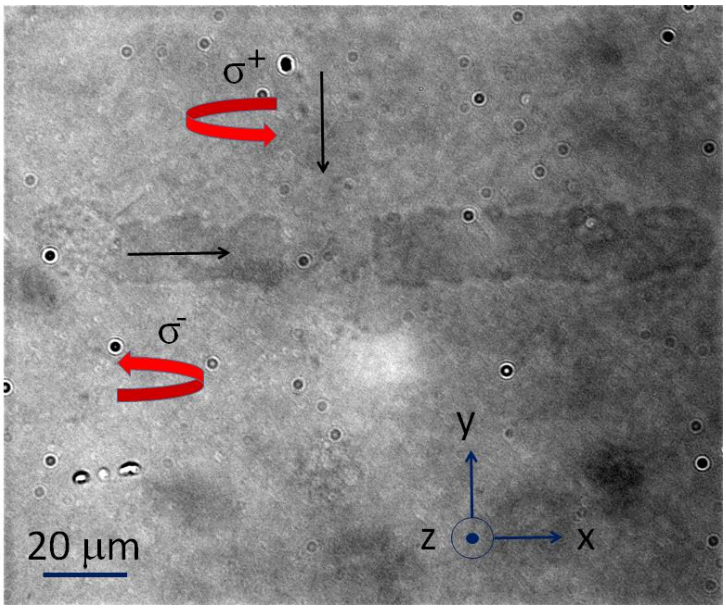

Figure III.24: MOKE hysteresis loop of a Ta (3 nm)/Pt (4 nm)/Co (0.6 nm)/Pt (4 nm) sample. Initially the magnetization is saturated along the –z vector. The laser has first been swept along the x direction and then along the –y direction. The black (resp. white) contrast indicates a magnetization along –z (resp. z). The sweeping speed of the laser on the sample is 1.4 µm/s. The fluence of the laser is 2.12 mJ/cm^2.

III.2.1.c) Hall voltage HD-AOS on Co/Pt layers

We decided to study the all optical switching process of the single Co/Pt layers via the change of the Hall voltage in hall crosses. For this we patterned the full films into Hall crosses with a width of 5 µm and swept the laser from the left side of the Hall cross to the right side. We first initialize the magnetization in a known state (I or II) by applying a saturating (+*z* or -*z*) magnetic field, before returning to remanence. Pulsed, circularly polarized laser light is focused on a ~46 µm diameter spot and swept in discrete steps along the *x*-axis arm (from –*x* to +*x*), with V_{Hall} monitored (0.2 second per point) during the passing of the laser beam over the Hall cross. A sketch of the laser beam on the Hall cross is shown on figure III.25. For each initial magnetic configuration (state up or down), we repeat this measurement strategy using the two different circular polarizations of the incoming light, σ^+ and σ^-. Figure III.26.a) (initial state down) and (b) (initial state up) illustrate the resulting V_{Hall} for each case, normalized to the magnitude at remanence, V_{Hall}^{AP}, and as a function of the relative laser beam position, *x*.

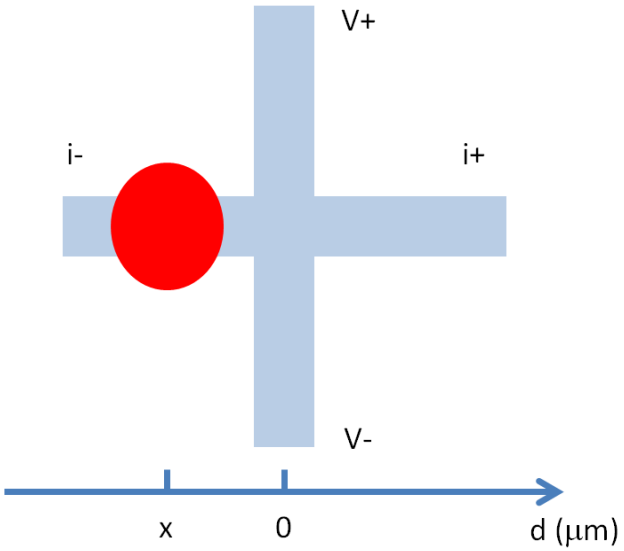

Figure III.25: Sketch of the Hall cross exposed to the laser. The laser beam is indicated by the red dot and its position on the cross is x. The center of the cross corresponds to d=0.

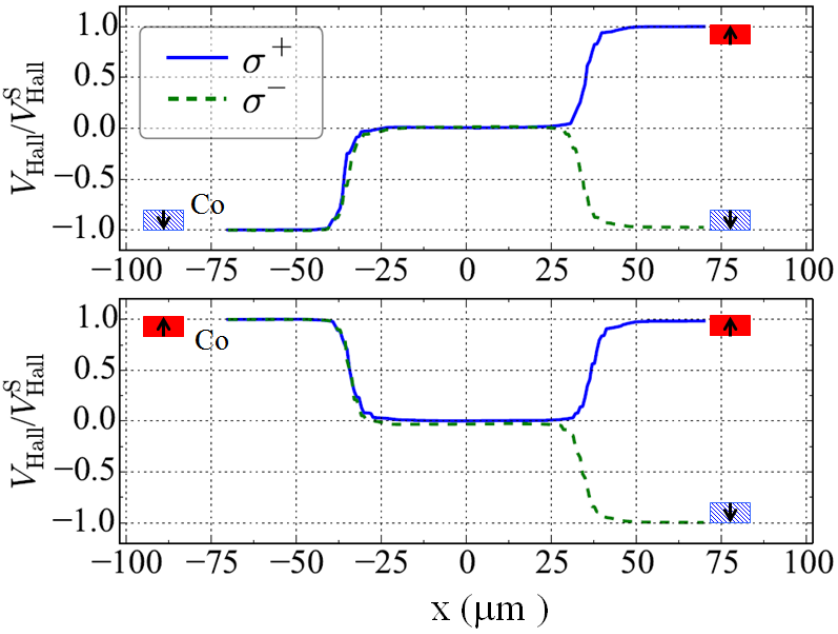

Figure III.26: Normalized Hall voltage measurements for a Ta (3 nm)/Pt (4 nm)/Co (0.6 nm)/Pt (4 nm) sample as a function of the position of the center of the laser beam on the Hall cross, x. The zero is taken at the center of the cross.

As seen on figure III.26 the initial magnetic state does not influence the final state after sweeping of the laser but the helicity of the light does. Between -75µm and -40µm, the laser is not yet on the center of the cross. At -37µm the effective edge of the Gaussian spot reaches the center and progressively demagnetizes the sample at the center of the cross until it leaves it. When the spot leaves the center,

the ferromagnetic layer remagnetizes up or down depending on the helicity of the light. This is a clear proof of HD-AOS. It is not surprising since this is similar to what has been observed before [124].

III.2.2) Femtosecond light on isolated CoFeB layers

III.2.2.a) PMA in CoFeB/Pt multilayers

CoFeB is a ferromagnetic material used mostly in magnetic tunnel junctions (MTJs) because of its high TMR ratio. Indeed in 2008, one of the highest TMR ever measured has been reported in a CoFeB/MgO/CoFeB stack (604%) [125]. This system had an easy axis of magnetization lying in the plane of the sample. Meanwhile the search for systems with an OOP easy axis of magnetization intensified because of their theoretical higher stability. A CoFeB/MgO based MTJ with a TMR ratio of 121% and an OOP easy axis of magnetization, more suitable for applications, has been reported two years later by the same group [126]. Since this paper had shown that it was possible to obtain a CoFeB interfaced with MgO (TMR ratio is high) and still with an OOP easy axis there was no need for a Pt interface in this system so people focused on the CoFeB/MgO system. A perpendicular easy axis of anisotropy can be obtained for the Pt/CoFeB/Pt system [127] [128]. In MgO/CoFeB based structures the annealing plays a central role [129]. Since the CoFeB recrystallizes in a bcc (001) structure [130], it induces strain on the CoFeB/MgO interface and promotes the PMA. The hybridization between the 3d orbitals of Fe and 2p orbitals of O also contributes to the enhancement of the PMA [131]. At the Pt/CoFeB interface the PMA is set mainly by the hybridization of Pt 5d and Co 3d orbitals.

III.2.2.b) VSM loops

Using DC sputtering with a base pressure under 5.5 $.10^{-8}$ Torr we grew Ta (3 nm)/Pt (4 nm)/CoFeB (t_{CoFeB})/Pt (4 nm) samples with t_{CoFeB}=0.3, 0.42, 0.54, 0.6, 0.66, 0.78 and 0.8 nm. Using MOKE we performed out-of-plane hysteresis loops. The one for a Ta (3 nm)/Pt (4 nm)/CoFeB (0.6 nm)/Pt (4 nm) sample is displayed on figure III.27.

Since the Co/Pt hybridization has the stronger contribution to the PMA at the CoFeB/Pt interface the coercive field of the Ta (3 nm)/Pt (4 nm)/CoFeB (0.6 nm)/Pt (4 nm) sample is lower (250 Oe compared to 500 Oe) than the one with the CoFeB layer replaced by a Co layer of the same thickness. All the other samples with CoFeB grown in the same serie also exhibit a strong perpendicular magnetic anisotropy.

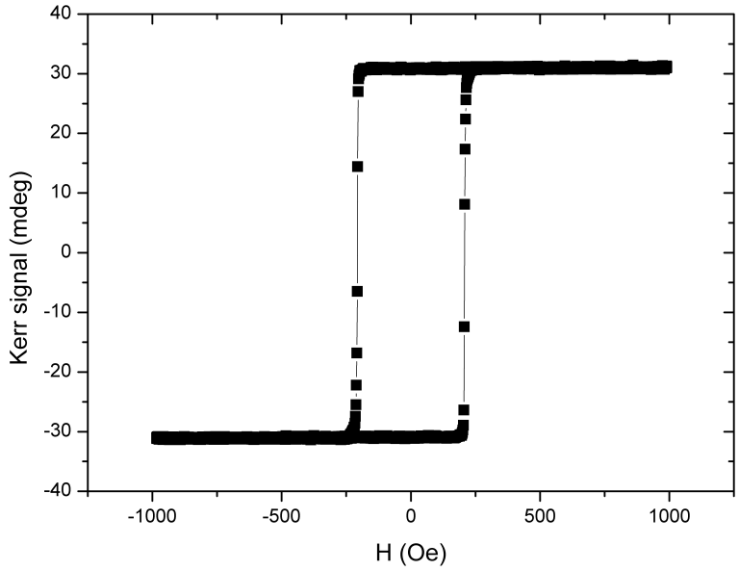

Figure III.27: Perpendicular MOKE hysteresis loop: Kerr signal as a function of field applied perpendicular to the film plane in a of a Ta (3 nm)/Pt (4 nm)/CoFeB (0.6 nm)/Pt (4 nm) sample.

III.2.2.c) HD-AOS on CoFeB layers

We then performed HD-AOS on those samples and imaged the result with MOKE microscope similarly to what has been done on Co in the part III.2.1. The resulting image for CoFeB (0.6 nm) is shown on figure III.28.

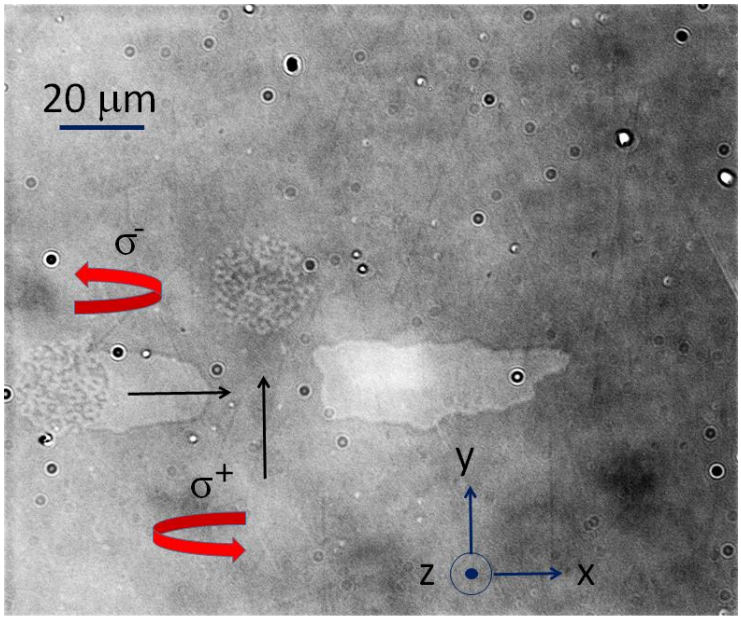

Figure III.28: MOKE image of a Ta (3 nm)/Pt (4 nm)/CoFeB (0.6 nm)/Pt (4 nm) sample. Initially the magnetization is saturated along the –z vector. The laser has first been swept along the x direction and then along the y direction. The black (resp. white) contrast indicates a magnetization along –z (resp. z). The sweeping speed of the laser on the sample is 1.4 µm/s. The fluence of the laser is 2.12 mJ/cm^2.

Figure III.28 proves that AO-HDS occurs for the CoFeB (0.6 nm). By performing the same measurement on the other Ta (3 nm)/Pt (4 nm)/CoFeB (t_{CoFeB})/Pt (4 nm) samples, we observe that AO-HDS also occurs for them. Similarly to what we have done with the Co stacks we observed the switching with a change of Hall voltage in a patterned cross of CoFeB (0.6nm) (not shown).

III.2.3) Femtosecond light on SFI

After having shown the AO-HDS behavior of ferromagnetic monolayers we can now use them to build a rare-earth free synthetic ferrimagnet (SFI). Our goal in this part is to design a SFI that can exhibit AO-HDS. By tuning the thicknesses and the ferromagnetic material we will see that it is possible to perform AO-HDS on a SFI. In this part all the sweeping measurements are performed at a sweeping speed of 1.4 μm/s and the fluence of the laser is 3.9 mJ/cm^2.

III.2.3.a) Engineering of SFI's

Using DC sputtering we grew a Ta (3 nm)/Pt (4 nm)/FM_1/Pt (0.4 nm)/Ru (0.9 nm)/Pt (0.4 nm)/FM_2/Pt (4 nm). The FM_1 (resp. FM_2) layer is composed Co with t_{Co} = 0.49 or 0.73 nm (resp. CoFeB (t_{CoFeB})/Pt (0.4 nm)/CoFeB (t_{CoFeB}) with t_{CoFeB} = 0.3, 0.42, 0.54, 0.66 and 0.78nm). In other words, FM_1= Co(t_{Co}) and FM_2= CoFeB (t_{CoFeB})/Pt (0.4 nm)/CoFeB (t_{CoFeB}). Varying thickness allows us to control the T_C of each layer and therefore its thermal response. A Pt/Ru/Pt spacer layer is inserted between the two FMs to provide interlayer AF coupling. Hysteresis loops obtained by VSM measurements (not shown) confirm two possible AF remanant magnetic states, with the magnetization, *M*, of the individual FM layers uniformly aligned out-of-plane and antiparallel to one another. To distinguish them, the remnant states are labelled State I, with FM1 pointing in *+z,* and State II, with FM1 layer magnetized in *–z*. Measurements of Hall voltage (figure III.29) to obtain the major and minor hysteresis loops are therefore sensitive to the orientation of each FM layer and confirm that the remanent states I and II are maintained in the patterned films and are not altered by the patterning process.

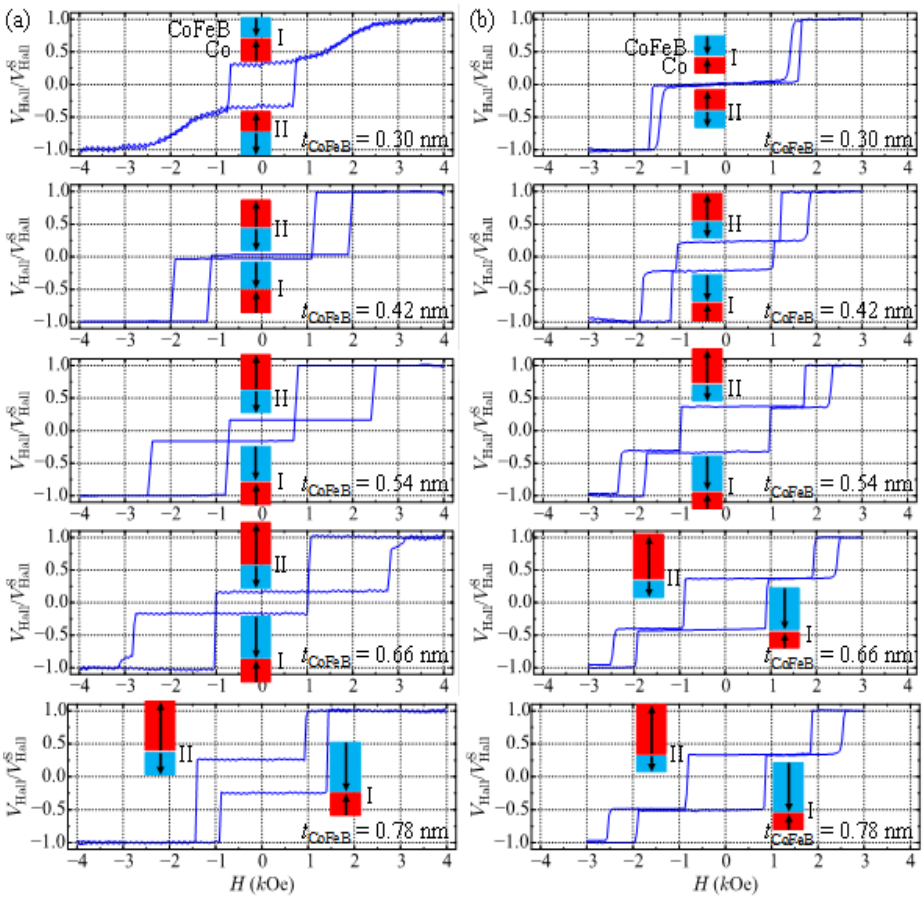

Figure III.29. Perpendicular Hall hysteresis loops of the synthetic ferrimagnetic heterostructures composed of two ferromagnetic layers FM_1 and FM_2 with different layer thicknesses. The layer thickness of FM_1: (a) t_{Co} = 0.73 and (b) 0.49 nm. The layer thickness of FM_2: 0.30 ≤ t_{CoFeB} ≤ 0.78 nm. The Hall voltage, V_{Hall}, is normalized to the voltage of the saturation state, V_{Hall}^{S}.

We then performed the laser sweeping experiments on those samples. We first initialize the magnetization in a known state (I or II) by applying a saturating (+z or -z) magnetic field, before returning to remanence. A pulsed, circularly polarized laser light is swept in discrete steps along the x-axis arm (from –x to +x), with V_{Hall} monitored (0.2 second per point) during the passing of the laser beam over the Hall cross. For each initial magnetic configuration (state I or II), we repeat this measurement strategy using the two different circular polarizations of the incoming light, σ^+ and σ^-. Figure III.30.a) (initial state I) and (b) (initial state II) illustrate the resulting V_{Hall} for each case, normalized to the magnitude at remanence, V_{Hall}^{AP}, and as a function of the relative laser beam position, x, for t_{Co} = 0.73 nm and t_{CoFeB} = 0.54 nm. The difference in magnetic material and thickness gives a T_c difference, $T_{C1} > T_{C2}$, between the two ferromagnetic layers. In figure III.30.a), one can clearly see a decrease in V_{AHE} as the front edge of the beam approaches the cross area, with the signal reaching V_{AHE}= 0 as the laser beam becomes centered on the cross. The loss in Hall voltage is attributed to an initial helicity-independent demagnetization of the cross into a multi-domain state. This behavior is observed in SFi's and single FM layers, and is due to the individual layers being heated by the central portion of the laser above T_C, causing long-range magnetic order to be lost. Upon cooling, the magnetization reorders, however, with no local preference for state I or II, the irradiated film is placed in a multi-domain, demagnetized state. We presume this effect occurs only when the electron

temperature is elevated above T_C of both individual layers, T_{C1} and T_{C2}. We find that this demagnetized state is stable, persisting after removal of the laser beam in AHE measurements. As the laser spot is leaving the Hall cross, a helicity-dependent remagnetization occurs, i.e. as the net magnetization is restored, the σ^+ beam switches from the initial state of State II to a final state of State I, while the σ^- polarized beam results in State II. Changing the initial state from State II to State I, in Figure 30.b) we observe the same dependence of the final state on laser helicity, demonstrating both HD-AOS in TM/FM SFi's and an independence of the switching mechanism on the initial state. It is apparent from this behavior that HD switching occurs in these SFi's, not within the beam centre (which remains demagnetized), but at the trailing edge of the beam profile.

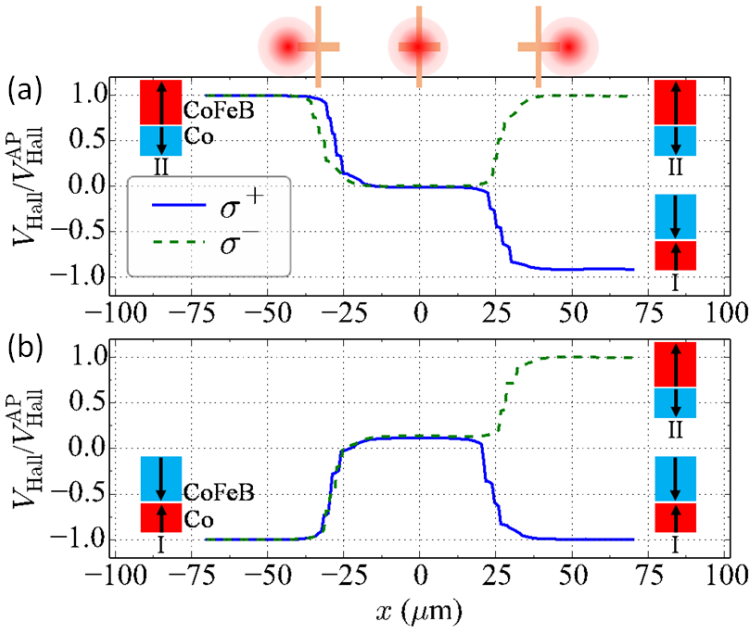

Figure III.30: The measured normalized Hall voltage, V_{Hall}/V_{Hall}^{AP}, as a function of the laser beam position relative to the center of the Hall cross, x. V_{Hall}^{AP} is the Hall voltage of the remanent magnetic state, State I (II). The sample is the synthetic ferrimagnetic heterostructure composed of FM_1 with t_{Co} = 0.73 nm and FM_2 with t_{CoFeB} = 0.54 nm. The initial magnetic state is (a) State II and (b) State I.

On first inspection, the composite SFi appears to behave analogously to a single FM layer (such as Pt/Co/Pt): provided the beam fluence is sufficiently large, $T>T_c$ and thermal demagnetization occurs, with multiple DWs nucleated. A ring around this central region exists where T is below T_c (so the film remains magnetized), but sufficiently large such that HD DW motion occurs. On sweeping the beam, this motion selectively expands one domain orientation over the other, re-magnetizing the SFi.

While this argument qualitatively explains the major observations presented in Figure III.30.a) and (b), and follows the prevailing wisdom built up for single FM reversal, if we consider the individual components of the SFi, with $T_{C1}\neq T_{C2}$ as is the case here, the situation inevitably becomes more complex. For these materials, while the central beam may still demagnetize the bar, a region of the beam exists where, for example, $T_{C1}<T<T_{C2}$, i.e. FM2 remains magnetized while FM1 has lost any long-range order.

In this region of the beam, the helicity dependent effects (and thus the HD-AOS) occur first only for the FM layer with the higher T_C (here FM_2) and not on the whole SFi.

Consequently, HD DW motion will be intimately linked to the precise ordering of the SFi on cooling. Tuning T_C of each sublayer in a SFi therefore offers the opportunity to tailor any helicity dependence, particularly when HD-DW motion occurs.

III.2.3.b) Role of the Curie temperature.

To test this hypothesis, we independently vary T_C in each layer. To minimize the effect of changing other parameters, including the fundamental mechanism behind any HD DW motion, we maintain the same materials combinations for FM1 and FM2 and instead implicitly tune T_C by varying FM thickness. Figure III.31.a) and (b) show the resulting variation in (a) T_{C2} as a function of t_{CoFeB}, along with (b) $M_s t_{CoFeB}$, the magnetic moment of the layer per unit area. The thickness range is chosen such that all FM layers show a completely out-of-plane remanence, as indicated by room temperature VSM measurements. In general, reducing t_{CoFeB} is found to reduce T_{C2} from bulk, due to a transition towards 2-D magnetic behavior [132], while also decreasing $M_s t_{CoFeB}$, following the direct proportionality between total moment and thickness (i.e. giving only minimal change in M_S). For comparison, in figure III.31.e) and (f) T_{C1} and $M_s t_{Co}$ are shown for two different tested thicknesses of FM1, t_{Co}= 0.49 nm and t_{Co}= 0.73 nm. Examining the two plots one can easily see for a given t_{Co} the critical FM2 thicknesses where T_{C2} exceeds T_{C1}, which in the case of t_{Co}=0.73 nm occurs above t_{CoFeB}~0.6 nm.

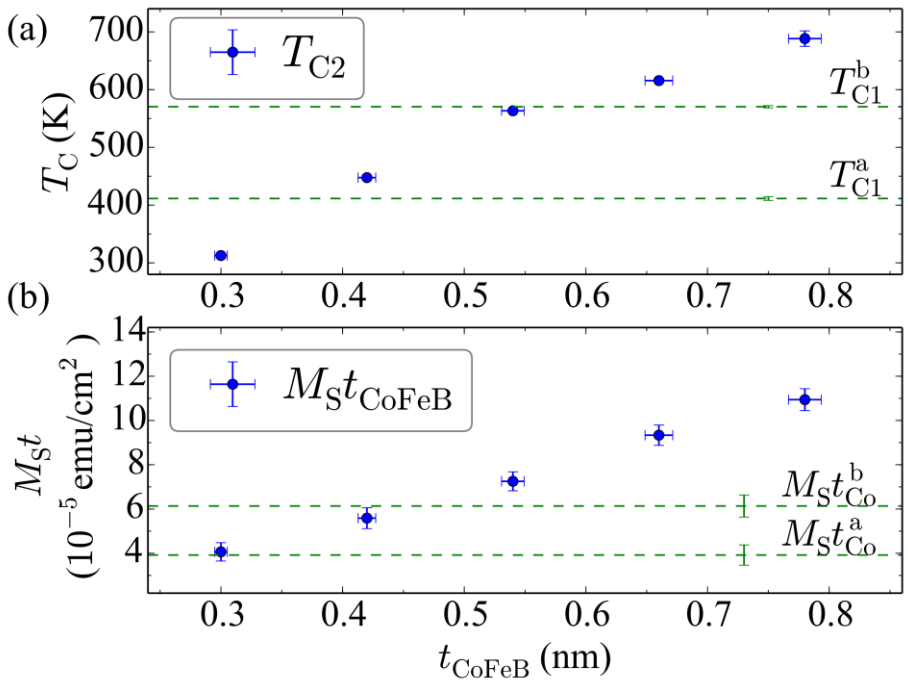

Figure III.31. Magnetic properties of the individual ferromagnetic films. Variations of (a) Curie temperature, T_C, and (b) the magnetization per unit area, $M_S t$, as a function of the ferromagnetic layer

thickness. The horizontal lines indicate the properties of the Co layer. T_{C1}^{a} is the T_C at t_{Co}^{a}=0.49 nm, and T_{C1}^{b} is the T_C at t_{Co}^{b}=0.73 nm.

If we now investigate AOS using the sweeping beam method in this thickness range, as shown in Figure III.32.a) – (c) for t_{Co}=0.73 nm, a pattern emerges: at low t_{CoFeB} (Figure III.32.a), t_{CoFeB}<0.66 nm), i.e. while T_{C1}>T_{C2}, we observe a similar helicity dependence of AOS to the previously discussed SFi [figure III.30.a) and III.30.c)], with σ+ light remagnetizing the SFi towards State I. Notably, moving to the point where T_{C1}~T_{C2} [figure III.32.b) t_{CoFeB}=0.66 nm] a complete loss of HD AOS is now found, with helicity-independent reversion to the initialized state. Finally, further increasing t_{CoFeB} until T_{C1} < T_{C2} restores HD AOS [figure III.32.c)]: however, now the helicity dependence has inverted and using the σ+ beam leads to final State II, e.g. when t_{CoFeB} = 0.77 nm [Figure 2(c)]. By tuning the T_C within each layer, we demonstrate direct control of HD AOS.

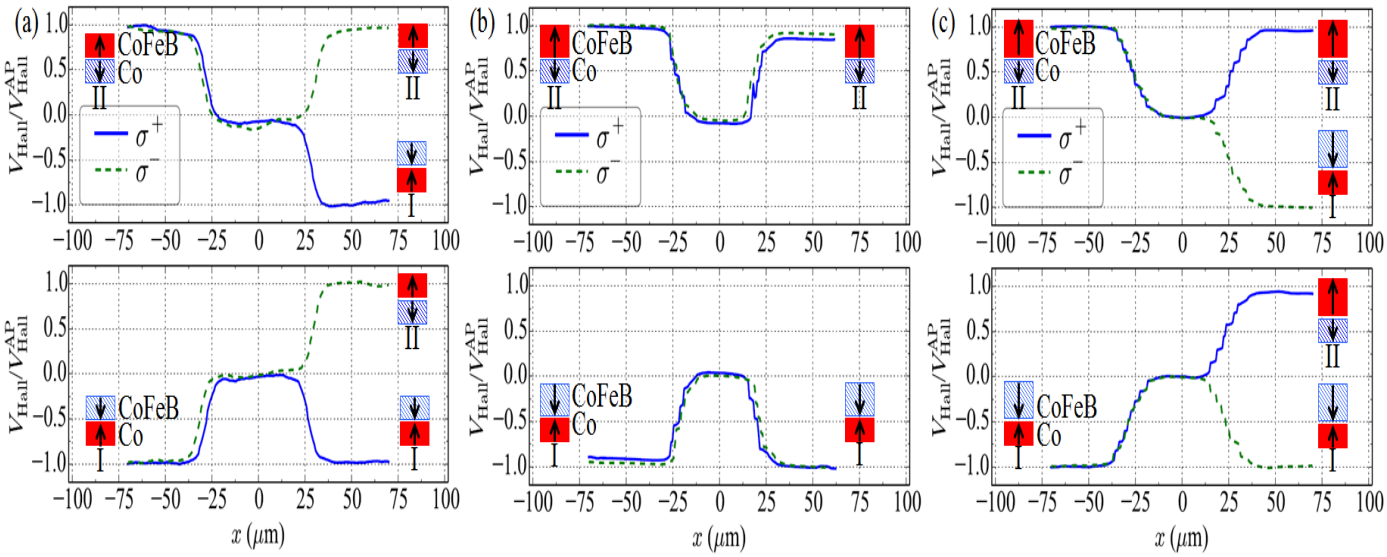

Figure III.32 : Variation of the normalized Hall voltage, $V_{Hall}/V_{Hall}^{AP}(x)$, of the synthetic ferrimagnetic heterostructures composed of FM_1 with a fixed layer thickness t_{Co} = 0.73 nm and FM_2 with different FM layer thicknesses, t_{CoFeB} = (a) 0.42 nm, (b) 0.66 nm, and (c) 0.78 nm. The initial state is State I or State II. The measurements are repeated using the laser beam with two different circular polarizations, σ^+ and σ^-.

To further verify the correlation between T_C and the HD AOS, we prepare a sample set with reduced t_{Co}=0.49 nm. From figure II.31.a), by reducing FM1, any crossover in HD should now occur at a lower FM2 thickness, t_{CoFeB} ~ 0.4 nm, where T_{C1} ~ T_{C2}. Once again, we examine AOS via the sweeping beam method. Figure III.33.a) to III.33.c) show the resulting $V_{Hall}/V_{Hall}^{AP}(x)$ for t_{CoFeB} = 0.42, 0.66, and 0.78 nm, respectively (t_{CoFeB} = 0.3 nm is not shown because the nearly identical Hall voltages of states I and II makes it difficult to distinguish the two states). Again, when T_{C1} ~ T_{C2} (III.33.a), t_{CoFeB}~0.42 nm) helicity-independent reversion occurs, while for T_{C2}>T_{C1} identical HD is found for all samples with σ+ now leading to final State II [figures III.33.b), III.33.c)].

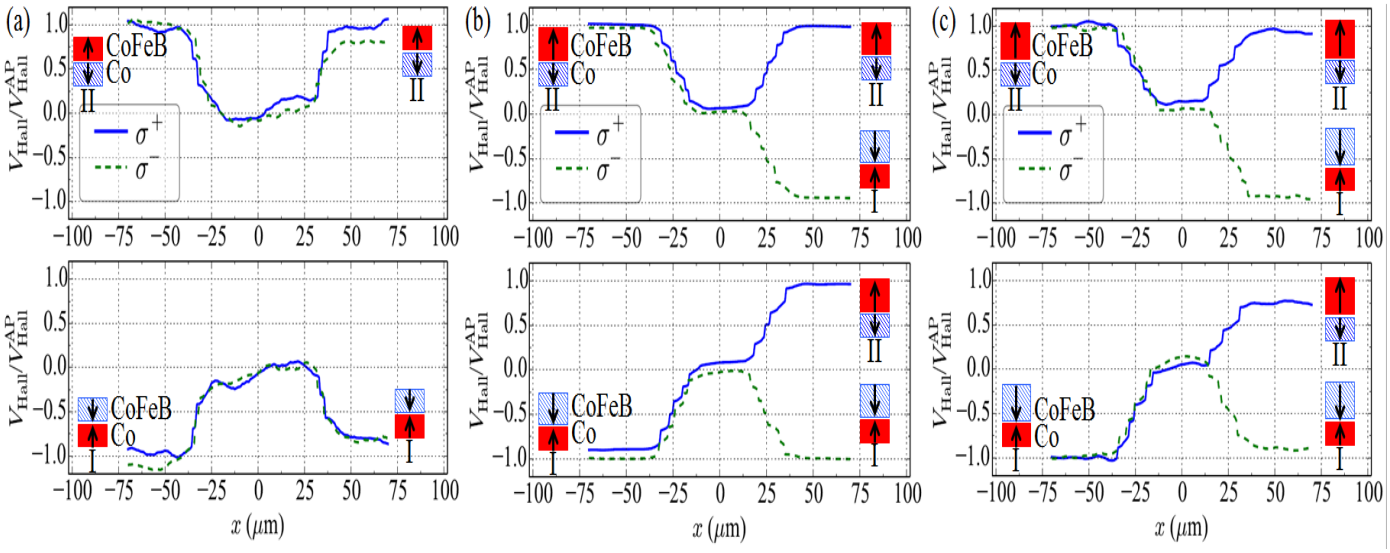

Figure III.33: Variation of the normalized Hall voltage, $V_{Hall}/V_{Hall}^{AP}(x)$, of the synthetic ferrimagnetic heterostructures composed of FM_1 with fixed layer thickness t_{Co} = 0.49 nm and FM_2 with different FM layer thickness, t_{CoFeB} = (a) 0.42 nm, (b) 0.66 nm, and (c) 0.78 nm. The initial state is State I or State II. The measurements are repeated using the laser beam with two different circular polarizations, σ^+ and σ^-.

These results cannot be understood by current models of HD AOS in single FMs, where switching is intrinsically set by the light helicity and is T_C independent. Here we propose a possible scenario to account for the observed T_C dependence of HD AOS. When irradiating an SFi, e.g. with $T_{C1}>T_{C2}$, due to the continuous distribution of electron temperature across the beam, a narrow ring exists where $T_{C1}>T>T_{C2}$ and FM_1 remains ordered, but demagnetized, while FM_2 loses any long-range order. As the interlayer exchange coupling scales with M_1 * M_2, where $M_{1(2)}$ is the magnetization of $FM_{1(2)}$, the interlayer coupling becomes inactive. HD DW motion occurs in FM_1 throughout the ring, without the presence of any interlayer exchange coupling, and the layer begins to remagnetize through HD DW motion. As the laser pulse is removed and the sample cools down, the re-ordering of FM_2 and restoration of AF exchange coupling forces FM_2 antiparallel to FM_1: the SFi ordering is dictated by FM_1. Should $T_{C2}>T_{C1}$, the situation becomes reversed and the helicity dependence of FM_2 dictates the ordering of the SFi. When T_{C1}~T_{C2} the ring's width collapses, no preference for DW motion direction exists (the coupled DWs within FM_1 and FM_2 are pushed in opposite directions, but remain AF coupled, and so do not move), and no, or at least weak, AOS occurs. Simple checks of the reversal symmetry of the SFi stack with $T_{C1}>T_{C2}$, as compared with single Co FM layers, confirm a consistent helicity dependence between the two, supporting the position that FM_1 dictates the ordering in these heterostructures (when $T_{C1}>T_{C2}$). Furthermore, measurements replacing the circular polarization with a linearly polarized light and an externally applied field (H_z~3 Oe) shows an equivalent symmetry to HD AOS (see figure III.34). There, a positive applied field remagnetizes the SFi in State I, while a negative field results in State II. We interpret the interaction of the circularly polarized light with M to be equivalent to an effective field in this case, promoting expansion of one domain at the expense of the other in a ring surrounding the laser beam.

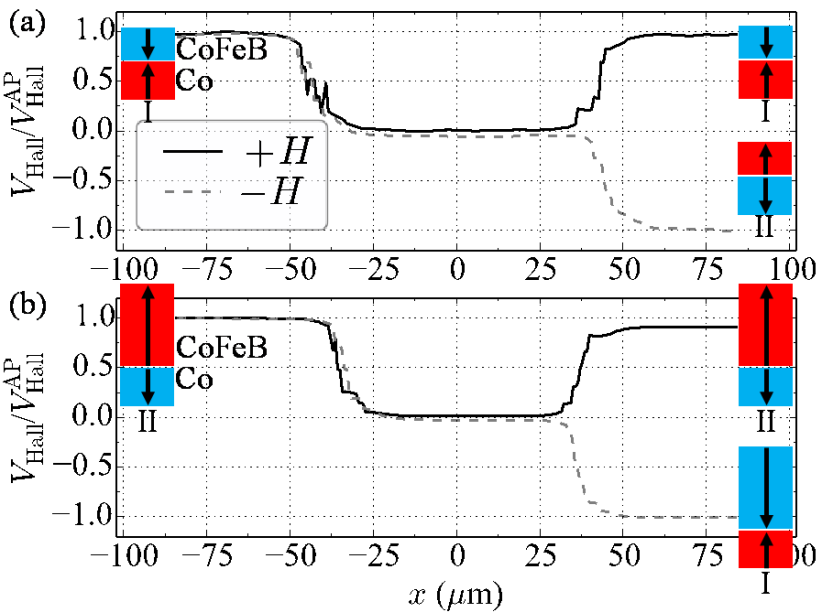

Figure III.34: Variation of the normalized Hall voltage, V_{Hall}/V_{Hall}^{AP}, as a function of the laser beam position, x. V_{Hall}^{AP} is the Hall voltage of State I or State II. x is the beam position relatively to the center of the Hall cross. The heterostructures are made of FM_1 with t_{Co} = 0.73 nm and FM_2 with (a) t_{CoFeB} = 0.30 and (b) t_{CoFeB} = 0.78 nm. The initial state is (a) State I and (b) State II. At each initial state, the measurement was repeated using two different magnetic field directions, $+H$ and $-H$. The magnetic field strength is 3 Oe.

III.2.3.c) Micromagnetic simulations

To further verify the proposed model, we performed micromagnetic simulations to study the magnetization dynamics induced by femtosecond laser pulses. Conventional micromagnetics is a zero temperature approach and is not well suited to describe dynamics when temperature varies in space and time. To solve this fundamental issue we use an improved framework valid for highly non-equilibrium micromagnetic simulations, based on the Landau-Lifshitz-Bloch equation (LLB) [133]. Importantly, this model accounts for all relevant parameters of the system, such as geometry, magnetic parameters, thermal and magneto-optical effects (see appendix for more details). We perform computer simulations with system characteristics similar to the experimental set-up. Notably, from simulations we extract values for $V_{Hall}/V_{Hall}^{AP}(x)$, which are in good qualitative agreement with the experimental results using the parameters in figure III.35 (see figure III.36).

	T_C^{Co} (K)	T_C^{CoFeB} (K)	M_S^{Co} (emu/cc)	M_S^{CoFeB} (emu/cc)
Sample a	550	450	1100	1000
Sample b	550	550	1100	1100
Sample c	550	650	1100	1200

Figure III.35: Curie temperature and saturation magnetization values of the bottom (T_C^{Co} and M_S^{Co}) and the top ferromagnetic layers (T_C^{CoFeB} and M_S^{CoFeB}) of the three simulated bilayer structures, with a Hall cross geometry.

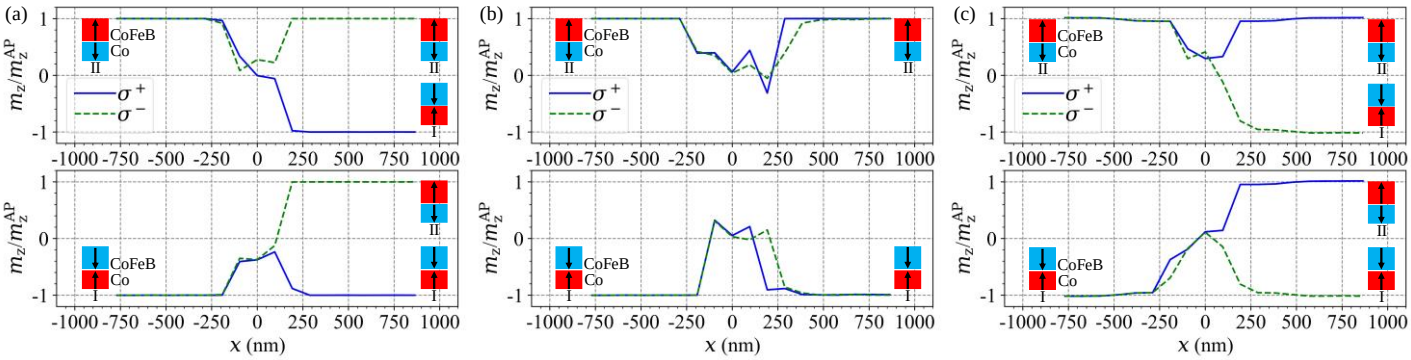

Figure III.36: (a) – (c) Variation of the normalized out-of-plane net magnetization averaged over the center square of the Hall cross, $m_z/m_z^{AP}(x)$, of the synthetic ferrimagnetic heterostructures composed of FM_1 and FM_2 with (a) $T_C^{Co} > T_C^{CoFeB}$, $M_S^{Co} > M_S^{CoFeB}$, (b) $T_C^{Co} = T_C^{CoFeB}$, $M_S^{Co} = M_S^{CoFeB}$, and (c) $T_C^{Co} < T_C^{CoFeB}$, and $M_S^{Co} < M_S^{CoFeB}$. m_z^{AP} is the net magnetization of State II, and x is the laser position. The initial state is State I or State II. The simulations are repeated using the laser beam with two different circular polarizations, σ^+ and σ^-.

We further obtained the transient magnetic configurations in the Hall cross during the laser sweeping process. In figure III.37, we show the simulated snapshots of the Hall cross, composed of two AF-coupled ferromagnetic layers with $T_{C1} > T_{C2}$. The top panel corresponds to an incident laser helicity σ^-, and the bottom panel corresponds to σ^+. The trailing edge of the σ^- beam restores the initial magnetic state and results in no-switching [top panel of figure III.37]. For σ^+, the switching occurs [bottom panel of figure III.37] and we observe a reversed, single domain state in the illuminated area. The results further validate the proposed switching behavior explanation: the FM layer with the highest T_C controls the helicity dependence of the SFi ordering.

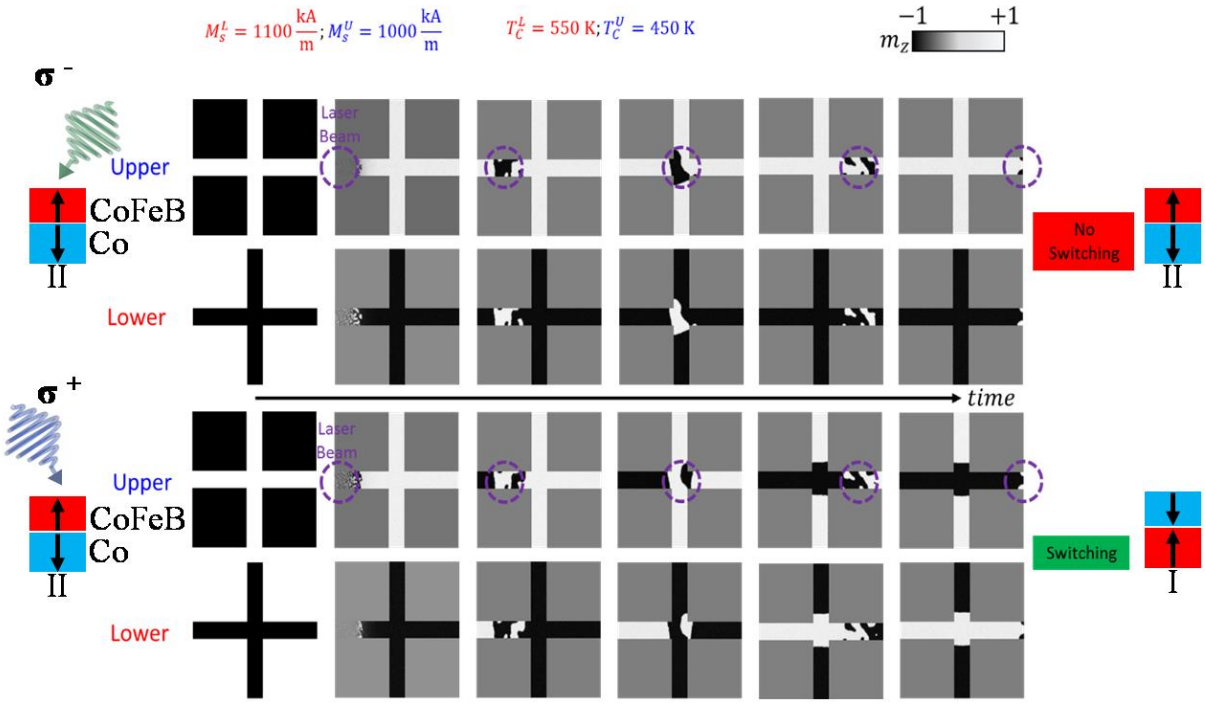

Figure III.37: Modelled transient snapshots of magnetic configurations in the Hall crosses. The crosses are composed of two ferromagnetic layers with $M_S^{Co} < M_S^{CoFeB}$ and $T_C^{CO} < T_C^{CoFeB}$. The snapshots were taken during the laser beam (indicated by the purple circle) sweeping from left to right. The initial magnetic state is the State II. The top panel of snapshots corresponds to the laser helicity of σ^-, whereas the bottom one corresponds to the helicity of σ^+. The purple circle indicates the position of the laser beam along the longitudinal x-axis. The final magnetic state (shown on the right) is the state in the center cross area.

An interesting property of a SFi is that by appropriate engineering of the layer structure one can control the so-called magnetization compensation point, i.e. the T at which the net magnetization of the SFi becomes zero (M_1=M_2). This point plays an important role for single-shot switching in GdFeCo [69], and a key question is whether it plays a similar role in HD-AOS. To probe this, we first examine figure III.31.B), where we presented the variation in SFi total moment per unit area as a function of t_{CoFeB}. As can be seen, at a critical t_{CoFeB} the SFi moments will be fully compensated, creating a synthetic AF.

However, t_{CoFeB} at the compensation point is found to be systematically larger than the HD inversion thickness, suggesting a limited role for the magnetic compensation in these samples. To further understand the effects of the saturation magnetization per unit area, we have performed additional simulations with different combinations of the saturation magnetization and the Curie temperature values. Figure III.38 shows the results of the three bilayers composed of the two ferromagnetic layers with a fixed saturation magnetization difference between the two ferromagnetic layers ($M_S^{Co} < M_S^{CoFeB}$) but with different Curie temperature ($T_C^{Co} > T_C^{CoFeB}$, $T_C^{Co} = T_C^{CoFeB}$, and $T_C^{Co} < T_C^{CoFeB}$). The switching behaviors still agree with the experimental observations: the ferromagnetic layer with the highest Curie temperature dominates the helicity dependency.

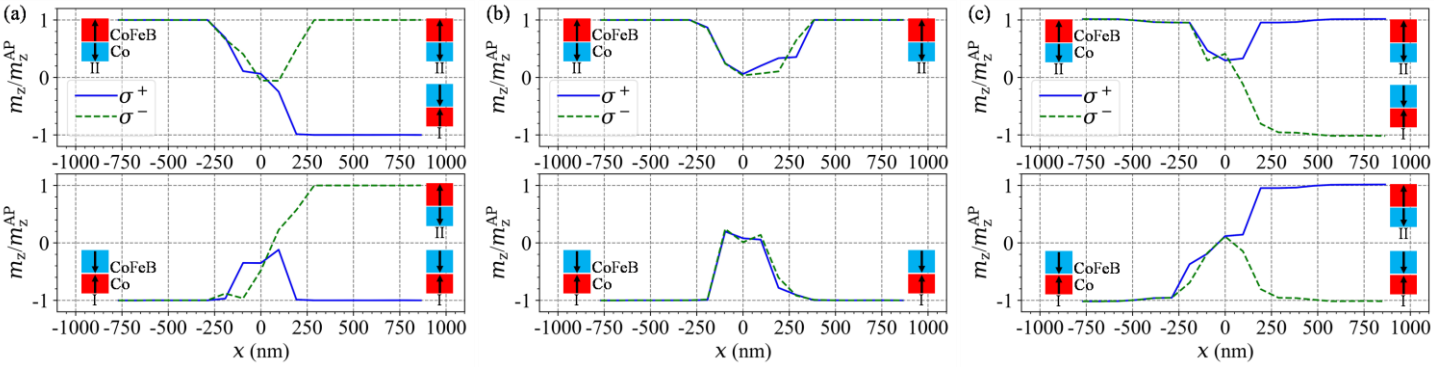

Figure III.38: (a) – (c) Variation of the normalized out-of-plane net magnetization averaged over the center square of the Hall cross, $m_z/m_z^{AP}(x)$, of the synthetic ferrimagnetic heterostructures composed of FM_1 and FM_2 with (a) $T_C^{Co} > T_C^{CoFeB}$, (b) $T_C^{Co} = T_C^{CoFeB}$, and (c) $T_C^{Co} < T_C^{CoFeB}$. For all three bilayers, $M_S^{Co} < M_S^{CoFeB}$. m_z^{AP} is the net magnetization of State II, and x is the laser position. The initial state is State I or State II. The simulations are repeated using the laser beam with two different circular polarizations, σ^+ and σ^-.

Figure III.39 shows the results of the three bilayers with the same saturation magnetization ($M_S^{Co} = M_S^{CoFeB}$) but with different Curie temperature. The results suggest that changing the saturation magnetization is irrelevant to the different switching behaviors.

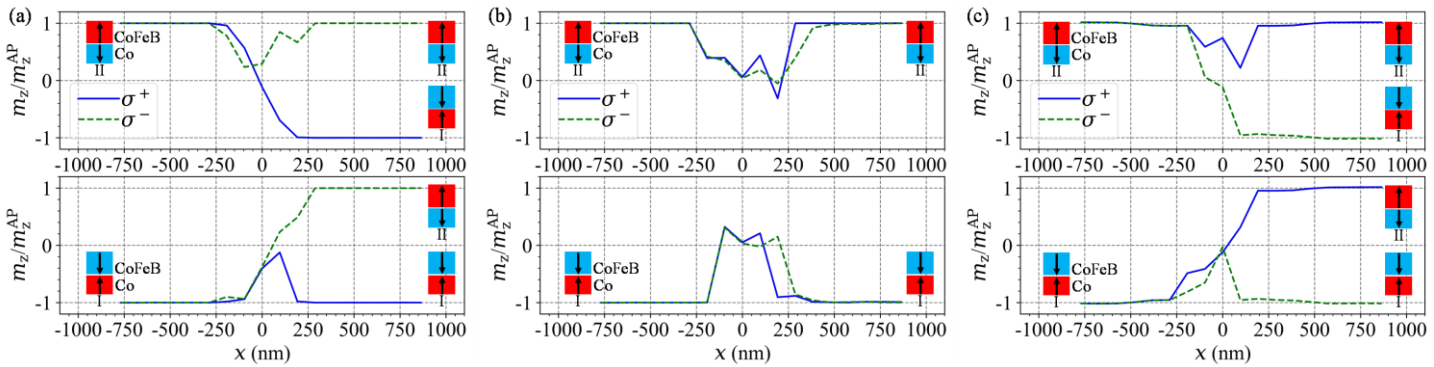

Figure III.39: (a) – (c) Variation of the normalized out-of-plane net magnetization averaged over the center square of the Hall cross, $m_z/m_z^{AP}(x)$, of the synthetic ferrimagnetic heterostructures composed of FM_1 and FM_2 with (a) $T_C^{Co} > T_C^{CoFeB}$, (b) $T_C^{Co} = T_C^{CoFeB}$, and (c) $T_C^{Co} < T_C^{CoFeB}$. For all three bilayers, $M_S^{Co} = M_S^{CoFeB}$. m_z^{AP} is the net magnetization of State II, and x is the laser position. The initial state is State I or State II. The simulations are repeated using the laser beam with two different circular polarizations, σ^+ and σ^-.

Finally, we have performed the calculations in the three bilayers with the same Curie temperature ($T_C^{Co} = T_C^{CoFeB}$) but with different saturation magnetization values, whose are displayed in figure III.40. All three bilayers show the helicity-independent back switching behaviors, regardless of different saturation magnetization values. Therefore, we conclude that having FM layers with different Curie temperatures is a key ingredient to determine the switching behaviors.

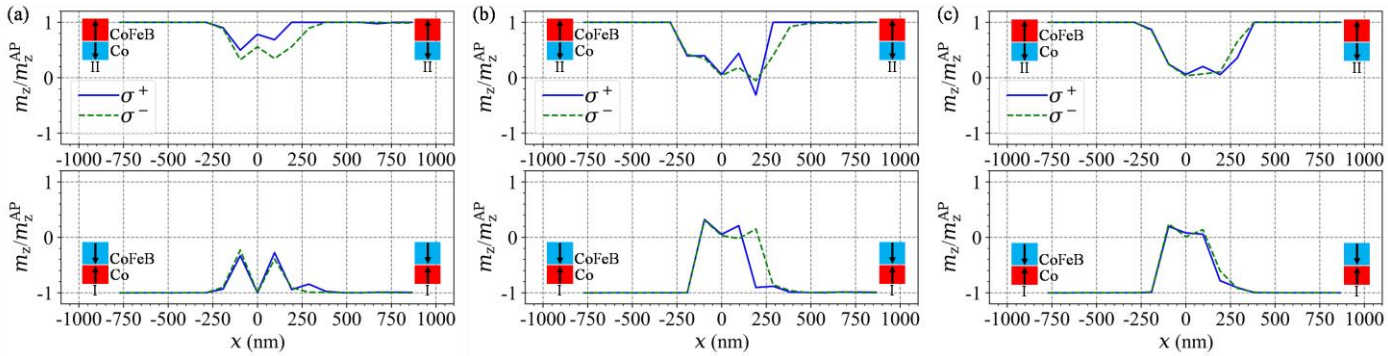

Figure III.40: (a) – (c) Variation of the normalized out-of-plane net magnetization averaged over the center square of the Hall cross, $m_z/m_z^{AP}(x)$, of the synthetic ferrimagnetic heterostructures composed of FM_1 and FM_2 with (a) $M_S^{Co} > M_S^{CoFeB}$, (b) $M_S^{Co} = M_S^{CoFeB}$, and (c) $M_S^{Co} < M_S^{CoFeB}$. For all three bilayers, $T_C^{Co} = T_C^{CoFeB}$. m_z^{AP} is the net magnetization of State II, and x is the laser position. The initial state is State I or State II. The simulations are repeated using the laser beam with two different circular polarizations, σ^+ and σ^-.

Figures III.38-40 provide numerical simulations for parameters at and around the compensation point (varying both T_C and $M_S t_{CoFeB}$ for the two FMs) and also show the prevailing role of Tc in determining the HD AOS, and rule out a significant contribution of the compensation point in these SFi's.

As a final point, we address the origin of the helicity independent back switching that occurs when $T_{C1} \sim T_{C2}$. When $T_{C1}=T_{C2}$, the discussed AOS ring width will collapses, resulting in a similar thermal response for each layer, and so nucleation and expansion of domains. Strong AF coupling will remain and consequently no net expansion of one domain structure over the other should take place from helicity dependent DW motion. Ordinarily the coupled DWs would propagate in opposite directions. Still, a heat gradient along the cross arms, due to the localized laser pulse is present. Even in ideal antiferromagnetic layers, where no net magnetization exists, it is predicted that heat gradients will drive domains towards a hot region [134] (in this case, the center of the laser spot position). The sweeping of the laser spot then causes domain expansion, as the DWs propagate along the heat gradient toward the laser. In this case, any region that has not otherwise been demagnetized due to direct exposure from the laser spot, e.g. the vertical arms of the Hall cross, will be expanded, thereby restoring the initial magnetization of the structure. In figure III.41, we show the calculated transient magnetic configurations in the Hall cross, in the case of $T_{C1} = T_{C2}$.

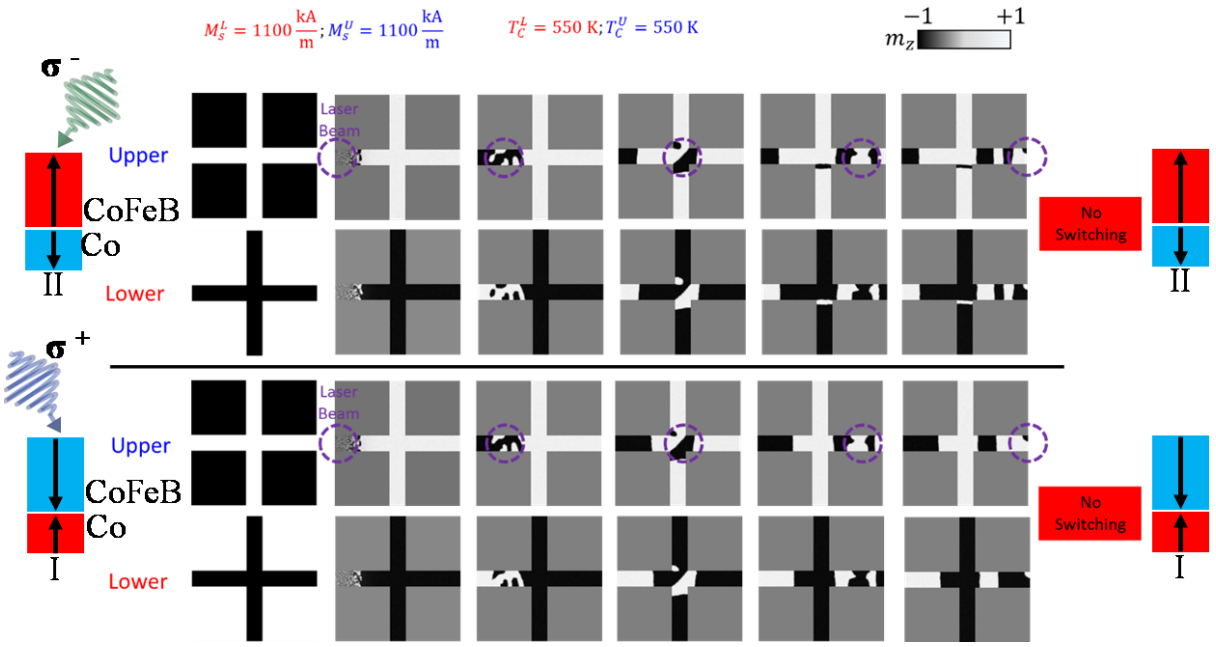

Figure III.41: Modelled transient snapshots of magnetic configurations in the Hall crosses. The crosses are composed of two ferromagnetic layers with $M_S^{Co} = M_S^{CoFeB}$ and $T_C^{Co} = T_C^{CoFeB}$. The snapshots were taken during the laser beam (indicated by the purple circle) sweeping from left to right. The initial magnetic state is the State II. The top panel of snapshots corresponds to the laser helicity of σ^-, whereas the bottom one corresponds to the helicity of σ^+. The purple circles indicate the position of the laser beam along the longitudinal x-axis. The final magnetic state (shown on the right) is the state in the center cross area.

While, in the horizontal wire before and after the vertical cross arm, we obtained a multi-domain state, the vertical arm breaks this randomizing effect and restores the initial magnetic state of the cross position. To further investigate the effect of the cross geometry, we performed additional simulations without the vertical arm, i.e., a wire geometry (not shown). The transient magnetic configurations show multiple domain states as the laser beam swept over the wire, confirming that the cross geometry is essential for the helicity independent back switching.

III.2.4) Conclusion and perspectives

In this section, we have studied the effect of polarized femtosecond light pulses on rare-earth free synthetic ferrimagnets (SFi). Those synthetic ferrimagnets are Co (t_1)/Pt/Ru/Pt/CoFeB (t_2)/Pt (0.4 nm)/CoFeB (t_2). For the Ru and Pt thicknesses we use, there is a strong antiferromagnetic coupling between the two magnetic layers showing strong perpendicular magnetic anisotropy. First we demonstrate all-optical helicity dependent switching (AO-HDS) in planar Hall crosses. We show by varying the thicknesses of the individual FM layers constituting the SFi, that the helicity dependence of the magnetic switching can be modulated. This behavior can be explained by the interaction between the laser polarization and the net magnetic moment at writing temperatures, which is governed by the relative T_C of each layer. Moreover, when the Curie temperatures of each layer are

matched, we observe a helicity-independent back switching, with the final magnetic configuration determined only by the initial state. In most materials to-date, helicity dependence is intrinsic, with back switching demonstrations limited to few rare-earth alloys [69] **or numerical calculations** [135]**. Here we successfully demonstrate each of these switching behaviors in Hall devices, made from the same materials system and commonly used ferromagnetic materials. The results provide a handle to all-optical control of magnetization, and a promising route to practical opto-spintronic devices.**

Conclusion of chapter III

In this part, we have studied two types of heterostructures with perpendicular anisotropy when exposed to femtosecond polarized light, namely exchange bias systems, (FM/AFM) bilayers, made of $[Pt/Co]_N$/ IrMn and a rare-earth free synthetic ferrimagnetic layers made of Co/Pt/Ru/Pt/CoFeB/Pt/CoFeB layers. For both systems the key parameters are the ordering temperatures of the layers (the blocking temperature for the AFM the Curie temperatures for the FM layers).

In the case of the exchange bias system made of a $[Pt/Co]_N$/ IrMn bilayer, at the appropriate laser fluence, a laser pulse heats the system at a temperature above T_B and below T_C. This way, the $[Pt/Co]_N$ferromagnetic magnetization switches according to the helicity of the light while the IrMn magnetic moments are thermally disordered. When the system cools down the interfacial moments of the IrMn layer align with the newly switched $[Pt/Co]_N$ moments and the exchange bias field is reset. It is thus of primary importance for the laser-induced exchange bias field reset that $T_B<T_C$.

In the case of the synthetic ferrimagnetic layers made of Co/Pt/Ru/Pt/CoFeB/Pt/CoFeB layers, if $T_C^{Co} > T_C^{CoFeB}$, , at the appropriate laser fluence, a laser pulse heats the system at a temperature aboveT_C^{CoFeB} and below T_C^{Co}. This way, the Co magnetization switches according to the helicity of the light while the CoFeB/Pt/CoFeB magnetic moments are thermally disordered. When the system cools down the moments of the CoFeB/Pt/CoFeB ferromagnetic layer align with the newly switched Co moments and the RKKY interaction is reset. The fact that $T_C^{Co} > T_C^{CoFeB}$ thus drives the helicity dependent all optical helicity-dependent switching process of the whole Co/Pt/Ru/Pt/CoFeB/Pt/CoFeB based synthetic ferromagnetic layer.

The main difference in the two studies is not the physics involved but how we conducted them. For the exchange bias system made of a $[Pt/Co]_N$/ IrMn bilayer it was easier to vary the laser fluence than changing the material parameters so we performed various experiments tuning the laser parameters. In the future, a materials study on exchange bias systems made of a FM/AFM bilayer to exhibit the role of the material parameters on all optical switching should be relevant. Indeed in a FM/AFM bilayer with $T_B>T_C$ (for instance in a Co/Ni/IrMn stack) we could think that a laser pulse could change the antiferromagnetic order at the interface and thereafter, during the cooling of the FM layer, induce a change of the ferromagnetic order due to the exchange at the FM/AFM interface.

In the study we performed on the AO-HDS process of the Co/Pt/Ru/Pt/CoFeB/Pt/CoFeB based synthetic ferrimagnetic (SFi) layer, we tuned material parameters while the laser parameters were kept constant. We could also vary the laser fluence in the SFi study to see if the threshold fluence for the switching behavior has the same tendency as the Curie temperature of the layer with the lower T_C.

The general principle of having two coupled layers with different ordering temperatures, which switching is driven by the switching of one of the layer, has already been exploited in a previous work [136]. In this work they show that it is possible to optically switch a Co/Pt ferromagnet with only one femtosecond light pulse by coupling it to a GdFeCo layer. They claim that the GdFeCo layer first switches and then the Co/Pt magnetization aligns with it because of the coupling. Using exchange coupled layers of different ordering temperatures to achieve the all optical switching is then a general idea that can be used in magnetic memories to have at the same time both the stability and the fast writing.

IV) Generation and displacement of magnetic textures exhibiting DMI

This chapter is divided into two main parts. The last part will deal with the interplay between light and skyrmionic bubbles while the upcoming part deals with the field-driven propagation of domain walls in $[Co/Ni/Pt]_N$ multilayers.

IV.1) Field-driven domain wall propagation in Co/Ni/Pt multilayers

Résumé en français: Dans cette partie, nous nous intéressons à la croissance de domaines magnétiques lorsqu'un champ magnétique statique est appliqué dans le plan de l'échantillon et lorsque des impulsions de champ magnétique dans le plan perpendiculaire à l'échantillon sont appliquées. D'après la littérature, cela génère des propagations majoritairement suivant la direction du champ magnétique appliqué dans le plan de l'échantillon et quelquefois perpendiculairement à ce champ. Dans notre cas, nous avons observé un phénomène plus complexe pour des multicouches de $[Co/Ni/Pt]_N$. Pour une répétition de $[Co/Ni/Pt]_N$, à faible champ, la direction de propagation suit la direction du champ statique appliqué. En revanche, son sens de propagation change à un champ non nul, contrairement à tout ce qui a été observé auparavant. Pour 3, 4 et 5 multicouches de $[Co/Ni/Pt]_N$, on observe une croissance des domaines dans des directions non observées auparavant. Le processus de propagation d'un domaine magnétique dans de telles conditions est étroitement lié à la configuration de sa paroi de domaine. Ne pouvant pas sonder directement la configuration de la paroi de domaine, nous avons cherché à comprendre quels sont les paramètres d'influence dans un tel système pour pouvoir proposer une théorie adaptée à nos résultats. Le lecteur peut ainsi trouver dans cette partie une étude comportant des variations d'épaisseurs de Co, Ni, Pt, l'addition d'une couche sacrificielle de Mg ou d'une couche d'Ir. Des possibles configurations de paroi de domaine seront exhibées ainsi que des théories phénoménologiques expliquant d'un point de vue énergétique la formation de telles parois. Toutes les mesures expérimentales montrées dans cette partie ont été faites à Centre for Memory and Recording Research (CMRR) à l'université de San Diego Californie (UCSD).

English summary: In this part, we focus our study on the propagation of magnetic domains that occurs when a constant in-plane magnetic field is applied simultaneously to pulses of a magnetic field perpendicular to the sample. In the literature, this experiment leads mostly to propagation in the direction of the axis of the in-plane field and sometimes in a direction perpendicular to this axis and included in the plane of the sample. However, in our study, we observed more complex results for $[Co/Ni/Pt]_N$ multilayers. For one repeat of $[Co/Ni/Pt]_N$, the direction of propagation follows the applied field. However, its direction changes at a non-zero in-plane magnetic field, unlike all the other systems studied before. For 3, 4 and 5 repeats of $[Co/Ni/Pt]_N$, we observe domain propagations in directions never observed before. The process of propagation of a magnetic domain wall in such conditions is deeply linked to the configuration of this domain wall. We were unable to directly probe the domain wall configuration. Thus we investigated to understand what the main parameters of influence are in our system, in order to be able to build a theory adapted to our experimental results. The reader will

find in this part a study including variation of thicknesses of Co, Ni, and Pt, the insertion of a sacrificial Mg layer or an Ir layer. Possible configurations of domain wall are exhibited, as well as theories explaining, from the energetic point of view, the formation of the corresponding domain walls. All the measurements presented in this part have been performed when I was at the Centre for Memory and Recording Research (CMRR) in the University of San Diego (UCSD).

IV.1.1) Properties of Co/Ni/Pt multilayers

There are three different interfaces in Co/Ni/Pt multilayers. The Co/Ni one has been demonstrated to promote the PMA both theoretically and experimentally [12] when layers grow textured according to the [111] crystalline direction. The presence of two magnetic layers brings a higher dipolar field but the interfacial anisotropy of 0.31 mJ/m^2 is enough, to obtain under several thicknesses conditions, the perpendicular easy axis of magnetization in Co/Ni multilayers [137]. The Ni /Pt interface also brings a contribution to the perpendicular anisotropy through hybridization. The Pt interfacial atoms also acquire a moment of 0.29μ_B /atom similarly to the Pt/Co interface.

IV.1.1.a) PMA in Pt/Co/Ni and VSM loops

Using DC magnetron sputtering, we grew on SiOx substrates Ta (3 nm)/Pt (3 nm)/ [Co (0.7 nm)/Ni (0.5 nm)/Pt (0.7 nm)]$_N$/Pt (3 nm) multilayers. The base pressure in the deposition chamber was lower than 5.5 x 10^{-8} Torr. Samples have N varying from 1 to 5. In order to assess static magnetic properties of the samples, we performed hysteresis loops at room temperature on those samples, both in the in-plane (IP) direction and the out-of-plane (OOP) direction using a VSM. The resulting hysteresis loops are shown on figure IV.1.

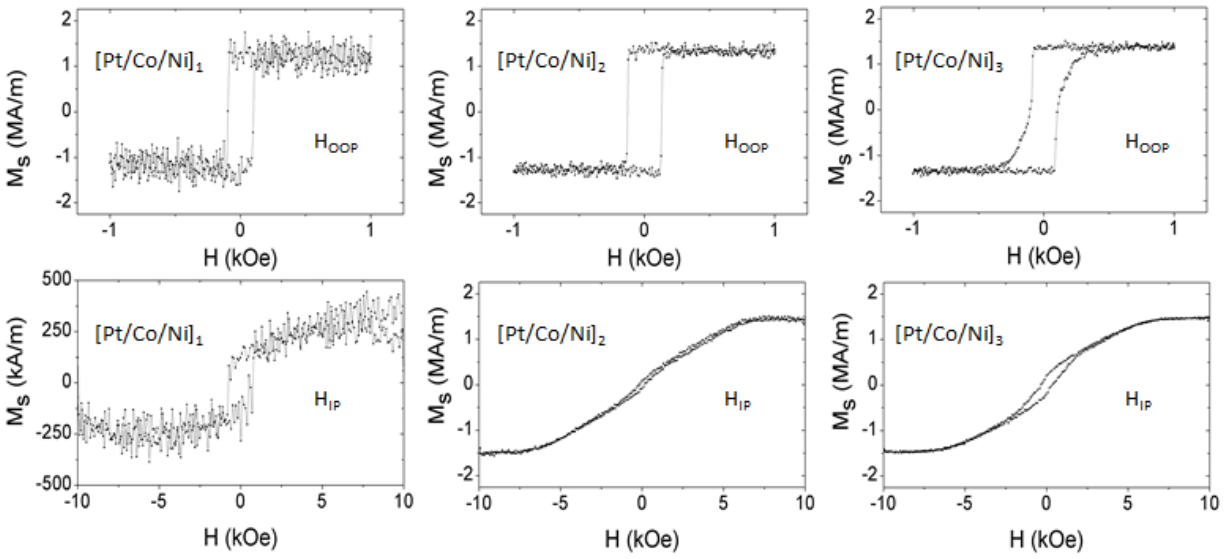

Figure IV.1: Hysteresis loops for samples with 1, 3, and 5 Pt/Co/Ni repetitions collected in the out-of-plane (top row) and in-plane (bottom row) orientations. All measurements were performed at room temperature.

The collected OOP loops indicate that all the samples exhibit a strong magnetic remanence at zero magnetic field and that they all have an easy axis of magnetization perpendicular to the film of the sample. We observe the appearance of a tail-like feature near the coercive field of the samples, suggesting that domains in form of stripes form during the reversal of the magnetization. By exanimating the IP loops, we deduce that the IP anisotropy field is not much altered by the variation of the number of repeats after 3 repeats.

IV.1.1.b) Domain shape observed on MOKE microscope

We performed the measurements of domain expansion under the influence of a static IP field and a pulsed out-of-plane field described in Je *et al.* [28] on the Ta (3 nm)/Pt (3 nm)/[Co (0.7 nm)/Ni (0.5 nm)/Pt (0.7 nm)]$_N$/Pt (3 nm) samples we grew. The setup we used in this type of measurement is depicted in part II.2.1.b). In our measurements, the length of the pulse is approximatively 0.1 ms. First we performed the pulse experiments on the five samples (N=1,2…5) by varying the strength of the magnetic field and we observed that, for a given sample, the shape of the domains was always the same whatever the value of the IP field was. However, from one sample to the other, those shapes are different. Those typical patterns of domains are shown on figure IV.2.

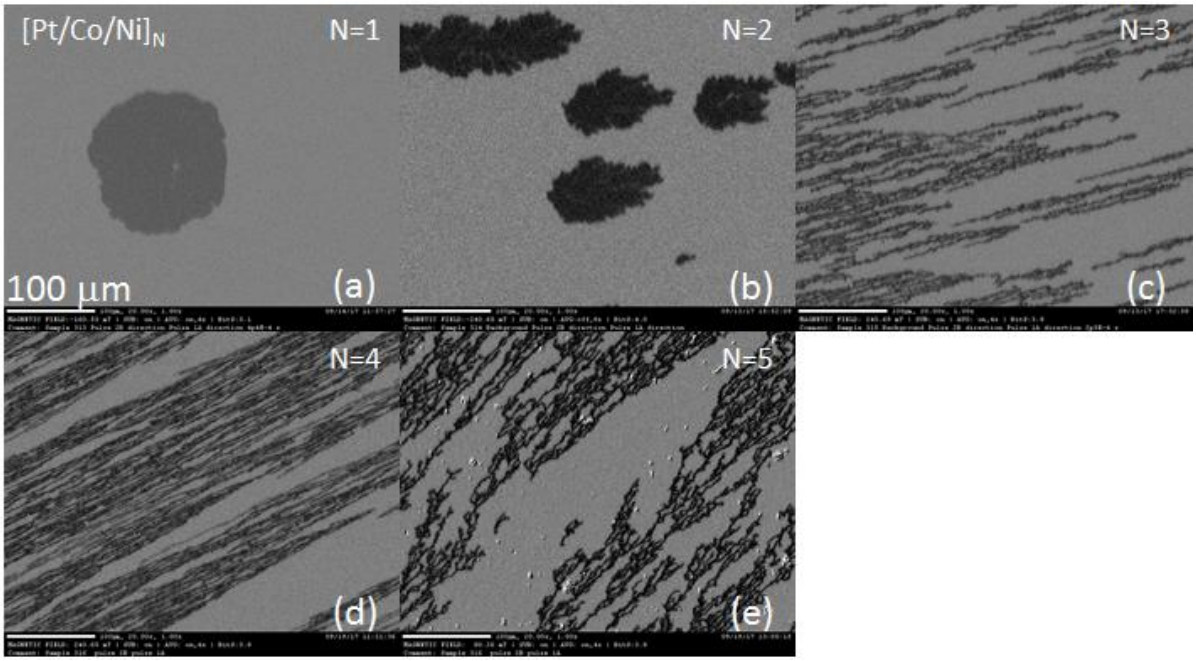

Figure IV.2: MOKE images of domain expansion in the [Pt/Co/Ni]$_N$ samples with a)N=1, b=2, c)N=3, d)N=4, e)N=5. The resulting domains are either bubbles (a), dendritic (b) or stripes (c-e).

We observe on figure IV.2 what we intuited from the OOP hysteresis loops. The system tends to form stripe domains for N=3, 4 and 5. For N=1, we observe a bubble domain, while for N=2 we observe what is called a dendritic domain, an intermediate between the bubble and the stripe domains.

IV.1.2) Domain propagation observed of Pt/Co/Ni multilayers

IV.1.2.a) Dependence on number of repeats (N)

The hysteretic behavior and domain shapes being characterized we now discuss possible scenarios to explain these results. Figure IV.3 shows a magnetic domain wall propagation at two different IP field values for N=1.

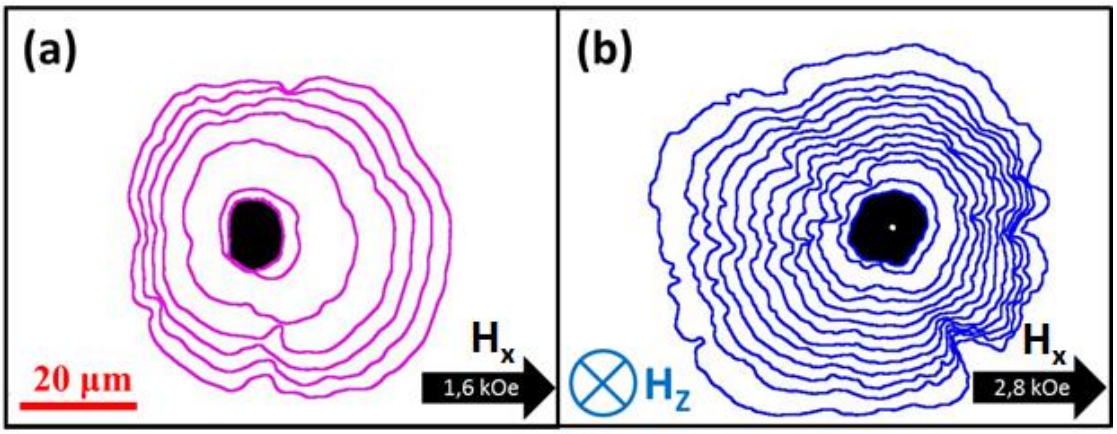

Figure IV.3) MOKE images of domain expansion in the $[Pt/Co/Ni]_1$ sample with (a) 1,6 kOe and (b) a 2,8 kOe in-plane field. The nucleation/growth pulses (Hz=100 Oe, ~0.1 ms in duration) were applied in the direction perpendicular to the plane of the sample.

For both values of the in-plane field, the main direction of propagation is in the direction of the applied in-plane field. At 1.6 kOe (a), the domains propagates mainly along the constant in-plane field while, at 2.8 kOe, the domain propagates mainly opposite to the applied in-plane field. By varying the value of the IP field and reproducing the experiment, we observe that the domains propagate mainly along the in-plane field for a field value between 0 Oe and 2.2 kOe and, above 2.2 kOe, they propagate mainly opposite to this IP field. This is opposite to most of the report on field-driven domain wall propagation [20] [28], since the expected behavior is that, for a given direction of the field and a given direction of the field, the domains always propagate mainly in the same direction, indifferently to the field value. However, this feature we observed has been reported before by Lau *et al.* [138] in a Si/TaN(3nm)/Pt(2.5nm)/[Co(0.2nm)/Ni(0.6nm)]2 /Co(0.2nm)/Ta(0.5nm)/TaN(3nm) sample.

We increased the number of repeats to N=2 and conducted the same study as N=1. We observed also the same three transitions as before: one at a negative field, one at zero field, and one at a positive field. The evolution of the expansion of the domain as a function of the in-plane field strength can be deducted from the MOKE images on figure IV.4. At a low field value (0.4 kOe) the domain grows more in the direction of the magnetic field. When we increase the field value (0.8 kOe and 1.2 kOe), we observe that the domains grow more in the direction perpendicular to the in-plane field. For 1.6kOe and 2kOe, the domain expands more in the opposite direction to the field and this direction stays the same for higher fields. We have no information for fields higher than 3.2kOe due to technical limitations.

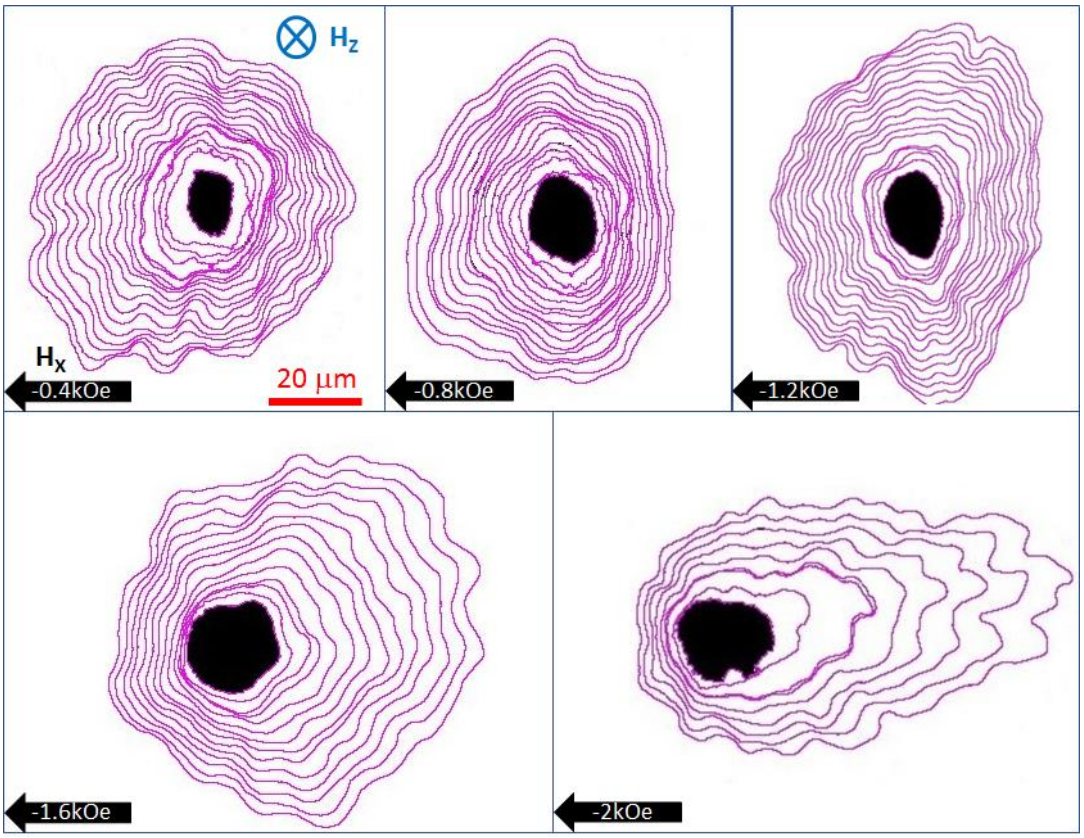

Figure IV.4: Kerr images demonstrating the propagation direction of stripe domains in the Pt/Co/Ni sample with N = 2 under the influence of several different in-plane fields in the – x direction.

We then conducted the same set of experiments for N=3. In this film, a much higher number of nucleation events is obtained. It is then harder to isolate a single domain. Thus, our images include several domains. We observed an unexpected propagation behavior as seen on figure IV.5. The direction of expansion of the domains is not anymore aligned with the field or perpendicular to it but there is a non-trivial tilt angle with this direction and the in-plane field. Furthermore, the images taken at different field values indicate that this direction changes with the strength of the in-plane field. We can note that at lower fields (0.4kOe and 1.2kOe), the domains propagate more in the direction of the in-plane field while, at higher fields (1.6kOe), the propagation occurs mainly in a direction opposed to this field. At first sight, this looks similar to the cases of N=1 and N=2.

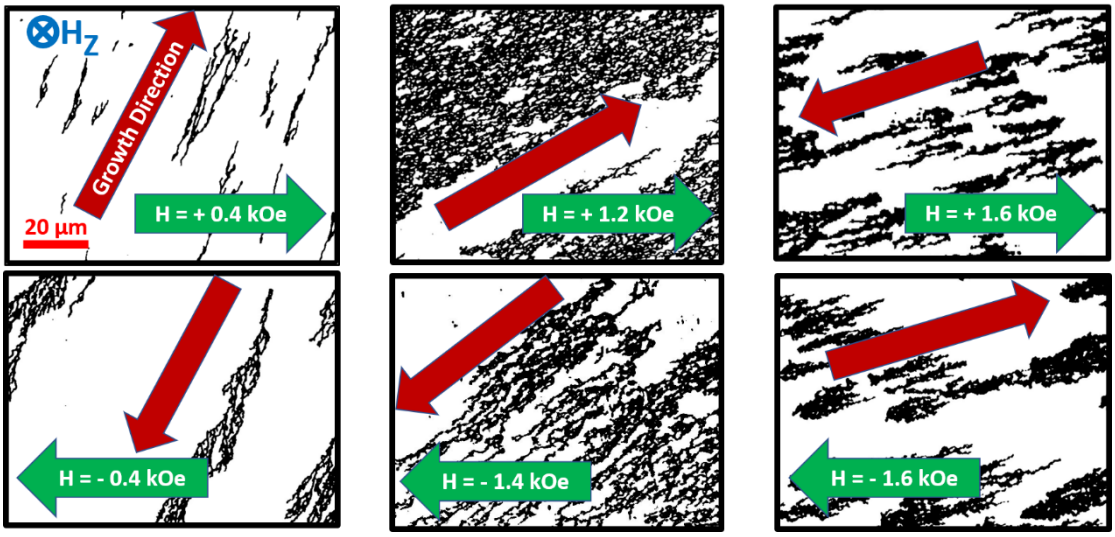

Figure IV.5: Kerr images demonstrating the propagation direction of stripe domains in the $[Pt/Co/Ni]_3$ sample under the influence of several different in-plane fields in the +/- x-directions

By conducting the same experiment for N=4 and N=5 with various field values, we observed what seemed to be a similar propagation behavior (not shown). In order to have clearer data, we conducted more systematic experiments. We measured the angle formed by the in-plane field and the vector of main propagation of the domains for different values of the in-plane field. The convention we used for this angle is depicted on Figure IV.6a). For the rest of the manuscript we call this angle the propagation angle for a convenience reason. The evolution of the propagation angle as a function of the in-plane field respectively for N=3, 4 and 5 is shown on figure IV.6b)-d) A look on the figure IV.6) confirms what we observed before. The evolution of the propagation angle with the field is similar for N=3, 4 and 5. At 0.5 kOe the domains propagate mainly in the +y direction with a small x component. It then gets always closer to the direction of the in-plane field until the magnetic in-plane field reaches a critical value (H_{crit}, approximatively 1.5 kOe). At this critical field, what seems to be a sharp transition on figure IV.6) occurs. At even higher fields, the propagation angle stays the same until at least 3.2 kOe, the domains propagate mainly against the applied field but with a small tilt angle with it. The existence of a non-null critical point at which the main direction of propagation goes from mainly along the in-plane field to opposite to it is a common feature of all the samples from N=1 to N=5. Furthermore, one really intriguing point is the existence of this persistent tilt angle above the critical field for N=3, 4 and 5. Indeed by increasing the value of the IP field we should be able to saturate all the domain walls aligned with the field at one point and have no tilt angle of propagation. This time, this result has not been observed yet in the literature.

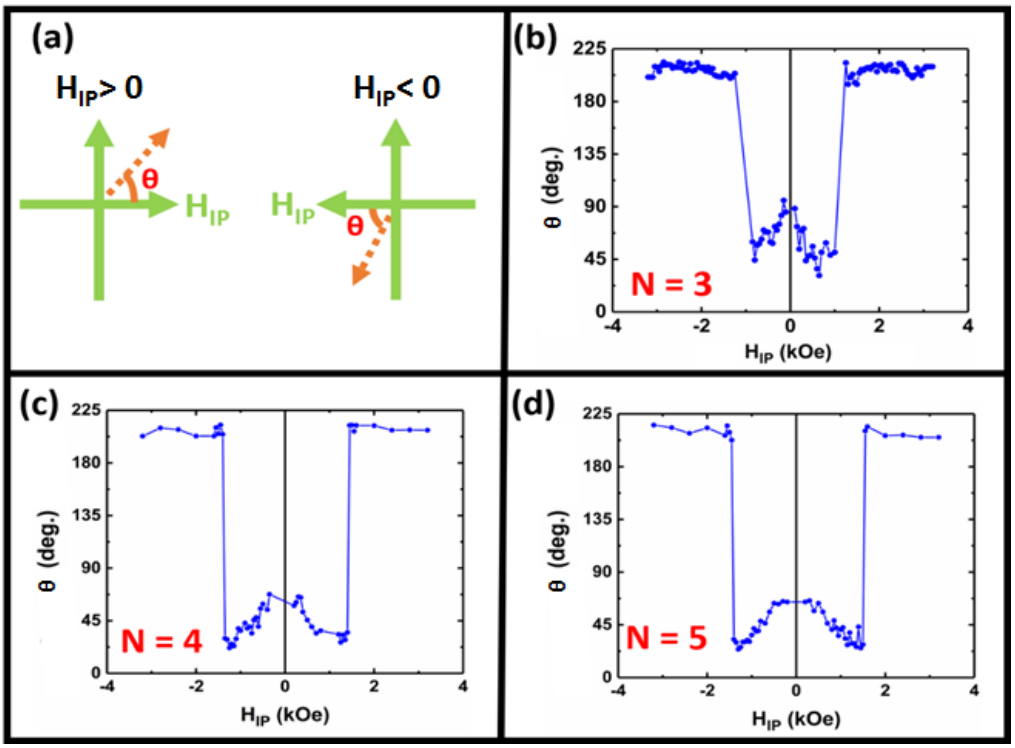

Figure IV.6: (a) Display of the convention used for the propagation angle (θ). Evolution of the propagation angle as a function of the applied in-plane field for (b) N=3, (c) N=4 and (d) N=5.

IV.1.2.b) Dependence on the thickness of Cobalt

Intrigued by the propagation direction at high fields for the $[Co/Ni/Pt]_N$ multilayers exhibiting stripe domains, we decided to tune growth parameters to study their influence. The first parameter we decided to change was the thickness of Co. We grew Ta (3 nm)/Pt (3 nm)/[Co (t_{Co} nm)/Ni (0.5 nm)/Pt (0.7 nm)]$_3$/Pt (3 nm) multilayers with t_{Co}= 0.39nm, 0.47nm, 0.55nm, 0.63nm, 0.71nm. For all those thicknesses of Co, we observe the same propagation behavior at positive field as before: a propagation mainly along the x axis (compared to the –x axis) at low field and the existence of a critical field at which the propagation occurs mainly opposite to the field and with a constant tilt angle, at least until 320mT. An increase in the thickness of Co has several effects. The first one is the enhancement of the total dipolar field because of a higher magnetic volume. This yields a decrease of the effective perpendicular magnetic anisotropy because the contribution of the dipolar energy in the total energy increases while the interfacial contribution is the same. This is the same as arguing that the shape anisotropy contribution in equation (1.10) of the total energy per volume is the same while the interfacial contribution decreases. The last and less trivial one is the decrease of the DMI. According to Yang *et al.* [139], the first atomic layer of Co in contact with Pt carries a strong positive DMI while the second and third layers carry a smaller negative DMI. Furthermore, even if we consider the DMI as being only carried at the interface, its contribution to the total energy is reduced with a higher magnetic volume due to its interfacial nature.

IV.1.2.c) Dependence on the thickness of Nickel

We grew a series of Ta (3 nm)/Pt (3 nm)/[Co (0.7 nm)/Ni (t_{Ni} nm)/Pt (0.7 nm)]$_3$/Pt (3 nm) multilayers with t_{Ni}= 0.3nm, 0.5nm, 0.7nm, 0.9nm, 1.1nm. The corresponding coercive fields extracted from the OOP hysteresis loops are shown on figure IV.7.

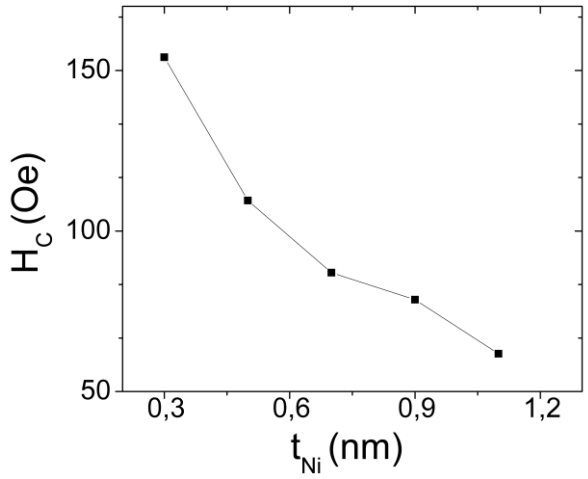

Figure IV.7: Evolution of the perpendicular coercive field as a function of the Ni thickness for Ta (3 nm)/Pt (3 nm)/[Co (0.7 nm)/Ni (t_{Ni} nm)/Pt (0.7 nm)]$_3$/Pt (3 nm) multilayers extracted from VSM hysteresis loops. All measurements were performed at room temperature.

We observe that the coercive field is lower as higher thicknesses. It is consistent with the decrease of the anisotropy explained earlier ($\propto 1/t_{Ni}$). The magnetic moment at saturation per volume decreases when the thickness (t_{Ni}) increases. This can be explained by two main arguments. Increasing the Ni thickness increases the Ni percentage, which decreases M_S because Ni moment is lower than Co moment. On the other hand, the Ni atoms at the interface have a higher total magnetic moment since they experience no orbital quenching due to interfacial hybridization. The higher the Ni thickness is the higher is the percentage of "volume Ni atoms/volume + interface Ni atoms", and subsequently, the lower the M_S is. The effect of an increase of the Ni thickness is similar to some extent to the one of Co. However, it has not been demonstrated by DFT to our knowledge that the DMI value changes through the Ni atomic layers.

By reproducing the field-driven domain wall propagation experiment, we still observed the same propagation behavior as for the N=3, 4 and 5. The magnetic domain walls propagate mainly along the applied field for low positive field values and, after a critical field, they propagate opposite to this field with a small tilt angle.

IV.1.2.d) Dependence on the thickness of Platinum

A relevant parameter to tune is the RKKY exchange stiffness between the Ni and the Co layers through the Pt layer. The strength of this coupling depends on the thickness of Pt [140], so we have grown Ta (3 nm)/Pt (3 nm)/ [Co (0.7 nm)/Ni (0.5 nm)/Pt (t_{Pt} nm)]$_3$/Pt (3 nm) samples with varying Pt thicknesses between 0.3 nm and 1.8nm. Once again, we observed the same propagation behavior for almost all the samples of this series. The domains grow for a low positive field mainly along the in-plane applied field, while after a critical field they seem to reach a "saturated regime" with propagation mainly along the –x direction with a small tilt angle. It seems to us that the only sample that does not behave like this is the one with 1.8nm of Pt. We observe the existence of a critical field but above this field, it is hard to see if there is a tilt angle or if the domains expend purely against the direction of the in-plane field. The evolution of the domain wall propagation pulse after pulse with an in-plane field of 2kOe (above the critical field) is shown on figure IV.8. As seen on this figure, the high number of nucleation events makes it harder to isolate a single propagation event.

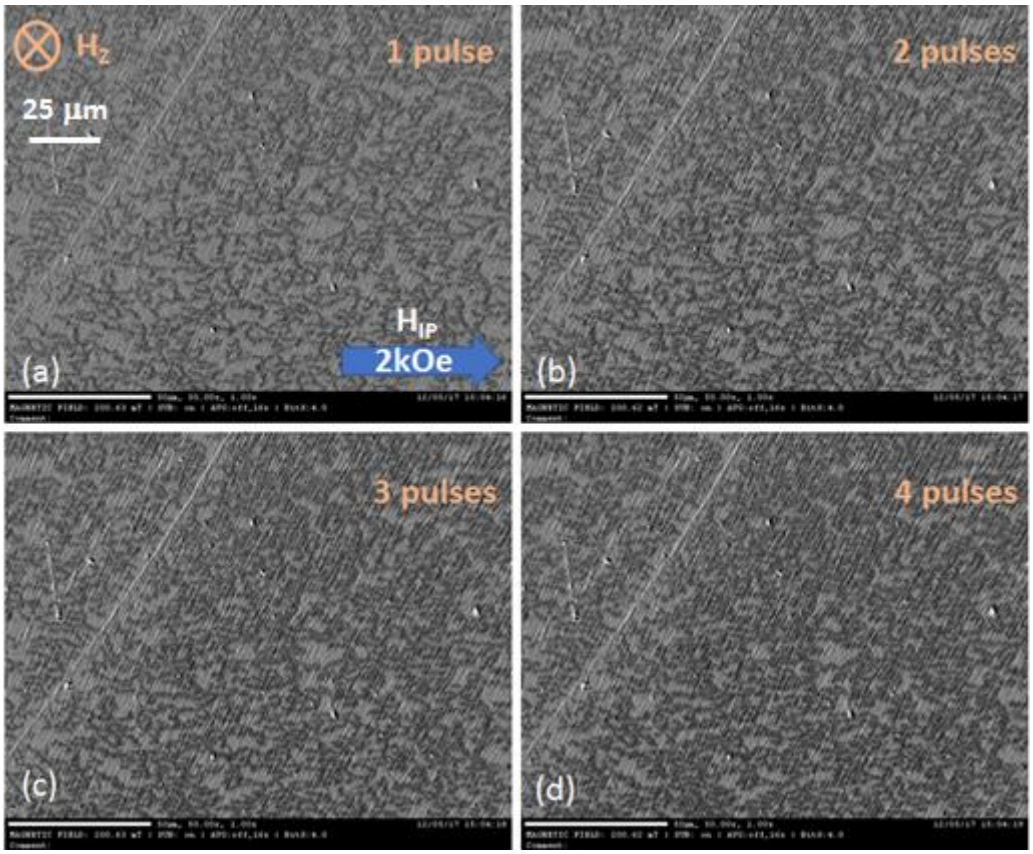

Figure IV.8: Kerr images demonstrating the propagation direction of stripe domains in the Ta (3 nm)/Pt (3 nm)/[Co (0.7 nm)/Ni (0.5 nm)/Pt (1.8 nm)]$_3$/Pt (3 nm) sample under the influence of a 2kOe in-plane magnetic field and after a)1, b)2, c)3 and d)4 pulses of out-of-plane field.

IV.1.3) Domain propagation observed with various interfaces

In the previous section, we changed the thicknesses of different layers (Co, Ni, and Pt). This leads to the changes of moment at saturation, total magnetic volume, dipolar field, anisotropy or exchange

stiffness. The same behavior of domain wall propagation in $[Co/Ni/Pt]_3$ occurs for a wide range of those parameters. In this section, we present variations of the basic stack of Co/Ni/Pt that are more based on the change of interfaces. Many magnetic parameters are dependent on the interfaces but the parameter we will mainly tune now is the interfacial DMI coefficient D.

IV.1.3.a) Sacrificial Mg layer

Since the DMI in our stacks is an interfacial phenomenon, tuning the interdiffusion and the roughness at the concerned interface seems to influence the strength of the DMI. This principle has been used by Lavrijsen *et al.* [32] and Hrabec *et al.* [20]. They have been able to quantify the change of DMI value. They modified a Co/Pt interface by increasing the Ar pressure during the deposition by magnetron sputtering. As described in the magnetron sputtering section of this manuscript (II.1.1), increasing the Ar pressure is supposed to lead to a better Co/Pt interface. The interface we chose to work on is the Ni/Pt interface. We inserted a sacrificial layer of Mg between the Ni and the Pt. The goal of the insertion of the Mg layer is to absorb the kinetic energy of the incident Pt atoms during the sputtering process. With less kinetic energy, the Pt atoms enter less into the Ni lattice and then the resulting Ni and Pt interface is better defined. Since the Pt atoms are significantly heavier than the Mg ones when the Pt atoms hit the Mg, Mg atoms are resputtered. If the Mg initial layer is not too thick, there is almost no Mg in the sample after the Pt deposition anymore. We took the idea of an Mg sacrificial layer from the paper of Swerts and al [141].

The samples of this series have the following stacks: Ta (3 nm)/Pt (3 nm)/[Co (0.7 nm)/Ni (0.5 nm)/Mg (0.3 nm)/Pt (0.7 nm)]$_N$/Pt (3 nm). We used the values N=3, 4 and 5. We also regrew the Ta (3 nm)/Pt (3 nm)/[Co (0.7 nm)/Ni (0.5 nm)/ Pt (0.7 nm)]$_N$/Pt (3 nm) series to have the same sputtering conditions when comparing a stack grown with a Mg sacrificial layer and the same stack without it. We measured the hysteresis loops in the out-of-plane configuration for the resulting 6 samples. Those are displayed on figure IV.9. Looking carefully at those curves, we observe a small increase of the coercive field when we add the Mg sacrificial layer (for N=3, Hc=125 Oe with Mg and 84 Oe without it, for N=4, Hc=108 Oe with Mg and 76 Oe without it and, for N=5, Hc=80 Oe with Mg and 73 Oe without it). This coercive field increase makes us think that the interface between Ni and Pt has a better quality, when grown with the Mg sacrificial layer. The DMI contribution from this interface should then be higher. However, we did not perform any direct quantitative measurement of the DMI (like using Brillouin light scattering).

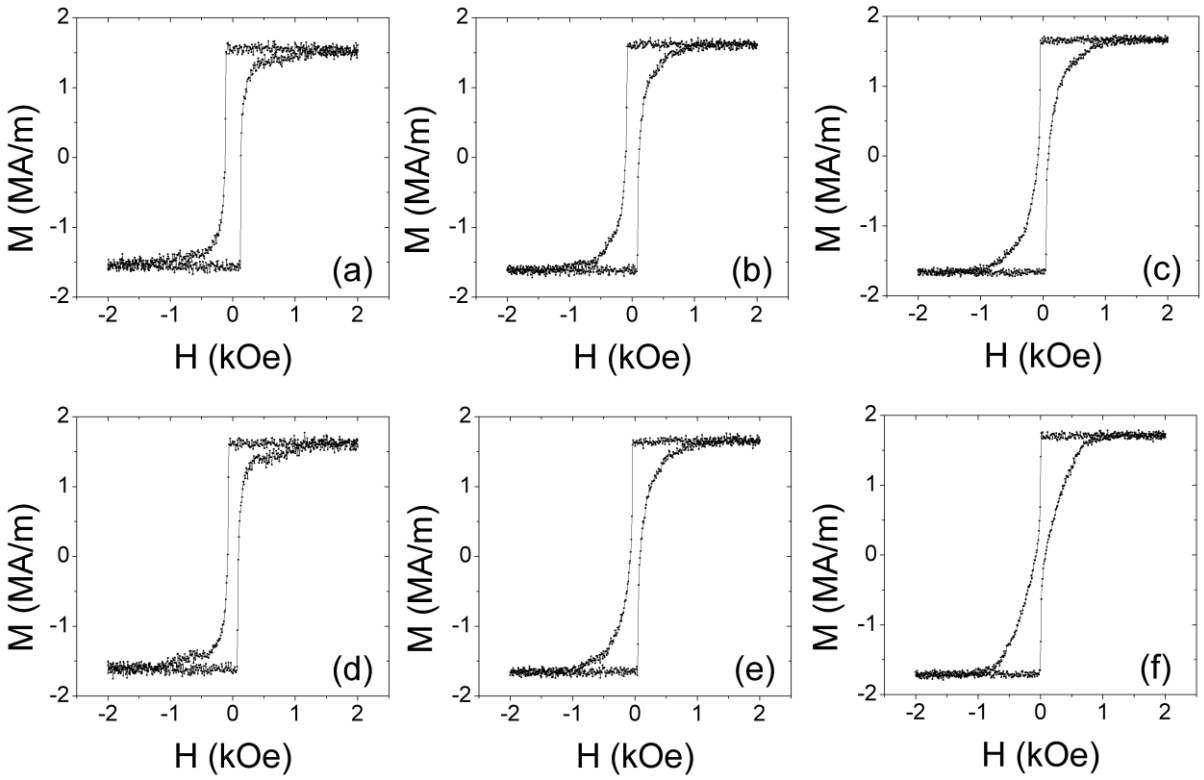

Figure IV.9: Hysteresis loops for Ta (3 nm)/Pt (3 nm)/[Co (0.7 nm)/Ni (0.5 nm)/ Mg (0.3 nm)/ Pt (0.7 nm)]$_N$/Pt (3 nm) samples with a)N=3, b)N=4 and c) N=5 and Ta (3 nm)/Pt (3 nm)/[Co (0.7 nm)/Ni (0.5 nm)/ Pt (0.7 nm)]$_N$/Pt sample with d)N=3, e)N=4 and f) N=5 collected in the out-of-plane orientation. All measurements were performed at room temperature.

We then decided to perform the field-driven domain expansion experiment on the samples grown with an Mg sacrificial layer. The results are similar to the ones obtained on the same stacks without an Mg sacrificial layer. The domain wall propagation is along the IP field for $H_{IP} < H_{crit}$ and is opposite to the IP field with a little tilt for $H_{IP} > H_{crit}$.

IV.1.3.b) Pt/Co/Pt

Up to now, we have tuned the anisotropy, the saturation moment, the dipolar field and the anisotropy, and obtained similar results in the whole series of [Co/Ni/Pt]$_N$ multilayers. A tempting idea is to say then that the Co/Ni interface is the cause of those particular results. In order to have more precise ideas of the role of the Co/Ni interface, we decided to take a different system close to ours that has been subject to many studies and to look if we can reproduce to some extent with this system what we observed with Co/Ni. We decided to study the Pt/Co/Pt system. The Pt/Co/Pt is a controversial system that has been extensively studied. There have been claims that the top and the bottom Pt interfaces are not equivalent [142]. The presence of a net DMI is a clue of this asymmetry [143].

First we grew Pt/Co multilayers with stripes domains, namely Ta (3 nm)/Pt (5 nm)/[Co (0.79 nm)/Pt (0.93 nm)]$_3$ sample. We then conducted the field driven domain expansion on this sample with an in-plane field of 2kOe. Resulting MOKE pictures obtained are shown on figure IV.10.

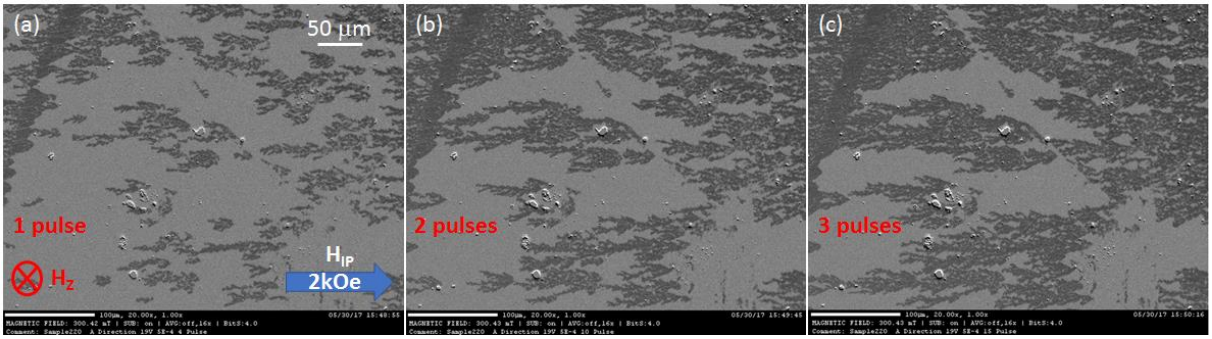

Figure IV.10: MOKE images demonstrating the propagation direction of stripe domains in the Ta (3 nm)/Pt (5 nm)/[Co (0.79 nm)/Pt (0.93 nm)]$_3$ sample under the influence of a 2kOe in-plane magnetic field after a)1, b)2 and c)3 pulses of out-of-plane field .

We clearly observe stripe domains. The propagation at 2kOe is opposed to the applied in-plane field. Actually, we observed that the propagation for in-plane fields varying between 0 and 3.2kOe is always in that direction. There is no small tilt angle as in [Co/Ni/Pt]$_3$. This tilt angle is consequently not a mandatory feature of the stripes domains.

We also grew Ta (3 nm)/Pt (5 nm)/[Pt (0.9nm)/Co (0.8nm)/ Mg(t_{Mg})/ Pt (0.9nm)]$_5$ samples. The Mg layer is also used in this stack as a sacrificial layer. The Mg thickness takes the following values : t_{Mg} = 0, 0. 1, 0.2, 0.4 and 0.6 nm. MOKE images at 2.8kOe for t_{Mg} = 0 nm are shown on figure IV.11).

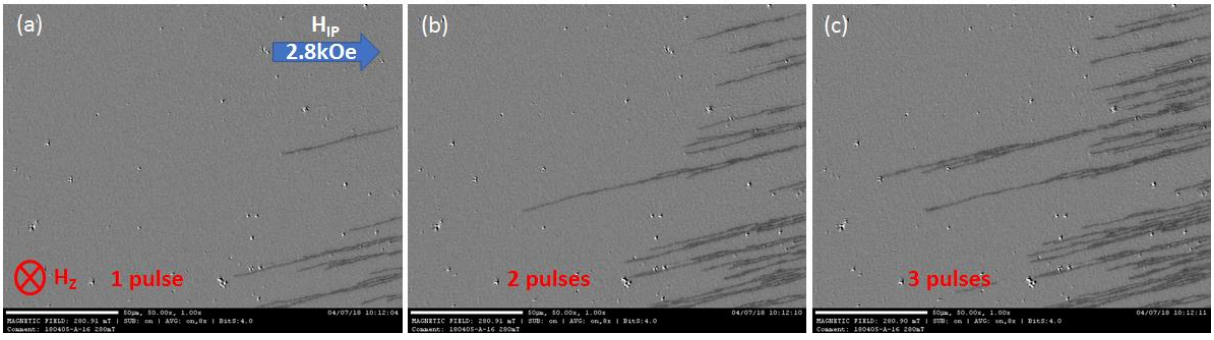

Figure IV.11: MOKE images demonstrating the propagation direction of stripe domains in a Ta (3 nm)/Pt (5 nm)/[Pt(0.9nm)/Co (0.8 nm)/Pt (0.9nm)]$_5$ sample under the influence of a 2.8kOe in-plane magnetic field after a)1, b)2 and c)3 pulses of out-of-plane field .

We observe on figure IV.11 the propagation with a tilt angle that we observed for Co/Ni/Pt samples exhibiting stripe domains. For $H_{IP}>H_{crit}$ this direction of propagation has been observed for all positive fields between 0 Oe and 3.2kOe in all the samples of this serie. We can conclude that this tilt angle is not a unique feature of [Co/Ni/Pt]$_N$ multilayers exhibiting stripes.

IV.1.4) Discussion on the mechanism

IV.1.4.a) Offset of the instrument

Before invoking any physical explanation, we wanted to be sure that our results were not due to a problem of misalignment of the coil with the plane of the sample. For this, we tilted the axis of the coil of +5° and -5°. We have still been able to observe the same angle of propagation in a Ta (3 nm)/Pt (3 nm)/[Co (0.7 nm)/Ni (0.5 nm)/Pt (0.7 nm)]$_3$/Pt (3 nm) sample in the two cases. This indicates that the misalignment of the coil is not the reason behind our results. We also wanted to know if, by any way, our sputtering process could induce any secondary anisotropy axis in the plane of the sample, wich could be responsible for our results. For this, we did the usual field-driven expansion of domains but when we put the sample on the stage of the MOKE microscope, we rotated the sample on the stage, having as axis of rotation the z axis. We did not notice any change of propagation angle in our sample when rotating the sample this way. Those two quick experiments we performed led us to think that the results we observe are intrinsic to the sample and do not depend on the experimental setup we used.

IV.1.4.b) Chirality of Bloch walls

A puzzling feature of our [Co/Ni/Pt]$_N$ multilayer is the change of direction that occurs at a critical field. There is actually one intuitive way to explain that the main direction changes at a certain value of the in-plane field. It is at the transition from the Bloch to Néel configuration of domain wall. With low values of DMI and a high enough dipolar field it is possible to have a ground Bloch configuration of DWs. The field driven expansion of a such a domain is shown on figure IV.12 and is extracted from DuttaGupta *et al.* [29]

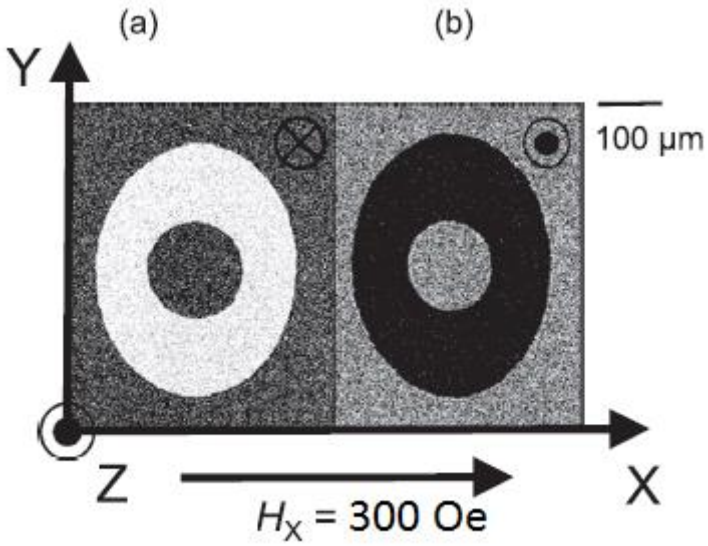

Figure IV.12: MOKE images of a DW expansion in a sample under constant out-of-plane field of 10 Oe under and a constant out-of-plane field (H_Z) of 300 Oe. Extracted from [29].

This image is interesting because the expansion of domains in the upward and downward directions should not be theoretically the same for a pure Bloch DW. This means that the DW configuration is more complex. A possible magnetic configuration of the domain walls explaining this expansion behavior is shown on figure IV.13.

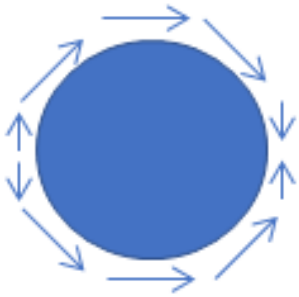

Figure IV.13: Possible domain wall configuration corresponding to the images shown on figure IV.12. The arrows represent the direction of the magnetization at the center of the domain wall between the blue and the white domains.

We can see on figure IV.13 two half Bloch wall configurations separated at the left and the right of the bubble domain by point of zero magnetization, i.e. Bloch points. We have the hypothesis that, in a single layer of Co/Ni/Pt we have the same phenomenon of initial Bloch configurations. The presence of Bloch points allows then for non-trivial magnetic textures deriving from a pure Bloch wall configuration as the one we showed on figure IV.13. The exact configuration is hard to find. It would need some computation or more direct observations.

IV.1.5) Conclusion and perspectives

In this part, we show a deviation from the field driven creep law in a material exhibiting DMI predicted and formulated by Je et al. [28]**:**

$$\mathbf{v} = \mathbf{v_0} \exp\left[-\alpha {H_Z}^{-\frac{1}{4}}\right] \qquad \textbf{(4.1)}$$

In this expression, the term α is supposed to depend symmetrically on the applied in-plane field. Several studies already showed that the domain wall velocity has also an antisymmetric component with the applied in-plane field [32] [33] [144]**. However, even this asymmetric contribution is not enough to explain the results we obtain. Indeed, we observed striking results. The field-driven propagation of domains in Co/Ni/Pt multilayers is not aligned with the axis of the applied in-plane field and the propagation angle depends on the strength of the in-plane field. To our knowledge, no explanation of our experiments for N≥2 could be found in the literature. Our work then could then lead to a better comprehension of the field-driven propagation of domain walls with DMI. We can also note that the measurement of DMI by field-driven expansion of a domain is already controversial and this gives different results than BLS** [145]**. Our results could then help having a more accurate method to measure the DMI. We can note that taking DMI values from DFT simulations found in the literature for the Pt/Co interface** [19] **and the Ni/Pt interface** [24]**, the**

theoretical value of the DMI in our Pt/Co/Ni/Pt stack is 2.85 meV/atom. In other units, itcorresponds to D=1.044 mJ/m^2 and a theoretical DMI field H_{DMI}= 2349 Oe. However, experimental DMI values can be very different from theoretical expectations [20] **so it is hard to have a net conclusion from the theoretical value of the DMI field in our sample.**

IV.2) Effect of the femtosecond light on skyrmionic bubbles

Résumé en français: Dans cette partie nous nous intéressons à la génération de bulles skyrmioniques dans une hétérostructure en couche mince par impulsion laser. Nous avons fait croître un échantillon de Ta/CoFeB/TaOx. En appliquant un champ de 3.1 Oe perpendiculaire au plan de l'échantillon nous n'observons pas de bulle mais des domaines magnétiques en forme de bande désordonnés. Cependant cet état magnétique est métastable. L'état le plus stable correspond à des bulles formant un réseau. A température ambiante, la barrière d'énergie séparant ces deux états est bien supérieure à l'énergie d'activation thermique. Nous avons exposé cet échantillon au laser femtoseconde utilisé dans les expériences précédentes tout en appliquant ce champ de 3.1 Oe. Cela a eu pour effet de créer un réseau de bulles là où l'échantillon a été exposé au laser. Cette création est indépendante de l'hélicité de la lumière utilisée. Notre interprétation de ce phénomène est que le laser apporte l'énergie thermique nécessaire pour surpasser la barrière d'énergie séparant l'état métastable de domaines en forme de bande et l'état stable d'un réseau de bulles. Nous avons étudié les caractéristiques principales de ce réseau de bulles créé à savoir le rayon des bulles, leur densité au sein du réseau ou encore le nombre moyen de voisin par bulle. Nous avons en particulier caractérisé l'influence de la fluence du laser sur ces paramètres. La croissance de l'échantillon et sa caractérisation magnétique ont été effectuées à Spintec à Grenoble. Les expériences nécessitant un laser femtoseconde ont été effectuées à l'Institut Jean Lamour à Nancy. Nous avons déjà publié une partie de ce travail [146].

English summary: In this part, we focus on the laser induced generation of skyrmionic bubbles in a thin film material. We grew a Ta/CoFeB/TaOx sample. By applying a magnetic field of 3.1 Oe perpendicularly to the plane of the sample we did not observe bubbles but disordered stripe domains. However this magnetic state is metastable. The more stable state corresponds to the one with a bubble lattice. At room temperature, the energy barrier separating those two states is much higher than the thermal energy. We exposed this sample to the femtosecond laser used in the previous experiments (chapter III) and applied at the same time a perpendicular static field of 3.1 Oe. As an effect, it creates a lattice of bubbles where the sample has been exposed to the laser. This creation is independent of the helicity of the light. Our interpretation of this phenomenon is that the laser brings the thermal energy needed to overcome the energy barrier splitting the metastable state of disordered stripe domains and the stable state of a lattice of bubbles. We studied the main characteristics of this skyrmions lattice such as the radii of the skyrmions, their density inside this lattice or the average number of neighbors per bubble. We characterized the influence of the laser fluence on those parameters. The growth of the sample and its magnetic characterizations has been performed at Spintec in Grenoble. The laser experiments have been performed at the Institut Jean Lamour in Nancy. We already published a part of this work [146].

IV.2.1) Existence of skyrmionic bubbles

IV.2.1.a) Sample grown and wedge principle

Using DC magnetron sputtering a sample of Ta(3nm)/$Co_{72}Fe_8B_{20}$(wedge)/TaOx(2nm , naturally oxidized) has been grown in Spintec with a base pressure lower than 5.5 x10^{-8} Torr. The wedged CoFeB layer thickness varies from 0.75nm to 1.03 nm. The sample has then been annealed for 30 minutes at 250 °C in order to enhance its PMA.

IV.2.1.b) Hysteresis loop and corresponding domains

Using a MOKE microscope we have been able to obtain its hysteresis cycle and image the magnetic domains for a thickness of CoFeB of approximatively 0.9nm at different points of this curve as seen on figure IV.14.

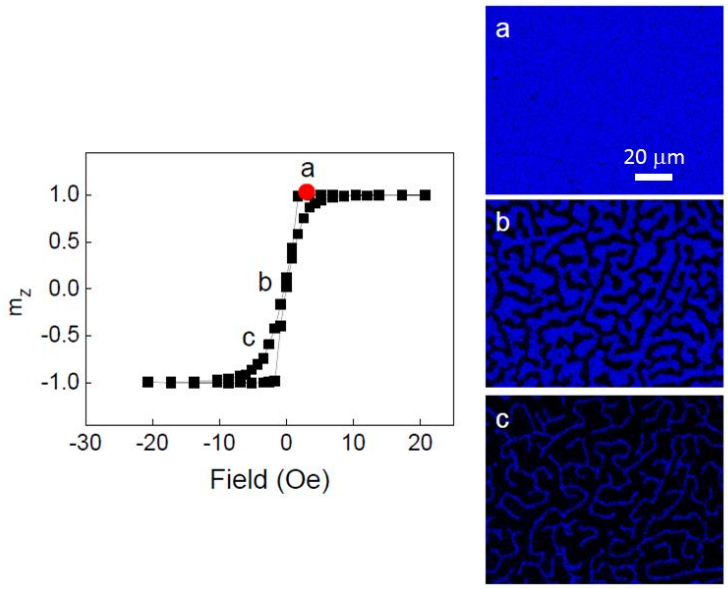

Figure IV.14: Normalized hysteresis loop of the Ta(3nm)/$Co_{72}Fe_8B_{20}$(wedge)/TaOx(2nm, naturally oxidized) sample obtained by MOKE and corresponding local MOKE microscope images at a) -3.1 Oe, b) 0 Oe and c) 3.1 Oe. Figure adapted from [146].

We used the image on figure IV.14 to obtain the width of the stripes at zero magnetic field. The theoretical domain width L_0 at remanence [147] is given by the expression:

$$L_0 = d\frac{\pi}{2}\exp\left(\frac{\sigma_{DW}}{4\lambda d} - \frac{1}{2}\right) \quad (4.2)$$

Where d is the film thickness, $\lambda = \frac{\mu_0}{4\pi}M_S^2$ the dipolar energy constant and σ_{DW} the domain wall energy. From the experimental values L_0 = 1.85 µm, d= 9 Å and M_S= 1 MA/m, we obtain σ_{DW} = 2.76 mJ/m^2. Using the measured effective anisotropy K_{eff} and the typical exchange stiffness A_{ex}= 12 pJ/m^2 and neglecting the contribution of the dipolar field, we obtain the corresponding energy of the Bloch

domain wall $4\sqrt{A_{ex}K_{eff}}$ = 3.25 mJ/m^2. This difference between the measured domain wall energy and the theoretical Bloch wall energy suggests that there is another contribution to the DW energy, namely in our case the DMI. It contributes to a level of -πD to this energy and turns the Bloch wall into a chiral Néel one [28] [23]. The estimated DMI energy is then D= 0.16 mJ/m^2. This is consistent with previous Brillouin light scattering (BLS) measurements performed on a similar stack [148].

IV.2.2) Laser experiments on skyrmionic bubbles

IV.2.2.a) Generation of skyrmionic bubbles

We studied the influence of the laser pulses on the Ta/CoFeB/TaOx sample described earlier. First, we saturated the sample magnetization with a positive magnetic field (along $\overrightarrow{H_Z}$) and then reduced its amplitude to 3.1 Oe. This state corresponds to the point (a) on figure IV.14 and it is still a single domain state. We then exposed the sample to a laser pulse of a fluence of 1.84 mJ/cm^2 and linear polarization. We observe the formation of skyrmionic bubbles of a diameter of approximatively 2.5 μm corresponding to the black dots on figure IV.15.a). By saturating the sample with a negative field (along $-\overrightarrow{H_Z}$), reducing its amplitude to -3.1 Oe and exposing it to a laser pulse with the same characteristics, we also observe the formation of skyrmionic bubbles but with the opposite contrast (b). We also investigated the role of the helicity of the light since we know that different helicities can affect differently the magnetization [4]. For figure IV.15.c) (resp. (d)), we saturated the sample and came back to a field value of 3.1 Oe, then used the same fluence of the light but with a σ^+ (resp. σ^-) helicity. We observe in both images the creation of the same type of skyrmions and no noticeable change is observed between both helicities. We conclude that the formation of bubbles is a thermally-driven process. For the rest of this chapter we will only work with the linear helicity.

We also image at remanence a region of thicker CoFeB (1 nm) on figure IV.15.e). We observe labyrinthine domains but with a smaller width. This is consistent with the reducing of the PMA that occurs for thicker CoFeB layers. We then saturated the sample and applied a field of 7 Oe before exposure to a laser pulse. The formation of bubbles of a smaller diameter (less than 1μm) is observed after laser exposure. This is a clue that this laser-induced generation of bubbles could be transposed to generate skyrmions which size is below the detection resolution of the MOKE. For practicality, the rest of the study is only composed of the study of the "big" skyrmionic bubbles obtained with 0.9 nm of CoFeB.

Next, we investigate the influence of the laser fluence on the generation of skyrmionic bubbles. This is the aim of figure IV.16. For better statistics, we wanted to maximize the number of bubbles on a wide film area. We swept the laser with a repetition rate of 5 kHz on the film from the position x=-20 μm and y=0 to x=20 μm. We then stopped the laser beam to sweep it again from the position y=-20 μm and x=0 to y=20 μm. The sweeping directions are indicated by the arrows in figure IV.16.a). We followed this process for different fluences of the light: (a) 1.49 mJ/cm^2,(b) 1.70 mJ/cm^2,(c) 1.84 mJ/cm^2, (d) 2.06 mJ/cm^2 and (e) 2.23 mJ/cm^2. For the lower laser fluence, bubbles are randomly generated. By increasing the laser fluence, we observe on the images a higher density of bubbles until they fully fill the space where the laser has been swept. For the higher laser fluences (for instance figure IV.16.e), there is a gradient of bubbles density from the boundary of the track of bubble left by

the laser sweeping to its center, the density of bubbles being higher in the center because the laser was swept twice there. Furthermore the central bubbles seem to have smaller radii than the ones on the boundary.

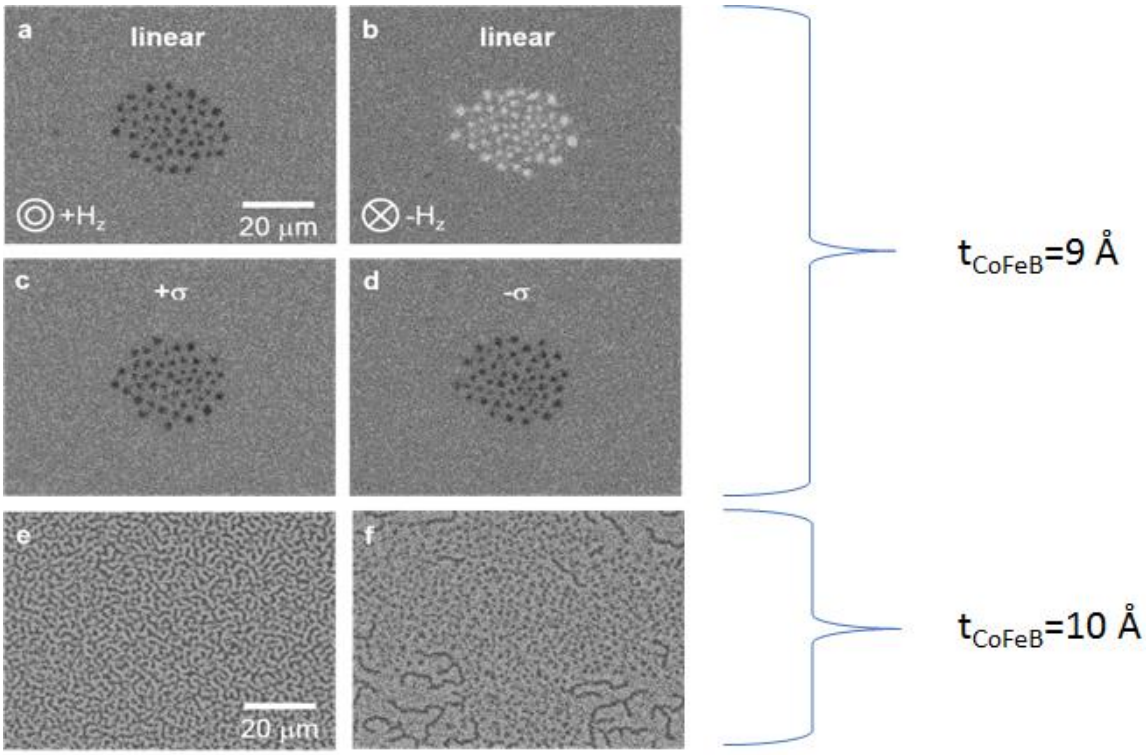

Figure IV.15: Laser-induced creation of bubbles (a) Nucleated bubbles from a saturated state (+z) by a 35-fs single laser pulse with a laser fluence of 1.84 mJ/cm^2 and linear polarization. (b): Bubble creation from an oppositely saturated state (+z) with linearly polarized light. (c)-(d). Bubble creation by a single laser with right-handed σ^+ polarization (c) and left-handed σ^- polarization (d). The DC magnetic field is +3.1 Oe for (a), (c) and (d) and -3.1 Oe for (b). (e-f): Much narrower stripe domains pattern for a thicker FeCoB (~10 Å) at zero field (e) and created bubbles smaller than 1 μm in diameter under the $\overrightarrow{H_Z}$ of +7 Oe. Particularly for part f, laser was swept over the film to increase the number of bubbles for visibility. Extracted from [146].

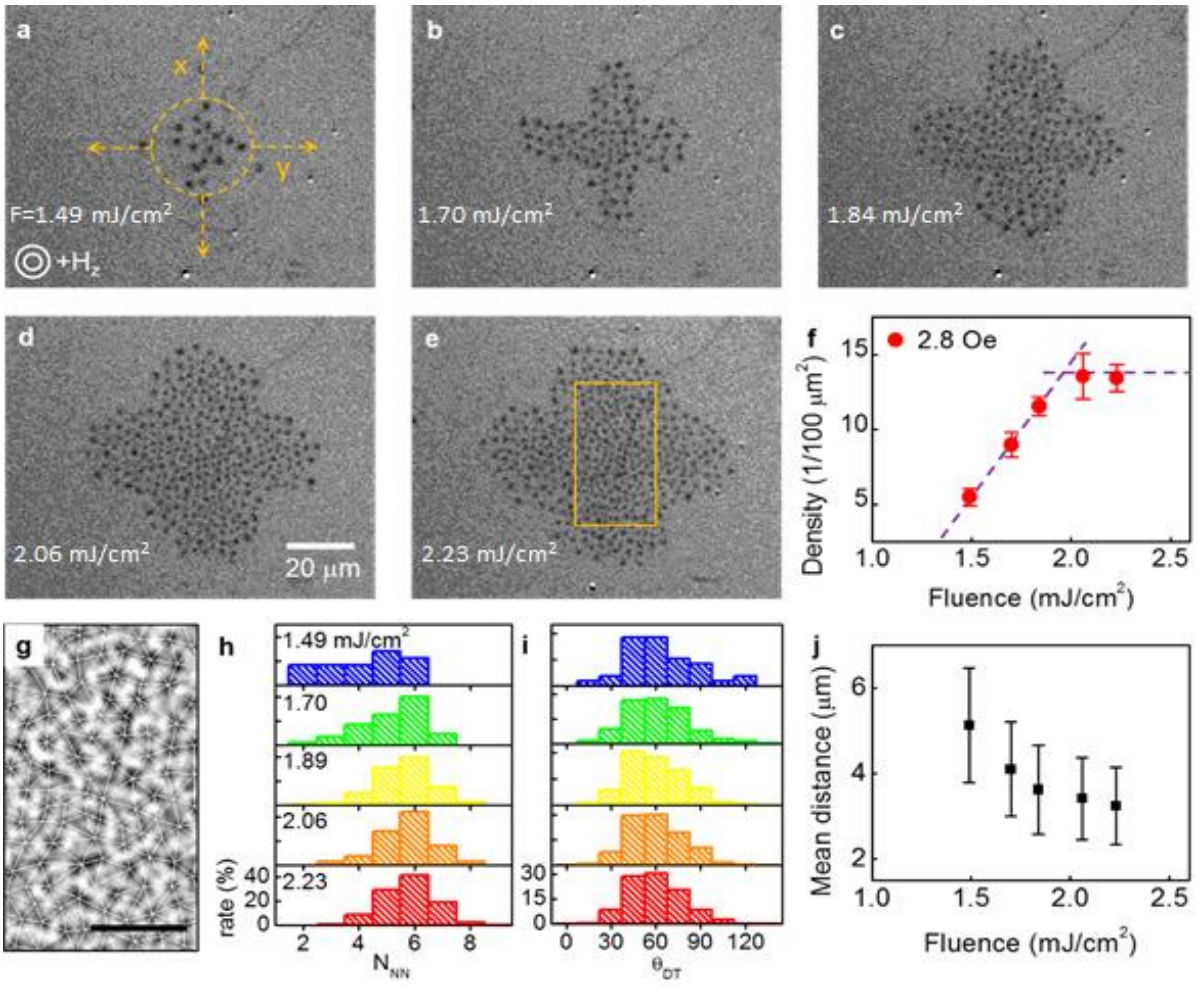

Figure IV.16: Laser fluence dependence of the bubble and bubble lattice creation. a-e. Magnetic images of ensemble of bubbles made by sweeping laser with laser fluences of 1.49 mJ/cm^2 (a), 1.70 mJ/cm^2 (b), 1.84 mJ/cm^2 (c), 2.06 mJ/cm^2 (d) and 2.23 mJ/cm^2 (e) in the presence of $\overrightarrow{H_Z}$ = +2.8 Oe. The orange rectangular marks the same area with (g). f. density of bubble with respect to the laser fluence. We set multiple squares of which lateral size is between 10 µm and 20 µm to sufficiently cover the bubble area and the bubbles in the squares are only counted. The dashed lines are guides to the eye. g. A typical example of Delaunay triangularization cropped from the rectangular in Fig. 3e. The scale bar is 10 µm. A band-pass filtering and mean filtering are used to enhance the magnetic contrast and thus to capture the centres of bubbles using a 2D Gaussian fit. h-i. The statistics of the nearest neighbour number N_{NN} and the angle of Delaunay triangles θ_{DT} obtained from Delaunay triangularization. Laser fluence increases from the top panel to the bottom panel. j. The mean distance between nearest bubbles as a function of laser fluence. Adapted from [146].

We analyse the density of bubbles in some specific regions as shown by the orange triangle on figure IV.16.e). The result is displayed on figure IV.16.f) as a function of the fluence. The density of bubbles increases with the laser fluence until it saturates around 2mJ/cm^2. By increasing the laser fluence the energy barrier that separates the ferromagnetic state to the bubble state can be overcome more easily and more bubbles are created. Furthermore bubbles exert a long distance dipolar interaction on each other [149] [150]. Thus the bubbles in the centre having more neighbours feel more repulsive forces

than the ones on the edge. This yields to a reduction of the radii of the central bubbles compared to the ones one the edge, as it can be observed on figure IV.16.e). For each of the studied fluences, we performed a Delauney triangularization on the images of the bubbles obtained by MOKE [48]. It consists in taking the center of each bubble as a node and to link the neighbours together. The resulting network is a Delauney network. An exemple of the resulting image of the Delauney triangularization on the bubble lattice is shown on figure IV.16.g). We extracted for each fluence the distribution of the neighbor number N_{NN} and the angle of the Delauney triangle θ_{DT} respectively on figures IV.16.h) and (i). We observe that, by increasing the laser fluence, the distributions are, for both N_{NN} and θ_{DT} respectively, centered on high peaks, at $N_{NN} = 6$ and $\theta_{DT} = 60°$ respectively. This means that the lattice formed by the bubbles is close to hexagonal.

IV.2.2.b) Repulsion of bubbles with laser exposure

A limit to the formation of a perfect hexagonal lattice in our material is the existence of local defects that pin the bubbles. The role of those pinning points is evidenced in the next experiment. We first generated bubbles at 3.1 Oe with the laser. Then, we decreased the laser fluence to bring enough energy to move the bubbles but not to generate new ones. We took a snapshot after each laser pulse. The resulting images obtained are shown on figure IV.17. On image (a) the full red circle marks the position of a bubble. On the image (b), taken after one laser pulse, this position is marked with a dashed red circle and we observe that the bubble has slightly moved from its previous position. After another light pulse, we mark a bubble on the image (c) taken with a full blue circle. On the image (d), taken after another supplementary laser pulse, this former position of the bubble is marked with a dashed blue circle and we observe that the bubble has slightly moved from its previous position. Two laser pulses later, on image (f), the full red circle marks the position of a bubble. On the image (g) taken after another supplementary laser pulse, this former position of the bubble is marked with a dashed red circle and we observe that the bubble has slightly moved from its previous position. On the same image (g), the full red yellow circle marks the position of a bubble. After another light pulse, we observe on figure (h) that two bubbles have been created from the single bubble (its location before the light pulse is marked with the yellow dashed circle).

We observe two different phenomenon after exposure of a bubble to a single light pulse: a single bubble moves slightly to its next equilibrium position until it stabilizes again (red, blue or pink circles) or two bubbles are created from one bubble and they move in opposite directions (yellow circle). Furthermore, it can be observed on the images that those phenomena always occur on the edge of the bubble lattice. We think that the bubbles are first pinned by local defect. Exposure to the laser brings enough heat for bubbles to be depinned. Because of the repulsion between bubbles they tend to move away from each other. The bubbles experiencing stronger dipolar repulsion are then in the edge of the bubble lattice and they furthermore do not meet another bubble when they move away from the center of the bubble lattice. Those bubbles are then pinned at another defect as seen on the images. The creation of pairs of bubbles is also a good clue of this phenomenon, because just afterwards, the two created bubbles move in opposite direction.

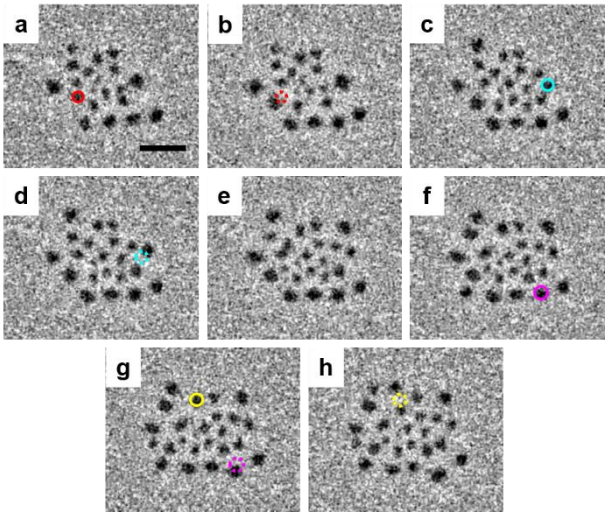

Figure IV.17: Repulsive bubble-bubble interaction. (a)-(h). Sequence of images taken after every single laser pulse. The circles with a dashed line indicate their previous positions labelled as circles with a solid line. The applied field $\overrightarrow{H_Z}$ is +2.8 Oe. The scale bar is 10 μm. Extracted from *[146]*.

IV.2.2.c) Retention of the bubbles generated by laser

The potential stability of skyrmions and bubbles is the feature that makes them appealing for the magnetism community. We studied the stability of our skyrmionic bubbles in the presence of out-of-plane magnetic fields. We know that each bubble in a lattice behaves differently to a single isolated bubble because of their mutual interactions. Thus, that may influence their stability, when exposed to an out-of-plane field. To study this lattice stability, we first generated a bubble lattice at 2.8 Oe, as we did on figure IV.16.e) by sweeping the laser on the sample in the ±x and ±y directions (figure IV.18.a)). We then turned off the magnetic field, resulting in a MOKE image shown on figure IV.18.b). We observed that the bubble domains remain stable and compact at the same location while labyrinthine domains form everywhere else on the sample. By applying now a field of -10 Oe we observe on figure IV.18.c), a Voronoi-like network (the space is divided into polygons). The application of a negative field tends to expand the bubbles, because it favors a ferromagnetic state through the Zeeman interaction. However the expansion of a single bubble is limited by the other bubbles next to it. This is due to the homochiral nature of the Néel domain walls of the bubbles, which is a topological protection [151]. For less packed bubbles, which are created at low laser fluence (figure IV.18.d)), the field stability seems to be weaker as seen from figures IV.18.d-f). This tends to show that when we apply an out-of-plane magnetic field, closely packed bubbles are more stable than isolated bubbles. In order to confirm our hypothesis, we conducted a more systematic and quantitative experiment. We first saturated the sample with a positive OOP field, and then applied a 2.8 Oe field called H_{ini}. We then swept the laser in the x and y directions, as we did on figure IV.16 for a chosen fluence. Depending on the fluence we used, we obtain a different initial number of bubbles that we call N_{ini}. We then applied a perturbation field H_{pert}. Then, we went back to H_{ini} and counted the number of remaining bubble N_{pert} due to the perturbation field applied before. This sequence was then repeated for higher amplitudes of H_{pert} until N_{pert} reaches 0, as seen on figure IV.18.g). Both positive and negative values

of perturbation fields were applied. The relevant indicator accounting for the level of stability for us is the retention ratio (RR) defined as $\mathrm{RR} = \frac{\mathrm{N_{pert}}}{\mathrm{N_{ini}}}$. We plotted RR as a function of H_{pert} for different values of H_{ini} on figure IV.18.h). We notice that for positive H_{pert} values, the retention ratio is independent of the initial number of bubbles. This consistent with the fact that the annihilation process of the bubbles at positive fields occurs by shrinking (a process in which the presence of other bubbles does not seem to play a role). For negative H_{pert}, we observe a N_{ini}-dependent evolution of RR. A higher initial number of bubbles (thus a more packed bubble lattice) results in a higher field stability of bubbles, as intuited before. We can furthermore note that the field needed to annihilate bubbles is bigger for negative field than for positive field because of the energy cost of annihilation of those homochiral Néel DWs.

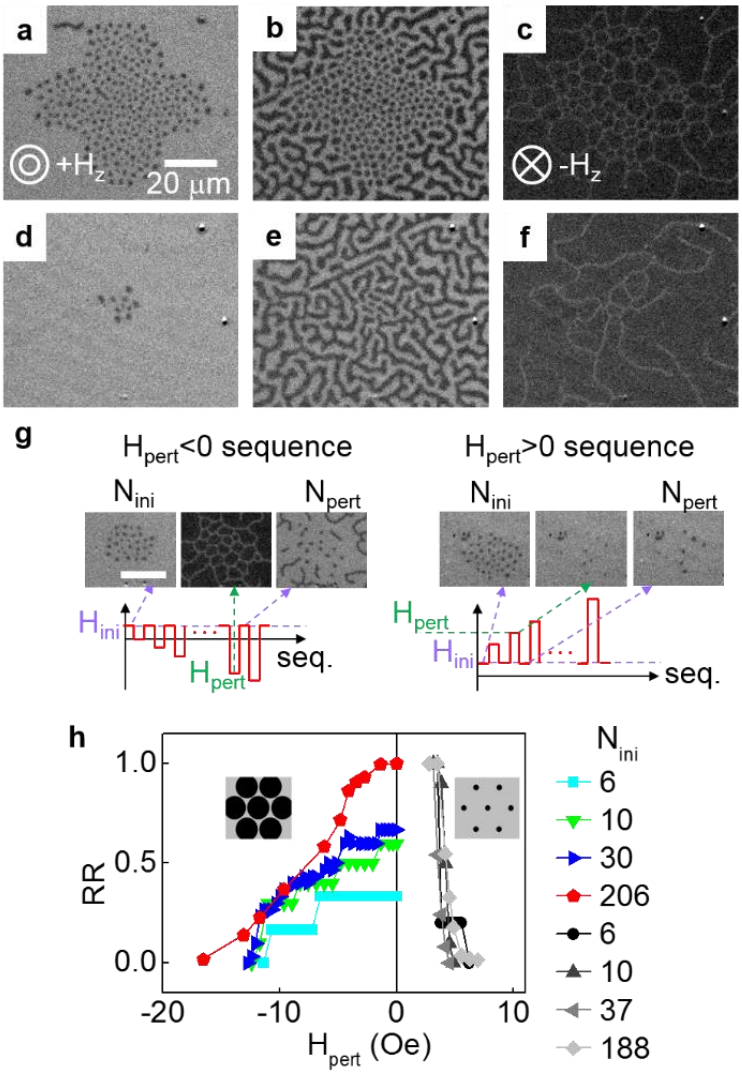

Figure IV.18: Response of ensembles of bubbles to the external magnetic field variation. (a)-(c): Change of magnetic domain morphology of a bubble lattice with respect to $\overrightarrow{H_Z}$. Initially, the bubble lattice is generated by laser pulses in the presence of $\overrightarrow{H_Z}$ of +2.8 Oe (a). Applied magnetic fields for (b) and (c) are 0 and +10 Oe, respectively. (d)-(f): Change of magnetic domain morphology of sparsely distributed bubbles with respect to $\overrightarrow{H_Z}$.The magnetic fields for (d), (e) and (f) are +2.8, 0 and +10 Oe, respectively. (g) Schematic representation of the sequence of the magnetic perturbation for the negative H_{pert} and positive H_{pert}. The scale bar is 10 µm. (h): Bubble retention ratio with respect to H_{pert}. The legend on the right shows N_{ini}. The insets illustrate the experimental situations for the negative (expansion) and positive (shrinking) H_{pert} sequences. Extracted from *[146]*.

IV.2.2.d) Erasing bubbles

An easy generation of the bubbles being a desirable feature, their easy annihilation is also wished. Indeed for a racetrack memory with skyrmions, the presence or absence of skyrmions is the information coded. Thus, writing the information consists in generating or erasing the skyrmions. The laser annihilation of bubbles is then an interesting idea. In order to test it, we first created a wide

skyrmion lattice area with an OOP field of 2.8 Oe by sweeping the laser with a fluence of 2mJ/cm^2 on the sample, as seen on figure IV.19.a). Then, we turned off the magnetic field and swept the laser on the sample on the y direction. For a better observation of the remaining bubbles, we applied once again a static OOP field of 2.8 Oe. The resulting image is shown on figure IV.19.b). We observe that there is no bubble lattice anymore where the laser has been swept, but there are labyrinthine domains instead. Where the laser has not been swept, the bubble lattice is still present. It seems to indicate that, with no applied field, the ground state is the one with stripes and the bubble state is a metastable state. This is coherent with the phase diagram obtained by Saratz *et al.* [147].

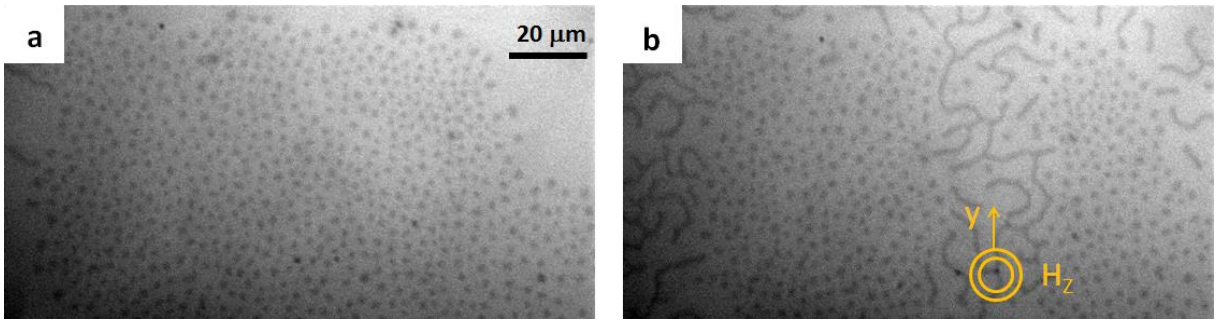

Figure IV.19: MOKE microscope image of the sample a) after laser sweeping at 2.8 Oe and b) after the field has been turned off, the laser has been swept along y and the field of 2.8 Oe has been put once again.

However the reader can notice that some bubbles still exist after being exposed to the laser. We can deduct from this that the bubble state is indeed a metastable state at zero magnetic field.

IV.2.3) Conclusion

In this part, we have seen that it is possible to generate skyrmionic bubbles using a femtosecond laser and a small static out-of-plane field. In this process, the helicity of the light does not play any role; this is a purely thermal process. When we increase the fluence of the light, we saturate the density of the bubbles and their size reaches a minimum. Those bubbles are then organized in a disordered hexagonal lattice and, interestingly, we have seen that skyrmions are more stable in a lattice than alone. We have also demonstrated that it is possible to erase the bubbles by sweeping the laser beam at zero field. Although previous studies on the generation of skyrmions with a laser exist [50]**, this has not been performed for skyrmions exhibiting a Néel wall contour. Our work provides a pathway through laser- induced generation of Néel skyrmions. We did not observe any minimum size threshold for the creation of those skyrmions. Thus it must be possible to generate stray-field Néel skyrmions of any size with the laser since they share the same energy profiles. Recently Caretta et al. reported on the creation of 20 nm DMI-skyrmions** [152]**. We can then ask ourselves if the generation of such quasi-particles is possible with light.**

Conclusion of chapter IV

In this chapter, we have been interested in the field-driven displacement of homochiral Néel walls in $[Co/Ni/Pt]_N$ multilayers and the generation of skyrmionic bubbles in a Ta/CoFeB/TaOx sample.

The first study starts from the surprising existence of a tilt angle of the direction of propagation of the domain walls with the in-plane applied field in $[Co/Ni/Pt]_N$ multilayers. We also observed a sudden change of direction of propagation at a non-zero field. This was hard to explain considering existing theories about domain wall propagation in the creep regime. We have performed a thorough study tuning different parameters. We observed the same evolution of propagation angle with the field for different magnetization at saturation M_S, different effective anisotropy constants K_{eff}, and different values of DMI constant D. However, we did not find a proper explanation of the phenomenon. Several ways can be explored to find a proper explanation. One way could be to image magnetic configuration of the domain walls using a Lorentz TEM or using micromagnetic simulation to find an appropriate set of parameters for the reproduction of our results.

We also studied the generation of Néel skyrmionic bubbles with light and a small out-of-plane film of $Ta/Co_{72}Fe_8B_{20}/TaOx$. We have seen that it does not depend on the helicity of the light. It is furthermore possible to create at high fluences a hexagonal lattice of bubbles and those are more stable than isolated bubbles. This is due to the natural protection of the homochiral Néel walls. We also showed that due to the repelling interaction between those bubbles it is possible to move a bubble with another. We can also erase those bubbles with the light at zero field. We did not observe any bottom limit on the size of the skyrmion for its creation with light. This lets us think that it would be possible to generate skyrmion of any size with the light.

General conclusion

My thesis was devoted to study experimentally known – as exchange bias- and new –as interfacial DMI- phenomena at different interfaces and their interplay with femtosecond pulse light or millisecond pulse magnetic field. In order to achieve that, I have grown on magnetron sputtering tools different magnetic nano-heterostructures.

This manuscript focuses on two disciplines of magnetism: femtomagnetism and spin-orbitronics. The first field consists in the study of the magnetization evolution at ultrashort time scales (typically the femtosecond timescale) and the second field focuses on phenomena or magnetic structures arising from the spin orbit interaction.

The manuscript is divided in four chapters. The aim of the first chapter is to introduce the basic notions for the comprehension of my whole work. In the second chapter, I present the set-ups and the experimental methods I used to elaborate the samples, characterize them magnetically and perform experiments of light-induced manipulation of the magnetization. My experimental results are described in chapters three and four. In the third chapter, we look into the interaction of heterostructures with circularly polarized light. In the fourth chapter we were interested in the propagation and generation of magnetic structures stabilized because of the Dzyaloshinskii Moriya interaction (DMI).

In the third chapter, the first heterostructures we looked into were ferromagnetic/antiferromagnetic (FM/AFM) bilayers, $[Pt/Co]_N$/IrMn exhibiting exchange bias. We have shown that it was possible to change the sign of the exchange bias field by modifying the helicity of the light, if the laser fluence is above the switching threshold of the $[Pt/Co]_N$ multilayer. First, we have characterized the coupling properties of our systems. We have then checked that laser can switch the magnetization of the ferromagnetic layer, even when the ferromagnetic layer is coupled to an antiferromagnetic layer. We have then shown that the final exchange bias field, after the use of the laser, is actually set by the exchange at the interface between the ferromagnetic and the antiferromagnetic layers. This modification of the exchange bias field can be a pulse cumulative process, if the laser fluence is above the switching threshold of the ferromagnetic layer. We have also evidenced that the reset of the exchange bias field via laser exposure could be used to nucleate domains at chosen areas and to control the direction of propagation. In general, the control of antiferromagnetic materials is interesting because there local magnetic moments are stable in time, due to the zero total moment. However, we only performed an indirect measurement of the interfacial magnetic configuration of the antiferromagnetic material but we do not know how it evolves in the bulk. Furthermore we did not evidence any effect of the helicity directly on the AFM layer. A perspective to do so could be to have a FM layer with a lower ordering temperature than the blocking temperature of the AFM.

In the second part of the third chapter, we studied the influence of pulses of circularly polarized light on different rare-earth free synthetic ferromagnetic materials. Those synthetic

ferrimagnetic materials are composed of two ferromagnetic layers antiferromagnetically coupled to each other through a Pt/Ru/Pt multilayer. We have been able to demonstrate all optical helicity dependent switching (AO-HDS), both for single ferromagnetic layers and synthetic ferromagnetic materials. We have noted that, in a synthetic ferromagnetic material, the two Curie temperatures of the two ferromagnetic layers must be distant enough for the all optical helicity dependent switching to be possible. We have been able to fulfill this criteria by working on [Pt/Co]/Pt/Ru/Pt/$[CoFeB/Pt]_2$ stacks with different thicknesses of CoFeB and Co. We have shown that the orientation of the magnetization of the ferromagnetic layer with the lower Curie temperature is imposed by the orientation of the magnetization of the ferromagnetic layer with the higher Curie temperature, due the exchange coupling between both ferromagnetic layers. We confirmed our hypothesis using micromagnetic simulations coupled to a 3 temperature model. In summary, the third chapter of the manuscript actually demonstrates the role of the ordering temperatures of two coupled magnetic layers in the all optical helicity dependent switching process. In both of the studied cases, a ferromagnet/ antiferromagnet bilayer and two ferromagnetic layers antiferromagnetically coupled to each other, the helicity of the light determines the orientation of the magnetization of the layer with the highest ordering temperature, while the orientation of the magnetization of the layer with the lower ordering temperature reorients during its cooling due the exchange coupling.

In the fourth chapter, we looked into magnetic structures exhibiting strong Dzyaloshinskii Moriya interaction. First, we were interested in the field-driven propagation of domain walls to measure the DMI constant [28] in the creep regime, when domain walls have a homochiral Néel nature [32] [144]. We performed this type of measurement on $[Co/Ni/Pt]_N$ multilayers and observed the existence of a tilt angle of the main propagation direction of the magnetic domains with the applied in-plane field. This tilt angle also evolves with the strength of the applied field. By varying the thicknesses of the different layers (Co, Pt, Ni) and the number of repeats, we obtained samples with various values of the materials parameters as saturation magnetization M_S or effective magnetic anisotropy constant K_{eff}. However, for the various set of parameters we explored, we did not observe any change in the evolution of the propagation angle with the amplitude of the in-plane field. Those results are surprising because they do not seem to fit in the existing theories of field-driven propagation of domain walls formulated, to our knowledge. It could then help to make emerge a more complete theory of the propagation of DMI stabilized structures.

We also studied in the second part of the fourth chapter another structure stabilized by DMI, skyrmionic bubbles. The sample in this study is a Ta (3nm)/$Co_{72}Fe_8B_{20}$(wedge)/TaOx(2nm, naturally oxidized). Applying only an out-of-plane field, it is not possible to observe those bubbles. We have shown that by applying a static out-of-plane field of only 3.1 Oe and sending only one pulse of the femtosecond laser we are able to generate those structures. We also observed that when increasing the fluence of the laser, we can create a hexagonal lattice of skyrmionic bubbles. We evidenced that such a lattice is more stable than a bubble alone. We observed some feature of those skyrmionic bubbles such as their reciprocal repulsion that can help them to be displaced or erased when we expose them to our laser with no applied field. Our light induced method of creation of skyrmionic bubbles is a good alternative way to the current induced method since it is potentially faster due to the shortness of a light pulse.

Conclusion générale

Durant ma thèse Cifre financée par Vinci Technologie, j'ai travaillé sur différentes hétérostructures magnétiques fabriquées dans enceintes de pulvérisation cathodique magnétron. J'ai tout particulièrement élaboré des systèmes présentant des propriétés de décalage d'échange dans une pulvérisation cathodique dessinée et mise au point en collaboration avec Vinci Technologie.

Ce manuscrit se concentre en fait sur deux disciplines du magnétisme: le femtomagnétisme et l'orbitronique de spin. La première discipline tient à l'étude de l'évolution de l'aimantation à des échelles de temps extrêmement courtes (typiquement à l'échelle de la femtoseconde) et la seconde discipline se concentre sur l'étude des phénomènes et structures magnétiques ayant pour origine le couplage spin-orbite.

Le manuscrit est divisé en quatre chapitres. Le but du premier chapitre est d'introduire les notions essentielles dont a besoin le lecteur pour une bonne compréhension du travail dans son ensemble. Dans le second chapitre je présente les instruments et méthodes expérimentales que j'ai utilisés pour élaborer les échantillons, les caractériser magnétiquement et effectuer sur ces derniers les expériences de manipulation de l'aimantation par impulsion laser femtoseconde polarisée. Dans ce manuscrit nos résultats expérimentaux sont divisés en deux chapitres (les troisième et quatrième chapitres), chacun d'entre eux divisés en deux sous-parties. Dans le troisième chapitre nous avons étudié l'interaction entre des hétérostructures magnétiques et la lumière polarisée circulairement. Dans le troisième chapitre nous nous sommes penchés sur la génération et le déplacement de structures magnétiques stabilisés grâce à l'interaction Dzyaloshinskii Moriya (DMI).

Dans le troisième chapitre la première hétérostructure que nous avons étudié est une bicouche ferromagnétique/antiferromagnétique, $[Pt/Co]_N$/IrMn présentant des effets de couplage d'échange. Nous avons montré qu'il est possible de changer le signe de champ d'échange en modifiant l'hélicité de la lumière dans le cas où la fluence du laser dépasse une valeur palier de renversement du $[Pt/Co]_N$. Dans un premier temps nous avons caractérisé les propriétés de couplage de nos systèmes. Nous avons ensuite vérifié que la couche ferromagnétique pouvait être retournée par le laser même lorsque qu'elle est couplée à une couche antiferromagnétique. Nous avons ensuite montré que le champ de décalage d'échange était donné par l'orientation de l'aimantation de la couche ferromagnétique après le passage du laser. Nous avons de plus montré que la modification du champ de décalage d'échange est un phénomène cumulatif avec le nombre d'impulsions laser si la fluence du laser est supérieur à une valeur seuil. Nous avons de plus montré que la possibilité de manipuler le décalage d'échange pourrait être utilisée pour contrôler la nucléation de domaines magnétiques à des endroits précis de l'échantillon et pour modifier leur direction de propagation. Lors de ces mesures nous avons donc pu modifier la configuration magnétique dans la couche antiferromagnétique à l'interface avec le ferromagnétique. Néanmoins, cette modification de l'orientation dans la couche antiferromagnétique ne semble pas être l'effet direct du laser mais être induite par la modification d'orientation de la

couche ferromagnétique via l'interaction d'échange. Pour vérifier ces conclusions il serait nécessaire de réaliser un système à décalage d'échange, dont la température de blocage de la couche antiferromagnétique est supérieure à la température de Curie de la couche ferromagnétique.

Dans la deuxième étude du troisième chapitre nous avons étudié l'influence d'impulsions de laser polarisé circulairement sur différents matériaux ferrimagnétiques de synthèse. Ces matériaux ferrimagnétiques de synthèse sont constitués de deux couches ferromagnétiques couplées antiferromagnétiquement par l'intermédiaire d'une couche de ruthénium. Nous avons pu montrer des phénomènes de retournement d'aimantation dépendant de l'hélicité pour les couches ferromagnétiques seules et pour les ferrimagnétique de synthèse. Nous avons constaté que les températures de Curie des deux couches ferromagnétiques doivent être assez éloignées pour le retournement tout-optique dépendant de l'hélicité soit possible (RTO-DH). Nous avons pu remplir un tel critère en travaillant avec un empilement de $[Pt/Co]/Pt/Ru/Pt/[CoFeB/Pt]_2$ en ajustant les épaisseurs respectives de CoFeB et de Co. Nous avons montré qu'après exposition au laser, l'orientation de la couche ferromagnétique dont la température de Curie est la plus faible est imposée par l'orientation de la couche ferromagnétique dont la température de Curie est la plus forte via le couplage d'échange. Nous avons confirmé cette hypothèse en utilisant des simulations micromagnétiques couplées à un modèle à 3 températures. En résumé le troisième chapitre de ce manuscrit démontre l'importance du rôle des températures d'ordre dans le retournement d'aimantation tout optique. Dans les deux cas étudiés, du couplage à l'interface ferromagnétique/antiferromagnétique et du couplage entre deux ferromagnétiques, l'hélicité du laser détermine l'orientation de la couche dont la température d'ordre est la plus grande tandis que l'orientation de la couche dont la température d'ordre est la plus petite s'oriente lors du refroidissement, par effet couplage.

Dans le quatrième chapitre nous avons étudié des structures magnétiques avec une forte interaction Dzyaloshinskii Moriya (DMI). Nous nous sommes d'abord penchés sur la propagation de parois de domaine induite par champ magnétique afin de mesurer la constante DMI [28] dans le régime de propagation visqueux quand les parois de domaine sont toutes de Néel et de même chiralité. Nous avons effectué ce type de mesure sur des multicouches de $[Co/Ni/Pt]_N$ et avons observé l'existence d'un angle non nul entre la principale direction de propagation des domaines magnétiques et celle du champ magnétique constant appliqué. La valeur de cet angle évolue avec l'intensité du champ magnétique statique appliqué dans le plan. En faisant varier les épaisseurs des différentes couches (Pt, Co, Ni) et le nombre de répétitions nous avons obtenu des échantillons avec différents paramètres de matériau tels M_S ou K. Cependant nous n'avons pas observé de changement dans l'évolution de cet angle avec le champ magnétique appliqué. Ces résultats sont surprenants car ils ne semblent pas être en accord avec les théories formulées sur la propagation de parois de domaines induite par champ magnétique. Cela peut donc aider à faire émerger un modèle plus complet décrivant la propagation de structures magnétiques stabilisées par DMI.

Dans la seconde partie du quatrième chapitre nous avons aussi étudié d'autres structures magnétiques stabilisées par DMI, les bulles skyrmioniques. L'échantillon que nous avons utilisé dans cette étude est un Ta (3nm)/$Co_{72}Fe_8B_{20}$/TaOx (2nm, oxydé naturellement). En appliquant seulement un champ magnétique perpendiculaire au plan de l'échantillon il n'est pas possible d'observer ce type de bulle. Nous avons montré qu'en appliquant un champ magnétique statique de seulement 3.1 Oe

et en envoyant simultanément une impulsion de laser femtoseconde, nous pouvons créer un réseau hexagonal de bulles skyrmioniques. Nous avons mis en évidence le fait aussi qu'un tel réseau est plus stable qu'une bulle seule. Nous avons aussi constaté quelques caractéristiques des bulles skyrmioniques comme leur répulsion réciproque qui permet de les déplacer ou de les effacer lorsqu'on les expose au laser sans appliquer de champ magnétique. Notre méthode de création des bulles skyrmioniques par laser est une bonne alternative à la génération par courant électrique puisque la génération par la lumière ne nécessite pas la présence de défaut pour être efficace.

Appendix

The purpose of this part is to give of information on the micromagnetic simulations performed in part III.2.3.c.

The magnetization dynamics induced by Laser pulses is studied micromagnetically by solving the Laudau-Lifshitz-Bloch eq. (LLB) coupled to the Three Temperature Model (3TM), which accounts for the space and temporal evolution of the electron, lattice and spin temperatures of the subsystems. Hereafter, we provide details of the evaluated samples, the Laser beam and the LLB & 3TM models. The micromagnetic results are given at the final part of this document.

Geometry and Laser properties

The system under study consists on a multilayer where two ferromagnetic (FM) layers are separated by a spacer, which generates an antiferromagnetic coupling between their local magnetizations. The Lower FM layer is on top of heavy metal (HM), and the upper FM is also under another similar HM layer. The geometry of the evaluated sample is shown in figure A.1. It is a cross with longitudinal (x-axis) and transverse (y-axis) branches. See all dimensions in the caption of figure A.1.

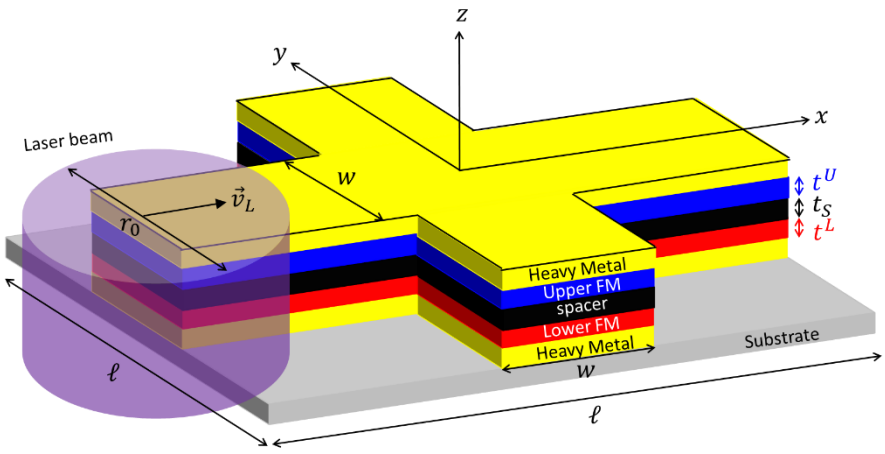

Figure A.I: Geometry of the studied multilayer with the representation of the laser beam (r_o is HWHM radius of the laser beam). The dimensions of the simulated sample are defined in the sketch: ℓ indicates the in-plane length of the computational region, w represents the width of the two orthogonal strips forming the cross, and t^L, t_S and t^U are the thicknesses of the Lower FM, the Spacer and the Upper FM strips respectively. The center of Laser beam is displaced from left to right along the longitudinal x-axis with a velocity $\vec{v}_L = v_L\vec{u}_x$, and its HWHM radius is $r_o = 2w$. The considered dimensions are: $\ell = 1536$ nm, $w = 192$ nm, $t^L = t_S = t^U = 0.8$ nm, and $v_L = 96$ m/s.

A Laser is sweeping from left to right along the longitudinal (x-axis) branch of the cross. The Laser spot is assumed to have a space Gaussian profile with a full width at half maximum (HWHM) defined by the radius r_0. Laser pulses are applied over the multilayer as the Laser is moving along the longitudinal branch of the cross. The temporal profile of these pulses is assumed to be Gaussian, with τ_L being its FWHM duration. Therefore, the power of the Laser is

$$P(\vec{r},t) = P_0 \exp\left[-\frac{r^2}{r_0^2/(4\ln 2)}\right] \exp\left[-\frac{(t-t_0)^2}{\tau_L^2/(4\ln 2)}\right] \quad \text{(A.1)}$$

where t_0 is the time at which the Laser power reaches its maximum power (P_0) in the center of the laser spot, or in other words, the central time of the Laser pulse. As the Laser is moving from left to right with a constant velocity ($\vec{v}_L = v_L \vec{u}_x$), each Laser pulse is applied at different locations $\vec{r}(t)$ along the longitudinal axis of the sample, $\vec{r}(t) = v_L t\, \vec{u}_x$. The center of the Laser spot is always focused at the center of the multilayer in the transverse axis (*i.e.* $y = 0$). The maximum power of the laser is $P_0 = F/(t_t \tau_L)$, where F is the laser fluence, and t_t is the total thickness of the multilayer (i.e. $t_t = t^L + t_S + t^U$).

Magnetization dynamics: Laudau-Lifshitz-Bloch eq. (LLB)

The evaluation of the local magnetization under these Laser pulses is described by the Laudau-Lifshitz-Bloch eq. (LLB). For simplicity, in what follows, we use $\vec{m}$ to denote the local magnetization in each of the two FM layers ($\vec{m}$ represents the local magnetization in the Lower FM layer $\vec{m} = \vec{m}^L$, and in the Upper FM layer $\vec{m} = \vec{m}^U$). Note that in general, both Lower and Upper FM layers have different magnetic properties. With this simplification in the notation, the optically-induced magnetization dynamics in each FM is described by the corresponding Laudau-Lifshitz-Bloch eq. (LLB), which is given by

$$\frac{d\vec{m}(\vec{r},t)}{dt} = -\gamma_0' \vec{m} \times \vec{H}_{eff} - \gamma_0 \frac{\alpha_\perp}{m^2}\left[\vec{m} \times \left(\vec{m} \times \left(\vec{H}_{eff} + \vec{H}_{th}^{\perp}\right)\right)\right] + \gamma_0' \frac{\alpha_\parallel}{m^2}\left(\vec{m} \cdot \vec{H}_{eff}\right)\vec{m} + \vec{H}_{th}^{\parallel} \quad \text{(A.2)}$$

where $\vec{m}(\vec{r},t) = \vec{M}(\vec{r},t)/M_s^0$ is the normalized magnetization with M_s^0 the saturation magnetization at $T = 0$, and $m = m(T) \equiv |\vec{m}|$. $\gamma_0' = \gamma_0/(1+\alpha^2)$ with γ_0 being the gyromagnetic ration and α is the Gilbert damping. $\alpha_\parallel$ and $\alpha_\perp$ are the longitudinal and transverse damping parameters given by:

$$\alpha_\parallel = \alpha\left(\frac{2T}{3T_C}\right)$$

$$\alpha_\perp = \alpha\left(1 - \frac{T}{3T_C}\right) \quad \text{(A.3)}$$

where T_C is the Curie temperature. Note that Eq. (A.2) is fully solved for the Lower and Upper FM layers. The effective field $\vec{H}_{eff}$ includes all the conventional interactions of the micromagnetic theoretical framework, and the magneto-optical field due to the Inverse Faraday Effect (IFE).

$$\vec{H}_{eff} = \vec{H}_{exch} + \vec{H}_{DM} + \vec{H}_{dmg} + \vec{H}_{ani} + \vec{H}_{int} + \vec{H}_m + \vec{H}_{MO} \quad \text{(A.4)}$$

where $\vec{H}_{exch}$ is the exchange contribution, $\vec{H}_{DM}$ is the DMI interaction, $\vec{H}_{dmg}$ is the demagnetizing field, and $\vec{H}_{ani}$ is the magnetic anisotropy. The interlayer exchange coupling ($\vec{H}_{int}$) is also considered. $\vec{H}_m$ represents the internal exchange field in the LLB eq, which is given by,

$$\vec{H}_m = \begin{cases} \frac{1}{2\chi_\parallel}\left(1-\frac{m^2}{m_e^2}\right)\vec{m}, & T < T_C \\ -\frac{1}{\chi_\parallel}\left(1+\frac{3}{5}\frac{T_C m^2}{(T-T_C)}\right)\vec{m}, & T > T_C \end{cases} \quad \text{(A.5)}$$

where $\chi_\parallel$ is the longitudinal susceptibility,

$$\chi_\parallel = \frac{\partial m_e}{\partial H_{ext}}\Big)_{H_{ext}\to 0} \quad \text{(A.6)}$$

where $m_e = m_e(T)$ is the equilibrium value of $m = m(T)$. Note that at a given instant of time, the local magnetization is not in general in thermal equilibrium. The LLB eq. can evaluate this non-equilibrium physics.

The magneto-optical field ($\vec{B}_{MO}(\vec{r},t) = \mu_0 \vec{H}_{MO}(\vec{r},t)$) is the local effective field due to the circular polarization of the Laser beam. This out-of-plane field ($\vec{H}_{MO}$) emerges as consequence of the Inverse Faraday Effect (IFE), and it can be expressed as

$$\vec{B}_{MO}(\vec{r},t) = (\sigma^{\pm})\, F\, \chi_{IFE}\, f_{MO}(\vec{r},t)\vec{u}_z \quad \text{(A.7)}$$

where $\sigma^{\pm} = \pm 1$ is the Laser helicity, and F (in $[(\mathrm{J/m^2})]$) is the Laser fluence and χ_{IFE} (in $[\mathrm{T/(J/m^2)}]$) is the inverse Faraday effect susceptibility. Therefore, the maximum value of the magneto-optical field ($B_{max} = F\, \chi_{IFE}$) is reached when the laser power reaches its maximum value, at the center of the laser beam. The space-temporal dependence of the magneto-optical field is described by the function $f_{MO}(\vec{r},t)$

$$f_{MO}(\vec{r},t) = \begin{cases} \exp\left[-\frac{r^2}{r_0^2/(4\ln 2)}\right]\exp\left[-\frac{(t-t_0)^2}{\tau_L^2/(4\ln 2)}\right], & t < t_0 \\ \exp\left[-\frac{r^2}{r_0^2/(4\ln 2)}\right]\exp\left[-\frac{(t-t_0)^2}{(\tau_L+\tau_d)^2/(4\ln 2)}\right], & t > t_0 \end{cases} \quad \text{(A.8)}$$

where $r = \sqrt{x^2+y^2}$ is the distance from the center of the laser spot to the center of the device, and t_0 represents the time at which the Laser pulse reaches its maximum power. τ_d represents the delay of the magneto-optical field with respect to the Laser pulse, and in agreement with several experimental observations, it accounts for some persistence of the magnetic field due to the optical signal. The temporal evolution of the normalized magneto-optical field (B_{MO}/B_{max}) and the normalized laser power (P/P_{max} where $P_{max} \equiv P_0$) at the center of the laser beam are both shown in

Fig. S5.2, where the laser pulse duration is $\tau_L = 200$ fs, and the delay of the magneto-optical field is $\tau_d = \tau_L$ (here σ^+). The fluence considered here is $F = 6\,\mathrm{J/m^2}$. Note that the space dependence of the magneto-optical field is the same as the Laser power, *i.e.* the magneto-optical field is Gaussian with a full width at half maximum (FWHM) defined by the radius r_0.

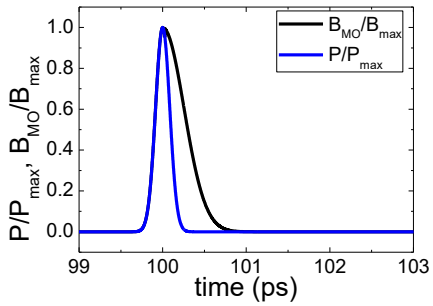

Figure A.2: Laser beam and magneto-optical field properties. Temporal evolution of the normalized magneto-optical field (B_{MO}/B_{max}) and the normalized laser power (P/P_{max} where $P_{max} \equiv P_0$) at the center of the laser beam. The laser pulse is $\tau_L = 200$ fs, and the delay of the magneto-optical field is $\tau_d = \tau_L$ (with σ^+). The fluence considered here is $F = 6\,\mathrm{J/m^2}$.

The LLB eq. also includes stochastic terms $\vec{H}_{th}^{\perp}$ and $\vec{H}_{th}^{\parallel}$ to account for stochastic fluctuations due to the thermal noise. The first one ($\vec{H}_{th}^{\perp}$) is a random thermal field orthogonal to the local magnetization, whereas the second one ($\vec{H}_{th}^{\parallel}$) describes the longitudinal noise, parallel to the local magnetization. Their statistical properties are summarized by:

$$\langle H_i^{\perp}(t)\rangle = 0 \tag{A.9}$$

$$\langle H_i^{\perp}(\vec{r},t)H_j^{\perp}(\vec{r}',t')\rangle = \frac{2K_B T(\alpha_{\perp}-\alpha_{\parallel})}{\gamma_0' M_s^0 V \alpha_{\perp}^2}\delta_{ij}\delta(t-t')\delta(\vec{r}-\vec{r}') \tag{A.10}$$

$$\langle H_i^{\parallel}(t)\rangle = 0 \tag{A.11}$$

$$\langle H_i^{\parallel}(\vec{r},t)H_j^{\parallel}(\vec{r}',t')\rangle = \frac{2\gamma_0' T\alpha_{\parallel}}{M_s^0 V \alpha_{\perp}^2}\delta_{ij}\delta(t-t')\delta(\vec{r}-\vec{r}') \tag{A.12}$$

$$\langle H_i^{\perp}(\vec{r},t)H_j^{\parallel}(\vec{r}',t')\rangle = 0 \tag{A.13}$$

In these expressions, the notation $\langle\cdots\rangle$ indicates the average over different stochastic realizations of the noise. K_B is the Boltzmann constant and V is the volume of the computational cell.

Disorder: In order to take into account the effects of disorder due to imperfections and defects in a realistic way, we assume that the easy axis anisotropy direction ($\vec{u}_K = \vec{u}_K(\vec{r}_G)$) is distributed among a length scale defined by a grain size. The average size of the grains is $10\ \mathrm{nm}$. Despite the fact that the direction of the uniaxial anisotropy of each grain is mainly directed along the perpendicular direction (z-axis), a small in-plane component lower than 5% is randomly generated over the grains. Although other ways to account for imperfections could be adopted, we selected this one based on previous studies, which properly describe other experimental observations.

Magnetic parameters: The magnetic parameters considered in the study are typical of Pt/Co multilayers. For simplicity, we assume that the exchange stiffness parameter ($A_{ex} = 1.5 \times 10^{-11}\mathrm{J/m}$), the perpendicular magnetic anisotropy constant ($K_u = 1.25 \times 10^6\ \mathrm{J/m^3}$), and the Gilbert damping ($\alpha = 0.5$) are common parameters for the Lower and the Upper FM layers. The saturation magnetization (M_S^L, M_S^U) and the Curie temperature (T_C^L, T_C^U) are in general different for the Lower and the Upper FM layers. These parameters are similar to the experimental ones. The DMI parameters are $D^L = +1.25\ \mathrm{mJ/m^2}$ and $D^U = -1.25\ \mathrm{mJ/m^2}$, and the interlayer exchange constant is $J^{ex} = -0.35\ \mathrm{mJ/m^2}$. The magneto-optical field induced by the Laser pulses is assumed the same in both layers, with $F\chi_{IFE} = 5\ \mathrm{T}$.

Temperature dynamics: Three Temperature Model (3TM)

The temperature evolution in the system under the action of the laser pulses can be described in terms of three subsystems involving the electron (T_e), the lattice (T_l) and the spin ($T_s \equiv T$) temperatures. Note that the relevant temperature for the magnetic system described by previously introduced LLB eq. is the spin temperature, $T_s(\vec{r},t) \equiv T(\vec{r},t)$, but this one depends on the temperature of the electron ($T_e(\vec{r},t)$) and the lattice ($T_l(\vec{r},t)$) subsystems, as given by the following coupled set of differential equations:

$$\begin{cases} C_e \frac{\partial T_e}{\partial t} = -k_e \nabla^2 T_e - g_{el}(T_e - T_l) - g_{es}(T_e - T_s) + P(\vec{r},t) \\ C_l \frac{\partial T_l}{\partial t} = -k_l \nabla^2 T_l - g_{el}(T_l - T_e) - g_{ls}(T_l - T_s) \\ C_s \frac{\partial T_s}{\partial t} = -k_s \nabla^2 T_s - g_{es}(T_s - T_e) - g_{ls}(T_s - T_l) \end{cases} \quad \text{(A.14)}$$

where C_i is the thermal capacity (in $[\mathrm{J/(m^3K)}]$) and k_i is the thermal conductivity (in $[\mathrm{W/(m \cdot K)}]$) of each system (i: e, l, s). g_{ij} are the coupling constants between subsystems (in $[\mathrm{W/K}]$) and $P(\vec{r},t)$ is the Laser power. Note that above Debye temperature, C_l and C_s can be considered as constant parameters, whereas, C_e is linear with the electron's temperature, $C_e = \gamma_e T_e$ where $\gamma_e = \frac{C_e(300\ \mathrm{K})}{300\ \mathrm{K}}$. The influence of the substrate can be also taken into account by adding an additional Newton-like term to the right hand side of the second one of these equations ($-(T - T_{sub})/\tau_{sub}$), where T_{sub} is the substrate temperature, and the τ_{sub} is a characteristic time which describes the heat transport to the substrate and the surrounding.

Thermal parameters: The typical thermal parameters found the literature were considered in the present micromagnetic analysis: $C_e(300\ \mathrm{K}) = \gamma_e T_e = 2.8 \times 10^5\ \mathrm{J/(m^3K)}$ at $T_e = 300\ \mathrm{K}$, $C_l = 2.8 \times 10^5\ \mathrm{J/(m^3K)}$, $C_s = 2.8 \times 10^5\ \mathrm{J/(m^3K)}$, $k_e = 91\ \mathrm{W/(m^3 \cdot K)}$, $k_l = k_s = 0$, $g_{ij} = 1.5 \times 10^{18}\ \mathrm{W/m^3}$, $T_{sub} = 300\ \mathrm{K}$, and $\tau_{sub} = 0.09\ \mathrm{ns}$.

By solving the 3TM eqs. with these typical parameters found in the literature, it is easy to see that under the application of a short laser pulse with ~ 100 fs, the 3TM eqs. predict an abrupt increase of the electron (T_e) and spin (T_s) temperatures followed by a decrease or relaxation towards room temperature. See an example of this temperature dynamics in figure A.3 for $\tau_L = 200$ fs. The lattice temperature (T_l) increases more slowly. After the Laser pulse, the three temperatures evolves to the same terminal value with a characteristic time of a few ~ 1 ps. Note also that in these time scale, the diffusive terms ($\nabla^2 T_i$) are negligible, and they only become important at the ns scale, when the substrate influence is also important.

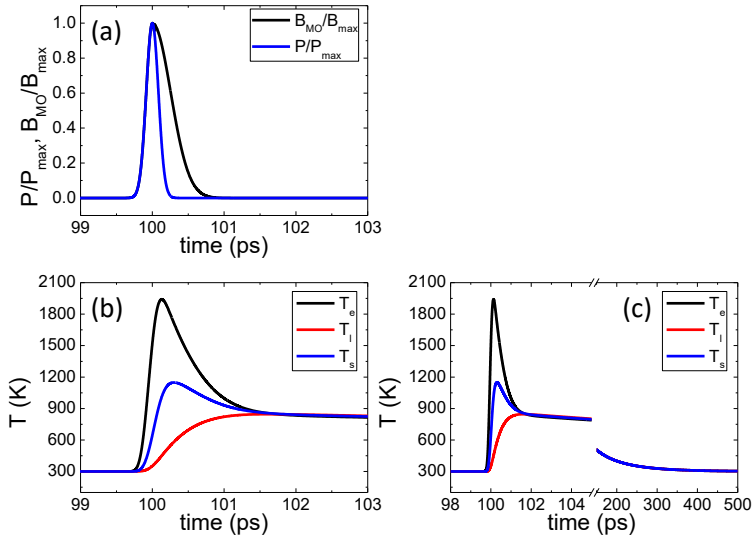

Figure A.3: Temporal evolution of the temperatures of the three subsystems (electrons, lattice and spins) in the center of the Laser beam as obtained from the 3TM. (a) Temporal evolution of the normalized magneto-optical field (B_{MO}/B_{max}) and the normalized laser power (P/P_{max} where $P_{max} \equiv P_0$) at the center of the laser beam. The laser pulse is $\tau_L = 200$ fs, and the delay of the magneto-optical field is $\tau_d = \tau_L$ (with σ^+). (b) Temporal evolution of the temperature of the three subsystems: electrons (T_e), lattice (T_l) and spins (T_s). These temperatures are evaluated at the center of the laser beam. (c) Same as in (b) with indication of the relaxation of the three temperatures towards room value for longer times. The fluence considered here is $F = 6\ \mathrm{J/m^2}$.

Numerical details: The FM layers and the spacer were discretized using a 3D finite difference scheme. The in-plane side of the computational cells is $\Delta x = \Delta y = 3\ \mathrm{nm}$, whereas the size of the computational cell in the perpendicular direction is $\Delta z = 0.8\ \mathrm{nm}$, which coincides with the thickness of the FM layers

and the spacer. The dimensions of the cross hall are given in Fig. 1. The center of the laser beam is displaced from the left to the right along the longitudinal x-axis with a velocity $v_L = 96\ \mathrm{nm/ns}$. A laser pulse is applied every $1\ \mathrm{ns}$, and therefore, 18 laser pulses are applied to cover the longtidinal axis of the cross, from left ($x = -768\ \mathrm{nm}$) to right ($x = +768\ \mathrm{nm}$). Micromagnetic simulations were performed with an adaptive time step: during each laser pulse, which is $\tau_L = 200\ \mathrm{fs}$ long, the time step is $\Delta t = 1\ \mathrm{fs}$. Once each laser pulse is turned off, the time step was enlarged to $\Delta t = 25\ \mathrm{fs}$ to speed up the computations. The delay of the magneto-optical field with respect to the laser pulse is $\tau_{MO} = 2\tau_L$. Several tests were performed with reduced cell sizes and time steps to assess the numerical validity of the presented results.

Bibliography

[1] M. Baibich, J. Broto, A. Fert, F. Nguyen Van Dau, F. Petroff, P. Etienne, G. Creuzet, A. Friederich and J. Chazelas, "Giant Magnetoresistance of (001)Fe/(001)Cr Magnetic Superlattices," *Physical review letters,* 1988.

[2] P. Garcia, "Perpendicular magnetic anisotropy in Pd/Co and Pt/Co thin-film layered structures," *Journal of applied physics,* vol. 63, no. 5066, 1988.

[3] E. Beaurepaire, J.-C. Merle, A. Daunois and J.-Y. Bigot, "Ultrafast Spin Dynamics in Ferromagnetic Nickel," *Physical Review Letters,* vol. 76, no. 22, 1996.

[4] C. Stanciu, F. Hansteen, A. Kimel, A. Kirilyuk, A. Tsukamoto, A. Itoh and T. Rasing, "All-Optical Magnetic Recording with Circularly Polarized Light," *Physical Review Letters,* vol. 99, no. 047601, 2007.

[5] S. Alebrand, M. Gottwald, M. Hehn, D. Steil., M. Cinchetti, D. Lacour, E. Fullerton, M. Aeschlimann and S. Mangin, "Light-induced magnetization reversal of high-anisotropy TbCo alloy films," *Applied Physics Letters,* vol. 101, no. 162408, 2012.

[6] S. Mangin, M. Gottwald, C.-H. Lambert, D. Steil, V. Uhlíř, L. Pang, M. Hehn, S. Alebrand, M. Cinchetti, G. Malinowski, Y. Fainman, M. Aeschlimann and E. Fullerton, "Engineered materials for all-optical helicity-dependent magnetic switching," *nature materials,* vol. 13, pp. 286-292, 2014.

[7] C.-H. Lambert, S. Mangin, B. Varaprasad, Y. Takahashi, M. Hehn, M. Cinchetti, G. Malinowski, K. Hono, Y. Fainman, M. Aeschlimann and E. Fullerton, "All-optical control of ferromagnetic thin films and nanostructures," *Science,* vol. 345, no. 6202, pp. 1337-1340, 2014.

[8] S. Parkin, M. Hayashi and L. Thomas, "Magnetic Domain-Wall Racetrack Memory," *Science,* vol. 320, no. 5873, 2008.

[9] I. Dzyaloshinsky, "A thermodynamic theory of "weak" ferromagnetism of antiferromagnetics," *J. Phys. Chem. Solids,* vol. 4, pp. 241-255, 1957.

[10] T. Moriya, "New mechanism of anisotropic superexchange interaction," *Physical review letters,* vol. 4, no. 5, 1960.

[11] F. Büttner, I. Lemesh and G. Beach, "Theory of isolated magnetic skyrmions: From fundamentals to room temperature applications," *Scientific Reports,* vol. 8, no. 4464, 2018.

[12] G. Daalderop, P. Kelly and F. den Broeder, "Prediction and Confirmation of Perpendicular Magnetic Anisotropy in Co/Ni Multilayers," *Physical Review Letters,* vol. 68, no. 5, 1992.

[13] J. Coey, "Magnetism and magnetic materials".

[14] B. Cullity and C. Graham, "Introduction to magnetic materials," 2009.

[15] L. Néel, "Anisotropie magnétique superficielle et structures d'orientation," *Le journal de physique et le Radium,* vol. 15, no. 4, 1954.

[16] A. Fert and P. M. Levy, "Role of Anisotropic Exchange Interactions in Determining the Properties of Spin-Glasses," *Physical review letters,* vol. 44, no. 23, 1980.

[17] A. Fert, *Mater. Sci. Forum,* Vols. 59-60, pp. 439-480, 1990.

[18] A. Fert, V. Cros and J. Sampaio, "Skyrmions on the track," *nature nanotechnology,* vol. 8, pp. 152-156, 2013.

[19] B. Dupé, M. Hoffman, C. Paillard and S. Heinze, "Tailoring magnetic skyrmions in ultra-thin transition metal films," *nature communications,* vol. 5, no. 4030, 2014.

[20] A. Hrabec, N. Porter, A. Wells, M. Benitez, G. Burnell, S. McVitie, D. McGrouther, T. Moore and C. Marrows, "Measuring and tailoring the Dzyaloshinskii-Moriya interaction in perpendicularly magnetized thin films," *Physical review B,* vol. 90, no. 020402(R), 2014.

[21] M. EL Hadri, P. Pirro, C.-H. Lambert, S. Petit-Watelot, Y. Quessab, M. Hehn, F. Montaigne, G. Malinowski and S. Mangin, "Two types of all-optical magnetization switching mechanisms using femtosecond laser pulses," *Physical review B,* vol. 94, no. 064412, 2016.

[22] K. Fukumoto, "Ph.D thesis," *Freien Universitat Berlin,* 2005.

[23] A. Thiaville, S. Rohart, E. Jué, V. Cros and A. Fert, "Dynamics of Dzyaloshinskii domain walls in ultrathin magnetic films," *EPL,* vol. 100, no. 57002, 2012.

[24] G. Chen, T. Ma, A. N'Diaye, H. Kwon, C. Won, Y. Wu and A. Schmid, "Tailoring the chirality of magnetic domain walls by interface engineering," *nature communications,* vol. 4, no. 2671, 2013.

[25] S. Lemerle, J. Ferré, C. Chappert, V. Mathet, T. Giamarchi and P. Le Doussal, "Domain Wall Creep in an Ising Ultrathin Magnetic Film," *Physical review letters,* vol. 80, no. 4, 1998.

[26] P. Chauve, T. Giamarchi and P. Le Doussal, "Creep and depinning in disordered media," vol. 62, no. 10, 2000.

[27] P. Metaxas, J. Jamet, A. Mougin, M. Cormier, J. Ferré, V. Baltz, B. Rodmacq, B. Dieny and R. Stamps, "Creep and Flow Regimes of Magnetic Domain-Wall Motion in Ultrathin Pt/Co/Pt Films with Perpendicular Anisotropy," *Physical review letters,* vol. 99, no. 217208, 2007.

[28] S.-G. Je, D.-H. Kim, S.-C. Yoo, B.-C. Min, K.-J. Lee and S.-B. Choe, "Asymmetric magnetic domain-wall motion by the Dzyaloshinskii-Moriya interaction," *Physical Review B,* vol. 88, 2013.

[29] S. DuttaGupta, S. Fukami, B. Kuerbanjiang, H. Sato, F. Matsukura, V. Lazarov and H. Ohno, "Magnetic domain-wall creep driven by field and current in Ta/CoFeB/MgO," *AIP Advances,* vol. 7, no. 055918, 2017.

[30] A. Hrabec, J. Sampaio, M. Belmeguenai, I. Gross, R. Weil, S. M. Chérif, A. Stahkevich, V. Jacques, A. Thiaville and S. Rohart, "Current-induced skyrmion generation and dynamics in symmetric bilayers," *nature communications,* vol. 8, p. 15765, 2017.

[31] A. Balk, K.-W. Kim, D. Pierce, M. Stiles, J. Unguris and S. Stavis, "Simultaneous control of the Dzyaloshinskii-Moriya interaction and magnetic anisotropy in nanomagnetic trilayers," *Physical review letters,* vol. 119, no. 077205, 2017.

[32] R. Lavrijsen, D. Hartmann, A. van den Brink, Y. Yin, B. Barcones, R. Duine, M. Verheijen, H. Swagten and B. Koopmans, "Asymmetric magnetic bubble expansion under in-plane field in Pt/Co/Pt: Effect of interface engineering," *Physical review B,* vol. 91, no. 104414, 2015.

[33] E. Jué, C. Safeer, M. Drouard, A. Lopez, P. Balint, L. Buda-Prejbeanu, O. Boulle, S. Auffret, A. Schuhl, A. Manchon, I. Miron and G. Gaudin, "Chiral damping of magnetic domain walls," *nature materials,* vol. 15, pp. 272-277, 2015.

[34] T. Skyrme, "A unified theory of mesons and baryons," *Nucelar Physics,* vol. 31, pp. 556-569, 1962.

[35] Y. Tchoe and H. J.H., "Skyrmion generation by current," vol. 85, no. 174416, 2012.

[36] Y. H.Y. and W. X.R., "Skyrmion Creation and Manipulation by Nano-Second Current Pulses," *Scientific reports,* vol. 6, no. 22638, 2016.

[37] F. Büttner, I. Lemesh, M. Schneider, B. Pfau, C. Günther, P. Hessing, J. Geilhufe, L. Caretta, D. Engel, B. Krüger, J. Viefhaus, S. Eisebitt and G. Beach, "Field-free deterministic ultrafast creation of magnetic skyrmions by spin–orbit torques," *nature nanotechnology,* vol. 12, pp. 1040-1044, 2017.

[38] D. Maccariello, W. Legrand, N. Reyren, K. Garcia, K. Bouzehouane, S. Collin, V. Cros and A. Fert, "Electrical detection of single magnetic skyrmions in metallic multilayers at room temperature," *nature nanotechnology,* vol. 13, pp. 233-237, 2018.

[39] W. Legrand, D. Maccariello, N. Reyren, K. Garcia, C. Moutafis, C. Moreau-Luchaire, S. Collin, K. Bouzehouane, V. Cros and A. Fert, "Room-Temperature Current-Induced Generation and Motion of sub-100 nm Skyrmionq," *Nanoletters,* vol. 17, pp. 2703-2712, 2017.

[40] K. Everschor, "Current-Induced Dynamics of Chiral Magnetic Structures : Skyrmions, Emergent Electrodynamics and Spin- Transfer Torques," *PhD thesis,* 2012.

[41] S. Mühlbauer, B. Binz, F. Jonietz, C. Pfleiderer, A. Rosch, A. Neubauer, R. Georgii and P. Böni, "Skyrmion Lattice in a Chiral Magnet," *Science,* vol. 323, no. 5916, pp. 915-919, 2009.

[42] A. Neubauer, C. Pfleiderer, B. Binz, A. Rosch, R. Ritz, P. G. Niklowitz and P. Böni, "Topological Hall Effect in the A Phase of MnSi," *Physical Review Letters,* vol. 102, p. 186602, 2009.

[43] C. Pappas, E. Lelièvre-Berna, P. Falus, P. M. Bentley, E. Moskvin, S. Grigoriev, P. Fouquet and B. Farago, "Chiral Paramagnetic Skyrmion-like Phase in MnSi," *Physical Review Letters,* vol. 102, p. 197202, 2009.

[44] S. Heinze, K. von Bergmann, M. Menzel, J. Brede, A. Kubetzka, R. Wiesendanger, G. Bihlmayer and S. Blügel, "Spontaneous atomic-scale magnetic skyrmion lattice in two dimensions," *nature physics,* vol. 7, pp. 713-718, 2011.

[45] G. Chen, A. Mascaraque, A. T. N'Diaye and A. K. Schmid, "Room temperature skyrmion ground state stabilized through interlayer exchange," *Appl. Phys. Lett,* vol. 106, p. 242404, 2015.

[46] S. Woo, K. Litzius, B. Krüger, M.-Y. Im, L. Caretta, K. Richter, M. Mann, A. Krone, R. M. Reeve, M. Weigand, P. Agrawal, I. Lemesh, M.-A. Mawass, P. Fischer, M. Kläui and G. S. Beach, "Observation of room-temperature magnetic skyrmions and their current-driven dynamics in ultrathin metallic ferromagnets," *nature materials,* vol. 15, pp. 501-505, 2016.

[47] O. Boulle, J. Vogel, H. Yang, S. Pizzini, D. de Souza Chaves, A. Locatelli, T. Onur Mentes, A. Sala, L. D. Buda-Prejbeanu, O. Klein, M. Belmeguenai, Y. Roussigné, A. Stashkevich, S. Mourad Chérif, L. Aballe, M. Foerster, M. Chshiev, S. Auffret, I. Mihai Miron and G. Gaudin, "Room-temperature chiral magnetic skyrmions in ultrathin magnetic nanostructures," *nature nanotechnology,* vol. 11, pp. 449-454, 2016.

[48] A. Soumyanarayanan, M. Raju, A. L. Gonzales Oyarce, A. K. Tan, M.-Y. Im, A. P. Petrovic, P. Ho, K. H. Khoo, M. Tran, C. K. Gan, F. Ernult and C. Panagopoulos, "Tunable room-temperature magnetic skyrmions in Ir/Fe/Co/Pt multilayers," *nature materials,* vol. 16, pp. 898-904, 2017.

[49] A. Fert, N. Reyren and V. Cros, "Magnetic skyrmions: advances in physics and potential applications," *nature reviews materials,* vol. 2, no. 17031, 2017.

[50] M. Finazzi, M. Savoini, A. Khorsand, A. Tsukamoto, A. Itoh, L. Duo, A. Kirilyuk, T. Rasing and M. Ezawa, "Laser-Induced Magnetic Nanostructures with Tunable Topological Properties," *Physical review letters,* vol. 110, no. 177205, 2013.

[51] G. Berruto, I. Madan, Y. Murooka, G. Vanacore, E. Pomarico, J. Rajeswari, R. Lamb, P. Huang, A. Kruchkov, Y. Togawa, T. LaGrange, D. McGrouther, H. Rønnow and F. Carbone, "Laser-Induced Skyrmion Writing and Erasing in an Ultrafast Cryo-Lorentz Transmission Electron Microscope," *Physical review letters,* vol. 120, no. 117201, 2018.

[52] N. Kiselev, A. Bogdanov, R. Schäfer and U. Rossler, "Chiral skyrmions in thin magnetic films: new objects for magnetic storage technologies ?," *J. Phys. D,* vol. 44, no. 392001, 2011.

[53] A. Bernand-Mantel, L. Camosi, A. Wartelle, N. Rougemaille, M. Darques and L. Ranno, "The skyrmion-bubble transition in a ferromagnetic thin film," *arXiv:1712.03154v3 [cond-mat.mtrl-sci],* 2018.

[54] F. Büttner, I. Lemesh and G. Beach, "Theory of isolated magnetic skyrmions : From fundamentals to room temperature applications," *Scientific reports,* vol. 8, no. 4464, 2018.

[55] W. Jiang, P. Upadyhya, W. Zhang, G. Yu, M. B. Jungfleisch, F. Y. Fradin, J. E. Pearson, Y. Tserkovnyak, K. L. Wang, O. Heinonen, S. G. Velthuis and A. Hoffmann, "Blowing magnetic skyrmion bubbles," *Science,* vol. 349, no. 6245, pp. 283-286, 2015.

[56] W. Meiklejohn and C. Bean, "New Magnetic Anisotropy," *Physical Review,* vol. 102, no. 5, 1956.

[57] R. Stamps, "Mechanisms for exchange bias," *J. Phys. D: Appl. Phys,* vol. 33, pp. R247-R268, 2000.

[58] D. Mauri, H. Siegmann, P. Bagus and E. Kay, "Simple model for thin ferromagnetic films exchange coupled to an antiferromagnetic substrate," *Journal of Applied Physics,* vol. 62, no. 3047, 1987.

[59] A. Malozemoff, "Heisenberg-to-Ising crossover in a random-field model with nniaxial anisotropy," *Physical review B,* vol. 37, no. 13, 1988.

[60] A. Malozemoff, "Mechanisms of exchange anisotropy," *Journal of Applied Physics,* vol. 63, no. 3874, 1988.

[61] A. Malozemoff, "Random-field model of exchange anisotropy at rough ferromagnetic-antiferromagnetic interfaces," *Physocal review B,* vol. 35, no. 7, 1987.

[62] J. Nogués and I. Schuller, "Exchange bias," *JMMM,* vol. 192, pp. 203-232, 1999.

[63] A. Berkowitz and K. Takano, "Exchange anisotropy - a review," *JMMM,* vol. 200, pp. 552-570, 1999.

[64] V. Baltz, B. Rodmacq, A. Zarefy, I. Lechevallier and B. Dieny, "Bimodal distribution of blocking temperature in exchange-biased ferromagnetic/antiferromagnetic bilayers," *Physical review B,* vol. 81, no. 052404, 2010.

[65] V. Baltz, "Thermally driven asymmetric responses of grains versus spin-glass related distributions of blocking temperature in exchange biased Co/IrMn bilayers," *Applied physics letters,* vol. 102, no. 062410, 2013.

[66] V. Baltz, "Antiferromagnets for spintronics: exchange bias, spin dependent transport," *HDR Thesis (Habilitation à diriger des recherches),* 2014.

[67] N. Bergeard, M. Hehn, S. Mangin, G. Lengaigne, F. Montaigne, M. Lalieu, B. Koopmans and G. Malinowski, "Hot-Electron-Induced Ultrafast Demagnetization in Co=Pt Multilayers," *Physical review letters,* vol. 117, no. 147203, 2016.

[68] Y. Yang, R. Wilson, J. Gorchon, C.-H. Lambert, S. Salahuddin and J. Bokor, "Ultrafast magnetization reversal by picosecond electrical pulses," *Science advances,* vol. 3, no. 1603117, 2016.

[69] I. Radu, K. Vahaplar, C. Stamm, T. Kachel, N. Pontius, H. Durr, T. Ostler, J. Barker, R. Evans, R. Chantrell, A. Tsukamoto, A. Itoh, A. Kirilyuk, T. Rasing and A. Kimel, "Transient ferromagnetic-like state mediating ultrafast reversal of antiferromagnetically coupled spins," *nature,* vol. 472, pp. 205-208, 2011.

[70] A. Khorsand, M. Savoini, A. Kirilyuk, A. Kimel, A. Tsukamoto, A. Itoh and T. Rasing, "Element-Specific Probing of Ultrafast Spin Dynamics in Multisublattice Magnets with Visible Light," *Physical review letters,* vol. 110, no. 107205, 2013.

[71] M. Lalieu, M. Peeters, S. Haenen, R. Lavrijsen and B. Koopmans, "Deterministic all-optical switching of synthetic ferrimagnets using single femtosecond laser pulses," *Physical review B,* vol. 96, no. 220411(R), 2017.

[72] A. Hassdenteufel, B. Hebler, C. Schubert, A. Liebig, M. Teich, M. Helm, M. Aeschlimann, M. Albrecht and R. Bratschitsch, "Thermally assisted all-optical helicity dependent magnetic switching in amorphous Fe100–xTbx alloy films," *Advanced Materials,* vol. 25, no. 22, pp. 3122-3128, 2013.

[73] A. Hassendeuteufel, J. Schmidt, C. Schubert, B. Hebler, M. Helm, M. Albrecht and R. Bratschitsch, "Low remanence criterion for helicity-dependent all-optical magnetic switching in ferrimagnets and heterostructures," *Physical review B,* vol. 91, no. 104331, 2015.

[74] M. El Hadri, M. Hehn, P. Pirro, C.-H. Lambert, G. Malinowski, E. Fullerton and S. Mangin, "Domain size criterion for the observation of all-optical helicity-dependent switching in magnetic thin films," *Physical review B,* vol. 94, no. 064419, 2016.

[75] R. Medapalli, D. Afanasiev, D. Kim, Y. Quessab, S. Manna, S. Montoya, A. Kirilyuk, T. Rasing, A. Kimel and E. Fullerton, "Multiscale dynamics of helicity-dependent all-optical magnetization reversal in ferromagnetic Co/Pt multilayers," *Physical review B,* vol. 96, no. 224421, 2017.

[76] Y. Quessab, R. Medapalli, M. El Hadri, M. Hehn, G. Malinowski, E. Fullerton and S. Mangin, "Helicity-dependent all-optical domain wall motion in ferromagnetic thin films," *Pysical review B,* vol. 97, no. 5, 2018.

[77] M. S. El Hadri, M. Hehn, G. Malinowski and S. Mangin, "Materials and devices for all-optical helicity-dependent switching," *Journal of Physics D: Applied Physics,* vol. 50, no. 133002, 2017.

[78] M. El Hadri, "Magnetization reversal mechanism leading to all-optical helicity-dependent switching," *Ph.D Thesis, Université de Lorraine,* 2016.

[79] L. Landau and E. Lifschitz, "On the theory of the dispersion of magnetic permeability in ferromagnetic bodies," *Phys. Z. Sowjet,* vol. 153, pp. 101-114, 1935.

[80] T. L. Gilbert, "A phenomenological theory of damping in ferromagnetic materials," *IEEE Transactions on Magnetics,* vol. 40, pp. 3443-3449, 2004.

[81] W. Brown, "Thermal fluctuation of fine ferromagnetic particles," *IEEE Transactions on Magnetics,* vol. 15, pp. 1196-1208, 2014.

[82] F. Bloch, "Nuclear Induction," *Physical review,* vol. 70, no. 7 and 8, 1946.

[83] U. Atxitia, O. Chubykalo-Fesenko, N. Kazantseva, D. Hinzke, U. Nowak and R. Chantrell, "Micromagnetic modeling of laser-induced magnetization dynamics using the Landau-Lifschitz-Bloch equation," *Applied physics letters,* vol. 91, no. 232507, 2007.

[84] J. Van der Ziel, P. Pershan and L. Malmstrom, "Optically-induced magnetization resulting from the inverse Faraday effect," *Physical review letters,* vol. 15, no. 5, 1965.

[85] L. Pitaevskii, "Electric forces in a transparent dispersive medium," *Sov. Phys. JETP,* vol. 12, no. 1008, 1961.

[86] P. Pershan, J. Van der Ziel and L. Malmstrom, "Theoretical discussion of the inverse Faraday effect, Raman scattering, and related phenomena," *Physical review,* vol. 143, no. 574, 1966.

[87] A. Kimel, A. Kirilyuk, P. Usachev, R. Pisarev, A. Balbashov and T. Rasing, "Ultrafast non-thermal control of magnetization by instantaneous photomagnetic pulses," *nature,* vol. 435, no. 2, 2005.

[88] M. Battiato, G. Barbalinardo and P. Oppeneer, "Quantum theory of the inverse Faraday effect," *Physical review B,* vol. 89, no. 014413, 2014.

[89] K. Vahaplar, A. Kalashnikova, A. Kimel, S. Gerlach, D. Hinzke, U. Nowak, R. Chantrell, A. Tsukamoto, A. Itoh, A. Kirilyuk and T. Rasing, "All-optical magnetization reversal by circularly polarized laser pulses: Experiment and multiscale modeling," *Physical review B,* vol. 85, no. 104402, 2012.

[90] A. Khorsand, M. Savoini, A. Kirilyuk, A. Kimel, A. Tsukamoto, A. Itoh and T. Rasing, "Role of Magnetic Circular Dichroism in All-Optical Magnetic Recording," *Physical review letters,* vol. 108, no. 127205, 2012.

[91] J. Gorchon, Y. Yang and J. Bokor, "Model for multishot all-thermal all-optical switching in ferromagnets," *Physical review B,* vol. 94, no. 020409, 2016.

[92] W. Brown, "Thermal Fluctuations of a Single-Domain Particle," *Physical review,* vol. 130, no. 1677, 1963.

[93] J. A. Thornton, "High rate thick film growth," *Ann. Rev. Mater. Sci.,* vol. 7, pp. 239-260, 1977.

[94] E. E. Fullerton, I. K. Schuller, H. Vanderstraeten and Y. Bruynseraede, "Structural refinement of superlattices from x-ray diffraction," vol. 45, no. 16, 1992.

[95] M. Faraday, "Experimental researches in electricity," *Phylosophical transactions of the royal society of London,* vol. 136, pp. 1-60, 1846.

[96] J. Kerr, "On rotation of the plane of polarization by reflection from the pole of a magnet," *The Londonc, Edinburgh, and Dublin Philosophical Magazine and Journal of Science,* vol. 3, no. 1877, 1877.

[97] M. Freiser, "A Survey of Magnetooptic Effects," *IEEE Transactions on Magnetics,* vol. 4, no. 2, pp. 152-161, 1968.

[98] S. Foner, "Versatile and sensitive vibrating-sample magnetometer," *Review on scientific instruments,* vol. 30, pp. 548-557, 1959.

[99] "http://www.lao.cz/data/ke-stazeni/MPMS_SQUID_VSM_eu_1_.pdf".

[100] P. Moulton, "Spectroscopic and laser characteristics of Ti:Al203," *J. Opt. Soc. Am. B,* vol. 3, no. 1, 1988.

[101] K. Wall and A. Sanchez, "Titanium Sapphire Lasers," *L. Lab. J.,* vol. 3, no. 3, 1990.

[102] D. Strickland and G. Mourou, "Compression of amplified chirped optical pulses," *Optics communications,* vol. 56, no. 3, 1985.

[103] "https://laser.gist.ac.kr/board/bbs/board.php?bo_table=rese_01, Extracted in September 2018.".

[104] P. Vallobra, T. Fache, L. Zhang, G. Malinowski, M. Hehn, J.-C. Rojas-Sánchez, E. Fullerton and S. Mangin, "Manipulating exchange bias using all-optical helicity-dependent switching," *Physical review B,* vol. 96, no. 144403, 2017.

[105] D. Weller, Y. Wu, J. Stohr, M. Samant, B. Hermsmeier and C. Chappert, "Orbital magnetic moments of Co in multilayers with perpendicular magnetic anisotropy," *Physical review B,* vol. 49, no. 18, 1994.

[106] G. Schütz, S. Stähler, M. Knülle, P. Fischer, S. Parkin and H. Ebert, "Distribution of magnetic moments in Co/Pt and Co/Pt/Ir/Pt multilayers detected by magnetic x-ray absorption," *Journal of Applied Physics,* vol. 73, no. 6430, 1993.

[107] K. Kyuno, J.-G. Ha, R. Yamamoto and S. Asano, "Theoretical study on the strain dependence of the magnetic anisotropy of X/Co(X=Pt,Cu, Ag, and Au) metallic multilayers," *Journal of Applied Physics,* vol. 79, no. 7084, 1996.

[108] A. Kohn, A. Kovács, R. Fan, G. McIntyre, R. Ward and J. Goff, "The antiferromagnetic structures of IrMn3 and their influence on exchange-bias," *Scientific Reports,* vol. 3, no. 2412, 2013.

[109] J. Nozières, S. Jaren, Y. Zhang, A. Zeltser, K. Pentek and V. Speriosu, "Blocking temperature distribution and long-term stability of spin-valve structures with Mn-based antiferromagnets," *Journal of applied physics,* vol. 87, no. 3920, 2000.

[110] A. Devasahayam and M. Kryder, "The dependence of the antiferromagnet/ferromagnet blocking temperature on antiferromagnet thickness and deposition conditions," *Journal of Applied Physics,* vol. 85, no. 5519, 1999.

[111] G. Malinowski, M. Hehn, S. Robert, O. Lenoble and A. Schuhl, "Magnetic origin of enhanced top exchange biasing in Py/IrMn/Py multilayers," *Physical review B,* vol. 68, no. 184404, 2003.

[112] G. Vallejo-Fernandez, L. Fernandez-Outon and K. O'Grady, "Antiferromagnetic grain volume effects in metallic polycrystalline exchange bias systems," *Journal of physics D: Applied Physics,* vol. 41, no. 112001, 2008.

[113] F. Garcia, J. Sort, B. Rodmacq, S. Auffret and B. Dieny, "Large anomalous enhancement of perpendicular exchange bias by introduction of a nonmagnetic spacer between the ferromagnetic and antiferromagnetic layers," *Applied Physics Letters,* vol. 83, no. 3537, 2003.

[114] A. Zarefy, L. Lechevallier, R. Lardé, H. Chiron, J.-M. Le Breton, V. Baltz, B. Rodmacq and B. Dieny, "Influence of Co layer thickness on the structural and magnetic properties of (Pt/Co)3/Pt/IrMn multilayers," *Journal of Physics D: Applied Physics,* vol. 43, no. 215005, 2010.

[115] S. van Dikjen, J. Moritz and J. Coey, "Correlation between perpendicular exchange bias and magnetic anisotropy in IrMn/[Co/Pt]n and [Pt/Co]n/IrMn multilayers," *Journal of applied physics,* vol. 97, no. 063907, 2005.

[116] G. Malinowski, S. van Dijken, M. Czapkiewicz and T. Stobiecki, "Correlation between exchange bias dynamics and magnetization reversal asymmetry in [Pt/Co]3/Pt/IrMn multilayers," *Applied physics letters,* vol. 90, no. 082501, 2007.

[117] H. van Kesteren and W. Zeper, "Controlling the Curie temperature of Co/Pt multilayer magneto-optical recording media," *Journal of Magnetism and Magnetic Materials,* vol. 120, pp. 271-273, 1993.

[118] A. Mekonnen, A. Khorsand, M. Cormier, A. Kimel, A. Kirilyuk, A. Hrabec, L. Ranno, A. Tsukamoto, A. Itoh and T. Rasing, "Role of the inter-sublattice exchange coupling in short-laser-pulse-induced demagnetization dynamics of GdCo and GdCoFe alloys," *Physical review B,* vol. 87, no. 180406(R), 2013.

[119] M. Vomir, R. Turnbull, I. Birced, P. Parreira, D. A. MacLaren, S. L. Lee, P. André and J.-Y. Bigot, "Dynamical Torque in CoxFe3–xO4 Nanocube Thin Films Characterized by Femtosecond Magneto-Optics: A π-Shift Control of the Magnetization Precession," *Nanoletters,* vol. 16, no. 8, pp. 5291-5297, 2016.

[120] T. Hughes, K. O'Grady, H. Laidler and R. Chantrell, "Thermal activation in exchange biased bilayers," *Journal of Magnetism and Magnetic Materials,* vol. 235, pp. 329-336, 2001.

[121] G. Ju, A. Nurmikko, R. Farrow, R. Marks, M. Carey and B. Gurney, "Ultrafast Time Resolved Photoinduced Magnetization Rotation in a Ferromagnetic/Antiferromagnetic Exchange Coupled System," *Physical review letters,* vol. 82, no. 18, 1999.

[122] F. Dalla Longa, J. Kohlhepp, W. de Jonge and B. Koopmans, "Resolving the genuine laser-induced ultrafast dynamics of exchange interaction in ferromagnet/antiferromagnet bilayers," *Physicalreview B,* vol. 81, no. 094435, 2010.

[123] A. Porat, S. Bar-Ad and I. Schuller, "Novel laser-induced dynamics in exchange-biased systems," *EPL,* vol. 87, no. 67001, 2009.

[124] M. El Hadri, P. Pirro, C.-H. Lambert, N. Bergeard, S. Petit-Watelot, M. Hehn, G. Malinowski, F. Montaigne, Y. Quessab, R. Medapalli, E. Fullerton and S. Mangin, "Electrical characterization of all-optical helicity-dependent switching in ferromagnetic Hall crosses," *Applied Physics Letters,* vol. 108, no. 092405, 2016.

[125] S. Ideka, J. Hayakawa, Y. Ashizawa, Y. Lee, K. Miura, H. Hasegawa, M. Tsunoda, F. Matsukara and H. Ohno, "Tunnel magnetoresistance of 604% at 300K by suppression of Ta diffusion in CoFeB/MgO/CoFeB pseudo-spin-valves annealed at high temperature," *Applied Physic Letters,* vol. 93, no. 082508, 2008.

[126] S. Ideka, K. Miura, H. Yamamoto, K. Mizunuma, H. Gan, M. Endo, S. Kanai, J. Hayakawa, F. Matsukura and H. Ohno, "A perpendicular-anisotropy CoFeB–MgO magnetic tunnel junction," *nature materials,* vol. 9, no. 2804, 2010.

[127] B. Cui, C. Song, G. Wang, Y. Wang, F. Zeng and F. Pan, "Perpendicular magnetic anisotropy in CoFeB/X (X = MgO, Ta, W, Ti, and Pt) multilayers," *Journal of Alloys and Compounds,* vol. 559, pp. 112-115, 2013.

[128] Y. Zhu, Z. Zhang, B. Ma and Q. Jin, "Thermal stability of CoFeB/Pt multilayers with perpendicular magnetic anisotropy," *Journal of Applied Physics,* vol. 111, no. 07C106, 2012.

[129] J. Scola, H. Polovy, C. Fermon, M. Pannetier-Lecœur, G. Feng, K. Fahy and J. Coey, "Noise in MgO barrier magnetic tunnel junctions with CoFeB electrodes: Influence of annealing temperature," *Applied Physics Letters,* vol. 90, no. 252501, 2007.

[130] K. Oguz, P. Jivrajka, M. Venkatesan, G. Feng and J. Coey, "Magnetic dead layers in sputtered Co40Fe40B20 films," *Journal of Applied Physics,* vol. 103, no. 07B526, 2008.

[131] R. Shimabukuro, K. Nakamura, T. Akiyama and T. Ito, "Electric fieldeffectsonmagnetocrystallineanisotropyinferromagnetic Fe monolayers," *Physica E,* vol. 42, pp. 1014-1017, 2010.

[132] M. E. Fisher and M. N. Barber, "Scaling Theory for Finite-Size Effects in the Critical Region," *Physical review letters,* vol. 28, no. 1516, 1972.

[133] U. Atxiatia, D. Hinzke and U. Nowak, "Fundamentals and applications of the Landau–Lifshitz–Bloch equation," *Journals of Physics D: Applied ,* vol. 50, no. 3, 2016.

[134] S. Selzer, U. Atxitia, U. Ritzmann, D. Hinzke and U. Nowak, "Inertia-Free Thermally Driven Domain-Wall Motion in Antiferromagnets," *Physical reviw letters,* vol. 117, no. 107201, 2016.

[135] S. Gerlach, L. Oroszlany, D. Hinzke, S. Sievering, S. Wienholdt, L. Szunyogh and U. Nowak, "Modeling ultrafast all-optical switching in synthetic ferrimagnets," *Physical review B,* vol. 95, no. 224435, 2017.

[136] J. Gorchon, C.-H. Lambert, Y. Yang, A. Pattabi, R. Wilson, S. Salahuddin and J. Bokor, "Single shot ultrafast all optical magnetization switching of ferromagnetic Co/Pt multilayers," *Applied physics letters,* vol. 11, no. 042401, 2017.

[137] F. den Broeder, E. Janssen, W. Hoving and W. Zeper, "Perpendicular Magnetic Anisotropy and Coercivity of Co/Ni Multilayers," *IEEE TRANSACTIONS ON MAGNETICS,* vol. 28, no. 5, 1992.

[138] D. Lau, V. Sundar, J.-G. Zhu and V. Sokalski, "Energetic molding of chiral magnetic bubbles," *Physical review B,* vol. 060401, 2016.

[139] H. Yang, A. Thiaville, S. Rohart, A. Fert and M. Chshiev, "Anatomy of Dzyaloshinskii-Moriya Interaction at Co/Pt Interfaces," *Physical review letters,* vol. 115, no. 267210, 2015.

[140] J. W. Knepper and F. Y. Yang, "Oscillatory interlayer coupling in Co/Pt multilayers with perpendicular anisotropy," *Physical review B,* vol. 71, no. 224403, 2005.

[141] J. Swerts, S. Mertens, T. Lin, S. Couet, Y. Tomczak, K. Sankaran, G. Pourtois, W. Kim, J. Meersschaut, L. Souriau, D. Radisic, S. Van Elschocht, G. Kar and A. Furnemont, "BEOL compatible high tunnel magneto resistance perpendicular magnetic tunnel junctions using a sacrificial Mg layer as CoFeB free layer cap," *Applied Physics Letters,* vol. 106, no. 262407, 2015.

[142] S. Bandiera, R. Sousa, B. Rodmacq and B. Dieny, "Enhancement of perpendicular magnetic anisotropy through reduction of Co-Pt interdiffusion in (Co/Pt) multilayers," *Applied physics letters,* vol. 100, no. 142410, 2012.

[143] A. Wells, P. Shepley, C. Marrows and T. Moore, "Effect of interfacial intermixing on the Dzyaloshinskii-Moriya interaction in Pt/Co/Pt," *Physical review B,* vol. 95, no. 054428, 2017.

[144] D.-Y. Kim, M.-H. Park, Y.-K. Park, J.-S. Kim, Y.-S. Nam, D.-H. Kim, S.-G. Je, H.-C. Choi, B.-C. Min and S.-B. Choe, "Chirality-induced antisymmetry in magnetic domain wall speed," *NPG Asia Materials,* vol. 10, no. e464, 2018.

[145] R. Soucaille, M. Belmeguenai, J. Torrejon, J.-V. Kim, T. Devolder, Y. Roussigné, S.-M. Chérif, A. Stashkevich, M. Hayashi and J.-P. Adam, "Probing the Dzyaloshinskii-Moriya interaction in CoFeB ultrathin films using domain wall creep and Brillouin light spectroscopy," vol. 94, no. 104431, 2016.

[146] S.-G. Je, P. Vallobra, T. Srivastava, J.-C. Rojas-Sanchez, T. H. Pham, M. Hehn, G. Malinowski, C. Baraduc, S. Auffret, G. Gaudin, S. Mangin, S. Béa and O. Boulle, "Creation of Magnetic Skyrmion Bubble Lattices by Ultrafast Laser in Ultrathin Films," *Nano letters,* vol. 18, no. 11, 2018.

[147] N. Saratz, U. Ramsperger, A. Vindigni and D. Pescia, ". Irreversibility, reversibility, and thermal equilibrium in domain patterns of Fe films with perpendicular magnetization," *Physical review B,* no. 184416, 2010.

[148] T. Srivastava, M. Schott, R. Juge, V. Krizakova, M. Belmeguenai, Y. Roussigné, A. Bernand-Mantel, L. Ranno, S. Pizzini, S.-M. Chérif, A. Stashkevich, S. Auffret, O. Boulle, G. Gaudin, M. Chshiev, C. Baraduc and H. Béa, "Large voltage tuning of Dzyaloshinskii-Moriya Interaction: a route towards dynamic control of skyrmion chirality," *Nanoletters,* 2018.

[149] S.-Z. Lin, C. Reichhardt, C. Batista and A. Saxena, "Particle model for skyrmions in metallic chiral magnets: Dynamics, pinning, and creep," *PHYSICAL REVIEW B,* vol. 87, no. 214419, 2013.

[150] X. Zhang, G. Zhao, H. Fanghor, J. Liu, W. Xia and F. Morvan, "Skyrmion-skyrmion and skyrmion-edge repulsions in skyrmion-based racetrack memory," vol. 5, no. 7643, 2015.

[151] M. Benitez, A. Hrabec, A. Mihai, T. Moore, G. Burnell, D. McGrouther, C. Marrows and S. McVitie, "Magnetic microscopy and topological stability of homochiral Néel domain walls in a Pt/Co/AlOx trilayer," *nature communications,* vol. 6, no. 8957, 2015.

[152] L. Caretta, M. Mann, F. Büttner, K. Ueda, B. Pfau, C. M. Günther, P. Hessing, A. Churikova, C. Klose, M. Schneider, D. Engel, C. Marcus, D. Bono, K. Bagschik, S. Eisebit and G. Beach, "Fast current-driven domain walls and small skyrmions in a compensated ferrimagnet," *nature nanotechnology,* vol. 10, no. 1038, 2018.

[153] T. Ostler, J. Barker, R. Evans, R. Chantrell, U. Atxitia, O. Chubykalo-Fesenko, S. El Moussaoui, L. Le Guyader, E. Mengotti, L. Heyderman, F. Nolting, A. Tsukamoto, A. Itoha, D. Afanasiev, B. Ivanov, A. Kalashnikova, K. Vahaplar, J. Mentink, A. Kirilyuk, T. Rasing and A. Kimel, "Ultrafast heating as a sufficient stimulus for magnetization reversal in a ferrimagnet," *nature communications,* vol. 3, no. 666, 2012.

[154] H. Okamoto, "The Ir-Mn (Iridium-Manganese) system," *Journal of Phase Equilibria,* vol. 17, pp. 60-62, 1996.

[155] M. Bersweiler, "From Sm1-xGdxAl2 electronic properties to magnetic tunnel junctions based on Sm1-xGdxAl2 and/or [Co/Pt] electrodes: Towards the integration of Zero Magnetization ferromagnets in spintronic devices," *Ph.D thesis Université de Lorraine,* 2014.

[156] M. Ali, P. Adie, C. Marrows, D. Greig, B. Hickey and R. Stamps, "Exchange bias using a spin glass," *nature materials,* vol. 6, pp. 70-75, 2007.

[157] S. Anisimov, B. Kapeliovich and T. Perel'man, "Electron emission from metal surfaces exposed to ultrashort laser pulses," *JETP,* vol. 39, no. 2, p. 375, 1974.

[158] H. Ebert, "Magneto-optical effects in transition metal systems," *Rep. Prog. Phys.,* vol. 59, pp. 1665-1735, 1996.

[159] T. Cornelissen, R. Córdoba and B. Koopmans, "Microscopic model for all optical switching in ferromagnets," *Applied physics letters,* vol. 108, no. 142405, 2016.

[160] A. Kirilyuk, A. Kimel and T. Rasing, "Ultrafast optical manipulation of magnetic order," *Reviews of modern physics,* vol. 82, pp. 2732-2779, 2010.

[161] F. Wihelm, P. Poulopoulos, G. Ceballos, H. Wende, K. Baberschke, P. Srivastava, D. Benea, H. Ebert, M. Angelakeris, N. Flevaris, D. Niarchos, A. Rogalev and N. Brookes, "Layer-Resolved Magnetic Moments in Ni/Pt Multilayers," *Physical Review Letters,* vol. 85, no. 2, 2000.

[162] C. Kittel, "Physical Theory of Ferromagnetic Domains," *Review of Modern Physics,* vol. 21, no. 4, 1949.

[163] B. Abbott and et al., "Observation of Gravitational Waves from a Binary Black Hole Merger," *Physical review letters,* vol. 116, no. 061102, 2016.

[164] A. Einstein, *Sitzungsber. K. Preuss. Akad. Wiss.,* vol. 1, no. 688, 1916.

[165] A. Einstein, *Sitzungsber. K. Preuss. Akad. Wiss.,* vol. 1, no. 154, 1918.

[166] G. Binasch, P. Grünberg, F. Saurenbach and W. Zinn, "Enhanced magnetoresistance in layered magnetic structures with antiferromagnetic interlayer exchange," *Physical review B,* vol. 39, no. 4828(R), 1989.

Abstract

During the last 20 years, nanomagnetism has attracted a growing interest in the scientific community due to its multiple applications for magnetic memories. At the nanometer scale, many of the properties of the magnetic materials arise from their interfaces with other materials (magnetic or non-magnetic). This explains the omnipresence of heterostructures composed of several layers of thicknesses in the range of the nanometer in the field of nanomagnetism. In the heterostructures we study, those interfacial properties are the exchange bias, the Dzyaloshinskii-Moriya interaction, the perpendicular magnetic anisotropy and the interlayer exchange between two ferromagnetic layers. First we study the modification of the exchange bias field in a [Pt/Co]xN/IrMn bilayer when we expose it to laser pulses of a femtosecond circularly polarized light. We demonstrate that the final exchange bias field after laser pulses results from the magnetic configuration of the [Pt/Co]xN multilayer. We then study the conditions required for a helicity-dependent all optical switching of a synthetic ferromagnetic material composed of a CoFeB /Pt /CoFeB and a Co ferromagnetic layers coupled antiferromagnetically and conclude that the key factors that drive the switching of the total magnetization are the Curie temperatures of both layers. We focused also on the field-driven propagation of Néel domain walls of the same chirality stabilized by the Dzyaloshinskii-Moriya interaction in [Pt/Co/Ni]xN multilayers. We finally demonstrated the possibility to generate skyrmionic bubbles with the femtosecond laser.

Keywords: All optical switching, exchange bias, Dzyaloshinskii-Moriya interaction

Résumé

Pendant les 20 dernières années, le nanomagnétisme a suscité un intérêt grandissant au sein de la communauté scientifique du fait de ses nombreuses applications pour les mémoires magnétiques. A l'échelle nanométrique beaucoup de propriétés des matériaux magnétiques découlent de leurs interfaces avec d'autres matériaux (magnétiques ou non). Cela explique l'omniprésence des hétérostructures composées de plusieurs couches d'épaisseur nanométrique dans le domaine du nanomagnétisme. Dans les hétérostructures que nous étudions, ces propriétés interfaciales sont le décalage d'échange, l'interaction Dzyaloshinskii-Moriya, l'anisotropie magnétique perpendiculaire et l'échange entre deux couches ferromagnétiques. D'abord nous étudions la modification du champ de décalage d'échange dans une bicouche [Pt/Co]xN/IrMn lorsque l'on l'expose à des impulsions laser de lumière polarisée circulairement. Nous montrons que le champ de décalage d'échange après exposition au laser résulte de la configuration du ferromagnétique [Pt/Co]xN. Nous étudions ensuite les conditions nécessaires à un retournement tout optique dépendant de l'hélicité d'un matériau ferrimagnétique de synthèse composé de deux couches de CoFeB /Pt /CoFeB et Co couplées antiferromagnétiquement et concluons que les facteurs clés qui gouvernent le renversement de l'aimantation totale sont les températures respectives des deux couches. Nous nous sommes aussi concentrés sur la propagation de parois de domaine de Néel de même chiralité stabilisées par interaction Dzyaloshinskii-Moriya dans des multicouches de $[Pt/Co/Ni]_N$. Nous avons finalement démontré la possibilité de générer des bulles skyrmioniques par le laser femtoseconde.

Mots clés : Retournement tout optique, décalage d'échange, interaction Dzyaloshinskii-Moriya